Computer Simulations of CO_2 Absorption in Amino Acid Ionics & Ion Conduction in Alkali Metal Battery Electrolytes

A
thesis submitted
In partial fulfilment of the requirements for the degree of

DOCTOR OF PHILOSOPHY

by

Prabhat Prakash

Roll No. 20143344

Indian Institute of Science Education and Research, Pune

2019

अभिकलित्र अनुकार द्वारा
अमीनो-अम्ल आयनिकों में कार्बन डाइऑक्साइड के अवशोषण
तथा
क्षार धातु बैटरी विद्युतपघट्यों में आयन चालन का अध्ययन

विद्यावाचस्पति

की उपाधि की आंशिक प्रति पूर्ति हेतु प्रस्तुत शोध-प्रबंध

प्रस्तुतकर्ता

प्रभात प्रकाश

अनुक्रमांक २०१४३३४४

भारतीय विज्ञान शिक्षण एवं अनुसन्धान संस्थान, पुणे

२०१९

Certificate

Certified that the work incorporated in the thesis entitled “Computer Simulations of CO_2 Absorption in Amino Acid Ionics & Ion Conduction in Alkali Metal Battery Electrolytes”, submitted by Prabhat Prakash was carried out by the candidate, under my supervision. The work presented here or any part of it has not been included in any other thesis submitted previously for the award of any degree or diploma from any other University or institution.

Date: Dr. Arun Venkatnathan

Supervisor

Declaration

I declare that this written submission represents my ideas in my own words and where others' ideas have been included, I have adequately cited and referenced the original sources. I also declare that I have adhered to all principles of academic honesty and integrity and have not misrepresented or fabricated or falsified any idea/data/fact/source in my submission. I understand that violation of the above will be cause for disciplinary action by the Institute and can also evoke penal action from the sources which have thus not been properly cited or from whom proper permission has not been taken when needed.

Date: March 31, 2020 Prabhat Prakash

Dedicated to my parents

Acknowledgements

Firstly, I express my sincere gratitude to all my teachers, who taught me the sheer purpose of knowledge, education, and experiments, at various stages of life. I thank my research supervisor Dr. Arun Venkatnathan for his valuable suggestions, continuous support and extensive encouragement throughout what is considered the last class of higher education. I thank him to tolerate blunt inquisitiveness and low patience of mine. His suggestions while tackling challenging problems and generosity towards my failures aided me to be on the path during this whole time.

Dr. Kumar Vanka and Dr. Pramod Pillai, who provided inputs and recommendations as my Research Advisory Committee members, for the last couple of years. Dr. Arnab Mukherjee and Dr. Suman Chakraborty for their advices as my Research Advisory Committee members for the first couple of years of my PhD. Dr. Srabanti Choudhury, Dr. Anirban Hazra and Dr. Prasenjit Ghosh for fruitful discussions and curricular advice.

Dr. Michael Zdilla and Prof. Stephanie Wunder (Temple University), who were always open and accessible for any discussion and advice. I thank them for teaching me various experimental aspects and being patient with my questions.

Prof. S. K. Sengupta (BHU), Dr. Biswajit Maity (BHU), Prof. Ranjit Biswas (SN Bose NCBS), Dr. Indrasen Singh (IIT Indore) for the motivations to pursue a career in scientific research. For their believe in me, which I did not had at the time I discussed my career choices with them.

The lab members of Venkatnathan lab- Minal, Praveen, Rakesh, Ardhra and Anna for all the scientific and non-scientific discussions and the fun we have had in the last few years. The lab members of Zdilla and Wunder labs at Temple University. Birane Fall and Jordan Aguirre for performing the majority of experiments included in this thesis, and to teach me various experimental techniques during my tenure at Temple U.

All the colleagues/friends from other theoretical/experimental groups at IISER Pune. My friends Ram Prakash Tripathi, Aalok Mishra and Raza Hussain, from BHU, who were there to make my world full of fun, and to discuss any topic outside research. Bappa Ghosh, Divya Singh and Shubham Singh, from IISER, who were my encyclopaedia and complaint box at the same time. Sumanth and Abhijit for hosting me in a most comfortable house during Temple visits. Raja Ghosh who became an integral part of the discussions in and outside research; whose brutally honest opinions and suggestions kept my self-appraisal in control. Rashmi Singh, for being my punching bag for any trouble/issue I faced in my personal or professional time.

Officials at chemistry office and academic office at IISER Pune, especially Tushar and Mayuresh, United States-India Education Foundation at New Delhi, especially , and Foreign Fulbright Program and Temple University at USA for their continuous support during my tenure as a Fulbright Nehru visiting researcher.

Ministry of Human Resources and Development Govt. of India for my graduate fellowship. I thank Department of Chemistry and IISER Pune for computational and other research infrastructure support.

My family members, Saurabh, Kirti, Pragati, Gaurav, Anil, and others for being always there for me.

IISER Pune Prabhat Prakash

Table of Contents

Ease of access in reading an electronic copy of this document:

- The above table of contents is hyperlinked to respective chapters/subchapters/appendix. For example, to follow section 2.1 Introduction, click either on 2.1, or "Introduction" or its page number.
- Opening this document in a document viewer will also provide a bookmark/navigation bar (usually appears as a panel in the left), where contents of the thesis can be easily accessed.
- Additionally, a List of Figures, and a List of Table in the following pages can be used to navigate respective Figures and Tables.
- All the citations of Figures, Tables and Equations (in black bold) are hyperlinked to the corresponding Figures.
- Links to internet content and citation of references are hyperlinked to the corresponding webpages/references.

List of Figures

List of Tables

List of Publications

1. **Prakash, P.**; Venkatnathan, A. Molecular Mechanism of CO_2 Absorption in Phosphonium Amino Acid Ionic Liquid. *RSC Adv.* **2016**, *6*, 55438–55443.

2. **Prakash, P.**; Venkatnathan, A. Site-Specific Interactions in CO_2 Capture by Lysinate Anion and Role of Water Using Density Functional Theory. *J. Phys. Chem. C* **2018**, *122* (24), 12647–12656.

3. **Prakash, P.**; Aguirre, J.; Van Vliet, M. M.; Chinnam, P. R.; Dikin, D. A.; Zdilla, M. J.; Wunder, S. L.; Venkatnathan, A. Unravelling the Structural and Dynamical Complexity of the Equilibrium Liquid Grain-Binding Layer in Highly Conductive Organic Crystalline Electrolytes. *J. Mater. Chem. A* **2018**, *6*, 4394–4404.

4. Fall, B.[†]; **Prakash, P.**[†]; Gau, M. R.; Zdilla, M. J.; Wunder, S. L.; Venkatnathan, A. Experimental and theoretical investigation of the ion conduction mechanism of tris(adiponitrile)perchloratosodium, a self-binding, melt-castable crystalline sodium electrolyte. *Chem. Mater.* **2019,** *31*, 8850–8863.

5. Fall, B.[†]; **Prakash, P.**[†]; Aguirre, J.; Chereddy, S.; Chinnam, P. R.; Dikin, D. A.; Zdilla, M. J.; Wunder, S. L.; Venkatnathan, A. A Soft-Solid Co-Crystalline Electrolyte Combining Advantages of Organics and Ceramics: Thermally, Electrochemically Stable, Highly Conductive (Adiponitrile)2LiPF6. *Manuscript under review.*

6. **Prakash, P.**; Ardhra, S.; Fall, B.; Venkatnathan, A., Zdilla, M. J.; Wunder, S. L. Stoichiometric Conversion, Melting and Dynamics of Ion Conduction in a Solid Cocrystalline Sodium Ion Battery Electrolyte. *Manuscript under preparation.*

[#]7. Gupta, A. K.; Reddy, S. A. D.; Rajasekar, P.; **Prakash, P.**; Boomishankar, R. Chloro-Bridged Hexanuclear Pd(II) Clusters Supported by Cis -Blocking Tris(Imido)Phosphate Trianions. *ChemistrySelect* **2017**, *2* (33), 10636–10641.

[#]8. Kumar, P. [†]; **Prakash, P.** [†]; Ramya, K. R.; Venkatnathan, A. Probing Translational and Rotational Dynamics in Hydrophilic/Hydrophobic Anion Based Imidazolium Ionic Liquid–Water Mixtures. *Soft Matter* **2018**, *14* (29), 6109–6118.

[#] Not included in this thesis

[†] Equal Contribution

List of Abbreviations

AA	Amino Acid
AAIL	Amino-Acid Ionic Liquid
AAS	Amino Acid Salts
ADN	Adiponitrile
B3LYP	Becke-3-parameter, Lee–Yang–Parr functional
BE	Binding Energy
BSSE	Basis Set Superposition Error
CHELPG	CHarges from ELectrostatic Potential (Grid)
CV	Cyclic Voltammetry
DCM	Dicyanomethane
DFT	Density Functional Theory
DMF	*N,N*-dimethylformamide
DSC	Differential Scanning Calorimetry
E_a	Activation Energy
EDS/EDX	Energy Dispersive X-Ray Spectroscopy
EIS	Electrochemical Impedance Spectroscopy
E_{nb}	Non-bonded Interaction Energy
IL	Ionic Liquid
fCP	fragment Counterpoise
FTIR	Fourier Transformed Infra-Red
LIB	Lithium Ion Battery
LICC	Lithium Ion Conducting Ceramic
LICGC	Lithium Ion Conducting Glass Ceramic
LISICON	Lithium Superionic Conductor
LSV	Linear Sweep Voltammetry
Lys	Lysine
Lys^-	Lysinate anion

M06-2X	Minnesota 06 global hybrid functional with 54% HF exchange
MD	Molecular Dynamics
MEA	Monoethanolamine
MEP	Minimum Energy Path
MP2	Møller–Plesset 2nd order perturbation
MSD	Mean Square Displacement
NASICON	Sodium Superionic Conductor
NEB	Nudged Elastic Band
NMR	Nuclear Magnetic Resonance
NpT	Isothermal-Isobaric Ensemble
NVT	Isothermal canonical Ensemble
OPLS-AA	Optimized Parameters for Liquid Simulations-All Atom
P_{4444}^{+}	*tetra*-Butylphosphonium
PAW	Projector Augmented Wave
PBE	Perdew, Burke and Ernzerhof GGA functional
PES	Potential Energy Scan
PXRD	Powder X-Ray Diffraction
PWDFT	Plane-Wave Density Functional Theory
RDF	Radial Distribution Function
RE	Reaction Energy
rig-fCP	rigorous fragment Counterpoise
RT	Room Temperature
RTIL	Room Temperature Ionic Liquid
SDF	Spatial Distribution Function
SEI	Solid Electrolyte Interface
SEM	Scanning Electron Microscope
SIB	Sodium Ion Battery
T_d	Decomposition temperature
T_g/T_{gs}	Glass transition temperature
T_m	Melting temperature
TGA	Thermal Gravimetric Analysis
vH ACF	van Hove Autocorrelation Function
XRD	X-Ray Diffraction
ZPE	Zero Point Energy

Abstract

This thesis presents modeling and simulations on absorbents for carbon dioxide capture and electrolytes for Li^+/Na^+ ion batteries.

In the first part of the thesis, Lysine amino acid based Ionic Liquids (IL) and Salts (AAS) are explored as potential replacements for conventional absorbents for carbon capture like amines, amine-alcohol blends, etc. Classical molecular dynamics (MD) simulations are performed to examine the molecular mechanism of CO_2 absorption in [tetrabutylphosphonium$^+$][Lys$^-$] IL. The simulations suggest that an interface of CO_2 molecules form at the IL surface within a short span of tens of picoseconds, and attains saturation around ten nanoseconds, where CO_2 molecules remain absorbed in the bulk IL layers. The interaction and absorption of CO_2 molecules leads a slightly higher mobility of anions than cations due to the preferential interaction of CO_2 molecules. Density Functional Theory (DFT) calculations are also employed to understand the mechanism for Lys$^-$-CO_2 reaction and participation of a single molecule of water in this reaction. The calculations show the existence of various non-bonded complexes and chemical reactions responsible for CO_2 absorption and desorption. The reaction mechanisms in each complex are characterized by energy parameters such as binding energy, activation energy, and reaction energy. The competitive reaction pathways which show the dominance of carbamate over bicarbonate products during CO_2 absorption are also discussed. The simulations and calculations serve as a predictive tool to develop efficient AAILs for CO_2 absorption.

In the second part of the thesis, the thermal stability and mechanism of ion conduction in a new generation of soft-solid *cocrystalline* electrolytes for Lithium and

Sodium Ion Batteries are investigated. Four cocrystalline solid electrolytes composed of alkali metal salts and organic solvents (adiponitrile (ADN) and *N,N*-dimethylformamide (DMF) solvents) in stoichiometric ratios, DMF·LiCl, $(DMF)_3NaClO_4$, $(ADN)_3NaClO_4$ and $(ADN)_2LiPF_6$ are examined for their structural complexity and mechanism of ion conduction. MD simulations on model structures of lithium ion electrolyte, DMF·LiCl, provide an atomic level understanding of various experimental properties: crystal packing arrangement, mechanism of decomposition, existence of a nanolayer of DMF molecules at the surface, and higher mobility of ions at surface compared to bulk. The DFT calculations show that small aggregates on the surface of cocrystal easily decompose compared to the large aggregates in the bulk. In the $(DMF)_3NaClO_4$ electrolyte, MD simulations reveal the mechanism of temperature dependent stoichiometric conversion and crystal melting from the analysis of structural properties. The size and number of ion-pair and ion-solvent clusters as a function of temperature provide proofs of stoichiometric conversion and melting of the electrolyte. The calculated diffusion coefficients at different temperatures show a competitive nature of ionic diffusion and the activation energy barrier calculated for Na^+ migration agrees with experiments. The minimum energy path calculated using periodic DFT calculations shows a S_N2 reaction type, with a planar transition state observed during the Na^+ ion migration, which occurs in one-dimension. The behavior of surface and bulk is modeled in $(ADN)_3NaClO_4$ and $(ADN)_2LiPF_6$ electrolytes, where the thermal stability is found to be in good agreement with TGA and DSC experiments. In contrast to $(DMF)_3NaClO_4$, the conduction of Na^+ ions in $(ADN)_3NaClO_4$ occurs in all the three dimensions via a solvent-anion assisted transition state. The migration of Li^+ ion in $(ADN)_2LiPF_6$ electrolyte was observed to occur via a solvent-only tetrahedral intermediate. The calculated jump probabilities from van-Hove autocorrelation function in these electrolytes provide insights to the contribution of interstitial dislocation in ion conduction.

Chapter 1:
Introduction

The rising concentration of carbon dioxide on the planet has raised concerns and thus the pursuit of eco-friendly and reliable energy storage sources has gained attention [1]. The alarming conditions of habitability on our planet can be addressed with two approaches: i) removal of CO_2 from energy production processes, e.g., gas separation, CO_2/SO_2 absorption, CO_2 reduction during pre- and post- combustion processes [2, 3], and ii) production of *clean energy* using *green materials* [4], e.g., production of lesser waste, safer energy devices, sustainable sources. The study of alternative materials for CO_2 absorption and safer metal ion batteries is one among the various ways to address the challenges in the research field of energy storage and environmental sustainability.

1.1 CARBON DIOXIDE ABSORBENTS

The absorption of post-combustion CO_2 occurs via chemical and/or physical interactions where CO_2 molecules are removed/separated from the exhausts and gas mixtures effectively. Since CO_2 is an acidic gas, where $C(CO_2)$ is an electrophile, a nucleophilic or basic nature for an absorbent is an essential requirement for CO_2 capture. One of the well-known examples for the CO_2 capture is the reaction of ammonia (NH_3) leading to the formation of ammonium carbamate [5]. In general, alkyl amines react with CO_2 in various stoichiometric ratios to produce carbamic acid/carbamates, where the reaction can be written as:

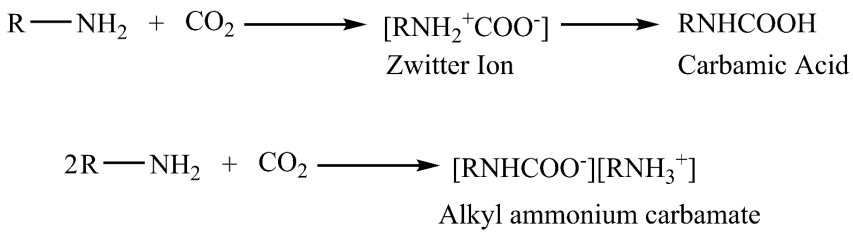

(1.1)

The presence of a single molecule of water leads to donation of a proton to amine (where amine behaves like a base), leading to the formation of hydroxide anions (OH), to produce bicarbonate, as follows:

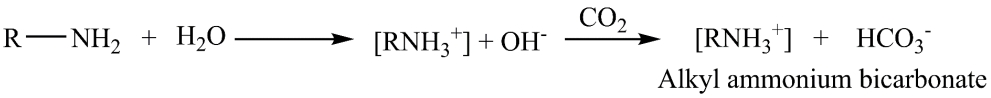

(1.2)

The above mechanisms **(1.1)** and **(1.2)** show that amines, amine-functionalized soft-materials (e.g., Ionic Liquids), and aqueous solutions of amine-salts are potential absorbents for CO_2 capture. The current generation of materials which show high CO_2 uptake are amine based compounds [6]. One of the most promising CO_2 absorbent is monoethanolamine (MEA, HO-CH_2-CH_2-NH_2). Several experimental investigations have been performed to calculate CO_2 uptake efficiency of MEA [7–9]. García-Abuín *et al.* [8] used ^{13}C and ^{1}H NMR techniques to demonstrate that along with bicarbonate, carbamate also forms during the chemisorption of CO_2 in a primary amine like MEA and secondary amines **(Figure 1.1)**. Fan *et al.* performed ^{1}H NMR experiments to study the vapor liquid equilibrium of aqueous MEA-CO_2 system. The authors in this work suggested that the carbamate formation dominates other reactions like protonation of amines, CO_2 reaction with H_2O, up to half-molar loading. Ramazani and coworkers [10] and Idem and coworkers [11] used various additives like potassium salts, and other amines to enhance the CO_2 capture by MEA.

However, the use of amines leads to corrosion of steel pipes, low thermal stability, high volatility and poor recyclability due to large enthalpy of CO_2 absorption [12–15]. For example, carbon steel shows high corrosion from amine absorbents like

MEA, methyl diethanolamine (MDEA) **(Figure 1.2).** As an alternative to amines, amino-acids [16], and aqueous solutions of amino-acid salts (AAS) [17] have been screened and characterised as potential CO_2 absorbents in various experimental [6, 18] and theoretical studies [19–22]. The use of Room Temperature Ionic Liquids (RTILs) has also been proposed as a probable alternative for CO_2 capture [23–25], where the choice of cations and anions can influence the type (chemisorption/physisorption) and capacity (in the units of molar ratio, molarity, wt%) of CO_2 absorption. A comparison of the chemical and physical properties of amines and RTILs, relevant to CO_2 capture, is shown in **Table 1.1**.

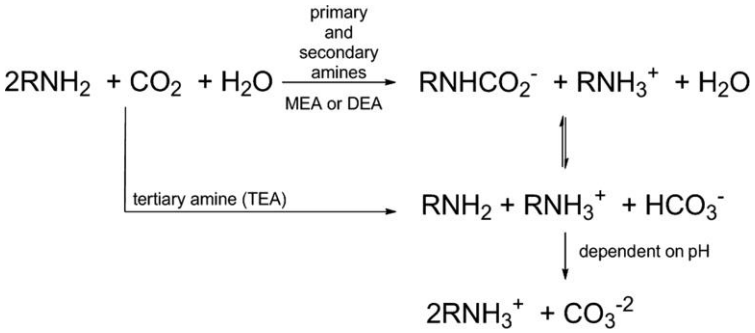

Figure 1.1. A comparison of reaction mechanism for CO_2 chemical absorption with different amines. Reprinted with permissions from [8] © 2013 American Chemical Society

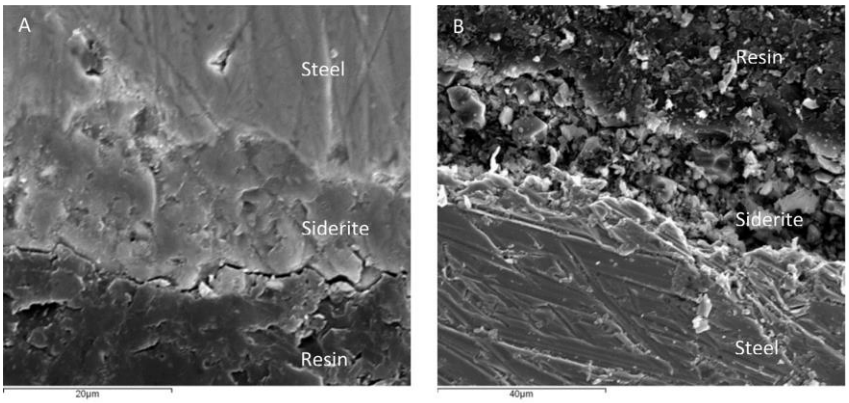

Figure 1.2. SEM images of corrosion of carbon steel (C1018) due to methyl diethanolamine studied over a period of 28 days: (A) 5 M MDEA at 1 week at ×2000 and (B) 5 M MDEA at 4 weeks at ×1500. Reprinted with permission from [26]. © 2016 Elsevier Ltd. All rights reserved.

Table 1.1. A comparison of various chemical and physical properties of amines and Ionic Liquids.

Properties	Amines	Ionic Liquids
Thermal Stability	Low	High
CO_2 reaction enthalpy	High (~100 kJ/mol)	Low (~20 kJ/mol)
Corrosion rate	High	Low
Recyclability	Low	High
Structural Tunability	Tedious	Easy
Volatility	High	Low

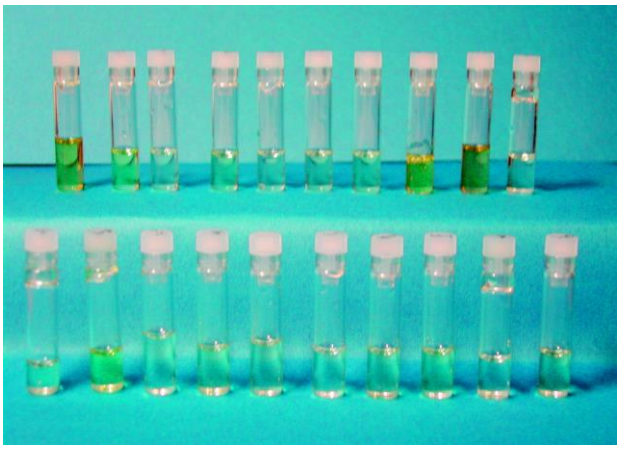

Figure 1.3. Imidazolium AAILs, synthesized using anion-exchange by Ohno and coworkers [27]. Upper side (left to right): [emim][Leu]; [emim][Lys]; [emim][Met]; [emim][Phe]; [emim][Pro]; [emim][Ser]; [emim][Thr]; [emim][Trp]; [emim][Tyr] and [emim][Val]. Lower side (left to right): [emim][Ala]; [emim][Arg]; [emim][Asn]; [emim][Asp]; [emim][Cys]; [emim][Gln]; [emim][Glu]; [emim][Gly]; [emim][His] and [emim][Ile]. Reprinted with permission from [27]. © (2017) American Chemical Society.

Since anions play a more significant role in CO_2 absorption [28], the presence of an amine group on anion enhances CO_2 capture in RTILs. Using this as one of the design principles, Ohno and coworkers synthesized a series of amino acid ionic liquids (AAILs) by exchanging the halide anions of RTILs with amino acid anions [27, 29] **(Figure 1.3)**.

AAILs combine advantages of high thermal stability (property of ILs) and presence of an inherent amine group (property of amino acids). In AAILs, amino acids with dual amine functionality **(Figure 1.4)** are a preferred choice as an anion compared to other amino acids. All the dual amine-functionalized amino acids contain two amine functional group as- one near the carboxylate group (characteristic to all amino acids, which forms a peptide bond), and the other- terminal group. The terminal amine functional group is- a primary alkyl amine in Lysine, a guanidium group in Arginine, a secondary aromatic amine (pyrazole) in Histidine and an amide in Asparagine and Glutamine. The high nucleophilicity on the terminal amine functional group of Lysine provides a higher CO_2 uptake ratio (2:1 in the molar ratio of CO_2:absorbent), compared to other amino acids. Zhou *et al.* [30] performed a comparative study of a non-amino acid anion-based IL, Lysine, and Lys^- AAIL for CO_2 absorption. The authors reported an enhancement in CO_2 uptake with the inclusion of Lys^- as an anion in AAIL and suggested that use of Lys^- as an absorbent over Lysine. **(Figure 1.5).**

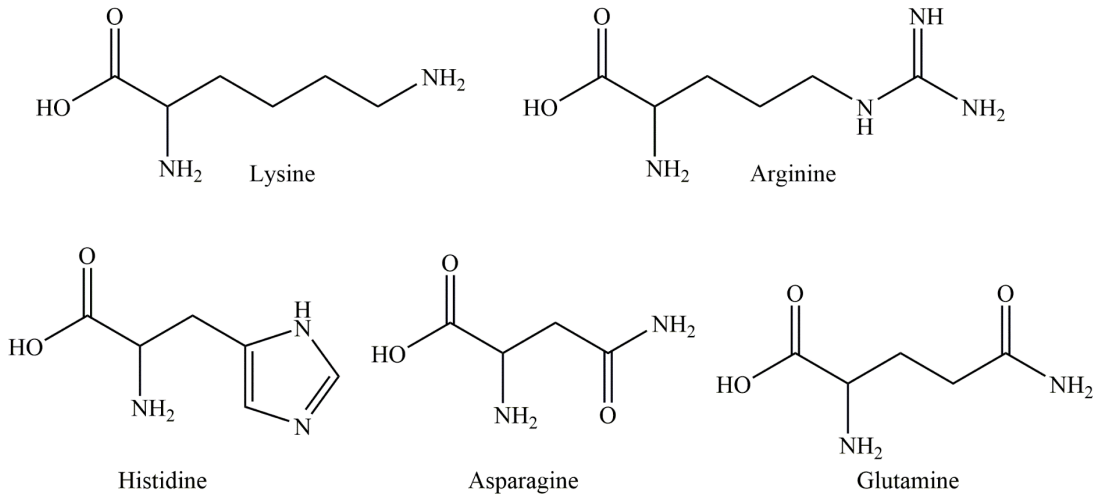

Figure 1.4. Chemical structures of dual amine functionalized amino acids.

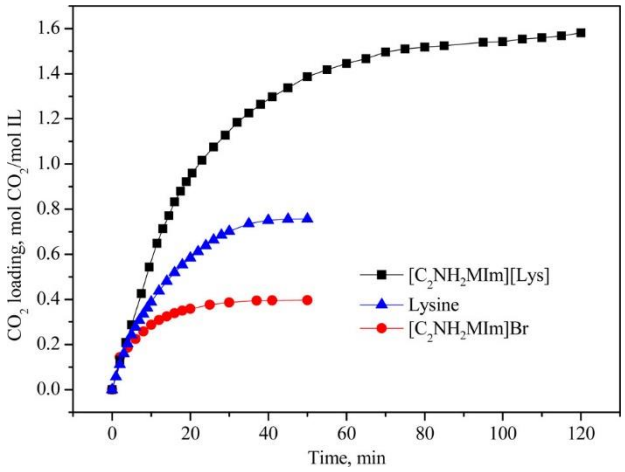

Figure 1.5. A comparison of CO_2 absorption in [C_2NH_2MIm][Br] IL, Lysine, and [C_2NH_2MIm][Lys] AAIL aqueous solutions (0.5 *M*) with CO_2 loading-30 mL/min, and at T = 313.15 K. Reprinted with permission from [31]. © (2017) American Chemical Society.

Apart from imidazolium cation based AAILs, ammonium [32] and phosphonium [37] cation based AAILs were investigated for their high absorption ratio (> 1 mol-CO_2/mol-IL). Brennecke and coworkers [33, 34] synthesized a family of trihexyl(tetradecyl) phosphonium [P_{66614}] cation-based AAILs and studied the kinetics of CO_2 absorption using two different experimental models [34]. The authors reported a very low glass transition temperature (< - 50 ^{0}C, favourable) and high thermal decomposition temperature (> 240 ^{0}C) in these AAILs. While one of their kinetic model demonstrated [P_{66614}][Lys] to be the highest in absorption capacity, the authors also showed that the same AAIL shows a significant contribution of physisorption [34]. **Table 1.2** shows a study of various alkyl-ammonium (and one alkyl-phosphonium) cation based AAILs which absorb CO_2 in a molar ratio of 1 – 2.1. Zhou et. al [30] and Saravanamurugan et. al [35] reported that these AAILs exhibit excellent recyclability during CO_2 capture.

In addition to AAILs, aqueous solutions of AAS (particularly, K^+Lys^-) have also been characterized and investigated for their performance as a CO_2 absorbent [36–42]. The major advantages of K^+Lys^- solutions are: low corrosive nature[39] and high absorption capacity [43, 44]. Shen *et al.* [36] performed absorption experiments and

viscosity measurements to show that absorption capacity of 2.5 *M* K^+Lys^- is equivalent to 30 % MEA solution. The advantage of K^+Lys^- is the relatively low corrosion of carbon steel [39] (which is roughly an order lower compared to MEA). The tunability in concentration of K^+Lys^- allows optimization of viscosity **(Figure 1.6)** and corrosion rate.

Table 1.2. CO_2 absorption capacity in AAILs. Adapted with permission from [35] © (2014) Wiley-VCH Verlag GmbH & Co. KGaA, Weinheim.

Ionic Liquid	**Time (h)**	**CO_2 uptake (CO_2/IL)**		
		mols/mols	mols/kg	wt%
$[N_{66614}][Lys]$	24	2.1	3.5	13.1
$[N_{66614}][Asn]$	24	1.9	3.3	12
	48	2	3.4	13.1
$[N_{66614}][Gln]$	24	1.5	2.5	9.5
	48	1.9	3.2	11.7
$[N_{66614}][His]$	24	1.8	3	11.1
	48	1.9	3.1	11.7
$[N_{66614}][Arg]$	24	1	1.6	6.6
	48	1.3	2.1	8.1
$[N_{66614}][Met]$	4	1	1.6	6.9
	24	1.2	1.9	7.8
$[P_{66614}][Lys]$	–	1.4[34]	2.3	8.7
	48	1.6	2.6	9.9

The various attempts to increase the capacity of CO_2 absorption and to decrease the rate of corrosion and the cost of regeneration [15, 45–50] also motivate an atomic scale understanding of structural properties, dynamics of absorption and reaction mechanisms. Using molecular dynamics (MD) simulations, Berne and coworkers [51] showed that RTILs like $[Bmim^+][PF_6^-]$ possess a sufficient residual space which

allows CO_2 to absorb without chemical interactions and reactions. Maginn and coworkers [52] and Chang and coworkers [53] performed MD simulations to understand absorption interface, structure, and molecular mechanism of CO_2 absorption in RTILs. Kim *et al.* [54], Jing *et al.* [55] and other works [19] screened different amines/amino functionalized absorbents and proposed plausible reaction mechanisms from quantum chemistry calculations. Hussain *et al.* [16] systematically studied the set of all amino acids in their neutral states and determined their CO_2 affinity using energetics (e.g. activation energy, reaction enthalpy) from density functional theory (DFT) calculations. da Silva [20] and coworkers studied the relative stability of carbamates of various amines and anions using quantum chemistry calculations. Similar to the aqueous solutions of amines, the competitive role of carbamate, bicarbonate and carbonate products was also examined in AAIL/AAS from experiments like NMR, IR, etc. [30, 40, 56, 57]. McDonald *et al.* [56], using NMR experiments, observed that in ammonium AAILs, carbamate formation dominates the process of CO_2 absorption up to a threshold, after which bicarbonate/carbonate formation leads the absorption. Shen and coworkers [40, 58] observed in NMR experiments that even highly concentrated salt solutions show significant bicarbonate/carbonate product formation during CO_2 absorption **(Figure 1.7)**. Such findings motivate the use of Lys^- in ILs and in aqueous environments as an absorbent.

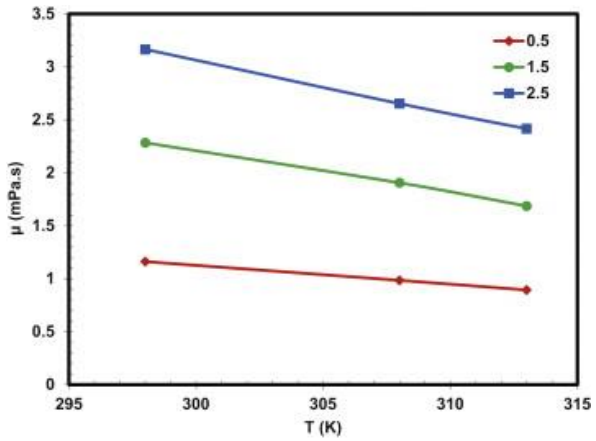

Figure 1.6. Viscosities of aqueous potassium lysinate solutions of different concentrations. Reprinted with permission from [39] © (2015) Elsevier B.V. All rights reserved.

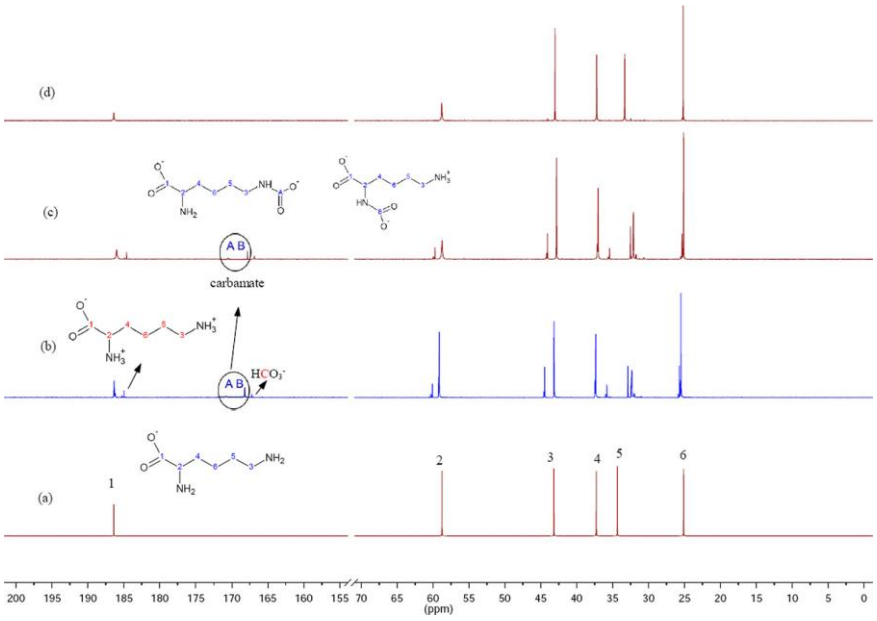

Figure 1.7. ^{13}C NMR spectra of aqueous K^+Lys^- solutions in D_2O: (a) fresh CO_2-free solution; (b) CO_2-lean solution at the 4th absorption− desorption run; (c) CO_2-lean solution at the 8th run, (d) CO_2-free solution after eight-cycle runs using acid and base treatment. Reprinted with permission from [40]. © (2017) American Chemical Society.

1.2 ALKALI METAL BATTERY ELECTROLYTES

An alkali metal battery consists of three compartments (or layers), a cathode (e.g. Alkali metal-transition metal-oxide), an anode (e.g., graphene/other intercalated support for alkali metal ions) and an electrolyte **(Figure 1.8)**. The desired properties for both the electrodes are, a facile and reversible redox reaction for alkali metal ions. The role of electrolyte is to serve as a medium for ion transport from cathode to anode (or vice versa), inhibiting electronic conduction. The current generation of liquid electrolytes possess low volatility and thus an issue of safety, flammability and poor mechanical strength [59–61]. Moreover, use of ethers and carbonate electrolytes (hard bases) also leads to unavoidable interactions of lithium and sodium alkali metal ions (hard acids) resulting in reduced ionic conductivity of the electrolyte. Hence solid electrolytes like ceramics, and certain Lithium/Sodium Superionic Conductors (LISICON/NASICON) have been synthesized and characterized using

electrochemistry experiments [62–68]. However, absence of electron insulation in such electrolytes causes dendrite formation. Thus, a new generation of electrolyte is required to be developed where ions can conduct like a liquid while the electrolyte remains stable like a solid. Various solid electrolytes can be categorized by parameters: chemical, redox and thermal stabilities, cost, area-specific resistance, etc. **(Figure 1.9)** [69]. While oxide electrolytes are costly and difficult to cast in devices, hydrides and sulphides lack chemical stability. Polymer electrolytes are cost effective and can easily form electrode interfaces but lack thermal stability and mechanical strength.

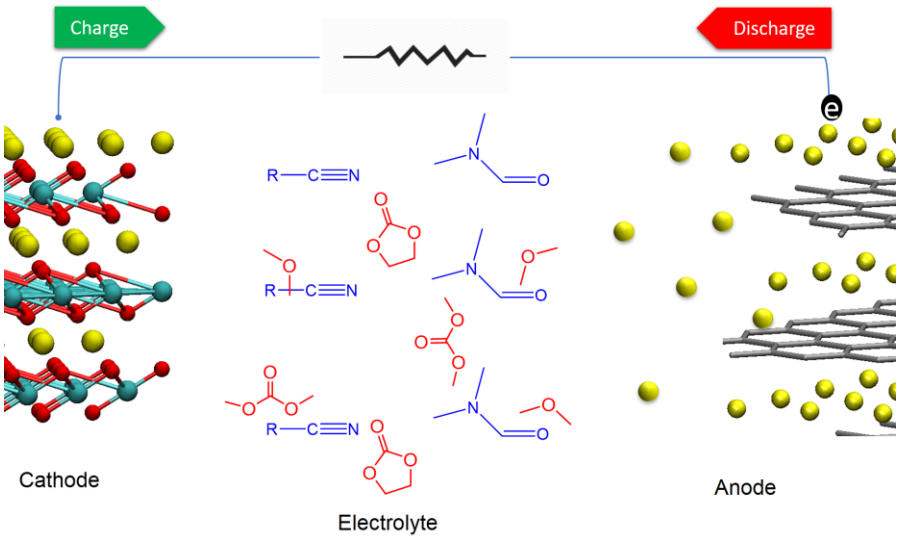

Figure 1.8. Schematic diagram of an alkali metal ion battery consisting of the cathode, elelctrolyte and anode layers. The electrolyte layer shows traditional organic solvents (red) like ethylene carbonate, and alternative cosolvents (blue) like alkyl nitriles. Charge and discharge arrows show the direction of movement of alkali metal ions inside the cell and electrons outside the cell, during charging and discharging.

The nature of ion conduction in liquid *vs.* solid electrolytes can be attributed to different factors at the atomic scale. For example, in liquid electrolyte, the ions move in a medium where structural relaxations, low hindrances and weak interactions in the fluid phase produce a smooth potential energy surface. In contrast, the solid-state electrolytes possess a rigid framework of crystals/glasses which leads to a highly

variable potential energy surface, constraining the process of ion conduction to be more kinetic in nature. **Figure 1.10** shows a comparison of Arrhenius plots of conductivity for solvates, polymers, amorphous, garnets and perovskite type electrolytes. The above panel in **Figure 1.10** also shows a schematic comparison of ionic conduction in solid *vs.* liquid electrolytes.

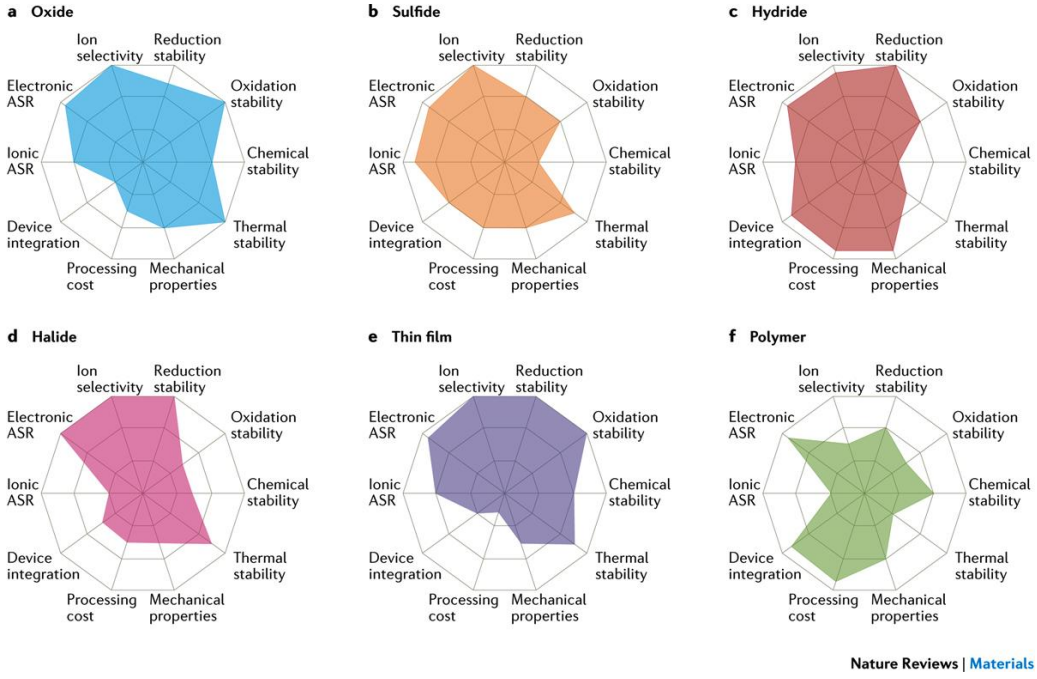

Figure 1.9. Radar plots of the performance properties of (a) oxide solid electrolytes, (b) sulfide solid electrolytes, (c) hydride solid electrolytes, (d) halide solid electrolytes, (e) thin-film electrolytes, and (f) polymer solid electrolytes. ASR, area-specific resistance. Reprinted with permission from [69]. © (2017) Macmillan Publishers Limited, part of Springer Nature.

In the current generation of solid electrolytes, the major challenge is to optimize interfacial resistance and inhibition of passivating solid electrolyte interface formation. For examples, ceramics offer considerable mechanical and thermal stability but exhibit a high resistance at the interface formed between the crystals – "grain boundary" of the crystals. This high resistance leads to a low conductivity in these regions and also in poor electrode-electrolyte contact [70]. A high grain boundary resistance is almost a characteristic to the oxide electrolytes and thus stems the pursuit

of new electrolytes with lower grain boundary resistance. Chi and coworkers [71] performed scanning transmission electron microscopy (STEM) imaging to visually inspect the grain boundary regions in a perovskite Li^+ ion conductor **(Figure 1.11).** The authors in this work also employed electron energy loss spectroscopy (EELS) and reported that the high grain boundary resistance in these solid electrolytes can be attributed to the Ti-O passive networks which completely inhibit Li^+ ion conduction in these regions. A similar observation about presence of a high inter-granular resistance was also reported in other studies [72, 73].

A possible solution to the problems encountered with the above traditional electrolytes is to prepare low-affinity, electronically insulated electrolytes of ionic salts (like LiCl, $NaClO_4$, $NaPF_6$, etc.) with organic solvents. The strong interactions between migrating cations (hard acid) with nucleophilic solvent functional groups (hard base) can be identified based on Pearson's concept of hard-soft acid-base [74]. Thus, various salt-solvent mixtures (solvates) were studied to optimize the choice of solvent as a soft base which would interact weakly with alkali metal ion -hard acid. Bryantsev *et al.* [75] performed DFT calculations on various solvents with functional groups carbonyl (C=O), nitrile (C≡N), etc. to screen them based on chemical stability in Li-air batteries. The trends of acidity constants, reaction free energy, etc. for various solvents calculated by the authors in the above work are useful in study of Li-ion battery. Borodin and coworkers [76] studied various solvates of lithium hexafluorophosphate ($LiPF_6$) in different glymes, nitriles, *tert*-amine and carbonate solvents. The authors crystalized $LiPF_6$ in a triglyme (G3), where $Li^+PF_6^-$ forms a contact ion-pair and another aggregate of $LiPF_6$ in diethyl carbonate (DEC). Other works [77–79] explored dinitrile solvents, particularly ADN, which is shown to improve retention of the battery capacity of 1 *M* $LiPF_6$ (EC:DMC:EMC) liquid electrolyte [79].

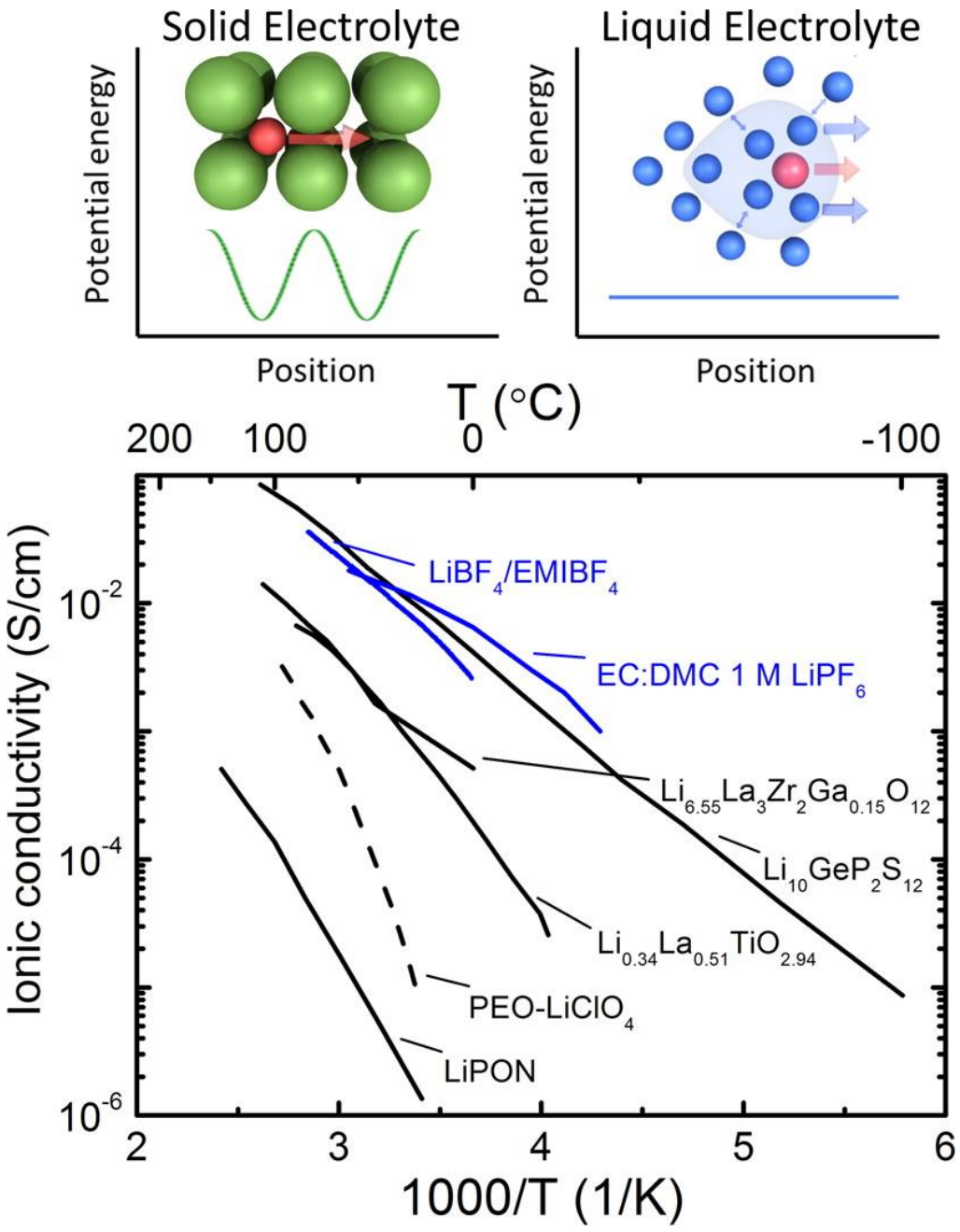

Figure 1.10. Total lithium-ion conductivity (unless otherwise mentioned) as a function of temperature adapted from Kamaya *et al.* [80] which includes liquid (blue) ethylene carbonate/dimethyl carbonate (EC/DMC) 1 M $LiPF_6$ [81] and IL $LiBF_4$/$EmiBF_4$ [82] polymer (dashed black) PEO-$LiClO_4$ [83] and inorganic solids (black) consisting of amorphous LiPON [84] and crystalline solids: perovskite $Li_{0.34}La_{0.51}TiO_{2.94}$ (bulk conductivity shown) [85] garnet $Li_{6.55}La_3Zr_2Ga_{0.15}O_{12}$ [86] and $Li_{10}GeP_2S_{12}$ [80]. Top right and top left show the potential energy of migration in liquid electrolytes of a charged species in red with a solvation shell of electrolyte molecules (highlighted in blue) and an interstitial mobile ion in a crystalline solid, respectively. Reprinted with permission from [87]. © (2015) American Chemical Society.

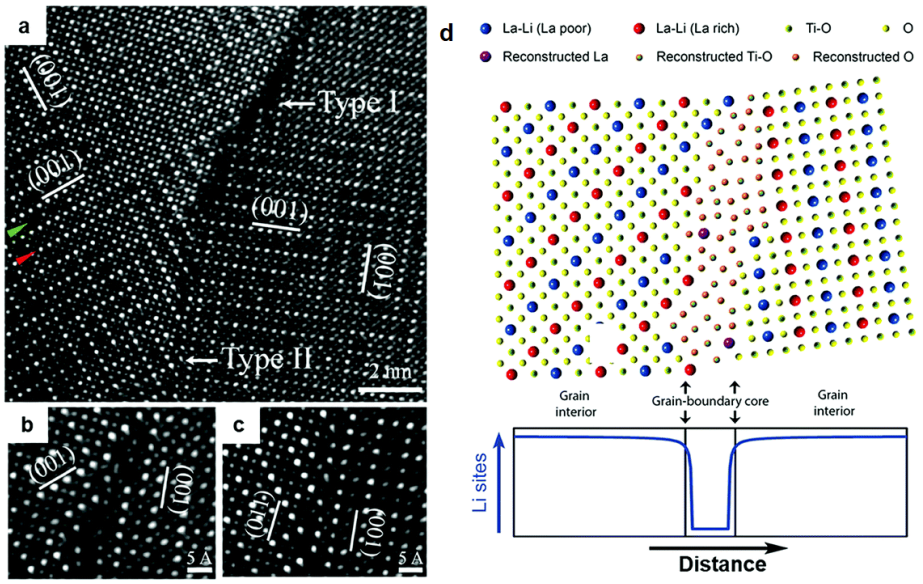

Figure 1.11. (a) HAADF-STEM image of a grain boundary (GB) exhibiting both dark- and normal-contrast regions, labelled as Type I and Type II, respectively. Within the grains, a row of atomic columns for a La-poor layer and one for a La-rich layer were indicated by green and red arrows on the left-hand side of the image, respectively. The (001) planes of the alternating La-rich/La-poor layers (arbitrarily designated as (001) planes in image) of different regions in the grain were marked to highlight the existence of nanodomains; **(b)** further magnified Type I GB feature; **(c)** further magnified Type II GB feature; **(d)** O-K edges for the Type I GB and the bulk. The spectra were normalized to the integrated intensity of the Ti-$L_{2,3}$ edge. The normalized O-K edge of the bulk was shifted vertically for clarification. Reproduced with permission from [71] Copyright (2014), the Royal Society of Chemistry.

Zdilla and coworkers [88–90] proposed that Pearson's concept of hard-soft acid-base can also be a useful tool to synthesize a variety of solid cocrystalline electrolytes which have low affinity solvent channel. In these cocrystals, alkali metal ion (hard acid, Li^+/Na^+) coordinates with functional groups of organic solvent (soft base), e.g., carbonyl group in DMF, and nitrile group in ADN. The preferential coordination of Li^+/Na^+ ion with solvent functional group forces the anion to usually occupies the interstitial space. The first of its kind, DMF·LiCl electrolyte showed a low activation energy barrier (E_a) with ionic conductivity comparable to other polymeric/oligomeric electrolytes **(Figure 1.13)** [88].

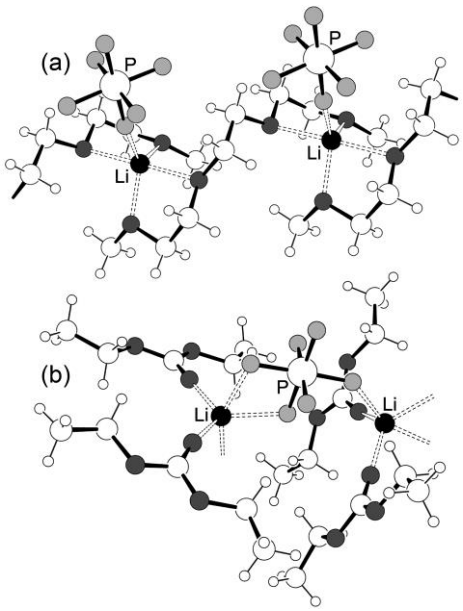

Figure 1.12. $PF_6^-\cdots Li^+$ cation coordination in the $LiPF_6$ solvates: (a) CIP-I $(G3)_1$:$LiPF_6$ and (b) AGG-Ib $(DEC)_2$:$LiPF_6$ reported by Borodin and coworkers. Reprinted with permission from [76]. © (2015) American Chemical Society.

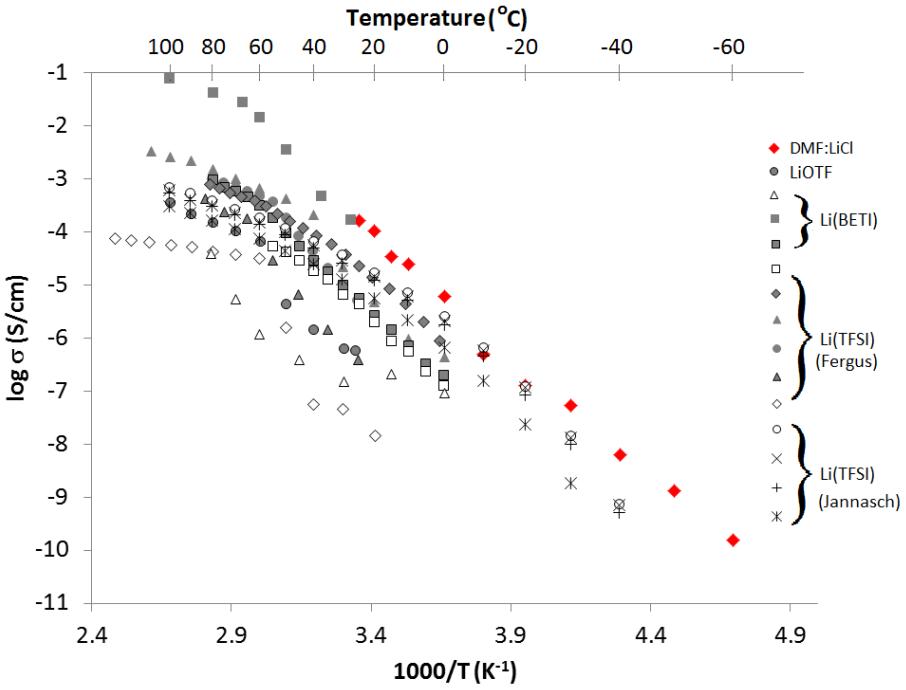

Figure 1.13. Conductivity of DMF·LiCl compared with PEO/LiX [68],[91]; Li(BETI) = $LiN(SO_2CF_2CF_3)_2$; Li(TFSI) = $LiN(SO_2CF_3)_2$. Reprinted with permission from [88] (Supporting Information). © (2017) American Chemical Society.

Using the same concept of cocrystallization, Zdilla and coworkers [89] also synthesized a sodium ion cocrystalline electrolyte- $NaClO_4(DMF)_3$, which exhibits a one-dimensional short distance channel of < 3.5 Å for Na^+ ions. A few novel features of this electrolyte are: melt-castability, malleability, and self-binding of grains. Unlike ceramics where the oxide layer passivates the ion conduction at grain boundaries, these cocrystalline electrolytes form liquid like layer which facilitates ion conduction with a lower barrier. The existence of soft grain boundaries was also confirmed from SEM [89]. These grains are observed to have a liquid like layer at the surface, possibly due to uncoordinated solvent molecules. A low resistance on the boundary of these grains in the cocrystalline electrolytes results in a desirable capacity of interfacial contact which is also essential for the formation of better interface with electrode. The modelling of grain boundaries, structure at decomposition/melting ion dynamics and mechanism of ion conduction were the questions where experimental techniques are limited to provide more insights.

1.3 COMPUTATIONAL METHODS

Experimental techniques are limited to size and time scales and do not always provide a sufficient understanding of absorbents and electrolytes. Thus, models of atoms and molecules on computers can be simulated to mimic chemical and physical processes. A typical molecular computer simulation follows a set of rules (e.g., Newton's equations of motion to calculate kinetic energy, Schrödinger's equation/classical potential energy parameters to calculate potential energy) and some initial information (e.g. structural formula, relative atomic positions) to model various chemical/physical processes **(**Figure 1.14**)**. In addition to the set of rules that govern the intrinsic motion of particles, algorithms are required to invoke physical conditions like energy minimizer, thermostat, barostat, etc. The output generated from the calculations is in the form of updated coordinates and velocities/gradients, which is transformed to standard properties relevant to physical chemistry.

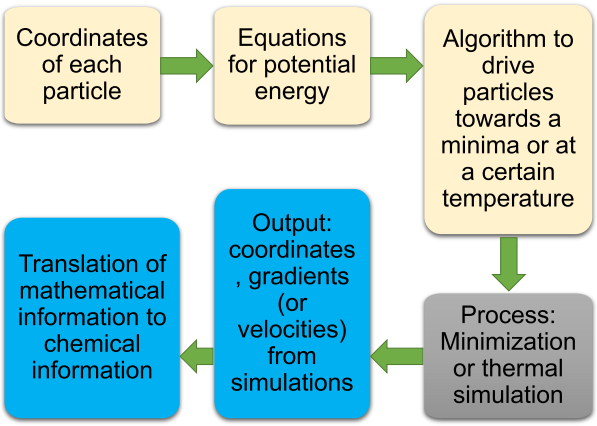

Figure 1.14. A schematic general computational calculation protocol showing the key steps involved in an atomic simulation.

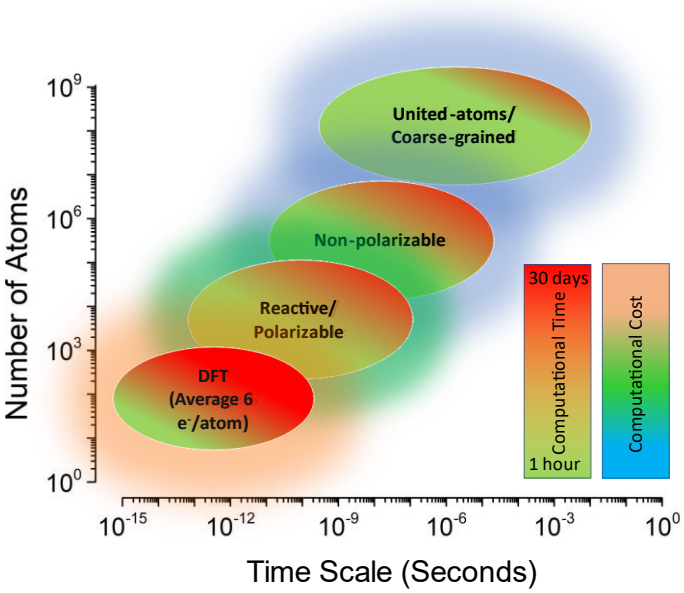

Figure 1.15. A comparison of size and time scales of a computer simulations with an approximate computational cost and computational time.

As the diversity in choice for inputs, processing and output shows, a universal computational method does not exist. The size-scale and timescale of studies decides the choice of a suitable theoretical method. For example, determination of a reaction mechanism would require energy minimization of reactant and product configurations, and frequency calculation or other methods to find transition states. Whereas understanding structural and dynamical properties of a material in condensed phase

would require simulations under isothermal or other suitable ensemble conditions. Furthermore, the choice of a suitable computational method would also depend on the computational cost **(Figure 1.15)**. For example, highly accurate quantum chemistry calculations may not be possible for a system for 1000 e^-s. Hence a judicious choice of method based on the scales of size and time, based on the properties of interest is required for a productive implementation of a computer simulation. A justification of employing a specific computational method is discussed for each research problem in the corresponding chapters in this thesis.

1.4 OBJECTIVES

The key objectives in this thesis can be classified as:

a) Study of Lysinate based CO_2 absorbents using,

   i) Classical Molecular Dynamics (MD) simulations

   ii) Gas-phase Density Functional Theory (DFT) calculations

to understand structure, dynamics, timescales, mechanism and energetics, and,

b) Study of Li^+/Na^+ ion battery cocrystalline electrolytes using,

   i) Classical MD simulations

   ii) Gas-phase DFT to develop force field parameters

   iii) Plane-wave periodic DFT calculations

to understand mechanism of crystal melting, surface *vs.* bulk behaviour, ionic mobility and mechanism of ion conduction.

1.5 SCOPE OF THE THESIS

Chapter 2 of the thesis presents MD simulation study of CO_2 absorption in *tetra*-butylphosphonium lysinate ($P_{4444}^+Lys^-$) IL. The simulations provide a direct

quantitative measure of the CO_2 absorption process with experiments. Further, preferential interaction of Lys^- anion with CO_2, competitive reactivity of amine groups in Lys^-, and the influence of absorption on mobility of ions are described in this chapter. **Chapter 3** of the thesis discusses the mechanism of CO_2-Lys^- reaction and role of water as an explicit molecule. DFT calculations provide key findings like preferential interaction of CO_2 molecule with near-carboxylate amine functional group in Lys^- anion. Moreover, the feasibility of bicarbonate formation during the CO_2-Lys^--H2O reaction is one of the important outcomes seen from this study.

Chapter 4, 5, 6 and 7 of this thesis cover modeling of structure, ionic mobility and mechanism of conduction in four different alkali metal battery electrolyte materials. **Chapter 4** of the thesis discusses first of these electrolytes formed with *N,N*-dimethylformamide and lithium chloride, DMF.LiCl. The cocrystalline electrolyte is modeled using MD simulations to understand experimentally observed behavior like structure, bulk/surface properties, and mechanism of Li^+ ion conduction. DFT calculations were also employed to understand the role of small-scale aggregates-oligomers in the stability of bulk and fluidity of surface of DMF.LiCl electrolyte. **Chapter 5** of the thesis presents findings from MD simulations and DFT calculations on a similar DMF based electrolyte for alternative and cost-effective SIB, $(DMF)_3NaClO_4$. The electrolyte is investigated for its stoichiometric conversion (from 3:1 to 2:1 of DMF:$NaClO_4$), diffusion of Na^+ ions and mechanism from plane-wave DFT calculations. **Chapter 6** of the thesis discusses the choice of adiponitrile molecule (ADN, N≡C-$(CH_2)_4$-C≡N) as a cosolvent of cocrystalline electrolytes and study of $(ADN)_3NaClO_4$ using MD simulations and plane-wave DFT calculations. **Chapter 7** of the thesis discusses the structural properties, ion dynamics, and mechanism of conduction in a LIB electrolyte: $(ADN)_2LiPF_6$. **Chapter 8** concludes the thesis with a brief discussion on key findings and future of the CO_2 absorbents, alkali metal battery electrolytes using computational approaches.

———*———*———

Chapter 2:

Molecular Simulation of CO_2 Absorption in tetrabutylphosphonium lysinate Ionic Liquid

2.1 INTRODUCTION

In this chapter, a molecular mechanism of CO_2 absorption in tetrabutylphosphonium lysinate IL using classical MD simulations is presented. A description of literature on experiments and simulations on CO_2 absorption is discussed. In one of the earliest attempts, Bates *et al.* [92] employed FTIR spectroscopy and observed a 0.5 molar absorption of CO_2 (at room temperature) in an amine functionalized imidazolium based IL. Similar absorption capacity was reported by Zhang *et al.* [93] on phosphonium AAILs, where the authors also observed enhanced absorption of CO_2 on addition of water in IL. Carvalho *et al.* [94] used bubble point determination approach and found that phosphonium ILs have higher CO_2 solubility compared to imidazolium ILs. Using calorimetric and react-IR spectroscopy methods, Gurkan *et al.* [33] observed an equimolar CO_2 absorption (at room temperature) in phosphonium based methioninate and prolinate AAILs. Wang *et al.* [95] measured enthalpy of absorption for a series of phosphonium based ILs and concluded that anions with large pK_a, show higher CO_2 absorption. Seo *et al.* [96] synthesized a range of aprotic heterocyclic anion based phosphonium ILs, and using volumetric measurements reported an equimolar CO_2 absorption (at room temperature). Eisinger *et al.* [97] reported a phase change (from solid to liquid) in a tetraethylphosphonium based IL. The authors concluded that

heat evolved during the phase change leads to reduced power consumption associated with CO_2 capture in post combustion industrial process.

Computational investigations using Molecular Dynamics (MD) simulations to model interactions between supercritical CO_2 and [Bmim][PF_6] IL were employed by Huang *et al.* [51]. The authors calculated structural properties and concluded that while CO_2 molecules can easily permeate into the IL phase, the ions of IL do not diffuse to the CO_2 phase. Subsequently, Perez-Blanco and Maginn [98] investigated absorption/desorption of CO_2 in [Bmim][Tf_2N] IL at various temperature and pressure conditions. The authors concluded that CO_2 molecules quickly absorb at the IL interface, and further diffuse to the bulk IL at longer timescales. Xing *et al.* [99] reported that the amine tethering on anion of an imidazolium IL enhances CO_2 absorption. The authors suggested that amine functionalization on the imidazolium cation leads to high interaction between cation and anion which results in low interaction of CO_2 with anion of IL, while amine functionalization on anion of IL weakens intra-IL interactions and facilitates accommodation of CO_2 absorption. Morganti *et al.* [100] and García *et al.* [101] compared the relative absorption of CO_2 and SO_2 in non-amine functionalized ILs and found preferential absorption of SO_2 over CO_2 in such non-amine ILs. Izgorodina *et al.* [102] showed that ILs containing large size anions (e.g. sulfonic, carboxylic and other bulky functional groups) are favorable candidates for CO_2 physisorption. Klähn and Seduraman [103] investigated several imidazolium-based ILs (with varying alkyl chain length of cation) and concluded that only the voids available in IL facilitate CO_2 absorption. The authors also concluded that ions slightly rearrange to accommodate CO_2 molecules in the bulk IL, and CO_2-IL interactions do not play any significant role.

Existing studies have provided very limited mechanistic details on CO_2 capture and for a limited type of ILs. The theoretical studies so far have not thoroughly examined the timescale of CO_2 absorption at IL interface and bulk. The actual process of CO_2 absorption in the bulk IL at very long timescales (~100 ns) has never been

explored. To examine these effects and propose a general mechanism of CO_2 absorption, an AAIL, tetrabutylphosphonium lysinate [P_{4444}][Lys] was chosen **(Figure 2.1)** which has large thermal stability, and the presence of multiple amine sites on the lysinate anion which can facilitate CO_2 capture. The computational details of simulations are presented in the next section. Section **2.3** discusses the mechanism associated with CO_2 absorption from MD simulations (using all atom force-fields). The properties calculated from MD simulations are: IL charge density, time dependent particle densities of CO_2 (at the interface and interaction with bulk IL), absorption isotherms at varying pressure and temperature, characterization of important molecular interactions between sites in IL and CO_2 via Radial Distribution Functions (RDFs) [104] and Spatial Distribution Functions (SDFs) [105] and effect of CO_2 absorption on dynamics of cations and anions of IL. A summary of important findings concludes this chapter. Additional figures, tables and information related to this chapter is provided in **Appendix A**.

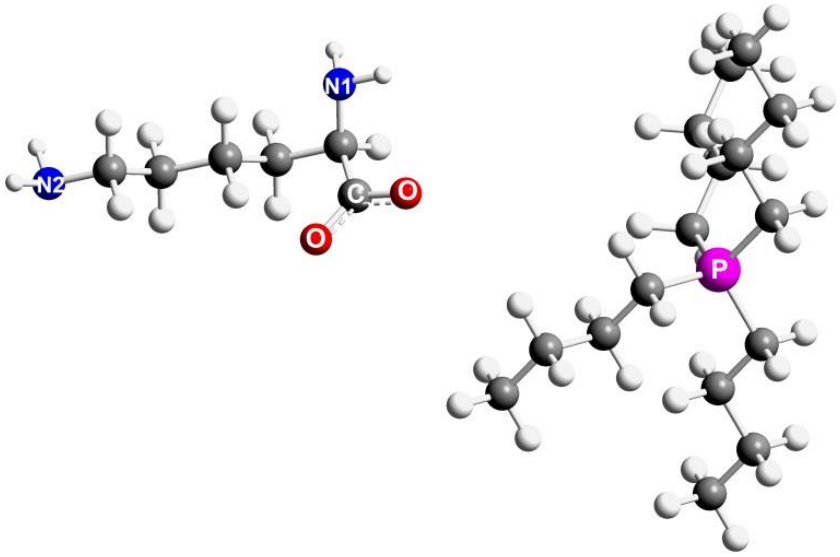

Figure 2.1. Structure of tetrabutylphosphonium lysinate (atom types defined for RDFs).

2.2 COMPUTATIONAL DETAILS

The computational model required for MD simulations was created using a box of 512 ion pairs of [P_{4444}][Lys] IL by annealing and equilibration using the *NpT* ensemble, at

T = 298 K and p_{IL} = 1 bar. Various initial templates of CO_2 molecules were created and equilibrated using *NpT* ensemble to maintain the pressure and temperature conditions. The equilibrated IL slab was centered in a cuboidal box of dimensions 9.0 x 9.0 x *z* nm, where *'z'* is derived as the length of the box required to contain a certain number of equilibrated CO_2 molecules (based on the required initial partial pressure and temperature). The IL slab was sandwiched between two layers using equilibrated CO_2 templates, where CO_2 molecules were initially separated by a vacuum layer of 1.0 nm from the surface of IL on each side of the box **(Figure A1)**. The initial vacuum was created to maintain an initial non-interacting behavior between CO_2 and IL based on earlier theoretical studies [52] on other ILs. All MD simulations for CO_2 absorption were performed at T = 298 K and 278 K; p_{CO_2} = 1, 10 and 20 bars. However, in order to examine the mechanism of CO_2 absorption, unless explicitly mentioned, all results are focused on simulations performed at T = 298 K, and p_{CO_2} = 20 bar in this chapter. The GROMACS 4.6.7 [106] program was used for MD simulations. The CO_2 molecules were modeled using flexible TraPPE force field [107]. The force field parameters for [P_{4444}][Lys] IL were taken from the work of Zhou *et al.* [108]. The force field parameters of the neat IL were benchmarked by performing MD simulations and the calculated structural and dynamical properties like density, RDFs and conductivity were found to be in good agreement with previously reported experimental [93] and simulation [108] studies **(Table A1)**. All simulations for CO_2-IL systems were carried out for 100 ns with a time-step of 0.5 femtoseconds at the *NVT* ensemble with temperature maintained using the Nosé-Hoover chain thermostat [109, 110] and a 1.4 nm cut-off for calculation of non-bonding interactions.

2.3 RESULTS AND DISCUSSION

2.3.1 CO_2 absorption at the interface and bulk

A time averaged charge density of [P_{4444}][Lys] IL shows, on absorption of CO_2, a highly ordered and structured bilayer (of opposite phase) at the surface forms **(Figure 2.2a)**. The cations and anions of IL reorient themselves to facilitate the formation of

the CO_2-IL interface. The area under the curve of positively charged outer region of the CO_2-IL interface is smaller than the negatively charged inner region. The existence of this bilayer facilitates the absorption of CO_2 molecules to the surface of IL. The charged bilayer formation at the CO_2-IL interface is a characteristic feature of CO_2 absorption and its formation is independent of thermodynamic conditions **(Figure A2)**. In comparison to vacuum-IL interface, the charge density is found more structured in CO_2-IL interface **(Figure A3)**. The charge bilayer formation (near the interface) supports the observations of Perez-Blanco *et al.* [98] and Dang *et al.* [53] on vacuum-[Bmim][NTf_2] IL interface.

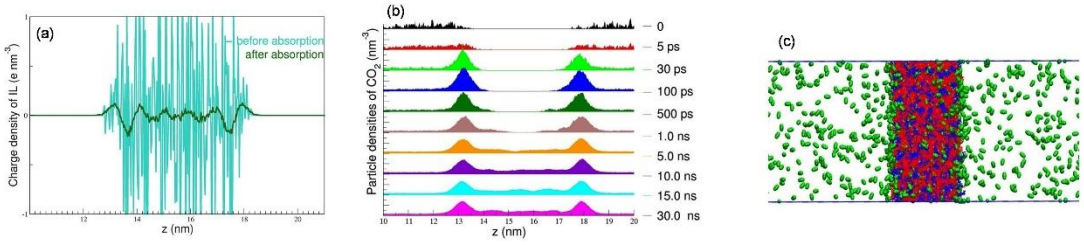

Figure 2.2. (a) Cross-section averaged charge densities of IL before (t = 0) and after absorption (averaged from t = 5 ns to t = 10 ns). **(b)** Particle densities of CO_2 in the z direction of the box, where the average width of the IL layer is 4.8 nm. **(c)** Snapshot of CO_2-IL interface, surficial and bulk CO_2 absorption at t = 30 ns, Color scheme is: Green (CO_2), Red (P_{4444}^+ cation) and Blue (Lys^- anion).

Perez-Blanco *et al.* [98] calculated the particle density profile of CO_2 molecules on absorption in [Bmim][NTF_2] IL. The authors observed the interfacial crossing of CO_2 occurs with an exchange time (between CO_2 and IL phase) of 2.5 ps at the interface. Following a similar approach, time-averaged particle densities of CO_2 were calculated to examine distribution of CO_2 in the box during the processes of absorption. The particle densities are calculated using a 100 ps time window (for densities calculated till t = 1.5 ns) and 1000 ps time window, from the average time (for densities calculated after t = 2.0 ns) **(Figure 2.2b)**. The results show that within the first few picoseconds; several layers of CO_2 molecules are absorbed near the surface of IL on both sides of the box. The intensity at the CO_2-IL interface increases

till 100 picoseconds. A slight decrease in CO_2 particle density at the interface starts around 1.0 ns, as CO_2 molecules can enter the bulk IL region. Around 10.0 ns, the densities at the interface attain saturation. The time of saturation can be defined as the time beyond which particle densities at the interface remain almost constant. The particle densities of CO_2 at the interface and in bulk IL remains almost constant between t = 30 ns and 100 ns, suggesting a total saturation of CO_2 density in all phases **(Figure A4)**. Similar features and trends in particle densities at other pressures and temperature are shown in **(Figure A5)**. A representative snapshot of absorption at t = 30 ns **(Figure 2.2c)** shows the presence of CO_2 molecules in the bulk IL layers. The quantitative measure of CO_2 uptake is seen from an absorption isotherm discussed in the next section.

2.3.2 Quantitative effects of pressure on CO_2 absorption

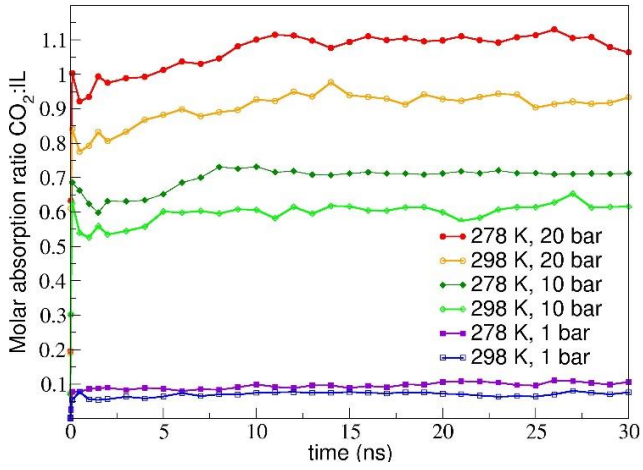

Figure 2.3. Molar CO_2 absorption ratio in IL as a function of simulation time.

The time dependent molar absorption ratio of CO_2:IL is calculated by an integration of CO_2 particle densities between two CO_2-IL interfacial boundaries. The absorption isotherm **(Figure 2.3)** shows a sharp blip at very short timescales (in few picoseconds) due to CO_2 absorption in the initially formed CO_2-IL interface. A slight decrease in absorption at timescale of 1 ns arises as CO_2 molecules at the interface diffuse into the bulk IL layers, where absorption reaches an asymptotic value within a timescale of 10

ns. At T = 298 K and p_{CO_2} = 20 bar, a 0.9 molar absorption ratio (calculated as an average using time dependent molar absorption values from *t* = 10 ns to *t* = 30 ns) is achieved, and is ~ 13 and 1.5 times higher than the absorption at p_{CO_2} = 1 bar and 10 bar respectively. At T = 278 K and p_{CO_2} = 20 bar, a maximum of 1.08 molar absorption of CO_2 per IL is achieved. The average molar absorption ratio values at other thermodynamic conditions are shown in **Table A2**. Due to the choice of a different cation, the theoretical values of molar absorption in this study are lower than the experimentally reported values of Goodrich *et al.* [34] (1.4 CO_2:IL molar absorption) and Saravanamurugan *et al.* [35] (1.6 CO_2:IL) with similar class of ILs.

2.3.3 Structural view of interactions between CO_2 and IL

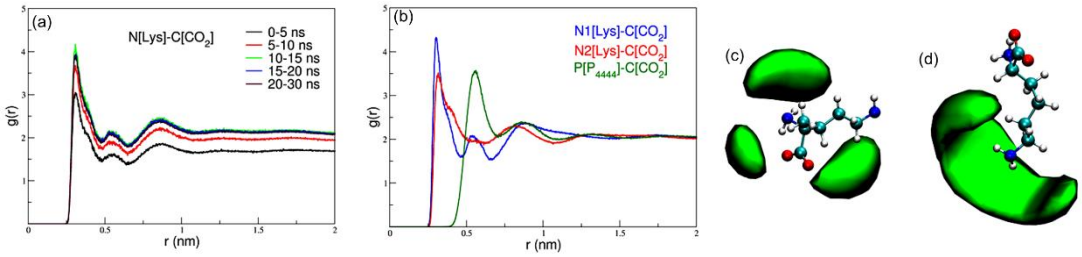

Figure 2.4. (a) Time dependent RDFs of anion-CO_2 interactions, **(b)** Averaged RDFs of anion-CO_2 and cation-CO_2 interactions, **(c)** SDF of C[CO_2] around N1,C,O[Lys], (d) SDF of C[CO_2] around the N2[Lys] site.

The interaction between CO_2 molecules and various interaction sites of the ILs are examined using calculation of RDFs and SDFs. RDF (Radial Distribution Function) is a time-independent pair correlation function of density, which can be written as:

$$g(r) = \frac{1}{\rho}\left\langle \sum_{i=1}^{N} \delta(\mathbf{r} - \mathbf{r_i}) \right\rangle \qquad \textbf{(2.1)}$$

Here, $\mathbf{r} - \mathbf{r_i}$ is the relative distance of the particle pairs, N is the number of particles and ρ is the mass density (under the approximation that the particles are homogeneously distributed). The integration of function g(r) with respect to r gives the value of coordination number. The P[P_{4444}], N1[Lys], N2[Lys], and C[CO_2] sites

are used for examination of structural features. The RDFs between the P site of the cation and N1, N2 sites of the anion for CO_2-IL and vacuum-IL systems show that interaction between cations and anions of IL decreases with CO_2 absorption **(Figure A6)**. A time dependent N1, N2-C RDF **(Figure 2.4a)** shows that structural features are similar at different times. However, the intensities of these RDFs increase till t = 10 ns, and then remains invariant till t = 30 ns, due to the saturation of CO_2 molecules at the CO_2-IL interface. In the time period of t = 10 to t = 30 ns, various RDFs were characterized which correspond to possible interactions between cation/anionic sites of the IL and CO_2 **(Figure 2.4b)**.

The cation-CO_2 RDF shows a broad first peak with a small secondary peak. However, the first peak position appears at larger distances from the interaction site (0.56 nm) and with relatively low intensity. This is because CO_2 molecules have less preference to interact with the cation, due to a large positive charge on the phosphorous atom and steric hindrance from the bulky alkyl (butyl) group. In contrast, the anion-CO_2 RDFs show the following features: The N1-C RDF show three distinct solvation shells, a sharp first peak with the highest intensity, a first minimum at shortest distance of 0.48 nm, secondary and a tertiary shell which can accommodate CO_2 molecules. Approximately 11 CO_2 molecules interact with the N1 site within the cut-off of 1.1 nm. The N2-C RDF shows the existence of two solvation shells, which are relatively less distinct, and smaller compared to structural features of N1-C RDFs. Further, ~ 4.5 CO_2 molecules can interact with the N2 sites within a cutoff of 1.1 nm. This suggests that CO_2 prefers to interact with the N1 site of the anion over N2. The results here support previous studies on conventional and AAILs. For example, CPMD calculations of Bhargava and Balasubramanian [111] on [Bmim][PF_6] IL and Shi *et al.* [112] on [Emim][OAc] IL also have shown that CO_2 molecules preferentially interact with anion. Gurkan *et al.* [33] provided spectroscopic evidences of CO_2 binding with [P_{66614}] based AAILs, a signature of COO^- formation (due to reactive

amine-CO_2 interactions). Luo *et al.* [113] suggested that multiple site cooperative interactions can enhance CO_2 capture in a pyridinium anion based IL.

To present a three-dimensional view of density distribution of CO_2 molecules around the amine sites of the anion, Spatial Distribution Functions (SDFs) were calculated using the TRAVIS [105] program (visualized using VMD [114]). The SDF of CO_2 molecules surrounding the N1 site **(Figure 2.4c)** shows three clouds of CO_2 densities, where two clouds are close to the carboxylate oxygen atoms, and the remaining cloud near the N1 site of the anion. However, only a single cloud of CO_2 is observed near the N2 site **(Figure 2.4d)** which confirms that the N1 site has preferential interaction with the CO_2 molecules, where the carboxylate group enhances CO_2 absorption.

2.3.4 Effect of CO_2 absorption on IL mobility

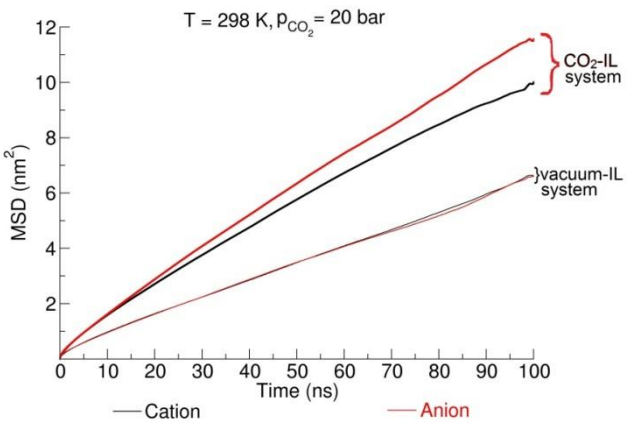

Figure 2.5. Mean Square Displacement of cations and anions of IL.

The influence of CO_2 absorption on dynamics of cations and anion of IL is examined by Mean Square Displacement (MSD) [104] **(Figure 2.5)**. To compare the effect of CO_2 absorption, a vacuum-IL system was simulated, where the MSD of cations and anions are similar. Both cations and anions of IL move faster in CO_2-IL system compared to in vacuum-IL system. In comparison to cations, anions move faster, and

this is due to preferred interaction of anion with CO_2 (as seen from RDFs as well). Similar trends are seen at other partial pressures **(Figure A7)**. The MD simulations of Perez-Blanco and Maginn [52] have shown that mobility of ions of IL remain unaffected with CO_2 absorption where they have calculated the dynamical properties up to 1 ns. The MSDs calculated in this work suggest that their [52] observations are valid only at short timescales. At timescales beyond 1 ns, CO_2 absorption increases the mobility of cations and anions. This mobility arises due to physical interaction of CO_2 molecules at the interface and bulk IL layers.

To check the reproducibility of CO_2 absorption events, additional MD simulations were also performed with different initial configurations and system sizes **(Figure A8)**. The simulations show that the structural and dynamical properties of CO_2-IL system remain unchanged by the choice of initial configuration **(Figure A9, Figure A10, Figure A11)**.

2.4 CONCLUSIONS

A molecular mechanism of high pressure CO_2 absorption in $[P_{4444}][Lys]$ IL is investigated using MD simulations. The charge densities show a structured ordering with opposite charged layers near the CO_2-IL interface. The particle densities show that that the interface is saturated with CO_2 molecules at around 10 ns. A maximum of 1.08 molar absorption of CO_2 can be achieved at T = 278 K and p_{CO_2}= 20 bar. The interaction and absorption of CO_2 leads to an increase in the mobility of cations and anions of IL, where higher mobility of anions indicate interactions of CO_2 molecules largely with anions. This increase in mobility of ions of IL is supported with the decrease in cation-anion interactions after CO_2 absorption (as seen from RDFs). An immediate outcome of this study will be an examination of the process of CO_2 desorption and the effect of humidification on CO_2 absorption/desorption in IL. Such findings can motivate experimental investigations to screen, synthesize and characterize efficient ILs for CO_2 capture and also optimize the functionality of anions to enhance absorption.

——*——*——

The content of this chapter and associated content in Appendix A are adapted from "Molecular Mechanism of CO_2 Absorption in Phosphonium Amino Acid Ionic Liquid"

RSC Adv. ***2016****, 6, 55438–55443.*

Chapter 3:
Mechanism of CO_2-Lysinate Reaction-Participation of Water as an Explicit Molecule

3.1 INTRODUCTION

In this chapter, mechanisms of CO_2-Lys^- reactions and CO_2-Lys^--H_2O reactions are examined using DFT calculations. A discussion on AAILs, and concurrent reports on reaction mechanisms participating in CO_2 absorption are presented. Among other computational methods, the quantum chemistry calculations have been widely employed to examine reaction pathways associated with CO_2 capture in amines and AA. Shim *et al.* [115] employed DFT calculations on monoethanolamine (MEA)-CO_2 reaction using the Polarized Continuum Model (PCM) and an explicit water model. The authors observed that in the absence of explicit water molecules, a second MEA molecule acts as a base for proton transfer during the formation of a carbamate product. An addition of a single water molecule also shows its role as a base to facilitate carbamate formation, though the authors concluded that, energetically, MEA is a preferred base compared to H_2O. Xie *et al.* [116] investigated the mechanism of MEA-CO_2 reaction with the computationally expensive CCSD(T) level of theory and reported the formation of zwitterionic intermediate (carbamate) to be the most favorable reaction path. The authors calculated the equilibrium concentration of zwitterionic carbamate intermediate (10^{-11} mol/L) and suggested that due to such a low concentration of this intermediate, it could not be detected experimentally. The

formation of bicarbonate, and role of water in CO_2-amine interactions have also been explored using quantum chemistry calculations of Minrup *et al.* [21], Matsuzaki *et al.* [117] and Kim *et al.* [118]. In another work, Sastry and coworkers [16] investigated interactions of 20 AA with CO_2 and calculated the Activation Energy barrier (E_a), Reaction Energy (RE) and Binding Energy (BE) using DFT calculations. The authors concluded that lysine has the third lowest E_a, with only arginine and proline to be much lower. Moreover, the authors found that the inclusion of a water molecule leads to a lower E_a barrier for easier CO_2 capture.

Such theoretical works provided differences and similarities in amine *vs.* AA reaction with CO_2. Since AA have amine functionality and can easily form anions, several experimental studies [30, 32, 55, 119, 120] have explored the possibility to use AAILs for CO_2 absorption. Zhou *et al.* [30] synthesized $[C_2NH_2MIm^+][Lys^-]$ IL and reported a 1.59 molar ratio absorption of CO_2 per IL (T = 313 K) with E_a barrier of 6.1 kcal/mol. The authors further observed a bicarbonate → carbamate reaction channel arising from CO_2 desorption (using ^{13}C NMR). Jing *et al.* [55] designed $[Lys]^-$ anion based ILs with the cation of diethylenetetramine and triethylenetetramine. The authors reported that CO_2 uptake exceeded the theoretical limit of 2.0 molar ratio in these ILs, which suggests the role of multiple-site-cooperative interactions in CO_2 absorption. Alternatively, aqueous solutions of potassium lysinate for efficient CO_2 capture have also been investigated by several experimental works [37, 39, 41, 57, 121, 122]. These studies primarily focused on changes in physical properties (density, viscosity, solubility), kinetics and the effect of water and temperature on CO_2 absorption. Costa and coworkers [123] concluded that the CO_2 affinity of $[NTf_2]^-$ anion based imidazolium ILs could be expressed as a function of BE and C-O bond length (in CO_2). Yamada [124] used the SMD (Solvation Model based on Density) [125] to compare the solvation effects on the reaction of CO_2 with $[Gly]^-$ based AAIL and MEA. Unlike MEA, the author found that the reaction barrier for CO_2 with $[Gly]^-$ did not show a dependence on the dielectric constant of the solvent medium. This finding motivates a

DFT study of AA anion-CO_2 reaction mechanism in the presence of explicit water molecules instead of a continuum solvation model.

Existing reports have highlighted the potential of $[Lys]^-$ anion based materials as an alternative to amines for carbon capture and storage. However, the understanding of reaction mechanisms involving CO_2 capture and the role of water as a base in $[Lys]^-$-CO_2 interactions have remained largely unexplored. In traditional amines, the most proposed mechanism of reaction of CO_2 in the presence of water is considered to follow carbamate → bicarbonate → carbonate path [55, 124, 126, 127]. This pathway considers amine to be the primary nucleophile for an attack on CO_2. However, AA anions like $[Lys]^-$ can take an alternative path of direct bicarbonate formation in which the first and rate-determining step is protonation of amine leaving the formation of hydroxide as shown in the **Equation (1.2)**, which subsequently results in a barrier-less reaction between OH^- and CO_2, producing bicarbonate. Yuan *et al.* [126] in their experimental work discussed this to be one of the pathways for the reaction of CO_2 in an aqueous mixture of cholinium glycinate and methyl diethanolamine. In case of neutral amines, this mechanism is less favorable, but it requires a systematic examination for AA anions where the path 1 is expected to be observed. The previous chapter discussed CO_2 absorption in $[P_{4444}]^+[Lys]^-$ IL using Molecular Dynamics (MD) simulations and examined the timescales of important absorption steps, site-specific interactions, and multiple site cooperation involved in $[Lys]^-$-CO_2 interactions. This chapter reports a more comprehensive study addressing all the possible pathways for $[Lys]^-$-CO_2 reaction, the effect of an explicit molecule of water, possibilities of direct bicarbonate formation mechanism and atomic interactions responsible for multiple site-cooperation. Though the inclusion of only one molecule of water neglects the solvation effects, it is worth modeling Lys^--H_2O interactions in a single molecular manner to understand bicarbonate/carbonate/carbamate formations – before addressing bigger clusters and condensed phase. Hence the calculations in this chapter would build the foundation for condensed phase calculations of larger scale. The

theoretical methods and brief protocols for calculations are provided in the next section, followed by results and discussion about the pathways of reactions and energetics. A summary of this work in provided at the end of the chapter.

3.2 COMPUTATIONAL DETAILS

All the calculations were performed using Gaussian 09-Rev.D01 software [128]. The geometries of reactants, intermediates, transition states, and products were optimized using the hybrid functional B3LYP [129] and M06-2X [130]. An empirical Grimme's dispersion correction (D3) [131] was used with M06-2X functional to describe long-range interactions. Standard 6-311++G(d,p) basis set was used for all calculations. For calculation of Binding Energies (BE), corrections from Basis Set Superposition Error (BSSE) and fragment relaxation were also incorporated by the rigorous-fragment-Counterpoise (rig-fCP) [132, 133] method **(Appendix B)**. All geometries for optimization were obtained from systematic radial and angular Potential Energy Scans (PES) of CO_2 around the pertinent reaction sites on the $[Lys]^-$ and $[Lys]^-$-H_2O species. The non-bonded complexes were first obtained, and transition states were searched using the mode redundant scans of the reaction coordinate with the full relaxation of the molecule. The transition states obtained from the PES were reconfirmed using the QST2 [134] method. The transition states were also validated using frequency calculations and the intrinsic reaction coordinate method. The relative energies provided in all the figures are calculated using electronic energies of the species, while ZPE corrected values are provided in the respective tables for all the reactions. Wherever required, enthalpy of reaction at T = 298 K ($\Delta H_{g,298}$) is calculated from enthalpies of reactants and products.

3.3 RESULTS AND DISCUSSION

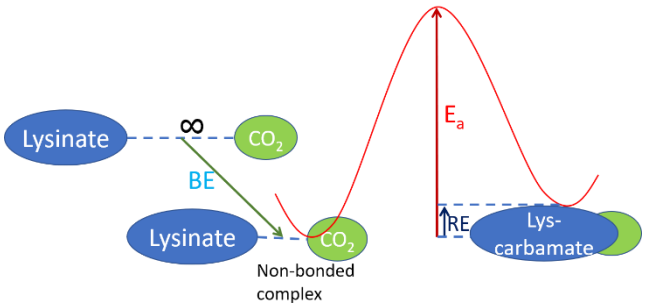

Figure 3.1. Schematic pathway with definitions of BE, E_a and RE in $[Lys]^-$-CO_2 reaction.

Figure 3.1 shows a general reaction pathway of C-N chemistry in AAILs. The reaction pathway can be understood by calculation of following energetics: Binding energy (BE) leading to the formation of a non-bonded complex, Activation Energy (E_a) barrier for C-N/C-O reaction, Reaction Energy (RE) denoting the stability of carbamate product/bicarbonate product. The various pathways observed in $[Lys]^-$-CO_2 and $[Lys]^-$-H_2O-CO_2 reactions are discussed in subsequent sections. Unless explicitly mentioned, the energetics and geometrical parameters discussed in the following sections are obtained using the B3LYP functional.

3.3.1 $[Lys]^-$-CO_2 reaction

The CO_2 molecule can interact with the amine sites of $[Lys]^-$ (near the carboxylate amine and terminal amine), and the carboxylate site. Unlike Lysine, which has different structures (canonical and zwitterionic); the $[Lys]^-$ anion possess only one stable structure observed from geometry optimizations. To examine the energetics, several radial PES were performed along the $C(CO_2)$-N1(near carboxylate amine), $C(CO_2)$-N2(terminal amine), $C(CO_2)$-CL(carboxylate carbon) and $C(CO_2)$-OL2(far to amine oxygen atom on the COO^- group) reaction coordinates **(Figure 3.2)**. The interaction of OL2 site with $C[CO_2]$ is preferred over OL1 site due to poor nucleophilicity of OL1 (OL1-H(N1) hydrogen bond is 2.11 Å). The optimized geometries of four non-bonded (NB) complexes, Nb1, Nb2, Nb3 and Nb4 obtained

from the different [Lys]$^-$-CO_2 PES are shown in **Figure 3.3**. The order of stability of these complexes (as seen from the calculated BE) is independent on the choice of DFT functional **(Table 3.1)**.

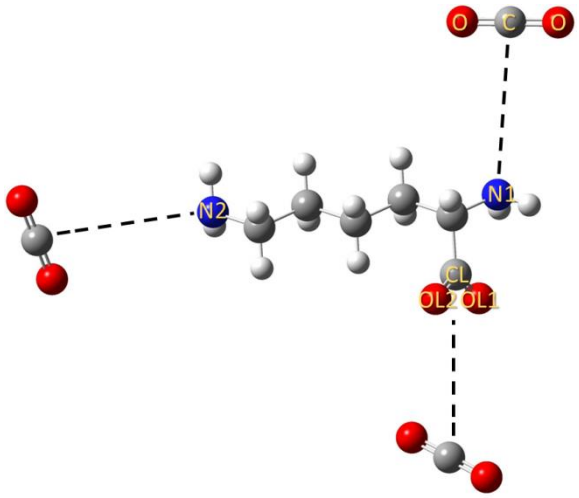

Figure 3.2. Possible reaction sites for [Lys]$^-$-CO_2 interactions.

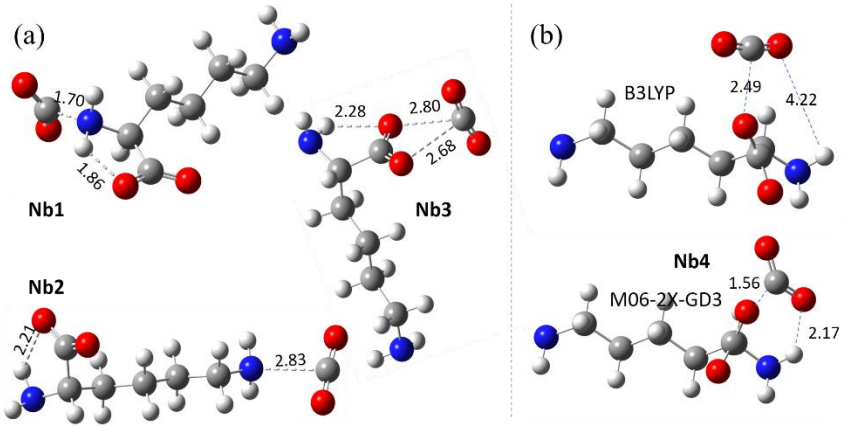

Figure 3.3. (a) B3LYP optimized geometries of the Nb1, Nb2 and Nb3 complexes, (b) B3LYP vs. M06-2X-GD3 optimized geometry of the Nb4 complex, observed in [Lys]$^-$-CO_2 reaction. Distances are shown in Å.

Table 3.1. ZPE corrected values of BE, E_a and RE for $[Lys]^-$-CO_2 reaction (in kcal/mol). Values of BE corrected using rig-fCP method are provided in parentheses.

Method	**B3LYP**			**M06-2X-GD3**		
Reactants	**BE**	**E_a**	**RE**	**BE**	**E_a**	**RE**
Nb1 N1[Lys]$^-$-CO_2	-6.15, (-6.93)	1.76	-0.23	-10.00, (-10.92)	0.57	-2.55
Nb2 N2[Lys]$^-$-CO_2	-3.27, (-3.55)	37.03	6.78	-5.37, (-5.60)	34.37	3.11
Nb3 CL[Lys]$^-$-CO_2	-7.77, (-8.06)	No reaction	No reaction	-11.42, (-11.95)	No reaction	No reaction
Nb4 OL2[Lys]$^-$-CO_2	-5.97, (-6.28)	No reaction	No reaction	-8.92, (-9.54)	No reaction	No reaction

The calculated BE suggests that Nb1, Nb3 and Nb4 complexes show a similar stability (-6.28 kcal/mol to -8 kcal/mol), whereas the Nb2 complex is relatively less stable with a BE of -3.55 kcal/mol. The weak-interactions, O-C[CO_2] bond lengths and OCO[CO_2] angles are listed in **Table 3.2**. The feasibility of $[Lys]^-$-CO_2 chemical reaction at different sites can be assessed by observing site-specific intermolecular distances in the NB complexes. The N1-C[CO_2] distance (1.70 Å) in the Nb1 complex is shorter compared to the N2-C[CO_2] distance (2.83 Å) in the Nb2 complex and CL-C[CO_2] distance (3.05 Å) in the Nb3 complex. The reason behind the close proximity of CO_2 molecule in the Nb1 complex compared to the Nb2 and Nb3 complexes is the presence of more nucleophilic environment provided by the COO^- group close to the N1 site. This also facilitates the abstraction of a proton from the N1-NH_2 group which leads to carbamate formation.

Table 3.2. Site-specific intermolecular distances of $[Lys]^-$-CO_2 reaction (in Å), O1-C and O2-C distances (in Å) and O1-C-O2 angle of CO_2 (in degree) in NB, TS and products.

	Method	**B3LYP**			**M06-2X-GD3**		
Optimized Structures		d (X[Lys]$^-$ - C[CO_2])	d (O1-C, O2-C) [CO_2]	∠O1-C-O2 [CO_2]	d (X[Lys]$^-$ - C[CO_2])	d (O1-C, O2-C) [CO_2]	∠O1-C-O2 [CO_2]
NB Complxes	**Nb1** **N1[Lys]$^-$ - CO_2**	1.697	1.212, 1.218	140.54	1.649	1.209, 1.215	139.81
	Nb2 **N2[Lys]$^-$ - CO_2**	2.834	1.162, 1.163	174.38	2.728	1.156, 1.157	174.76
	Nb3 **CL[Lys]$^-$ - CO_2**	3.054	1.165, 1.165	169.60	2.926	1.158, 1.159	170.64
	Nb4 **OL2[Lys]$^-$ - CO_2**	2.490	1.163, 1.166	169.62	1.558	1.208, 1.221	137.90
TS	**Ts1** **N1[Lys]$^-$ - CO_2**	1.567	1.230, 1.234	135.39	1.560	1.223, 1.227	135.87
	Ts2 **N2[Lys]$^-$ - CO_2**	1.539	1.198, 1.295	135.31	1.526	1.193, 1.285	135.83
Products	**P1** **N1[Lys]$^-$ - CO_2**	1.502	1.243, 1.244	132.38	1.494	1.237, 1.238	132.44
	P2 **N2[Lys]$^-$ - CO_2**	1.363	1.206, 1.381	119.60	1.362	1.200, 1.386	120.13

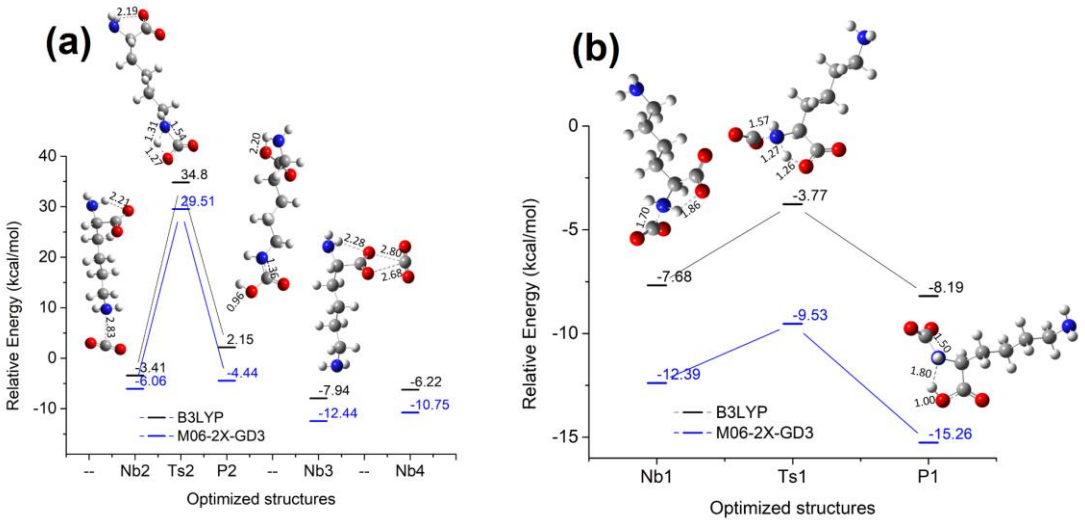

Figure 3.4. Relative energy (electronic only, in kcal/mol) profile of reactions in the (a) Nb2 and (b) Nb1 complexes from B3LYP and M06-2X-GD3 functionals. The BE of the Nb3 and Nb4 are also shown in (a) for comparison. ZPE corrected values of BE, E_a and RE for the same are provided in Table 1. All the geometries (distances in Å) shown in (a) and (b) are optimized using the B3LYP functional.

Unlike the Nb1, Nb2 and Nb3 complexes, the optimized geometry of Nb4 complex is different from the calculations using B3LYP and M06-2X-GD3 methods **(Figure 3.3b)**. The smaller OL2-CO_2 distance (1.56 Å) in M06-2X-GD3 optimization arises from a stationary point in which H(N1) forms a stronger hydrogen bond (2.17 Å) with O[CO_2]. This also results in a larger bending of OCO angle (138^0) in the geometry optimized using the M06-2X-GD3 functional compared to the B3LYP functional (170^0). However, the differences in the optimized geometry of the Nb4 complex do not change the order of stability of the NB complexes **(Table 3.1)**.

As observed from the PES, the Nb3 and Nb4 complexes do not provide a reaction pathway suggesting that these complexes bind CO_2 with weak interactions only, leading to physisorption. The scans on the Nb1 and Nb2 complexes show a reaction pathway with a product formation. The reaction at the Nb2 complex follows a concerted C-N2 bond formation and proton transfer from N2 to O[CO_2] **(Figure 3.4a)**. However, the calculated E_a for this reaction is significantly large (~ 37 kcal/mol)

which makes the reaction less likely to occur. The high E_a barrier is similar to various primary amine-CO_2 reactions, where a R-NH-COOH (carbamic acid) type product forms via an R-NH_2^+-COO^- type transition state. An "intermolecular" proton transfer from the N2 site to the CO_2 in the Nb2 complex is confirmed (from frequency calculation) by the Ts2 transition state. This intermolecular proton transfer reaction is similar to that observed in the reaction between CO_2 and primary amines which is usually catalyzed with another molecule of amine or water as a base to make the reaction facile. In contrast, the Nb1 complex shows a different pathway where the C-N1 bond is formed with an insignificant E_a barrier (~ 1 kcal/mol) with a similar value of RE due to facile transfer of a proton from the N1 to the COO^- group **(Figure 3.4b)**. The Ts1 transition state also confirms (from frequency calculation) an "intramolecular" proton transfer from the N1 site to the COO^- group of $[Lys]^-$ in the Nb1 complex. The intramolecular proton transfer observed in the Nb1 complex reduces the E_a barrier significantly and leads to a stable "carbamate-carboxylic acid product" instead of "carbamic acid-carboxylate." The N2 vs. N1 mechanism of the reaction can also be examined from the O-C bond lengths in CO_2. As the N2-C[CO_2] bond formation (in Nb2) involves proton transfer from N2 to CO_2, the O-C bond lengths are not equivalent in the transition state TS2 and product P2. However, in the reaction at the Nb1 complex, the O-C bond lengths of CO_2 are equivalent in TS1 and P1.

The mechanism of $[Lys]^-$-CO_2 reaction in the Nb1 complex could not be observed in Lysine [16] as the presence of a proton on COO^- or N1-NH_2 group eliminates the possibility of proton abstraction by the COO^- group. To summarize, the Nb1, Nb3 and Nb4 complexes are more favorable for CO_2 absorption via weak interactions. The Nb2 complex shows weaker stability with a very large E_a barrier which limits its role to physisorption. The Nb1 complex forms a stable product via intramolecular proton transfer and hence contributes to chemisorption. Similar trends are seen from calculations performed using the M06-2X-GD3 functional. The M06-

2X-GD3 optimized geometries of the NB complexes, transition states and products **(Figure B1)**.

Table 3.3. BE (in kcal/mol), weak interactions (distances in Å) and OCO angle (in degree) in optimized geometries of the NB complexes from [Lys^-]-H_2O-CO_2 reaction. rig-fCP corrected values of BE are provided in parentheses.

Method	B3LYP				M06-2X-GD3			
Reactants	BE	d (H1-O, H2-O)[H_2O]	d (O1-C, O2-C)[CO_2]	∠O1-C-O2 [CO_2]	BE	d (H1-O, H2-O)[H_2O]	d (O1-C, O2-C)[CO_2]	∠O1-C-O2 [CO_2]
Nbw1n	0.39, (-0.55)	0.961, 0.984	1.214, 1.236	136.55	-6.54, (-7.66)	0.959, 0.977	1.211, 1.231	136.60
Nbw1h	-3.92, (-4.24)	0.961, 1.003	1.161, 1.163	174.67	-5.96, (-6.60)	0.959, 0.998	1.155, 1.157	174.35
Nbw2o	-6.78, (-7.07)	0.962, 0.990	1.162, 1.163	172.63	-10.89, (-12.6)	0.967, 0.975	1.156, 1.157	173.73
Nbw2h	-4.29, (-4.60)	0.961, 1.004	1.161, 1.163	174.00	-7.96, (-7.88)	0.959, 1.016	1.156, 1.158	173.53
Nbw3o	-3.69, (-4.13)	0.969, 0.980	1.160, 1.164	173.82	-7.66, (-7.80)	0.968, 0.972	1.154, 1.160	172.89
Nbw3n	-3.12, (-3.66)	0.971, 0.974	1.202, 1.207	144.29	-7.67, (-7.87)	0.968, 0.969	1.206, 1.211	141.19
Nbw3h	-4.81, (-5.22)	0.977, 0.978	1.162, 1.162	172.95	-7.56, (-7.54)	0.973, 0.974	1.157, 1.157	172.95
Nbw4h	-3.23, (-3.60)	0.961, 0.990	1.161, 1.162	175.76	-5.55, (-5.80)	0.959, 0.985	1.156, 1.156	175.37
Nbw5n	-4.07, (-4.28)	0.969, 0.988	1.164, 1.165	170.80	-7.00, (-7.06)	0.970, 0.977	1.158, 1.159	171.60

3.3.2 [Lys]$^-$-H_2O-CO_2 reaction

Since [$Lys]^-$ acts as a strong nucleophile to bind CO_2 from various reaction sites, the mechanism of binding can also be influenced with the presence of water as in the real-time application of AA anion-based salts and solids, where water is commonly used.

From $[Lys]^-$-H_2O PES, five $[Lys]^-$-H_2O NB complexes are obtained: Nbw1, Nbw2, Nbw3, Nbw4 and Nbw5 **(Figure 3.5)**. The BE of these complexes is -13.05, -15.12, -17.76, -10.06 and -17.77 kcal/mol respectively (values with M06-2X-GD3 are -13.77, -16.83, -19.75, -10.31, and -24.25 kcal/mol respectively **(Figure B2)**. A PES of CO_2 molecule with each of the above NB complexes provides various reaction possibilities as discussed further. The BE and weak-interactions observed in the optimized geometry of Nbw# + CO_2 NB complexes (namely Nbw#x where # = 1/2/3/4/5 - suffix associated to complexes in **Figure 3.5** and x = h/o/n - suffix associated to the interaction of CO_2 with h = water, o = OL2 and n = N1/N2 of Nbw#) are provided in **Table 3.3**.

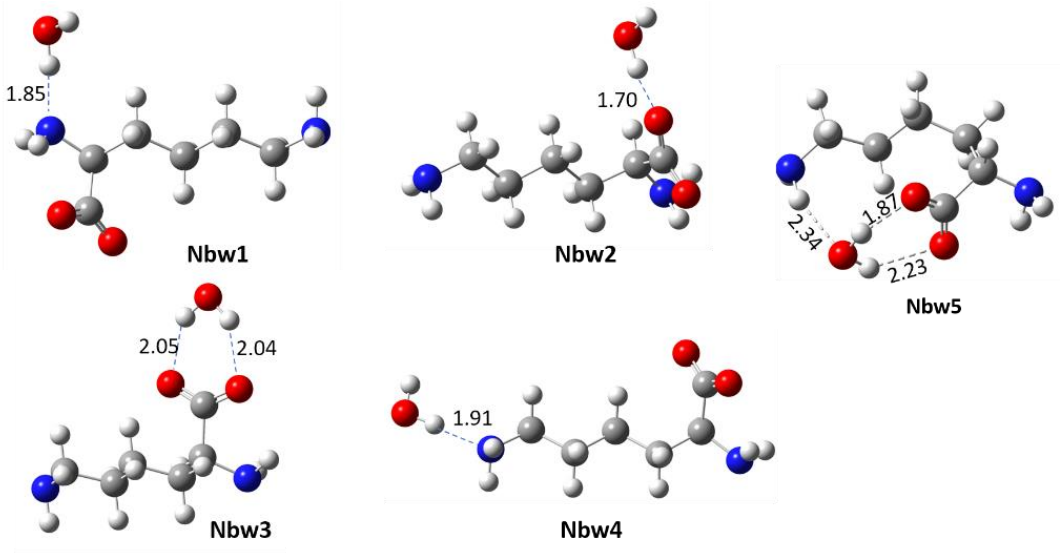

Figure 3.5. Optimized geometries of $[Lys]^-$-H_2O complexes using the B3LYP functional. Bond distances are shown in Å.

From several PES of CO_2 around the Nbw1 complex, two NB complexes (Nbw1h and Nbw1n) were obtained **(Figure 3.6)**, where the Nbw1h complex is formed when the CO_2 molecule closely approaches the O[H_2O] and, the Nbw1n complex is formed due to cooperative interactions of the N1 amine group and H_2O with CO_2. The interactions lead to a shorter N1-C distance (1.61 Å) and significantly reduced OCO

angle in CO_2 (136.6^0). In the Nbw1n complex, water stabilizes the CO_2 molecule close to the N1 amine group with two hydrogen bonds, one with H[N1] and the other with O[CO_2]. Though the calculated value of BE with ZPE for the Nbw1n complex is + 0.39 kcal/mol, the electronic only and rig-fCP corrected values (-2.07 and -0.55 kcal/mol respectively) suggest it to be moderately stable **(Table 3.4)**. However, the BE of the Nbw1n complex calculated using the M06-2X-GD3 functional also suggests it to be more stable compared to the Nbw1h complex.

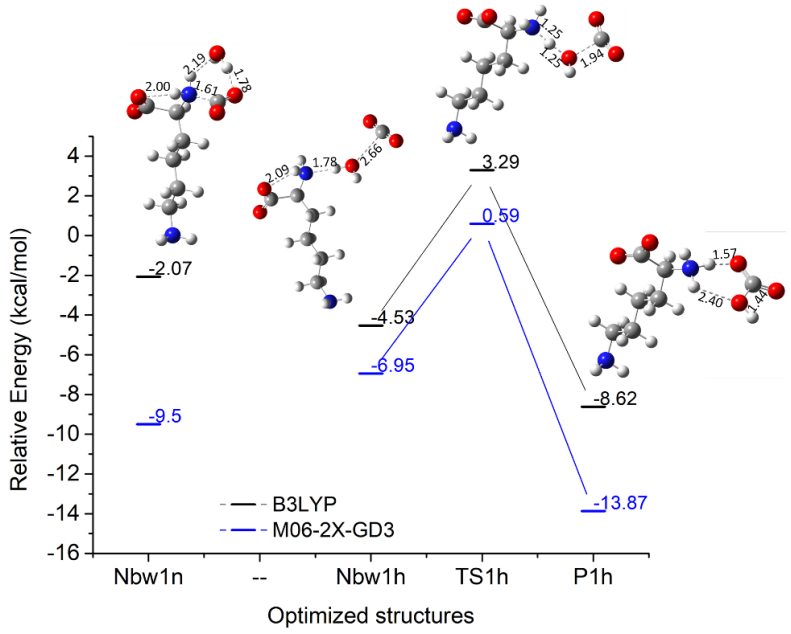

Figure 3.6. Relative energy (electronic only, in kcal/mol) profile of CO_2 + Nbw1 reaction from B3LYP and M06-2X-GD3 functionals. All the geometries (distances in Å) shown are optimized using B3LYP functional.

A chemical reaction at the Nbw1n complex is not observed and hence should be considered contributing towards physisorption. The Nbw1h complex showed a slight bending in CO_2, but its comparative stability arises due to the H[H_2O]-N1[NH_2] hydrogen bond. In the Nbw1-CO_2 PES, a closer approach of CO_2 to H_2O leads to proton abstraction from the H_2O to $[Lys]^-$, with E_a barrier of 6.30 kcal/mol from the transition state Ts1h. The frequency calculation for the Ts1h transition state also

confirms the proton transfer with the formation of a new N1-H[H_2O] hydrogen bond (1.25 Å) and weakening of the O-H bond (1.25 Å) in the H_2O molecule. The calculated RE (-1.78 kcal/mol) for this reaction suggests an exothermic product formation. The net reaction involving the Nbw1h complex can be written as:

$$NH_2\text{-}(CH_2)_4\text{-}C(H)(COO^-)\text{-}NH_2 + H_2O + CO_2 \rightarrow NH_2\text{-}(CH_2)_4\text{-}C(H)(COO^-)\text{-}NH_3^+ + HCO_3^- \quad \textbf{(3.1)}$$

with $\Delta H_{g,298}$ to be - 6.75 kcal/mol. The optimized geometry of the product for this reaction (P1h) is a Lysine-bicarbonate complex, in which Lysine exists in the zwitterionic form stabilized by two hydrogen bonds with the HCO_3^-. The reaction is more likely to proceed in the forward direction and hence should be considered to contribute towards chemisorption significantly.

Similar to Nbw1, in the Nbw2 complex, two possibilities of a reaction are explored, resulting in Nbw2o and Nbw2h complexes **(Figure 3.7)**. Both B3LYP and M06-2X-GD3 optimized geometries suggest Nbw2o be more stable primarily due to two hydrogen bonds formed by H_2O with OL2 and O[CO_2] respectively, with a weak-interaction between OL1 and C[CO_2]. Similar to the Nbw1n complex, no chemical reaction is observed in the Nbw2o complex, suggesting CO_2 binds in the form of physisorption only. However, the Nbw2h complex follows the formation of Lysine-bicarbonate product P2h, with E_a barrier of 4.69 kcal/mol as observed from the transition state Ts2h. The overall reaction can be written as:

$$NH_2\text{-}(CH_2)_4\text{-}C(H)(COO^-)\text{-}NH_2 + H_2O + CO_2 \rightarrow NH_2\text{-}(CH_2)_4\text{-}C(H)(COOH)\text{-}NH_2 + HCO_3^- \quad \textbf{(3.2)}$$

Table 3.4. ZPE corrected values of E_a and RE (in kcal/mol) for [Lys^-]-H_2O-CO_2 reaction involving different NB complexes.

Method		B3LYP		M06-2X-GD3	
Reactants	NB complexes	E_a	RE	E_a	RE
Nbw1 + CO_2	Nbw1n	No reaction	No reaction	No reaction	No reaction
	Nbw1h	6.30	-1.78	6.25	-5.07
Nbw2 + CO_2	Nbw2o	No reaction	No reaction	No reaction	No reaction
	Nbw2h	4.69	3.06	3.75	-0.82
Nbw3 + CO_2	Nbw3o	No reaction	No reaction	No reaction	No reaction
	Nbw3n	4.68	4.41	3.30	2.48
	Nbw3h	7.72	6.74	5.98	5.43
Nbw4 + CO_2	Nbw4h	14.61	6.94	12.67	1.52
Nbw5 + CO_2	Nbw5n	No reaction	No reaction	No reaction	No reaction

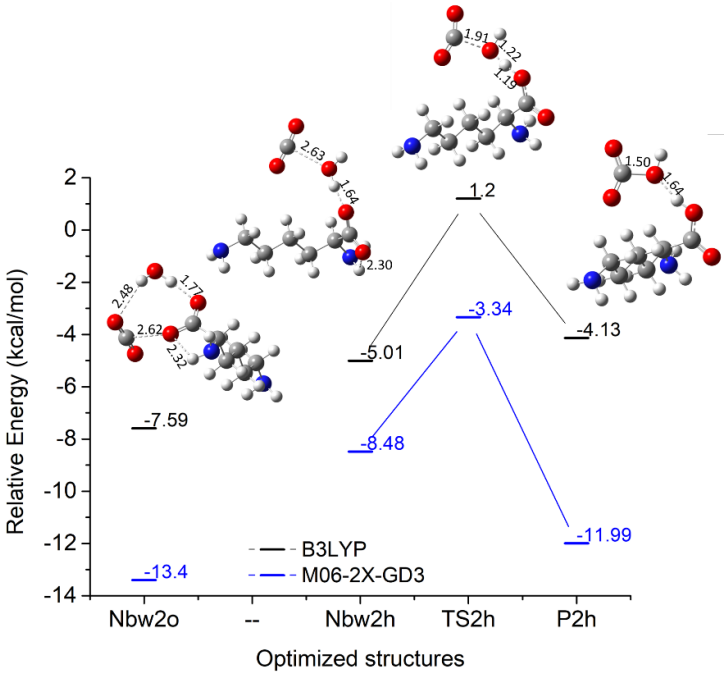

Figure 3.7. Relative energy (electronic only, in kcal/mol) profile of CO_2 + Nbw2 reaction from B3LYP and M06-2X-GD3 functionals. All the geometries (distances in Å) shown are optimized using the B3LYP functional.

The reaction **(3.2)** differs from reaction **(3.1)** in two ways: i) the product structure P2h contains a non-zwitterionic Lysine and ii) presence of only one hydrogen bond between the Lysine-HCO_3^- complex. These factors oppositely contribute to the stability of the P2h product and manifest in a positive value of RE (3.06 kcal/mol). The calculated $\Delta H_{g,298}$ for the overall reaction 3 is -2.17 kcal/mol. Such smaller values for RE and $\Delta H_{g,298}$ suggest the possibility of the reaction to oscillate in either direction. Hence the reaction 3 may be observed in both chemisorption and possible desorption of CO_2.

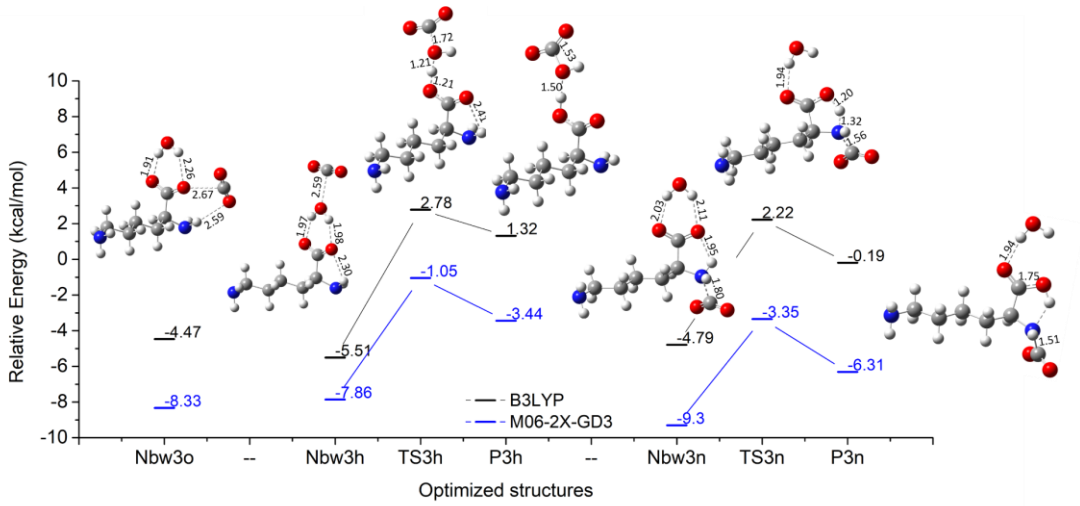

Figure 3.8. Relative energy (electronic only, in kcal/mol) profile of CO_2 + Nbw3 reaction from B3LYP and M06-2X-GD3 functionals. All the geometries (distances in Å) shown are optimized using the B3LYP functional.

The reaction between the Nbw3 complex with CO_2 leads to three NB complexes: Nbw3o, Nbw3h, and Nbw3n. **Figure 3.8** shows the relative stability of these complexes with reference to Nbw3 + CO_2. The order of stability of the complexes is: Nbw3n < Nbw3o < Nbw3h. However, the BE calculated using the M06-2X-GD3 functional shows that these complexes have similar stability. Though the Nbw3o complex does not lead to a chemical reaction, three hydrogen bonds (two strong hydrogen bonds between the H_2O and COO^- group and one moderate hydrogen bond between H[N1] and O[CO_2]) stabilize the complex. This illustrates that the Nbw3o complex is likely to participate in physisorption. The Nbw3n complex is

slightly less stable than the Nbw3o complex due to the presence of H[H_2O]-OL2 and H[H_2O]-OL1 hydrogen bonds which reduces the OL1-H[N1] interaction. The N1[NH_2]-CO_2 interactions in the Nbw3n complex are similar to the Nb1 complex, except an additional H_2O molecule exists in the Nbw3n complex. The lower stability of the Nbw3n complex compared to Nb1 is observed by a longer OL1-H[N1] hydrogen bond (1.95 Å) in the Nbw3n complex, compared to the corresponding bond distance (1.86 Å) in the Nb1 complex. Other geometrical parameters like OCO bending and N1-C[CO_2] distance also confirm the adverse effects of water leading to poor CO_2 reactivity in the Nbw3n complex. The presence of H_2O in proximity to the COO^- group inhibits the formation of carbamate in the Nbw3n complex as supported by higher E_a barrier (4.68 kcal/mol from the Ts3n transition state) and RE (4.41 kcal/mol for the P3n product) compared to Ts1 and P1 observed for the Nb1 complex, respectively. The Nbw3h complex shows the reaction profile similar to that seen in the Nbw2h complex. However, the calculated E_a barrier (7.72 kcal/mol from the Ts3h transition state) for the reaction at the Nbw3h complex is higher compared to that observed in the Nbw2h complex (4.69 kcal/mol). The Nbw3h complex forms P3h as final product with a more positive RE (6.74 kcal/mol) compared to Nbw2h → P2h due to the presence of a H_2O molecule near the COO^- group. The overall reaction involving the Nbw3h complex is similar to reaction 3. The calculated $\Delta H_{g,298}$ for the net reaction Nbw3h → P3h is 2.35 kcal/mol, which suggests the reaction to be endothermic. In short, the reaction pathways and the trends in energies in the Nbw3n and Nbw3h complexes are similar to that seen in the Nb1 and Nbw2h complexes, respectively. However, the differences arise where H_2O-COO^- interactions make [Lys]$^-$-CO_2 reactions less favorable in the Nbw3n and Nbw3h complexes. The calculated value of RE and $\Delta H_{g,298}$ of Nbw3h → P3h suggests the reaction to more likely proceed in the reverse direction and is expected be observed during the process of CO_2 desorption.

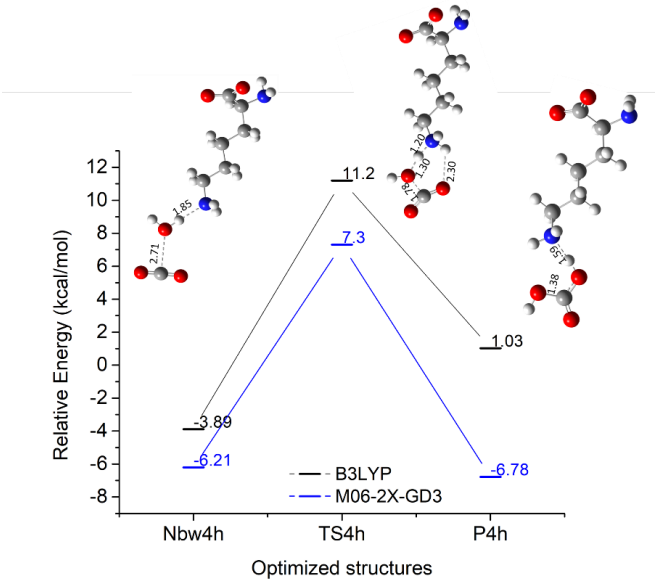

Figure 3.9. Relative energy (electronic only, in kcal/mol) profile of CO_2 + Nbw4 reaction from B3LYP and M06-2X-GD3 functionals. All the geometries (distances in Å) shown are optimized using the B3LYP functional.

The Nbw4 complex with CO_2 forms the Nbw4h complex **(Figure 3.9)**, where only two weak-interactions are observed. One of the interactions is between CO_2 and Nbw4 (C[CO_2]-O[H_2O] distance = 2.71 Å) and the other is a hydrogen bond within the Nbw4 complex (H[H_2O]-N2[NH_2] distance 1.85 Å). The calculated BE and OCO angle of CO_2 is similar in Nbw4h and Nb2 complexes. But the chemical reaction in the Nbw4h complex differs from the Nb2 complex due to the presence of H_2O which serves as a bridge between CO_2 and the N2 site. In the Nbw4h complex, the N2 amine group abstracts a proton from H_2O with an E_a barrier of 14.61 kcal/mol (from the transition state Ts4h) and forms the product P4h with RE = 6.94 kcal/mol. This reaction pathway is similar to the pathways observed for Nbw#h (# = 1, 2, 3) reactions (direct bicarbonate formation). The expected product for the reaction in the Nbw4h complex is Lysine-bicarbonate. However, a barrier-less proton transfer occurs from NH_3^+[N2] to HCO_3^- to form the product P4h: [Lys]$^-$-carbonic acid. The overall reaction can be written as:

NH_2-$(CH_2)_4$-C(H)(COO^-)-NH_2 + H_2O + CO_2 → NH_2-$(CH_2)_4$-C(H)(COO^-)-NH_2 + H_2CO_3

(3.3)

A large positive value of RE (6.94 kcal/mol) and $\Delta H_{g,298}$ (2.60 kcal/mol) though suggest that the reaction is more likely to occur during the process of CO_2 desorption. The Nbw4h complex can still be observed in the physisorption like the Nb2 complex.

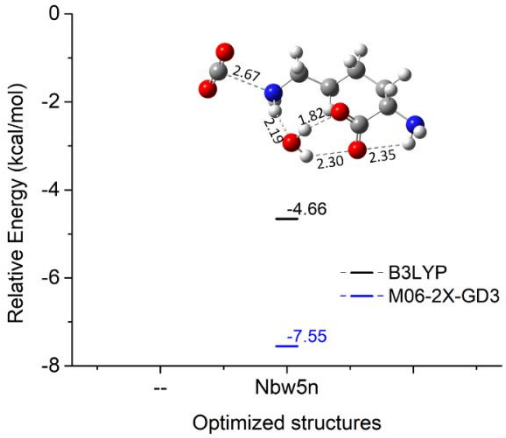

Figure 3.10. BE (electronic only, in kcal/mol) of CO_2 + Nbw5 reaction from B3LYP and M06-2X-GD3 functionals. Optimized structure of the Nbw5n complex (distances in Å) using the B3LYP functional.

The fifth complex, Nbw5n shows unique characteristics. This complex is formed by Nbw5-CO_2 weak-interactions. The Nbw5 complex cyclizes the $[Lys]^-$ to form a ring-like complex involving three hydrogen bonds formed by H_2O **(Figure 3.5)**. From the Nbw5 + CO_2 PES, a chemical reaction pathway is not observed after the formation of Nbw5n complex. The Nbw5n complex contains four hydrogen bonds **(Figure 3.10)** which vary between 1.82 Å to 2.35 Å with various interaction sites such as: H_2O, N1, N2 and, OL1 and OL2 in COO^-. The OCO angle in the Nbw5n complex (170.8^0) is smaller than that observed in the Nb2 complex (174.4^0). In comparison with the Nbw4h and Nb2 complexes, the Nbw5n complex is more stable (BE = -4.28 kcal/mol), which suggests its occurrence in the physisorption of CO_2.

To summarize the $[Lys]^-$-H_2O-CO_2 interactions, four direct bicarbonate formation reaction pathways are observed out of which the one which forms close to the N2 site, which further converts to carbonic acid after abstraction of a proton from Lysine. The form of Lysine in the product P1h is zwitterionic, and in the products P2h and P3h – canonical. This can be understood as the proximity of N1/COO^- to water decides which form of Lysine to form in the product. The complexes observed close to the N2 site (Nbw4h and Nbw5n) are not expected to show their occurrence during chemisorption. The Nbw5n complex is the only complex observed here with a remarkable stability. Though $[Lys]^-$ is cyclized in this complex, it can be assumed that the hydrogen bonding interactions of H_2O with N2 and COO^- groups overcome the structural stress of cyclization and result in comparatively better stability. The M06-2X-GD3 optimized geometries for all the Nbw#x complexes, transition states and products are provided in **Appendix B** **(Figure B3)**.

3.4 CONCLUSIONS

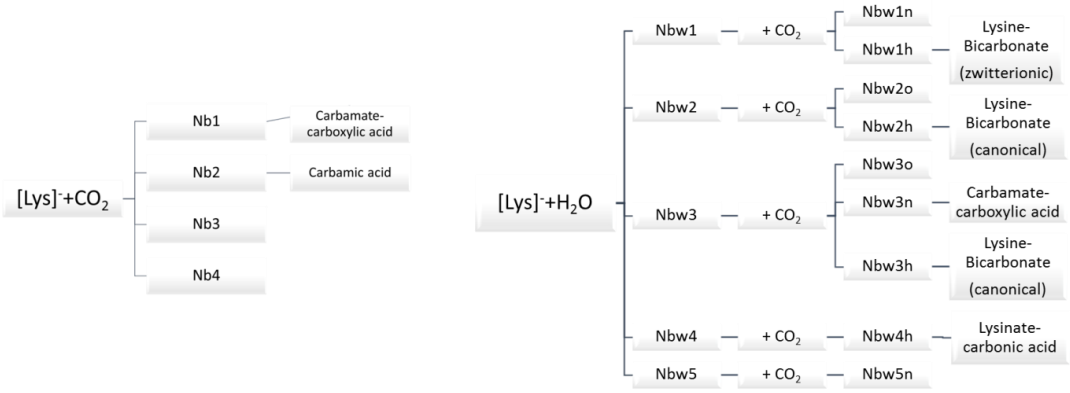

Figure 3.11. All the NB complexes, chemical reaction possibility and product type in $[Lys]^-$-CO_2 and $[Lys]^-$-H_2O-CO_2 interactions.

The various interactions possible between $[Lys]^-$-CO_2 and effect of water are explored using DFT methods, which are summarized in **Figure 11.** Four different NB complexes are observed to contribute towards physisorption in $[Lys]^-$-CO_2 reaction,

out of which only one (Nb1) shows a facile reaction to form a carbamate product. The presence of the COO^- group close to the N1[NH_2] group in [Lys]$^-$ and absence of proton compared to lysine are two important influences in this reaction. The carbamate/carboxylic acid product forms in the Nb1 complex with a small E_a barrier compared to the Nb2 complex.

The [Lys]$^-$ forms five different types of NB complexes on addition of a single H_2O molecule. In three of these complexes (Nbw#, # = 1, 2, 3), H_2O forms hydrogen bonds close to the N1[NH_2] and carboxylate sites. The remaining two complexes have H_2O in close proximity of N2[NH_2] site. The linear Nbw4 complex is least stable of all five, while the other complex, Nbw5, cyclizes [Lys]$^-$ to form the most stable [Lys]$^-$-H_2O NB complex with three hydrogen bond interactions involving N2[NH_2] and OL1, OL2[COO^-]. Examination of [Lys]$^-$-H_2O-CO_2 interactions suggests the formation of nine different NB complexes (Nbw#x), out of which only five undergo a chemical reaction which can be attributed to processes of chemisorption and desorption. The Nbw1h complex shows an exothermic reaction leading to the formation of the lysine-bicarbonate adduct. The reaction in the Nbw2h complex is observed with a negative value of $\Delta H_{g,298}$ (~ -2 kcal/mol) but a positive RE (~ 3 kcal/mol) to form P2h lysine-bicarbonate. Hence Nbw2h to P2h pathway can participate in both CO_2 absorption and desorption. The Nbw3h and Nbw4h complexes also follow a reaction profile similar to Nbw2h, to form P3h and P4h, lysine-bicarbonates via Ts3h and Ts4h. The E_a barrier from Nbw4h to Ts4h (~ 15 kcal/mol) is highest of all the five reactive complexes. The value of $\Delta H_{g,298}$ are positive in both cases with ~ 7 kcal/mol of RE. Such energetics suggested that P3h and P4h can follow a reverse reaction to release CO_2. Additionally, the reaction at the Nbw3n complex shows an inhibiting role of a single water molecule close to the COO^- group of [Lys]$^-$ in the Nb1 complex. The other four non-reactive complexes, Nbw1n, Nbw2o, Nbw3o and Nbw5n, do not lead to a chemical reaction, hence their stability from calculated BE suggest the participation of these (except Nbw1n, where BE is -0.55 kcal/mol) in physisorption of CO_2.

The insights from this detailed mechanistic investigation can provide an understanding of carbamate-carboxylic acid and direct bicarbonate formation in $[Lys]^-$ -CO_2 reaction. The effect of a single water molecule can drive the reaction with a smaller E_a barrier for bicarbonate formation, though a larger E_a barrier exists for carbamate-carboxylic acid formation. The results from M06-2X-GD3 functional are useful to compare the calculated energetics and geometries for complexes (salts, ILs) in further studies where a long-range correction may play an important role.

———*———*———

The content of this chapter and associated content in Appendix B are adapted from "Site-Specific Interactions in CO_2 Capture by Lysinate Anion and Role of Water Using Density Functional Theory."

J. Phys. Chem. C ***2018****, 122 (24), 12647–12656*

with permissions from © American Chemical Society 2018

Chapter 4:
Understanding the Structure and Ion Dynamics in a Cocrystalline Electrolyte for Lithium Ion Batteries

This chapter contains results and discussions from experiments which were performed in full by the collaborators to this work from Dr. Zdilla and Dr. Wunder's lab at Temple University.

4.1 INTRODUCTION

In this chapter, a combined experimental and theoretical investigation of structure and dynamics in a cocrystalline Lithium ion electrolyte is presented. The mechanism of ion conduction in solid electrolytes is relevant to develop better electrolytes. Solid state electrolytes are key component to develop thermally and mechanically stable metal-ion batteries [63, 70]. In the case of inorganic lithium (or sodium)-ion conducing glass ceramics (LICGCs), which are single ion conductors, the mechanism of ion conduction includes contributions from both grain particles and grain boundaries. In inorganic Li^+ and Na^+ ion conductors, the resistance to cation migration through the grains is usually lower than [85, 135–138] or comparable to [139–142] the grain boundary resistance, and such materials often require high-temperature heat treatment to compress and sinter the grains [143, 144]. Although many LICGCs have been discovered with high bulk ionic conductivities, some approaching those of liquid electrolytes, a major problem is their high interfacial resistance at the electrodes due to their inherently high

moduli, which prevents good adhesion [145]. Solid polymer electrolytes typically have low ionic conductivities but have better adhesion and compatibility with the electrodes.

Zdilla, Wunder and co-workers reported the formation of soft-solid co-crystal electrolytes composed of lithium or sodium salts and low molecular weight organic compounds such as *N,N*-dimethylformamide (DMF) [88, 89], pyridine [146] and isoquiniline [90]-based ligands. The DMF systems form highly conductive molecular crystals with channels for ion migration. In one system [89], a thin (~300 nm thick) layer of liquid was observed surrounding the micron sized crystallites which was pressed into pellets, forming a 3-D interconnected path for Li^+ or Na^+ conduction **(Figure 4.1)**.

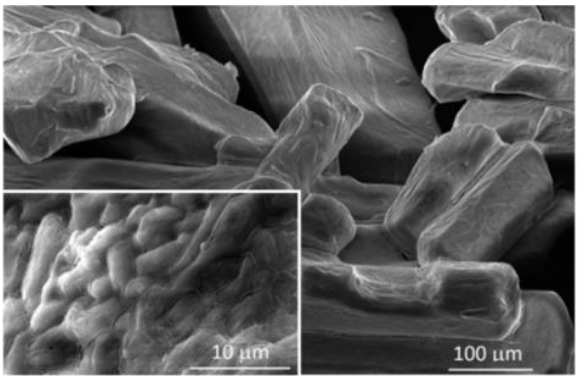

Figure 4.1. SEM of $NaClO_4(DMF)_3$ crystals showing liquid surface layer. Inset: crystallites from crushed pellet showing reformation of liquid grain boundary layer.

Unlike inorganic ceramic electrolytes, this liquid layer has lower interfacial resistance than the bulk resistance of the grains based on complex electric modulus analysis of electrochemical impedance data [89]. This layer also provides better contact with the electrodes (although in the case of DMF cocrystals, DMF is not compatible with Li^0 metal). Soft-solid crystals have attributes of both inorganic and polymer electrolytes, but in order to make them suitable for use in lithium or sodium batteries, higher conductivities and temperature stability windows are desirable. In order to guide future development of these materials, a better understanding of their

behaviour is needed. For example, the DMF·LiCl co-crystal decomposes at approximately 360 K (before it melts) [13], but the $NaClO_4$·DMF_3 [89] can be melted and recrystallized. Why this is the case is difficult to address using experiment alone; MD modelling represents the approach of choice for understanding the connection between molecular behaviour and bulk properties.

While there has been significant modeling work on ion migration in both inorganic ceramic and polymer electrolytes [147–152] this approach has not yet been used for the new class of synthetic soft-solid crystalline electrolytes. MD simulations can provide an understanding of structure and dynamics in the atomic and nano-scale regime of solids and co-crystalline molten salts [153, 154]. The work presented in this chapter is the first experimental investigation of the grain boundary behavior of a molecular organic/salt cocrystal (DMF·LiCl) with development of accurate dynamical models. The computational approaches used in this chapter can be categorised as, i) MD simulations based on a non-polarizable potential to characterize structure and dynamics of a DMF·LiCl co-crystal for comparison to experimental findings, and ii) DFT calculations on a set of salt-DMF aggregates. A series of MD simulations at various temperatures offer atomic level insights in structure, stability and ionic diffusion which support experimental observations. In particular, the simulations predict and explain the temperature dependent onset of liquid-like behavior for the surface species while the bulk atoms remain in the original lattice configuration. Additionally, the onset of decomposition of the whole lattice is in agreement with the experimental behaviour of the DMF·LiCl co-crystal. The excellent agreement between experiment and modelling illustrates that these approaches are amenable to investigation of this class of materials in general.

4.2 EXPERIMENTAL DETAILS

4.2.1 General

Because DMF·LiCl is highly hygroscopic, operations were performed under strictly dry conditions using glovebox and Schlenk line techniques. Details of the preparation

of the DMF·LiCl co-crystals have been previously described [88]. Liquid solutions of DMF and LiCl were prepared by simple mixing and heating, when necessary, to aid dissolution. Powder diffraction data was obtained on a Bruker APEX II DUO diffractometer using Cu-K_α radiation. Melting points were determined under N_2 purge at a 10 ºC/min scan rate, with a TA Instruments DSC 2920 differential scanning calorimeter (DSC). Scanning electron microscopy (SEM) images were obtained with a Quanta 450F (FEI Co.) using secondary (SE) and backscatter (BS) detectors.

4.2.2 Electrochemical Measurements

Ionic conductivities were measured by AC electrochemical impedance spectroscopy (EIS) using a Gamry Interface 1000 potentiostat/galvanostat/ZRA in the frequency range 10−100 kHz. Temperature-dependent conductivities were obtained using stainless steel blocking electrodes, which were temperature controlled in a gas chromatography oven. Nyquist plots, Z'' vs Z', are a common way of representation of complex impedance data. The reported conductivities were obtained from Nyquist plots, from fits of the slanted line impedance data to an equivalent circuit to extract the bulk resistance (R).

4.2.3 Computational details

A class-1 all atom force field for DMF·LiCl co-crystals is extracted using the X-Ray diffraction and IR spectroscopy data of Chinnam et. al [88]. Details of force field parameters are given in the **Appendix C**. Since interatomic non-bonded potentials play an important role in the lattice construction, the electrostatic charges were calculated on the Gaussian-G09 [128] platform using the CHELPG [155] method with B3LYP [129, 156] hybrid functional and an aug-cc-PVQZ basis set. This basis set and functional best suited for DMF, are used to map the electrostatic potential of the DMF·LiCl structure obtained from XRD data obtained at 100 K. The choice of the basis set is determined using an estimation of the dipole moment and heat of vaporization of liquid DMF **(Figure C1, Table C1)**

An initial configuration of 125 unit cells (5 x 5 x 5) with a system size of 7000 atoms in a monoclinic box of 3.3 x 3.6 x 8.4 nm^3 was created and optimized using the steepest-descent algorithm for a maximum of 10000 steps. The energy minimized configuration was used to construct two different structural inputs to understand bulk *vs.* surface behavior of this co-crystal: System *S* is a slab of DMF·LiCl of the same dimensions with periodic boundary conditions to observe the properties of the bulk. System *V,* is a DMF·LiCl nanocrystal in a vacuum, where the cocrystalline slab was placed at the center of a box of 9.9 x 10.8 x 25.2 nm^3. All simulations were performed using the GROMACS 5.0.7 [157] code; at the *NpT* ensemble with a velocity-rescale [158] temperature bath (at the desired temperature) and an isotropic Berendsen [159] pressure coupling (1 bar). The equations of motion were integrated using the leap-frog algorithm with a standard time-step of 1 fs; sufficiently small enough to observe the behaviour of condensed materials. A cut-off of 1 nm was used for calculation of both electrostatic and van der Waals forces, where increase in cut off length showed negligible change to the potential energy. In general, simulations were performed for 2.5 ns, but wherever required for identification of linearity in diffusion, the simulations were extended up to 5 ns. The densities and heats of vaporization (the latter of which is not experimentally reported in this case) were determined for *S* type of systems from 100 K to 400 K. Additional figures, tables, experimental and computational content is provided in **Appendix C**.

4.3 RESULTS AND DISCUSSION

4.3.1 Experiments on structure and conductivity

Although the visual appearance of the DMF-based co-crystalline electrolytes is that of "dry" crystals **(Figure 4.2)**, evidence of an amorphous (liquid or glass) phase comes from SEM, EIS, and DSC data. SEM images of the rounded edges of microcrystalline domains **(Figure 4.3)** show that individual crystallites do not have well defined edges, but instead exhibit a liquid like surface that connects grains to one another. Upon excessive drying, whether under vacuum or under argon atmosphere, the liquid-like

grain boundary evaporates, resulting in striations in the crystals and smaller crystallite grains with gaps between them **(Figure 4.3)**. This behaviour is consistent with observations using electrochemical impedance spectroscopy, which gives excellent conductivities[88] for an organic lithium electrolyte in the realm of 10^{-4} S cm^{-1}, while an overdried sample (i.e. held under vacuum or argon dried for 8h) exhibited an order of magnitude decrease in conductivity **(Figure 4.4)**.

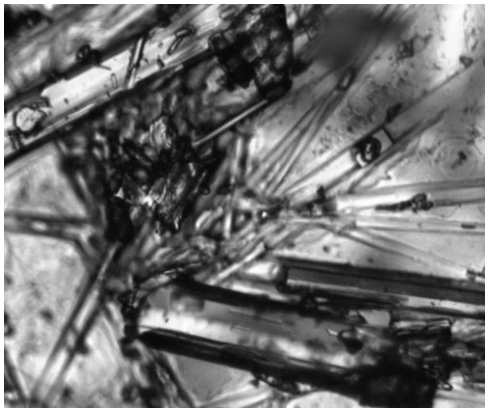

Figure 4.2. Optical microscope image of crystals of DMF·LiCl.

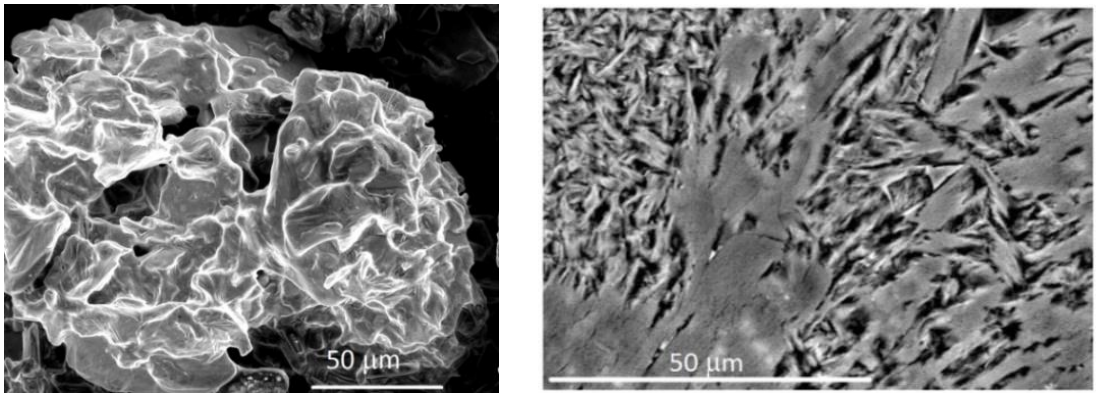

Figure 4.3. Left: SEM of DMF·LiCl showing crystals with smooth liquid grain boundaries. **Right:** DMF·LiCl after drying in argon overnight showing gaps between crystal grains from evaporation of liquid DMF interface.

The first report on these cocrystals suggested that for a freshly prepared sample of DMF·LiCl, grain boundary resistance is negligible [88]. This is consistent with a

liquid salt/DMF electrolyte at the grain interface, which would be expected to be highly conductive (in the range of 10^{-3} S cm^{-1}). However, upon loss of this liquid binding layer upon excessive drying, the grain boundary resistance becomes dominant, resulting in a drop in conductivity by an order of magnitude, from 1.6 x 10^{-4} to 1.3 x 10^{-5} S cm^{-1} **(Figure 4.4)**. Differential scanning calorimetry (DSC) data for the co-crystals **(Figure C2)** shows melt transitions that correspond with peaks at ~ -10, -20 and 20 ^{0}C, similar to those observed in the DSC trace of liquid solutions of LiCl in DMF (since the bulk DMF·LiCl decomposes before it melts, it shows no melt transitions). Therefore, these signals were assigned to the surface liquid phase based on comparison to measurements of concentrated DMF-LiCl solutions in the concentration range of 0.2M to 5M. While these concentrations are rather lower than the theoretical molarity of the one-to-one adduct (11.35 M, based on crystallographic density of 1.306 g/mL) [88], bulk solutions of increased molarity were not achievable due to solubility limits. Rather than exhibiting the normal colligative freezing point depression, these solutions, when frozen, instead form low melting solvate crystals, which have different powder XRD signatures than the 1/1 DMF·LiCl bulk co-crystal **(Figure C3)**. Although the structure of these crystals is currently unknown, they melt and recrystallize reproducibly, forming a liquid at temperatures > -10 ^{0}C, similar to the liquid boundary phase of the bulk DMF·LiCl crystals.

Unlike $(DMF)_3NaClO4$ (which melts and recrystallizes), cocrystals of DMF·LiCl decompose at about 60 °C, resulting in DMF evaporation and leaving LiCl salt behind based on XRD. If the crystals are overdried, the liquid binding layer is lost **(Figure 4.3)**, and the measured conductivity drops from 1.6 x10^{-4} S cm^{-1} to 1.3 x 10^{-5} S cm^{-1} **(Figure 4.4)** due to the increased grain boundary resistance. While these behaviours are non-ideal for practical electrolytes, they offer the opportunity to investigate observed bulk properties at the molecular level using MD simulations, which may be applied to other members of this new materials class.

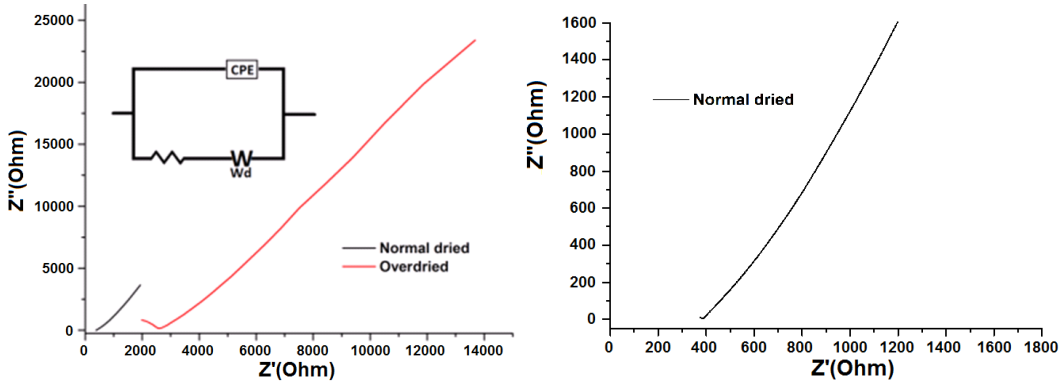

Figure 4.4. Left: Impedance spectra of fresh DMF·LiCl (black) and overdried (8h) DMF·LiCl (red). Fitting to equivalent circuit gives conductivities of 1.6 x 10^{-4} S cm^{1} for fresh DMF·LiCl and 1.3 x 10^{-5} S cm^{-1}. Frequency range 10-100 kHz. **Right**: Expanded view of impedance spectra of fresh DMF·LiCl.

4.3.2 MD simulations on structure

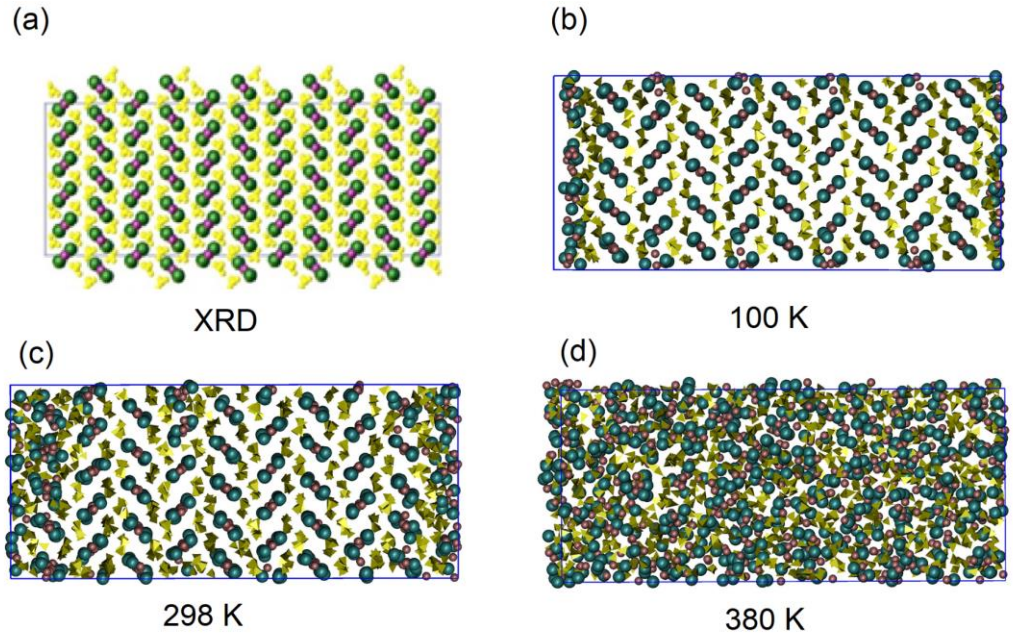

Figure 4.5. Experimental structure of a 5x5x5 array of unit cells from (a) XRD and MD snapshots of DMF·LiCl in system *S* at different temperatures- (b) 100 K, (c) 298 K, (d) 380 K, after equilibration. Irregularities at the unit cell boundaries are artefacts of the non-periodic display of the visualization. Yellow: DMF, Purple: Li, Green: Cl.

In constructing MD models of bulk and surface behaviours of DMF·LiCl, System *S* (for "solid") describes a periodic solid of 5 x 5 x 5 unit cells, and is used to calculate thermal and structural properties of DMF·LiCl co-crystals in their bulk phase. MD

simulations at 100 K show a resemblance of the supercell to the experimentally determined X-ray crystal structure **(Figure 4.5)**. The calculated density of the bulk (1.209 g/mL) at 100 K is lower by ~7 % compared to experiment (1.306 g/mL) [88]. Since the co-crystals of the material decompose to give LiCl(s) instead of vaporizing, it is not possible to compare the calculated enthalpies of vaporization ΔH_{vap} with experiment. However, the calculated ΔH_{vap} for liquid DMF differs by ~ 6 % with previous experimental and theoretical studies [160]. The temperature-dependent variation in density and ΔH_{vap} of DMF·LiCl is shown in **(Figure C1)**. In this system, melting and decomposition phenomena appear to be surface phenomena, and are not modelled by the bulk behavior of System *S*; these properties will be discussed in a subsequent section.

The perturbations in Li^+ and Cl^- ionic frameworks increase significantly above room temperature. At 380 K, a visual observation shows that the fluctuations in structure overwhelm the ionic and ion-dipole framework completely and the lattice collapses **(Figure 4.5)**. The simulations show a decomposition temperature in the range observed experimentally in the thermogravimetric analysis (TGA) experiments, and visually observed in a melting point apparatus (starts at 350 K and is complete by 420 K).

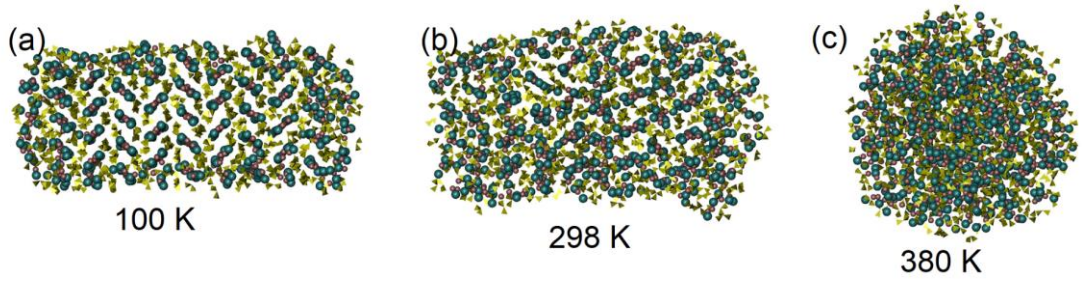

Figure 4.6. Snapshots of DMF·LiCl in system *V* at different temperatures after equilibration.

While System S predicts bulk behaviour, results from SEM **(Figure 4.3)** suggest that evaporation of the liquid grain boundaries triggers the start of electrolyte failure and decomposition: a surface phenomenon. In order to model this, MD

simulations were performed on system *V* (for vacuum) which is a nanocrystal of DMF·LiCl in a simulation box, 27 times larger than periodic box (used in system *S*). These simulations permit molecules on the surface of the solid co-crystal to leave the bulk and initiate melting or evaporation. At 100 K, the slab of DMF·LiCl in this large box behaves like a solid and the molecules at the surface and in the bulk behave almost identically **(Figure 4.6)**. However with an increase in temperature, the DMF molecules and ions on the surface show different characteristics compared to the bulk. Between 220 K and 300 K, a structure consisting of an inner solid bulk inside an outer liquid layer is observed. This models the observed structural anomaly of the material and matches well to the experimental description of a bulk solid in equilibrium with a boundary liquid. It is in remarkable agreement with the previously reported conductivity behaviour, where it was shown that at ~ 210 K, approximately the melt temperature of DMF, the conductivity of DMF·LiCl dropped off abruptly (and was too low to measure) [88]; the conductivity of a 1M LiCl solution in DMF also decreased abruptly at this temperature.

The presence of a vacuum on each side of system *V* provides free space to the ionic framework and DMF molecules at the surface; due to the lack of lattice stabilization by favourable intermolecular/interionic contacts in vacuum, high fluctuations are observed at the surface. At higher temperatures (~ 360 K), a first molecule of DMF migrates from the surface to the vacuum region, leaving its own ion pair (Li^+ and Cl^-) at the surface. This behaviour can be considered as the onset of the evaporation of the liquid boundary layer and ultimately, the decomposition of this material. The result is consistent with the comparative morphology of fresh vs. dried crystals from SEM **(Figure 4.3)**, and with observation from powder X-ray diffraction that thermal decomposition leads to loss of DMF, but not of LiCl, since in the powder XRD pattern of decomposed solid, diffraction peaks are seen for both DMF·LiCl and cubic LiCl salt **(Figure 4.7)**.

System *S* represents an infinite array of unit cells and hence it is used to calculate a number of useful structural parameters for the bulk phase. The RDF between Li^+ and Cl^- atoms **(Figure 4.8)** shows a first coordination sphere around Li^+ with a first maximum at 0.238 nm at 100 K, corresponding to the coordinating Cl atoms. To observe the effect of temperature on $Li^+\cdots Cl^-$ framework fluctuations, RDFs were calculated at all temperatures. The structure shows smooth and continuous secondary solvation shells at higher temperatures which indicate vanishing lattice boundaries with increase in temperature. In the primary solvation shells, except for a slight rightward shift of the peak maxima and a slight decrease in intensity, no significant signature of a singularity associated with a phase transformation was observed until 350 K. However at 380 K, not only is an increase in intensity of RDF observed but also the peak maxima are shorter by 0.01 nm, compared to 350 K, which indicates stronger Li^+ Cl^- interactions during decomposition, consistent with the experimentally observed formation of LiCl(s) upon decomposition based upon XRD data **(Figure 4.7)**.

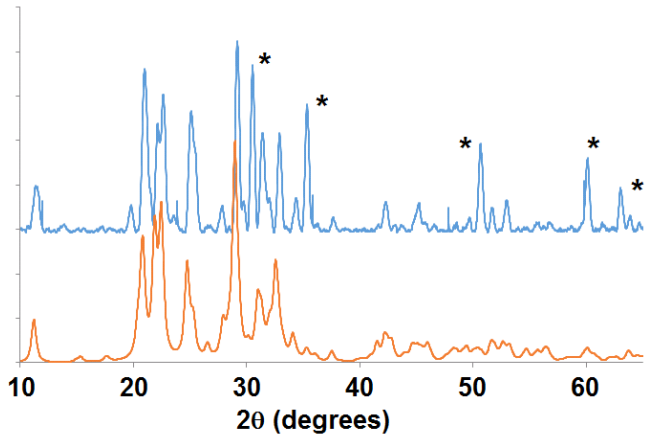

Figure 4.7. Powder pattern of decomposed DMF·LiCl (blue) showing a mixture of DMF·LiCl peaks (orange: calculated powder pattern from crystal structure of DMF·LiCl) and cubic LiCl peaks marked with *.

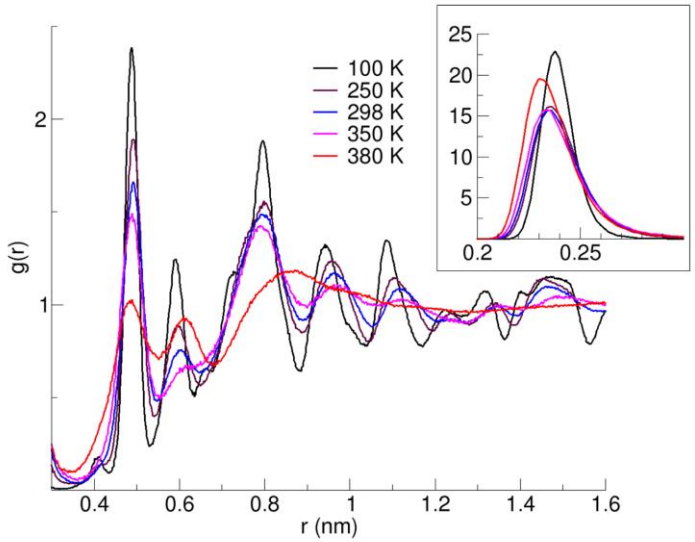

Figure 4.8. Site-site RDF between Li^+ and Cl^- in the system *S*; Inset shows peak of the primary solvation shell.

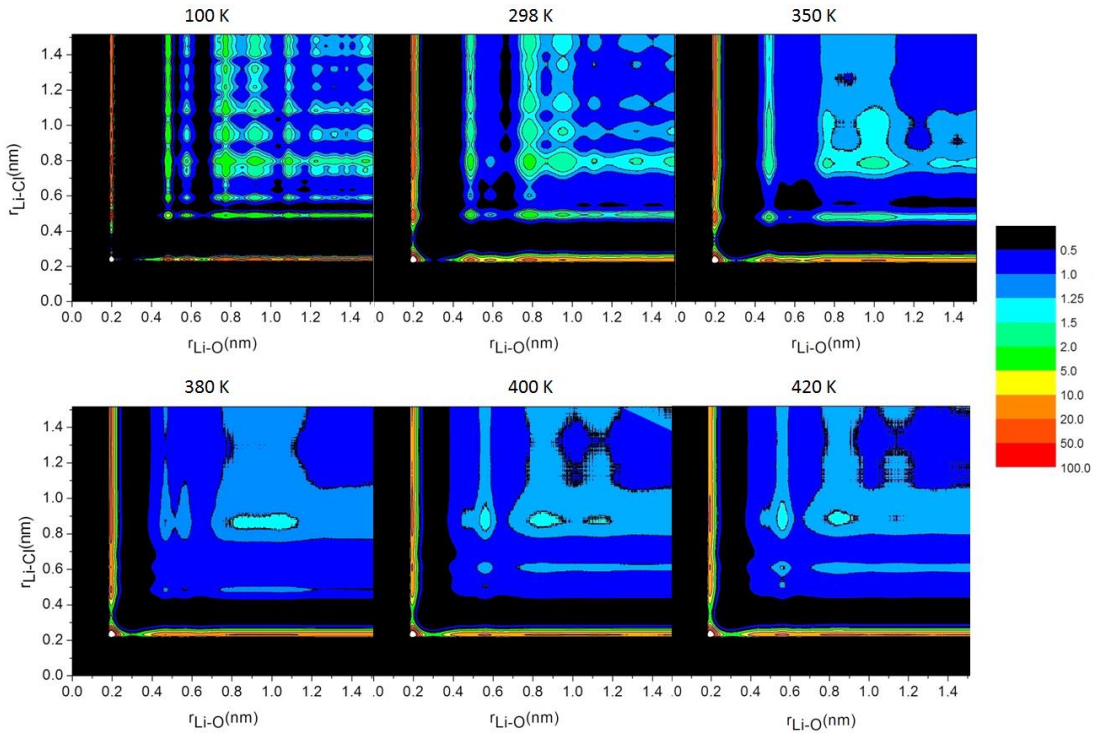

Figure 4.9. Combined Distribution Functions of Li-O vs Li-Cl radial distributions in system S.

Since the solid state structure of the co-crystal largely depends on the framework formed with $O\cdots Li^+\cdots Cl^-$ atoms, Combined Distribution Functions

(CDFs) were calculated at different temperatures to observe the cumulative change in $O\cdots Li^+$ and $Li^+\cdots Cl^-$ radial distributions **(Figure 4.9)**. The CDF at 100 K shows a very ordered secondary solvation structure of both site-site interactions. There are at least three and two distinct shells of Li^+ around the O and Cl^- sites respectively. However, at room temperature, secondary shells show a continuous CDF, though signatures of higher probability on this distribution show the ordered structure of the system in bulk. The CDF at 350 K shows almost vanishing structures of both sites (O and Cl^-) with respect to the Li^+ ion, which fades further with increasing temperature (T = 380 K, 400 K and 420 K).

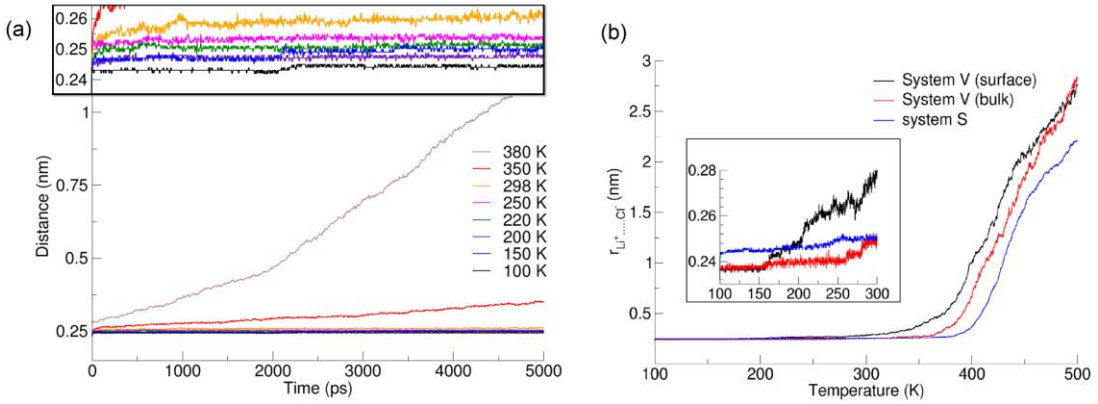

Figure 4.10. $r_{intra(Li+\ldots Cl-)}$ *vs.* (a) time in system *S* and (b) temperature in systems *S* and *V* ($r_{intra(Li+\ldots Cl-)}$ from XRD is 0.233 nm). Variations at low temperatures are shown as insets.

To understand the relationship between decomposition temperature and structure, the average distance between Li^+ and Cl^- ions present on the same DMF·LiCl residue was calculated (referred to as "intra-residue") with respect to simulation time for each temperature **(Figure 4.10a)** using System *S*. The distances show marginal increases at lower temperatures (100 K – 220 K), moderate increases at room temperature and an almost linear increase at T ≥ 350 K. To further confirm these findings, simulated annealing was performed (from 100 K to 500 K) with continuous jumps of 20 K for 500 ps each (for a total time of 10.5 ns) for system *S*. The intra-

residue average Li^+-Cl^- distance, $r_{intra(Li+\cdots Cl-)}$ *vs.* time/temperature plot (blue colored line in **Figure 4.10b**) shows a- sudden increase in distance around 380 K.

To compare dynamical behavior of the surface vs. bulk, system *V* was used, examining samples of 100 ion pairs each on the surface and bulk. **Figure 4.10b** shows a comparison between the average distances of ions in bulk (red) *vs.* surface (black) from system *V* and system *S* (blue) with time/temperature. The average inter-ionic $r_{intra(Li+\ldots Cl-)}$ distance at low temperatures is similar in the bulk and on the surface. However, as the temperature increases and approaches 300 K, a difference in average distance between the surface and bulk becomes pronounced, which keeps increasing and differs drastically around the region of decomposition. Further, the trends for the bulk in system V are similar to the trends for system S, for which there is no removal of DMF. In the very low temperature regime (100 – 150 K), $r_{intra(Li+\ldots Cl-)}$ is similar in the bulk and on the surface. Above 200 K, $r_{intra(Li+\ldots Cl-)}$ is larger on the surface compared to the bulk. At T > 350 K, the difference in distances between bulk and surface becomes much larger. This provides a quantitative justification for the material behavior, which is liquid-like at the surface but behaves as a solid in the bulk. Unlike with the bulk system, the density in the liquid region was not calculable due to an apparent gradient in the simulated density near the edge of the nanocrystal **(Figure C6)**. Further, the density in the interfacial regions is also not uniform in all directions of the simulation box. However, a qualitative density distribution can be obtained by using very fine grids perpendicular to the X, Y and Z directions of the simulation box. The density distribution in System V (T = 298 K) shows a gradual decrease from the bulk to the interfacial regions in all three directions of the box **(Figure C6)**.

4.3.3 MD simulations on ion-dynamics

Since the co-crystals of DMF·LiCl show better experimental temperature dependent conductivity compared to other organic solids [88], MSD was calculated to estimate ion mobility of the material using Nernst-Einstein's equation [161]. At T< 200 K, due to the very slow mobility of ions a linear regime for the applicability of Nernst-

Einstein's equation was not observed and hence the conductivities are not calculable from MD. Uncorrelated to this theoretical limit, the conductivities were also not experimentally measurable below this temperature [88]. However, at T > 200 K a linear regime could be obtained for the MSD *vs.* time plot, ionic conductivity (σ) of the co-crystals were calculated at several temperatures. The plot of log σ *vs.* T shows two jumps between 250 – 300 K and T ~ 350 K. These jumps can be correlated to the partial melting of the lattice layers and the initial stages of decomposition respectively. While the values of log σ **(Figure 4.11)** are an order of magnitude higher at 298 K, the experimentally observed conductivity of 10^{-4} S cm^{-1} is predicted at 250K, a temperature only about 17% different from room temperature. The differences in absolute value between experimental and simulated conductivities are likely due to the exclusion of covalent character in modelled interactions among O---Li---Cl networks in the force field. For example, the conductivities reported by Deng et al [162] on two solid lithium based electrolytes were overestimated by at least an order of magnitude. The values of conductivities obtained from the MD simulations thus provide a qualitative picture and are typical for ab-initio MD simulations on other solid electrolytes [163].

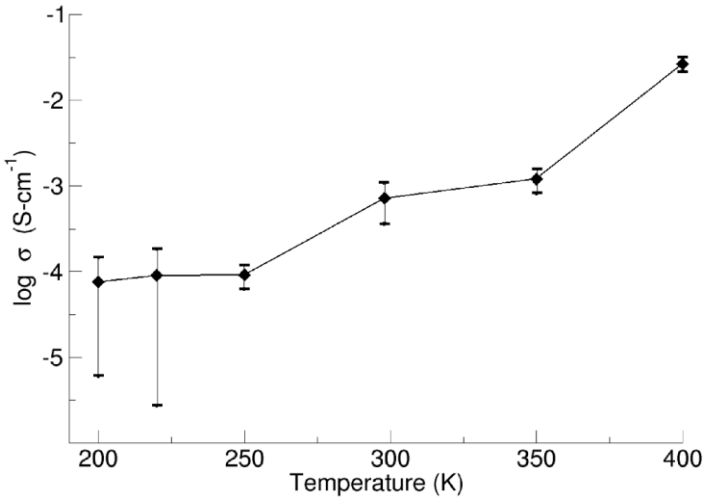

Figure 4.11. log of ionic conductivity *vs.* T calculated from MD simulations on system *S*.

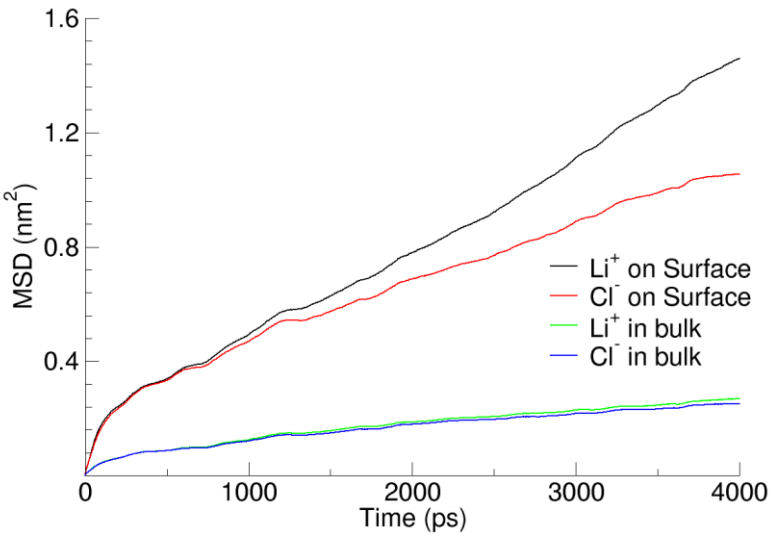

Figure 4.12. Mean Square Displacement (MSD) vs. time of Li^+ and Cl^- ions in systems *V* on surface and in bulk at T = 298 K. Similar trends of higher mobility at the surface are found at other temperatures **(Appendix C)**.

To understand the dynamics of ions in the bulk and on the surface, system *V* was used to calculate MSD of Li^+ and Cl^- ions at fixed temperatures for a sample of 200 ions (100 Li^+ and 100 Cl^-) each in the bulk and on the surface. The MSDs **(Figure 4.12)** show that Li^+ and Cl^- ions on the surface are roughly an order of magnitude more mobile compared to bulk at room temperature. Ionic conductivities in these liquid-like grain boundaries should indeed be high, based on the measured ionic conductivities of 1 M solutions of LiCl in DMF, which are approximately two orders of magnitude greater than bulk conductivities of the solid DMF·LiCl co-crystals, and diverge further at lower temperatures. Both the experimental conductivity measurements (solid DMF·LiCl and liquid LiCl-DMF solutions) and the MD treatment of System *V* (which considers both the solid bulk and the liquid-like boundary) are consistent with the experimental observation that the liquid-like grain boundary contributes negligible resistance to an assembly of pressed crystals.

4.3.4 Energetics of interactions from MD simulations and DFT

The contribution from various interactions in the DMF·LiCl co-crystals is required to understanding the stability of the systems and the mobilities of their components.

These relationships are examined here in two ways: 1) by non-bonded potentials or Interaction Energies (IE_{nb}) derived from MD simulations on a large assembly, and 2) by more computationally rigorous DFT calculations on a smaller assembly. Due to the charge dense nature of Li^+ and its corresponding characterization as a "hard" Lewis acid, the interactions in this system are classified as hard (Li^+---DMF and Li^+---Cl^-) and soft (DMF---Cl^- and DMF---DMF) interactions.

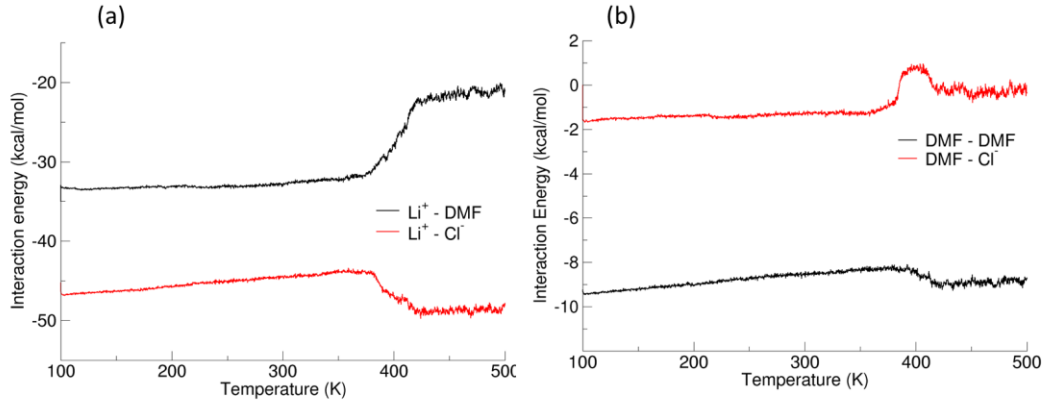

Figure 4.13. Non-bonded interaction energies *vs.* T in system *S* for **(a)** hard and **(b)** soft interactions. The non-bonding interaction energies are obtained from normalized vdW + Coulomb potential energy values from the simulation trajectory.

For the hard interactions **(Figure 4.13a)** in the MD simulations, IE_{nb} of Li^+---DMF is ~ -33 kcal/mol at 100 K which decreases by -1 kcal/mol up to 380 K. As expected, due to stronger electrostatic interactions, the IE_{nb} of Li^+---Cl^- is more negative (~ -47 kcal/mol at 100 K), which reduces slightly with increasing temperature (~ -45 kcal/mol at 380 K). At the point of transition (T ~ 380 K), while the IE_{nb} of Li^+---DMF drops significantly and saturates to ~ -21 kcal/mol (between 400 K - 500 K), the Li^+---Cl^- interactions become stronger at T > 380 K (by ~ -5 kcal/mol). Hence, both types of hard interactions show opposite trends at the transition point. This suggests that the transition point is actually the start of lattice decomposition, and results in aggregation of LiCl(s) and expulsion of DMF from the lattice, as is observed experimentally by powder XRD analysis of the product **(Figure 4.7)**.

The soft DMF---Cl^- interactions **(Figure 4.13b)** show an IE_{nb}= -1.7 kcal/mol from 100 K - 380 K which reduces beyond the transition point (IE_{nb} ~ 0 kcal/mol at 400 K). The DMF---DMF interactions (IE_{nb} ~ -9.4 kcal/mol at 100 K) reduce slightly to -8.4 kcal/mol at T = 380 K. After the transition point, these interactions show a marginal increase to IE_{nb} ~ -9.0 kcal/mol, promoting self-aggregation of DMF with itself concomitant with expulsion from the LiCl lattice. For all interactions, IE_{nb} attains saturation at T > 420 K, which can be considered as the temperature of complete decomposition of the co-crystals. Although, the energy scales of hard and soft interactions differ by an order of magnitude, a complex interplay of various interactions is responsible for lattice stability and decomposition. The stabilization of Li^+Cl^- interactions beyond the transition point can be seen by a further lowering of ΔH_{vap} by ~ 5 kcal/mol energy, which can cause the vaporization of some DMF molecules from the co-crystal (for DMF, ΔH_{vap} = 10-11 kcal/mol) [164]. This behaviour is observed experimentally when DMF·LiCl thermally decomposes, resulting in boiling off DMF, leaving LiCl behind as a solid. An examination of ionic charge densities **(Figure C5)** supports the lattice decomposition temperature predicted by structure and dynamics.

To examine the decomposition behaviours with increased computational rigor, the intra-crystal interaction energies of the co-crystal and dimerization and tetramerization energies were calculated using DFT using B3LYP functional and 6-311++G(d,p) basis set. The interaction energies are calculated using Fragment Counterpoise (fCP) [132] and rigorous fCP (rig-fCP) [133] methods **(Table 4.1)** which provide more accurate energies with correction for Basis Set Superposition Error and fragment relaxations. The monomers and dimers are expected to be more abundant on the liquid-like surface while larger aggregates (modelled here by tetramers) are more likely to be found in the bulk. The structures of monomers, dimers, optimized dimer, and optimized tetramers are analogous to experimentally observed connectivity and

are illustrated in **Figure 4.14** with detailed structural parameters provided in the **Table C2**.

Table 4.1. Interaction energies of fragments, dimers and tetramers of DMF·LiCl from DFT calculations

Structures	Interactions	Energy (kcal/mol)
		rig-fCP
	Monomer relaxations (all opt)	
M1	DMF·Li^+-----Cl^-	-123.96
M2	DMF-----LiCl	-27.32
	$(DMF·LiCl)_2$ dimerization	
D1	Normal (sp[a])	-24.82[c]
D2	Invert (sp)	-24.14[c]
D3	Normal (opt[b])	-23.73
D4	Invert (opt)	-23.94
	$(DMF·LiCl)_4$ tetramerization from monomer (all opt)	
T1	Li_2Cl_2 junction normal	-69.86
T2	Li_2Cl_2 junction invert	-84.49
T3	O_2Li_2 junction normal	-54.42
T4	O_2Li_2 junction invert	-54.26
	$(DMF·LiCl)_4$ tetramerization from dimer (opt)	
T5	Li_2Cl_2 junction	-28.46

[a]From Single point energy of XRD crystal structure

[b]From optimized geometry

[c]rig-fCP not used, due to no optimization of geometry, IE is calculated using fCP method.

Configurations, definitions of *normal* and *invert* keywords are provided in the **Appendix C**.

All optimized geometries are minimum energy structures confirmed by frequency calculations. The M1 and M2 represent optimized DMF·LiCl monomer in the form of DMF·Li^+---Cl^- and DMF---LiCl fragments respectively **(Figure 4.14)**. As seen from **Table 4.1**, the interaction energy of the DMF·Li^+---Cl^- (in M1) is of the order of bond dissociation energy (> 100 kcal/mol), and hence it is difficult to observe such pair dissociations from MD simulations. However, DMF---LiCl interactions in M2 are significantly lower (~ -28 kcal/mol) in energy. Such configurations can facilitate the decomposition of the co-crystal to form DMF and LiCl, as observed

experimentally at the decomposition temperature. The single point structures D1 and D2 have non-planar Cl atoms associated to O_2Li_2 bridges, while optimized geometries of D3 and D4 **(Figure 4.14)** contain $O_2Li_2Cl_2$ atoms in the same plane. Though there are structural differences in single point and optimized structures of the dimer, the dimerization energies observed from single point (D1, D2) and optimized geometry (D3, D4) are similar.

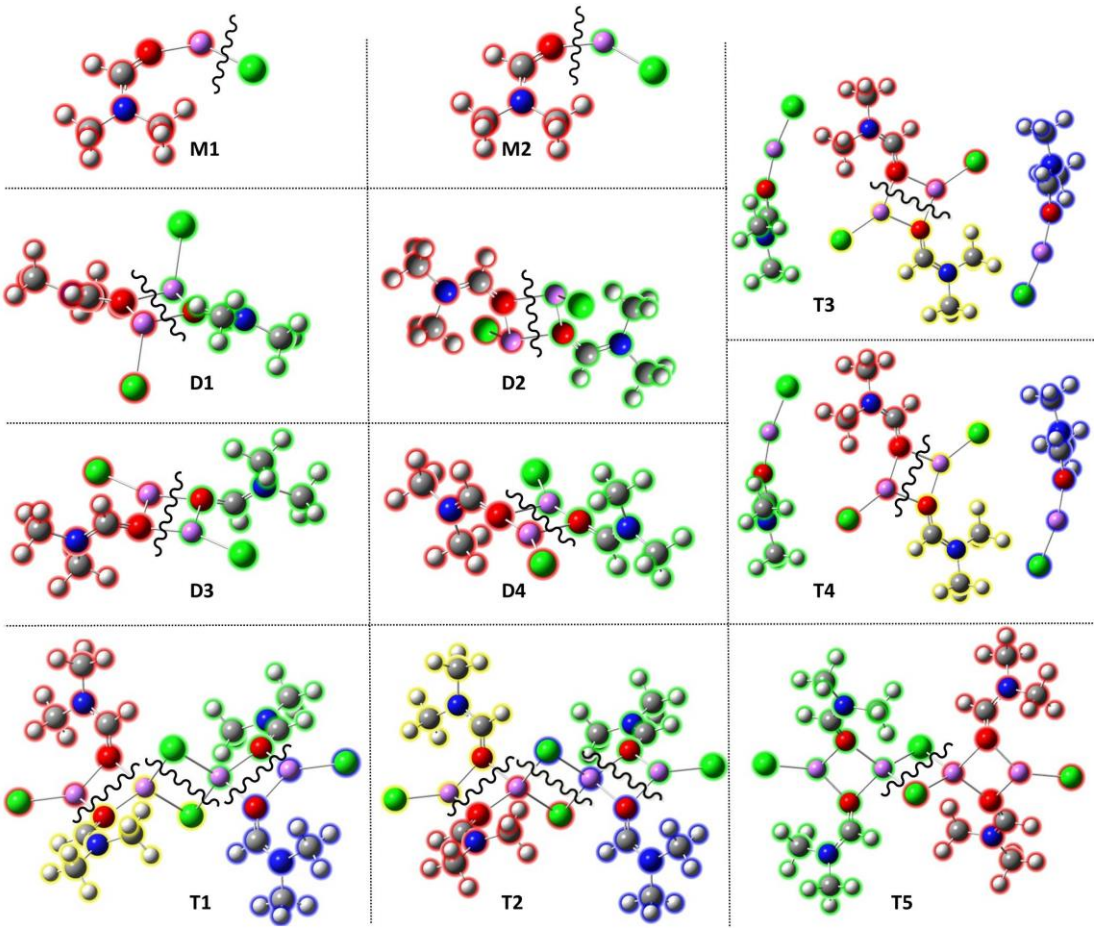

Figure 4.14. Single point (D1 and D2) and optimized geometries (all other) of structures with the color clouds indicating dissociating fragments for determination of interaction energies. A complete list of IE values is given in table S2 with colored text corresponding to the same-colored fragment in each illustrated system. Wavy lines are used to show the cleavage points for dissociating fragments.

The dimerization energies are slightly lower compared to the M2 interaction energy which alludes to the higher possibility of dimer dissociation compared to M2 fragment dissociation. The tetramerization energies (4 M → T1, T2, T3, or T4) are >

50 kcal/mol for all possible configurations. Here, T1 and T2 are tetramers of hard Li---Cl multi-bridges, and T3 and T4 are comparatively weaker tetramers containing softer O---Li multi-bridges. The IEs show that decomposition of T1, T2, T3 and T4 tetramers to the corresponding monomer is energetically unfavourable. The decomposition of T5 to monomer requires ~ 50 kcal/mol as the path of the decomposition follows T5 → D(i) →M1 or M2. Though the calculated interaction energies are gas phase quantum chemistry calculations, it can be concluded that the low energy requirement for dimer to monomer dissociation and self-decomposition of monomer are more likely to be observed at grain boundaries, promoting ion mobility, while the higher energy requirement for dissociation of larger aggregates (more likely to be found in the interior) favours leaving the bulk structure intact. This is consistent with the experimentally observed liquidity and high conductivity at the grain boundaries, the decomposition of co-crystals before boiling, and evaporation of DMF molecules during decomposition. The interaction energies for the smaller units of DMF·LiCl (e.g. monomer and dimer) and the larger aggregates (tetramer) supports the preferential decomposition/dissociation of cocrystals on the surface over the bulk.

4.4 CONCLUSIONS

This chapter produces a detailed analysis of dynamical behaviours in crystals of DMF·LiCl at the molecular level using MD and DFT quantum calculations assisted with experimental analysis of the surface liquid grain binding behaviour using microscopy, DSC, and XRD. The findings from simulations accurately predict a number of experimentally observed phenomena about this system, namely: the crystal packing arrangement, the temperature of decomposition, the mechanism of decomposition by expulsion of DMF from the LiCl lattice, the liquid like boundary layer, the evaporation of DMF from the surface of the crystal, the physical density, bulk conductivity, and most importantly, the increased mobility of ions in the boundary layer vs. the bulk. More specifically, the simulations predict that the structural organization of Li^+ and Cl^- ions remains unaffected as observed from RDFs from 100

K to 350 K. However, the CDFs show vanishing secondary solvation structures in the bulk system indicating the collapse of structure at around 350 K. The average intra-residue Li^+---Cl^- distances show higher fluctuations on the surface compared to the bulk, which is further supported by the examination of ionic mobility in DMF·LiCl. The observed liquid-like behaviour at the surface is likely applicable to a wide range of "soft" solid electrolytes, such as this, and another previously reported DMF-$NaClO_4$ system [89]. Similarly, they may be applicable to other soft-solid systems like polymer electrolytes, but not likely to ceramic electrolytes due to their rigidity, and large melting points. The non-bonding IEs from simulations show that the Li^+---Cl^- interactions firmly stabilize post-decomposition whereas the DMF---Li^+ interactions are destabilized. Results from DFT ascertain the preference of decomposition of the material before any melting from the analysis of fragmentation, dimerization and tetramerization processes. The most favourable process is dimer to monomer dissociation, after which follows decomposition of crystals to DMF and LiCl, as observed experimentally. The MD simulations and DFT calculations in this chapter validate the approach as a valuable tool for understanding the behaviour of this promising new class of electrolyte materials at the molecular level.

———*———*———

The content of this chapter and associated content in Appendix C are adapted from "Unravelling the Structural and Dynamical Complexity of the Equilibrium Liquid Grain-Binding Layer in Highly Conductive Organic Crystalline Electrolytes."

J. Mater. Chem. A ***2018****, 6, 4394–4404*

with permissions from © The Royal Society of Chemistry 2018.

Chapter 5:
Stoichiometric Conversions in Cocrystalline Solids: Case of a Sodium Ion Battery Electrolyte

This chapter contains results and discussions from experiments which were performed in full by the collaborators to this work from Dr. Zdilla and Dr. Wunder's lab at Temple University.

5.1 INTRODUCTION

In this chapter, a molecular modeling of stoichiometric conversion, translational dynamics of ions and mechanism of ion conduction of a cocrystalline sodium ion electrolyte- $(DMF)_3NaClO_4$ is presented. Sodium-ion batteries (SIBs) are promising as potential low-cost alternatives to lithium-ion batteries (LIBs), particularly when device volume is of secondary importance, such as in large-scale energy storage applications [165]. These devices have potential economic promise due to the higher abundance and lower cost of sodium. As an electrolyte for SIBs, Sodium Superionic Conductors (NASICON) [66, 166], ceramics [167], polymers and their composites, and liquid electrolytes (e.g. non-flammable organic solvents [168], ILs [169]) have been synthesized and characterized. The above electrolytes can be broadly categorized based on their physical hardness: hard solids and soft solids. Hard solids like ceramics and NASICONs exhibit excellent mechanical and thermal stability but show poor conductivity compared to liquid electrolytes [61, 62, 66]. Despite reports on certain ceramics which demonstrate excellent ionic conductivities [61, 170], high resistance

in the contact layers formed between the grains (grain boundary) leads to poor intergranular (grain boundary) and interfacial (electrode/electrolyte) conductivity [65, 171]. At a molecular scale, ion migration in such materials occurs via complex mechanisms including interstitial ion displacements, defect jumps and superionic diffusion [87, 172–174]. In several hard-solid SIB/LIB electrolytes, the presence of a relatively stable anionic sublattice favors migration of Na^+/Li^+ ions due to a lower E_a barrier and a high transference number [70, 175]. However, the strong affinity of cations to the anionic sublattice leads to low ionic conductivity. Further, facile electron donation/acceptance to/by the anionic sublattice results in poor electron insulation (which is ideally more suited for the design of cathode materials).

To provide higher electron insulation and low-affinity between cations and anionic sublattice, development of soft-solid electrolytes for Li^+/Na^+ ion migration has been explored. Inorganic salts like LiCl, $NaClO_4$ form co-crystalline structures with organic solvents like DMF, ADN stable at ambient temperature [88, 89]. These cocrystals exhibit low E_a barrier (85 kJ/mol and 25 kJ/mol, respectively, from impedance spectroscopy), and ionic conductivity at room temperature from 10^{-3} S cm^{-1} to 10^{-5} S cm^{-1}. Experiments like SEM have suggested the presence of a liquid like layer at the surface/interface of the cocrystals of these electrolytes, which also results in low grain boundary resistance. The advancement in the development of electrolytes is accelerated with computer simulation methods like MD simulations and DFT calculations which elucidate the thermal stability and mechanism of ion conduction. Islam and coworkers used MD and *ab-initio* MD simulations to model the diffusive behavior in Na^+ ion electrolytes [166]. The authors extensively examined the path of Na^+ ion conduction and ascertained the migration to be three-dimensional in nature. Further, DFT is also employed to calculate the minimum energy path (MEP) during ion conduction in other works [173, 176].

In the previous chapter, thermal stability and ion conduction in a cocrystalline electrolyte DMF.LiCl for LIB was modeled using classical MD simulations and gas

phase DFT calculations. While MD simulations provided the understanding of melting/decomposition at molecular scale, DFT calculations provided atomic scale explanation of ionic clusters at surface/in bulk. The objective of this chapter is to model Na^+ ion mobility and melting/stoichiometric conversion of a cocrystalline electrolyte synthesized in a 3:1 stoichiometric ratio of DMF and $NaClO_4$ as- $(DMF)_3NaClO_4$. This is of interest due its low E_a barrier for ion conduction, high room temperature conductivity and melt-cast ability. An experimental work [89] reported that the $(DMF)_3NaClO_4$ electrolyte starts melting around 55 ^{0}C. The TGA profile of the electrolyte showed a gradual decay of mass with a shoulder around 150 ^{0}C **(Figure 5.1**, where TGA for 3:1 cocrystals is reproduced from Zdilla and coworkers [89]**)**.

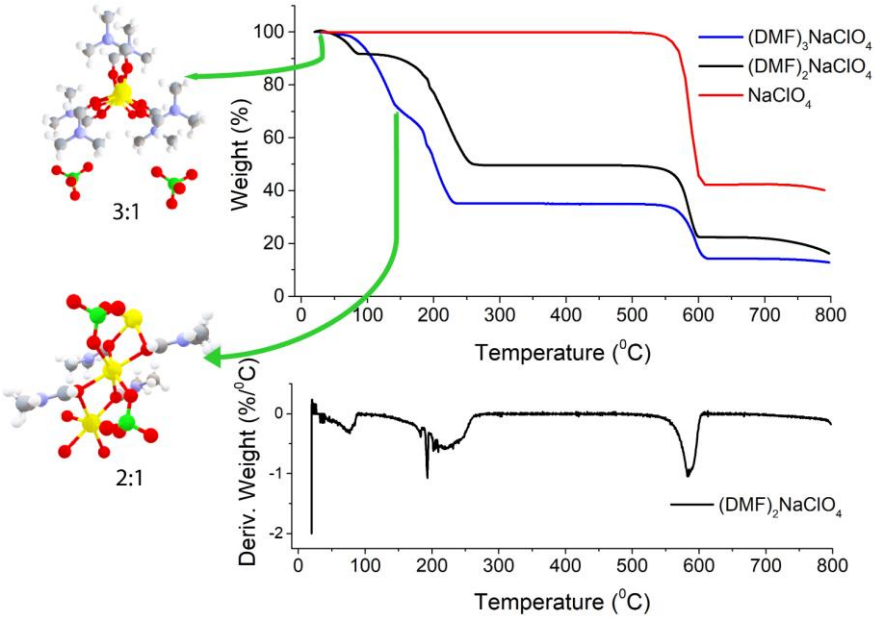

Figure 5.1. TGA and DTGA of $(DMF)_2NaClO_4$ showing the geometry of 2:1 cocrystals in the right. TGA for $(DMF)_3NaClO_4$ is reproduced from Zdilla and coworkers [89] with its geometry shown in the left. The abundance of 3:1 and 2:1 at the corresponding temperatures is marked on the TGA plot for $(DMF)_3NaClO_4$.

Further, the cocrystals were pressable as well and a visual inspection suggested the removal of solvent (DMF) from the electrolyte, without a significant change in crystallinity. This chapter reports new thermally transformed crystals (which correspond to a shoulder in appeared in TGA at 150 ^{0}C) and the pressed crystals result

in a new cocrystalline electrolyte composed with DMF and $NaClO_4$ only, but in a different stoichiometric ratio- 2:1, already reported in literature as $(DMF)_2NaClO_4$. [177]. This stoichiometric transformation is confirmed form single-crystal XRD, PXRD and TGA. In 3:1 cocrystals, every Na^+ ion is coordinated with six O(DMF) atoms and ClO_4^- ions occupy the interstitial space in the crystal. In 2:1 stoichiometry- every Na^+ ion coordinates with only four O(DMF) atoms and two O(ClO_4^-) atoms. The TGA of $(DMF)_2NaClO_4$ along with DTGA and the abundance of different stoichiometric structures during heating of $(DMF)_3NaClO_4$ is shown in **Figure 5.1.** A list of chemical and physical properties of 3:1 *vs.* 2:1 stoichiometric cocrystals of DMF-$NaClO_4$ is presented as **Table 5.1**.

Table 5.1. Comparison of structural features and melting/decomposition in stoichiometric cocrystals of DMF and NaClO4.

Stoichiometry	3:1[1]	2:1[2]
Crystal System	Hexagonal	Monoclinic
Space Group	P-62c	P2/c
Na---Na distance in primary channel (in Å)	3.23	3.40
Na---Na distance in secondary channel (in Å)	12.00	8.54
Na---O(DMF) distances (in Å)	2.40	2.34, 2.44
Na---ClO_4 distances (in Å)	7.11 (Na---Cl)	2.36, 2.51 (Na---O)
T_m (from DSC) (in ^{0}C)	55	70[3]
T_d (from TGA) (in ^{0}C)	50	40

As seen from single-crystal XRD, the cocrystals of DMF-$NaClO_4$ have a one-dimensional channel of Na^+ ions where the distance of successive Na^+ ions is 3.23 Å, in 3:1 stoichiometry (and 3.40 Å in 2:1 stoichiometry). Such sufficiently small interionic distances facilitate vacancy site induced jumps, when a defect of Na^+ ion is created during ion transport from the electrode/electrolyte or intergranular interface. This chapter reports findings from classical MD simulations and DFT calculations about the structure, dynamics and mechanism of ion conduction in $(DMF)_3NaClO_4$

[1] All data is reproduced from Zdilla and coworkers [89].
[2] All data, except T_m and T_d, is reproduced from Rao and coworkers [177].
[3] DSC data for 2:1 is provided in **Figure D1**, **Appendix D**.

cocrystalline electrolyte. Henceforth, further discussion will be on the $(DMF)_3NaClO_4$ cocrystals (unless explicitly mentioned).

5.2 COMPUTATIONAL DETAILS

The structural, electrochemical, thermal and physical aspects of $(DMF)_3NaClO_4$ cocrystals require understanding of interactions at atomic scale. However, implementation of a uniform set of computational techniques to study SIB/LIB electrolytes is a challenging task [174]. For example, classical MD simulations are considered to be an effective tool to observe ion conduction and jump events [176, 178], whereas accuracy of results and understanding at electronic level is the key benefit of employing *ab-initio* MD simulations [179]. Plane-wave DFT calculations can extract MEP, electronic properties like electrochemical stability (from band structure), and defect formation enthalpy [180]. Hence, a combined approach with suitable combination of these methods is required to extract valuable insights [166, 174]. A supercell consisting 6x6x12 unit cells of $(DMF)_3NaClO_4$ was created in a periodic box to perform MD simulations. The details of development and adaptations in force-field parameters, along with the general simulation protocols are provided in **Appendix D**. The 6x6x12 supercell was then converted to two different model structures- model *P*, where the supercell was placed in a periodic box and simulated under *NpT* ensembles, and model *V*, where the supercell was placed in a box with sufficient vacuum to simulate surface effects under *NVT* ensemble.

Periodic DFT calculations were performed using the QUANTUM ESPRESSO v6.2 [181, 182] code. Using a cut-off of 40 Rydberg (Ry) for wavefunction, and 200 Ry for charge density, PBE functional [183] was used with Kresse-Joubert projector-augmented wave [184] (KJPAW) basis. The convergence threshold for wavefunction was set to 10^{-7} Ry and for geometry relaxation to 10^{-3} Ry-Bohr^{-1}. A supercell of 1x1x3 (252 atoms) with a Γ-only k-mesh (since the box lengths were 12 x 12 x 19.5 Å^3) was used to determine MEP. The nudged elastic band (NEB) and climbing-image NEB

(CI-NEB) [185] calculations were performed to calculate E_a for Na^+ conduction with 9 intermediate images.

5.3 RESULTS AND DISCUSSION

5.3.1 MD simulations on stoichiometric conversion and structure

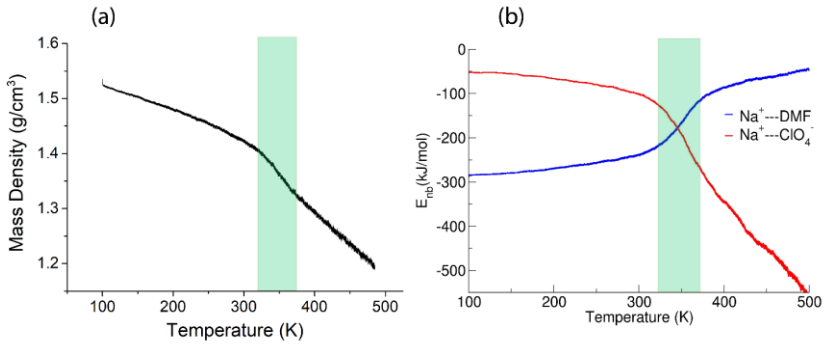

Figure 5.2. (a) Mass density and **(b)** non-bonded interaction energy E_{nb} of $(DMF)_3NaClO_4$ in model P during simulated heating from 100 K to 500 K with a heating rate of 20 K/ns. The highlighted region shows a rapid drop of density in a and extreme change in ion-solvent vs. interionic interactions in b during the process of melting of cocrystals.

The cocrystalline $(DMF)_3NaClO_4$ as model *P* was annealed in a continuous heating bath from T = 100 K to T = 500 K with a heating rate of 20 K/ns. The system density and non-bonded (vdW and Coulombic) components of potential energy, E_{nb} (normalized with respect to number of pair interactions), were calculated as a function of temperature to observe the structural transformations **(Figure 5.2)**. The mass density of $(DMF)_3NaClO_4$ shows that on heating, the density decreases linearly in the temperature range T = 100 to T = 325 K and then, decays sharply in the range 325 K to 375 K. The graph shows a linear decrease in density again in the range 375 K to 500 K. This suggests that possibly significant structural change in the crystal interior occur in the temperature range 325 K – 375 K. The calculated E_{nb} with respect to temperature suggests that the Na^+ cations, which are primarily coordinated with six DMF molecules in the cocrystals, have a higher E_{nb} with DMF molecules compared to ClO_4^- anions, from 100 K – 325 K. This implies the role of ion-solvent interactions in the formation of cocrystals.

In the structural transformation window (T = 325 K – 375 K, as seen from mass density plot, **Figure 5.2a**), the Na^+ cations switch their preference of interaction from DMF to ClO_4^- anions, which suggests that $NaClO_4$ forms as ion-pairs which are either solvated or phase separated in DMF **(Figure 5.2b)**. The visuals at T < 325 K **(Figure D2)** show that the Na…Na (in blue) and Na…O(DMF) (in green) networks are more abundant in the cocrystals at low temperatures. However, at T = 325 K **(Figure 5.3a)**, ClO_4^- anions replace the DMF molecules from coordination sphere of Na^+ ions and coordinate in bridged manner, very similar to $(DMF)_2NaClO_4$. As the cocrystals melt (T > 325 K), the Na…Na and Na…O(DMF) networks break and Na…O(ClO_4^-) networks (in red) form largely suggesting formation of $NaClO_4$ ion pairs.

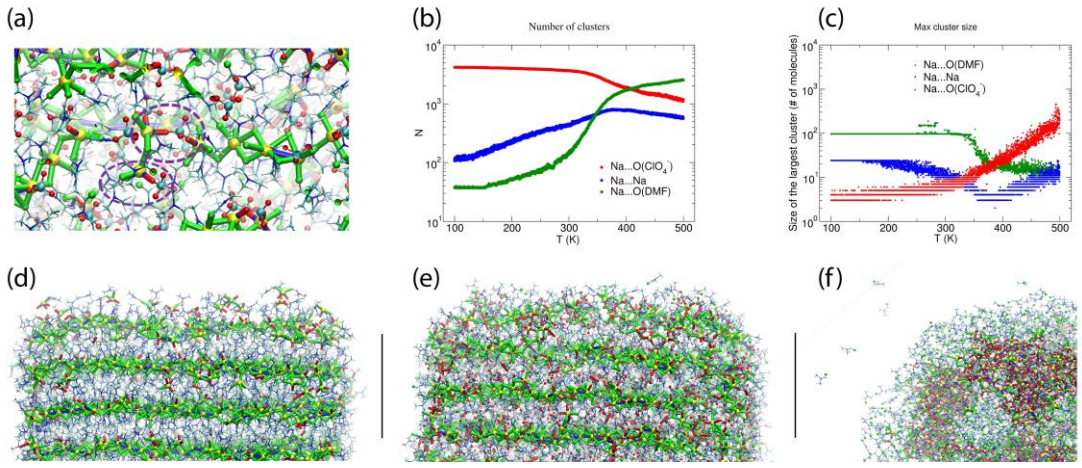

Figure 5.3. (a) Na...O(ClO_4^-) and Na...O(ClO_4^-)O...Na frameworks showing the abundance of Na...O(ClO_4) clusters at 325 K, **(b)** number of total clusters (counting clusters of size of one atom also) and **(c)** size of the largest cluster of Na…O(ClO_4^-) (≤ 2.2 Å), Na…Na (≤ 3.5 Å) and Na…O(DMF) (≤ 3.0 Å) during simulated heating of model P (a,b,c); The distribution of number of clusters with respect to their size is provided in **Figure D3**; Snapshots of supercell of $(DMF)_3NaClO_4$ simulated as model V at **(d)** 100 K, **(e)** 300 K, **(f)** 400 K, Color scheme: Spheres (atoms): Yellow- Na, Red- O(ClO_4), Green- O(DMF), Cyan Cl(ClO_4^-) ; tubes (dynamic bonds): Blue- Na…Na, Red- Na…O(ClO_4^-), Green- Na…O(DMF); lines- DMF.

The abundance of these networks as a function of temperature is quantified from cluster analysis using the simulation trajectory **(Figure 5.3b and Figure 5.3c)**. The cluster analysis shows that $\{Na…3O(DMF)\}_n$ networks of 96 atoms (consisting Na and O(DMF) atoms) form parallel to the *z*-axis (*c*-crystallographic direction) of the

simulation box at T < 300 K. This network also represents the abundance and stability of Na^+ ion channel in the *z*-direction. At low temperatures (T < 300 K), size of the largest clusters is big and total number of clusters is small for Na…O(DMF) and Na…Na clusters. The size of the largest of Na…O(DMF) and Na…Na clusters decreases with temperature and the number of these clusters increases, which affirms the visual observation of breaking of Na…O(DMF) and Na…Na networks above T > 300 K **(Figure D2)**. At T < 300 K, many (~ 2000) small (< 10, Na and O atoms in the largest cluster) Na…O(ClO_4^-) clusters exist in the system (most of which could be a single Na or O atoms) which increase in size and decrease in number as the temperature increases. Conclusively, large clusters (of the size of >1000 atoms) of $NaClO_4$ form after the melting of cocrystals.

The simulated heating approach is used to calculate the interplay of non-bonded interactions during melting. To understand the distribution of clusters with respect to their size, the model *P* was simulated under isothermal-isobaric ensemble at constant temperatures: T = 100 K (20 ns), 233 K (40 ns), 273 K (40 ns), 298 K (40 ns), 325 K (40 ns), 350 K (20 ns). The histograms of the distribution of different sized clusters at various constant temperatures **(Figure D3)** show that the Na…Na and Na…O(DMF) clusters are predominantly abundant at low temperatures. While in case of Na…O(ClO_4^-) clusters, most of the clusters are monoatomic (i.e. Na…O(ClO_4^-) do not have a bond) at low temperatures, which increases to a size of 10 atoms (i.e. three to four ion pair clusters) at T = 325 K. The cluster analysis also suggests that Na…O(ClO_4^-) clusters, which form after the Na…O(DMF) networks collapse, are small in size, indicating solvation of small clusters of ion-pairs in DMF, rather than phase separation.

To understand the nature of pair interactions in the structure of $(DMF)_3NaClO_4$, RDFs are calculated at various temperatures for model *P* **(Figure D4)**. The RDFs suggest that in the first solvation shell of Na^+ cations, DMF molecules occupy the shell at a distance of 3 Å to 3.5 Å, at T = 100 K, whereas, ClO_4^- anions do not interact with

Na^+ primary solvation shell and only interacts with a distance > 5 Å. However, the Na---O(DMF) coordination number decreases as the temperature increases from 233 K to 298 K **(Figure D5)**. In the coordination sphere of Na^+ cation, ~ 2 O(DMF) are replaced by ~ 2 O(ClO_4^-) anions at a distance of 2 Å, at 298 K. This infers that $(DMF)_2NaClO_4$ could also form from $(DMF)_3NaClO_4$, provided that the residual DMF is removed from the system. The simulations do not model a direct formation of $(DMF)_2NaClO_4$ but the results from cluster analysis and calculated coordination numbers though indicate that the Na^+ cations form clusters with 4:2 coordination of DMF:ClO_4^- at T ≥ 298 K. As the crystals melt, at T = 325 K, 350 K, coordination of O(ClO_4^-) supersedes the coordination of DMF around Na^+ cations. Overall, the $T_{m,\ simulation}$ = 325 K (= 52 ^{0}C) predicted from annealing simulations, cluster analysis and RDFs, matches closely with the experimental $T_{m,\ DSC}$ = 55 ^{0}C.

While model *P* mimics the interior behavior of the cocrystals, the nature of surface of $(DMF)_3NaClO_4$ was modeled using model *V*. The model *V* was constructed by placing the supercell used in model *P*, in a larger box of 15x15x18 nm^3 with sufficient vacuum present at the either side of the supercell to avoid any possible interactions with its periodic image. From the simulated annealing of model *V* from T = 100 K to 500 K – with a heating rate of 20 K/ns, only a visual inspection was enough to extract these valuable outcomes: i) At T = 100 K, the surface of cocrystals is fluid, with the presence of Na^+…O(ClO_4^-) clusters and free DMF molecules, which are usually minutely abundant in bulk **(Figure 5.3d)**; ii) At room temperature, the surface becomes more abundant with Na^+…O(ClO_4^-) clusters and free DMF, the presence of Na^+…O(ClO_4^-) networks is also visible in bulk **(Figure 5.3e)**; iii) At T = 400 K, the DMF molecules from the surface evaporate (a conceptual imitation of mass loss during TGA) and more and larger Na^+…ClO_4^- clusters form exhibiting decomposition of electrolyte.

5.3.2 MD simulations on ion dynamics

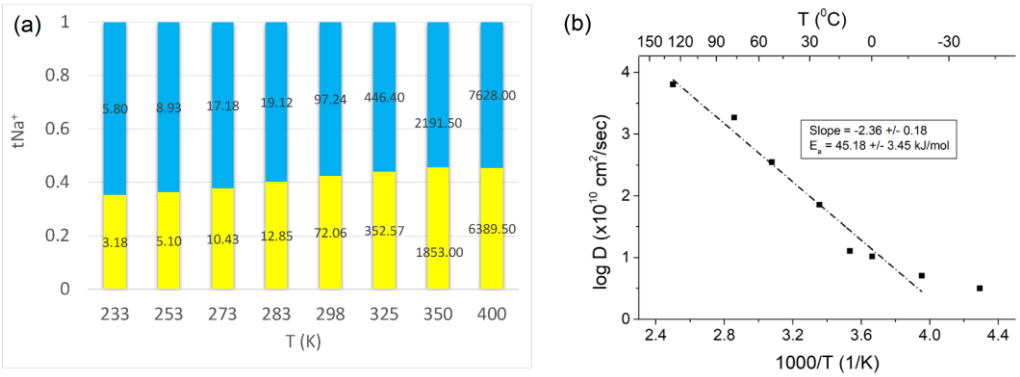

Figure 5.4. (a) Transference numbers of Na^+ (yellow) and ClO_4^- (blue) calculated from MD simulations using Einstein's equation. Values of diffusion coefficients D_i (10^{-10} cm^2/sec) are provided in the respective bars, **(b)** log (D_{Na^+}) vs. 1/T plot for $(DMF)_3NaClO_4$ from simulations on model P; the data points were fitted to a straight line (the lowest temperature point was neglected).

The $(DMF)_3NaClO_4$ cocrystals possess a conductivity of 3 x 10^{-4} S cm^{-1} with E_a barrier of 25 kJ/mol for Na^+ ion conduction calculated from impedance spectroscopy measurements[89]. In the previous work[89], transference number for Na^+ ions was not calculable from chronoamperometry due to reactivity of $(DMF)_3NaClO_4$ with Na^0 metal, and from pulse-field gradient NMR due to broadness in signals. MSD *vs.* time plots for Na^+ **(Figure D6)** and ClO_4^- **(Figure D7)** ions are calculated from a series of constant temperature simulations on model *P* to obtain diffusion coefficients (D_i) using Einstein's equation. The MSD *vs.* time plots show that at low temperatures (T ≤ 283 K) the early diffusion of Na^+ ions is super-diffusive, due to the initial cage vibrations. However, with sufficiently long timescales (40 ns), a linearity in diffusion was observed even at low temperatures (T = 233 K to 273 K). Hence, from the linear regime of MSD *vs.* time plots, D_i for Na^+ and ClO_4^- were calculated for T = 233 K to T = 400 K **(Figure 5.4a)**.

The cluster analysis and RDFs suggest that at high temperature (> T_m), the cocrystals do not phase separate, but appear as small-scale ion-pair clusters of $NaClO_4$ solvated in DMF. This suggests that the cocrystals behave as a supercritical solution of $NaClO_4$ in DMF, and the calculation of D_i is relevant, at these high temperatures (T

= 325 K, 350 K and 400 K). The calculated D_i provide a transference number, t_{Na^+} = 0.43, at 298 K and exhibit that the fraction of mobility of Na^+ ions in the net ionic mobility increases with temperature. The values of D_{Na^+} are fitted to Arrhenius equation to calculate E_a for Na^+ ion conduction **(Figure 5.4b)**. The fitted data provides an E_a barrier of 45 kJ/mol for Na^+ ion conduction in the cocrystals.

To analyze the nature of Na^+ cation mobility, self-part of van Hove autocorrelation functions (vH ACF) were calculated for time intervals of 100 ps, 1ns and 10 ns **(Figure D8)**. The generalized form of vH ACF is:

$$G(r,t)= \frac{1}{N}\left\langle \sum_{i=1}^{N}\sum_{j=1}^{N} \delta\left(\mathbf{r} + \mathbf{r_i}(0) - \mathbf{r_j}(t)\right)\right\rangle \quad \textbf{(5.1)}$$

where, $\mathbf{r} + \mathbf{r_i}(0) - \mathbf{r_j}(t)$ represents the distance term with cross/self- correlation in time and for the pair. The general form of vH ACF **(5.1)** includes both self and distinct correlations. The distinct part of vH ACF and $t = 0$ is static pair correlation function, i.e. RDF. The self-part of vH ACF correlates the jumps by center of mass of an ion in time t, as:

$$G_s(r,t)= \frac{1}{N}\left\langle \sum_{i=1}^{N} \delta\left(\mathbf{r}+\mathbf{r_i}(0)-\mathbf{r_i}(t)\right)\right\rangle \quad \textbf{(5.2)}$$

The transformed function, $r^2.G_s(r)$, at a constant time interval provides a probability distribution function for an ion to travel a distance r. The vH ACF shows that at low temperatures, the primary mode of Na^+ ion mobility is cage vibrations and short-distance (< 5 Å) jumps, whereas a few spikes associated with long-distance jumps (> 10 Å) are also observed with a miniature probability. As the temperature increases above room temperature, the primary peak associated with short-distance jumps decreases, indicating interstitial migration of Na^+ ions.

5.3.3 Plane wave DFT calculations for the mechanism of ion conduction

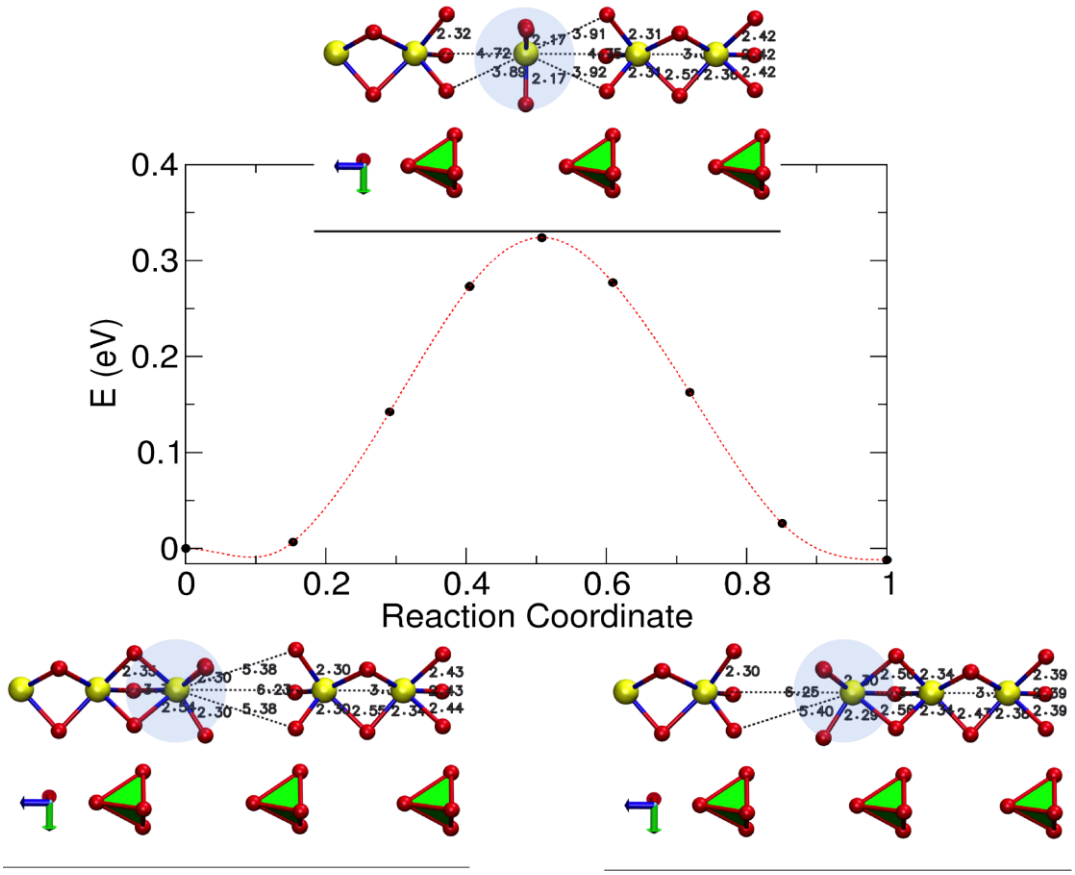

Figure 5.5. MEP of Na^+ ion conduction in $(DMF)_3NaClO_4$ extrapolated from NEB calculations. Color scheme: Red- O (DMF) free, red atoms in tetrahedral green cages- O in ClO_4^- anions, yellow- Na^+ ions. Distances shown as text are in the units of Å.

The reason for short-distance Na^+ ion jumps in $(DMF)_3NaClO_4$ is the array of Na^+ ions with an interionic distance of 3.23 Å, as suggested from the structure obtained as the unit cell from single-crystal XRD. To understand jumps which occur at short-distances, plane-wave DFT calculations were performed to obtain the MEP for Na^+ ion jump to the adjacent vacancy site. A 1x1x2 supercell of $(DMF)_3NaClO_4$ was created and relaxed without any restrictions of symmetry on the structure. Further, a pair of defected supercells was created carrying one Na^+ ion defect at adjacent site in each of the 'image'. The two images which only differ in the location of vacancy sites, are considered 'reactant' and 'product' geometries, indistinguishably, to optimize the MEP using climbing-image nudged elastic band [185] (NEB) calculations **(Figure**

5.5). The extrapolated path of Na^+ ion to migrate to a vacancy site in the *c*-crystallographic direction (at a distance of 3.23 Å) shows E_a = 0.34 eV (= 33 kJ/mol) close to the experimental value of 25 kJ/mol. The E_a barrier improved slightly, to 0.32 eV when SCF calculations were performed with a hybrid functional PBE0 on the PBE geometries. Additionally, the migration of Na^+ ion occurs via formation of a transition state, very similar to the trigonal planar transition state in a S_N2 reaction of methyl chloride with hydroxide anion. The transition state structure for Na^+ ion migration has Na^+ ion and three O(DMF) atoms present in the same plane, in a trigonal planar structure. The extrapolated MEP suggests that the carbonyl group on DMF molecules assist in delivering Na^+ ion from the occupancy site to a vacancy site with a small barrier and can be termed as 'solvent-assisted' migration.

5.4 CONCLUSIONS

To summarize, classical MD simulations provide explanation of stoichiometric conversion and melting behaviour of $(DMF)_3NaClO_4$. The nature of ion conduction and determination of t_{Na^+} from MD simulations is the immediate impact of present work. Typically, diffusion coefficient for cations in hard-solids is calculated by performing high-temperature simulations, where cations attain linearity in diffusion and anionic sublattice remains thermally stable. However, in soft-solid cocrystalline electrolytes, a higher stability of cationic sublattice leaves a marginal window of temperature to observe linear diffusion. The classical MD simulations with sufficiently long timescales here report E_a barrier for conduction of Na^+ from Arrhenius plot (45 kJ/mol) for diffusion coefficients which is in the same order of magnitude of experimental value (25 kJ/mol). The DFT calculations suggest a solvent assisted MEP for Na^+ cations with a barrier of 33 kJ/mol which is closer to the experimental barrier. An atomic scale model of crystal melting, role of interionic/ion-solvent interactions in stoichiometric conversion, transference number for Na^+ ions and mechanism for Na^+ ion migration in this chapter provide valuable understanding for the development of optimal electrolytes for SIBs.

———*———*———

Chapter 6:

Investigating Stability, Ionic Mobility and Mechanism for Ion Transport in an Adiponitrile based Sodium Electrolyte

This chapter contains results and discussions from experiments which were performed in part by the collaborators to this work from Dr. Zdilla and Dr. Wunder's lab at Temple University.

6.1 INTRODUCTION

In this chapter, a combined experimental and theoretical investigation of freshly synthesized adiponitrile (ADN) cosolvent based cocrystals of sodium perchlorate, $(ADN)_3NaClO_4$, is presented. The cathode [186], anode [187, 188] and electrolyte [189] materials are under investigation for use in sodium (Na^+) ion batteries. Na^0 metal, which has the lowest reduction potential (-2.71V) and highest theoretical capacity (1165 mAh-g^{-1}) of potential anodes for Na batteries, still has practical electrochemical limitations, and due to its chemical similarity to Li, presents essentially the same set of challenges as exist in Li batteries. For example, Na^0 forms unstable solid electrolyte interphases (SEIs), and has problems associated with growth of sodium metal dendrites, which can break off, decreasing capacity, or worse: span the separator and short the cell. Na^0 metal batteries further experience large volume changes upon cycling, complicating maintenance of optimal interfacial contact of components in devices. Solutions of sodium salts in volatile and flammable ethylene and dimethyl

carbonate (DEC) [189] solvents present the same flammability and explosivity concerns as in LIBs and form unstable SEIs with the Na^0 metal anode [190]. Research to resolve these problems has focused on the development of new anodic materials and the formation of engineered SEIs on Na^0 metal or by tailoring the electrolyte [191]. One of the approaches is the use of concentrated electrolytes [192–194]; High ionic concentrations have been demonstrated to reduce the reactivity of the organic electrolyte solvent molecules with Na^0 metal anodes [169, 194–196] and thus improve electrochemical stability. For example, reductive stability of a lithium electrode to acetonitrile was improved in super concentrated (> 4M) solutions of electrolyte species in acetonitrile, where all the acetonitrile molecules were coordinated to Li^+ ions, so that salt (rather than solvent)-derived surface films are formed on the anode [192]. In a sodium system, it was shown that there are no uncoordinated solvent molecules available for reaction with Na^0 metal, suggesting ligation of ions by solvents mitigates Na^0 metal corrosion by solvent molecules [169].

Solid-state electrolytes [68, 197] have advantages over organic liquid electrolytes since they are less flammable and there is not continual diffusion of reactive liquid solvent molecules to the electrode surfaces; this prevents diffusional corrosion, decreases capacity loss, and helps maintain a thin, conductive SEI. Polymer electrolytes with sodium salts [198, 199] have good adhesion to the electrodes and are processible, but have low ionic conductivity (~ 10^{-5} $S \cdot cm^{-1}$), while inorganic electrolytes (e.g., beta-alumina, NASICON [66] , Na_3PS_4 [170], $Na_3Zr_2Si_2PO_{12}$ [200]) can have higher conductivities and may inhibit dendrite growth since their shear moduli are sufficiently high. However, these are reactive toward the electrode, and also brittle; it has now been established that there is rapid growth of dendrites through the grain boundaries of ceramic electrolytes; composite materials have thus been investigated that seek to combine the beneficial properties of the inorganic and organic electrolytes [167, 200].

The lack of suitable purely inorganic or purely organic solid electrolytes has motivated the pursuit of new solid electrolytes with high ionic conductivity and good adhesion to the electrodes in sodium batteries. Composite materials have thus been investigated that seek to combine the beneficial properties of the inorganic and organic electrolytes [167, 200]. The research groups of Zdilla and Wunder synthesized and characterized soft-solid co-crystalline electrolytes containing $NaClO_4$ and LiCl salts in DMF solvent, [88, 89] which were hypothesized to adhere weakly to Li^+ and Na^+ ions due to its "soft" (polarizable) electronic structure. This is because the presence of multiple bonds in the DMF matrix molecules results in a Lewis acid base orbital mismatch according to the Pearson Hard-Soft Acid Base Theory (HSAB) [74] leading to weak interactions with the "hard" (charge dense, non-polarizable) Li^+ and Na^+ ions. These co-crystalline electrolytes exhibit high ionic conductivity over a wide temperature range. In particular, the $(DMF)_3NaClO_4$ co-crystalline electrolyte showed appreciable malleability and press-castability, and an extremely low activation energy barrier for ion conduction [89]. Finally, a novel feature was an intrinsic surface nano-liquid layer caused by the decreased lattice energy at the crystal surface, and which was observed experimentally and explained using MD and DFT [88, 201]. This surface liquid layer is a conductive, ionic, nanoconfined solution and serves as a conductive binder between the solid grains. Upon pressing, the larger grains fragment to form new grains and reestablish the surface nano-liquid layers at their surfaces, and rebind to one another.

This chapter presents a new organic crystalline electrolyte with improved electrode stability, good conductivity, a low activation barrier, and high sodium ion transference number (t_{Na^+})- $(ADN)_3NaClO_4$. Dinitrile based electrolytes are promising, exhibiting a potential window of ~ 6V against Na/Na^+ [202]. Among these, ADN has several favorable characteristics that make it suitable for sodium batteries. In particular, it has a high flash point (163 ^{0}C) [203] and high anodic stability (~ 5V) [77]. DFT calculations suggest an excellent electrochemical stability window of ADN

against Na/Na^+ (7.34 V) [204]. As in the case of other dinitriles, the excellent resistance towards electrochemical oxidation [197] enables their use with high-voltage cathodes [78, 205, 206]. In contrast to other organic solvents such as the commercially used ethylene carbonate (which reacts with the anode and forms sodium carbonate and alkyl carbonates in the presence of $NaClO_4$ [207]), ADN contains nitrile groups which have lower reactivity towards sodium metal. The use of ADN as a monomer precursor in the industrial manufacture of nylon 6,6 ensures its availability at low cost. Other investigations have shown ADN to be a superior choice over other dinitriles [208], with potential applicability as a solvent for supercapacitors [209, 210] and Li^+ ion liquid electrolytes [211]. Further, computational investigations suggest that ADN has higher solvation energy for Li^+ and Na^+ compared to other solvents such as DEC, dimethylsulfoxide (DMSO), ethylene carbonate (EC) and propylene carbonate (PC) [173]. Finally, the HSAB-soft nature of the nitrile group should present a labile attachment of HSAB-hard Na^+, permitting ion conduction through a lattice of these functional groups. The above chemical and physical properties strongly favor the use of ADN as a solvent and co-solvent for liquid and crystalline electrolytes. $NaClO_4$ has high ionic conductivity (on the order of 10 $mS \cdot cm^{-1}$) in non-aqueous solvents (similar to $NaPF_6$ [189]), and a high melting point (468 ^0C). And despite its high reduction potential, the perchlorate anion can be compatible with alkali metal anodes, and can help form a passivating SEI [212].

The synthesis, structural characterization, thermal and electrochemical analysis of $(ADN)_3NaClO_4$ are presented. This material exhibits a room temperature (RT) conductivity of $\sigma = 4 \times 10^{-5}$ $S \cdot cm^{-1}$, an activation energy barrier of 37 $kJ \cdot mol^{-1}$, and a t_{Na^+} of 0.71. The use of a more Na^0-compatible electrolyte matrix—ADN—facilitates cycling experiments and transference number measurement, representing an innovation for this class of materials. An atomistic investigation of structure and mechanism of decomposition (from classical MD simulations), and pathway of ion conduction (from DFT calculations) is presented in the subsequent sections.

6.2 EXPERIMENTAL DETAILS

6.2.1 General

Sodium metal, ADN, $NaClO_4$ (both used as received) and diethyl ether (Et_2O) were purchased from Sigma-Aldrich. The Et_2O was distilled using sodium benzophenone ketyl as a water/oxygen scavenger. Single-crystal and powder X-ray diffraction data were obtained on a Bruker KAPPA Apex II DUO with sealed-tube Mo K_α and Cu K_α sources, a TRIUMPH^{TM} monochromator for the molybdenum tube, and an Oxford Cryostream low temperature device. Thermal degradation data of $(ADN)_3NaClO_4$ crystals were obtained on a Thermogravimetric Analysis (TGA) TA Instruments Hi-Res TGA 2950 at a ramp rate of 10 °C-min^{-1}, purged with ultra-pure N_2 gas. The melt and crystallization temperatures were obtained using a TA Instruments 2920 Differential Scanning Calorimeter (DSC), with the sample in hermetically sealed Tzero aluminum pans, from -110 °C to 120 °C at a scan rate of 10 °C/min, under ultra-pure N_2 purge. Scanning Electron Microscope (SEM) images were acquired using a field emission SEM (FEI Quanta 450). Temperature-dependent bulk impedance data was measured by AC impedance spectroscopy using a Gamry Interface 1000 potentiostat/galvanostat/ZRA in the frequency range 0.1 Hz−1MHz. between 70 ^{0}C and -40 ^{0}C (or -77 ^{0}C). The cell was thermally equilibrated for 30 minutes at each temperature before the bulk impedance was measured during both the cooling and heating cycles.

6.2.2 Synthesis

Crystals prepared from excess AND ("rinsed"): 1.3 g (10.6 mmol) of $NaClO_4$ was dissolved in 8.0 mL (71.8 mmol) of ADN to crystallize co-crystals in excess solvent. The mixture was heated to 150 ^{0}C under an argon atmosphere. Crystalline material started to form upon cooling to room temperature (RT). A single crystal was removed from the precipitate made from excess and for X-ray analysis, and the remaining powder was rinsed inside the pressure flask five times with excess Et_2O, and then dried under vacuum for ~ 20 minutes to remove residual amounts of ADN and Et_2O. The

cocrystals were then heated above T_m to 160 °C and recooled to melt cast the material for the electrochemical measurements.

Crystals prepared from a stoichiometric mixture of $NaClO_4$ and ADN ("unrinsed"): The sample was prepared in the same manner as that given above except that 2.0 g (16.4 mmol) of $NaClO_4$ was dissolved in 6.0 mL (52.7 mmol) of ADN, and the solid sample that forms upon cooling was used as is, and was not rinsed.

6.2.3 Characterization

Single crystal data were obtained by mounting a single crystal on a MiTeGen^{TM} loop with Paratone-N oil. Data were collected using Mo Kα radiation at -173 ^{0}C, reduced using the Bruker Suite, and refined using the SHELX package [213]. Powder samples were caked onto the tip of a glass fiber using paratone-N oil. The powder X-ray diffraction data was obtained using a Cu K_α radiation at -173 ^{0}C. The theoretical powder pattern was generated from the single crystal data using Mercury (CCDC) and was compared with the experimental data to confirm the crystal structure $(ADN)_3NaClO_4$.

6.2.4 Electrochemistry

Electrochemical Impedance Spectroscopy (EIS) was used to obtain the conductivity data using either self-standing pellets, prepared by pressing the $(ADN)_3NaClO_4$ powder at 800 psi in a hydraulic crimper within an argon-purged glove box, or by cooling stoichiometric $(ADN)_3NaClO_4$ melts onto Whatman (GF/A) glass microfiber filters, (Sigma-Aldrich). In the first case, the powder was placed between one of the ~ 1 cm^2 stainless-steel (SS) blocking electrode disks and the top plunger of the crimper. After compression, the top plunger was replaced with the other SS blocking electrode. The conductivity measurements were acquired in a homemade electrochemical cell placed in a N_2 purged, temperature-controlled gas chromatography (GC) oven. Resistivities were determined either by fitting to an equivalent circuit **(Figure E1)**, or

extrapolating from the tail of the Nyquist plot when the equivalent circuit overparameterized the data (higher temperatures).

For all the other electrochemical measurements, the $(ADN)_3NaClO_4$ was melt cast at 85 - 115 ^{0}C (above T_m) onto a glass microfiber filter matrix (Whatman GF/A), where it crystallized upon cooling. While discoloration of Na metal (it looked tarnished) was observed upon addition to liquid ADN for several months at RT, the liquid solvent remained clear and became slightly yellowish, indicating that there was a minimal dissolution of the reaction products. However, since $NaClO_4$ is not soluble in ADN at RT (although $NaClO_4$ is reactive towards Na metal), it was not possible to observe the reactivity of a solution of $NaClO_4$ in ADN with Na metal. In some experiments where Na^0 metal was used, the Na^0 was pretreated with 0.25 M $NaPF_6$ in ADN/EC 1/1, since the Na^0 metal retained a lustrous appearance. Interfacial resistance at open circuit voltage was obtained as a function of time in a $Na^0/(ADN)_3NaClO_4/Na^0$ cell. CV and LSV were obtained using a $SS/(ADN)_3NaClO_4/Na^0$ cell with SS as the working electrode and Na^0 as both the counter and reference electrodes. The LSV data was between open circle voltage and 6.0 V and the CV data between -0.75 and 4.5 V. Sodium cycling experiments were performed in a symmetric $Na^0/(ADN)_3NaClO_4/Na^0$ cell that was stabilized for > 4 days. After cycling experiments were completed, sodium ion transference numbers (t_{Na^+}) were obtained using the same cell via DC polarization measurements with correction for internal resistivity **(Figure E5)**.

6.2.5 Computational details

MD Simulations: The structure, thermal behavior and interstitial (between the grains) dynamics of the crystalline electrolyte were modeled using all-atom force-field using classical MD simulations. The protocol for force-field development and derived parameters are given in **Appendix E**. The atomic charges for were derived using quantum calculations in Gaussian 9.0 package [128] and equilibrium bonded parameters were based upon the structure from single crystal X-ray diffraction analysis.

The input construction of the $(ADN)_3NaClO_4$ supercell required for MD simulations are as follows: A supercell of 8x8x8 unit cells (total of 20,250 and 82,944 atoms, respectively) was constructed. For the calculation of non-bonded forces (Coulombic and Lennard-Jones) and construction of neighbor lists, a cut-off distance of 14 Å was used. The time-step to integrate the equation of motion of atoms in the supercell was chosen to be 1 fs. The configuration of the supercell was energy minimized using the steepest-descent algorithm. The energy minimized configuration of the supercell was equilibrated for 20 ns in the isothermal-isobaric (*NpT*) ensemble, where a constant temperature and pressure were maintained using the velocity-rescale thermostat [158] and isotropic Berendsen barostat [159], respectively. The timescale of the simulations was sufficient to obtain the convergence of the density and potential energy. The equilibrated configurations were used as templates to construct three input models: (1) Model P (periodic) – to simulate the bulk material; (2) model V (in vacuum) – to simulate surface effects of the material with a vacuum-surface interface; (3) model D (defect) – to simulate interstitial/vacancy dislocations of Na^+ ions in a supercell with Schottky (vacancy) defects. The simulations performed on Models P and V were used for calculation of structural properties and thermal decomposition or melting of the crystalline electrolyte. Since the jump rate for ion hopping in typical electrolyte materials is very small, extremely long simulation time scales would be needed to observe ion jumps from MD simulations at room temperature. Considering this limitation, multiple Model Ds were constructed with four Na^+ and four ClO_4^- ion defects created randomly at different locations in the supercell and simulated at elevated temperature (T = 423 K and 473 K). The results from these simulations were used for the analysis of dynamical properties such as translational diffusion and the Arrhenius activation barrier of conduction for Na^+ in the cocrystals. Before initiating the production run simulations on models P, V and D at any temperature, the models were pre-equilibrated to adjust to the new spatial and thermal conditions. The production run simulations were performed for 10 – 15 ns under the canonical-isothermal *NVT* ensemble conditions with the Nosé-Hoover thermostat [109, 110].

GROMACS 5.0.7 [106] code was used for all MD simulations and the VMD 1.9.3 [114] program was used for model construction and visualization.

PWDFT Calculations: Plane-wave DFT (PWDFT) calculations were performed using QUANTUM ESPRESSO v6.2 [181, 182] code. PBE functional [183] along with KJPAW [184] basis was used with cut-offs of 40 Ry for wavefunction and 200 Ry for charge density. An electronic convergence threshold of 10^{-7} Ry and force convergence for atomic relaxation of 10^{-3} Ry-Bohr^{-1} were used for all the calculations. Supercells of 2x1x1 and 1x1x2 size (containing 324 atoms) and hence a Γ-only k-mesh were used for all the calculations. To observe the atomistic mechanism of Na^+ ion transport in the cocrystal, CI-NEB [185] method was used to calculate the activation barrier (E_a) of Na^+ jumps in a supercell with Schottky defects. The path of these jumps was traced using interpolation from 13 images while the convergence threshold for these images was 0.01 eV-Å^{-1}.

6.3 RESULTS AND DISCUSSION

6.3.1 Structure and thermal stability from experiments

The solubility properties of $NaClO_4$ in ADN were quite surprising; there is virtually no solubility of the $NaClO_4$ in liquid ADN at room temperature, but after dissolution at higher temperatures and cooling to room temperature, co-crystallization of $(ADN)_3NaClO_4$—rather than phase separation of the two—occurs. Alteration of the stoichiometry of ADN and $NaClO_4$ did not, in any instance, lead to isolation of a cocrystal with different stoichiometry, but always gave the 3:1 cocrystal (with the excess reagent left unreacted). When Na metal is placed in ADN, the ADN solution does not discolor, and the metal remains lustrous for several days, though after a period of months, the metal surface loses its luster due to the normal level of oxygen contamination in the glove box. In the analysis of grain-binding behavior of this solid electrolyte, three different preparations of this sample are described below.

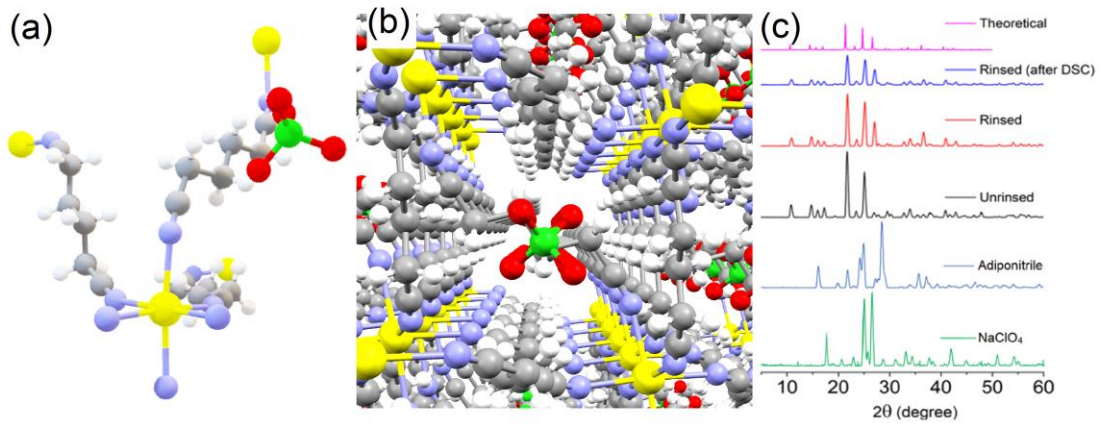

Figure 6.1. (a) Stoichiometric unit of $(ADN)_3NaClO_4$ Six symmetry equivalent ADN molecules (3 shown here) surround an octahedrally coordinated sodium atom, and the perchlorate ion lies in a pocket surrounded by the aliphatic central carbons of six symmetry equivalent ADN molecules; **(b)** Crystal packing of the $(ADN)_3NaClO_4$ complex shows linear parallel ionic channels of Na^+. The presence of Na^+ channels in the complex allows migration of Na^+ in a low affinity matrix.; **(c)** The X-ray powder diffraction of unrinsed and rinsed $(ADN)_3NaClO_4$ before and after DSC matches with the theoretical pattern generated from the single crystal X-ray diffraction. Differences in intensity of some Bragg reflections is attributed to preferred orientations of crystallites in the analyzed crystal pellets. The patterns for frozen ADN, and $NaClO_4$ are also placed for reference. Na^+: yellow, Cl: green, O: red, C: grey.

When crystals were prepared from excess ADN, the resulting cocrystals isolated at room temperature were wetted with unreacted ADN, which was rinsed five times with diethyl ether to remove the unreacted ADN and dried under vacuum. This material is referred to the "rinsed" sample, which is important because the rinsing of the crystal surface decreases the grain-binding ability of the solid electrolyte (vide infra). The loss of grain boundary contact may be mitigated by melt-casting: the melting of the above crystalline material and re-cooling to room temperature. References to melted/cooled samples refer to this sample. Finally, a sample was prepared from a precise 3:1 stoichiometric ratio of ADN:$NaClO_4$. This sample was not rinsed in order to maximally maintain the gain binding capability (vide infra) and is referred to as the "unrinsed" sample.

The single crystal X-ray crystallographic structure identified the composition as $(ADN)_3NaClO_4$. The compound crystallizes in the rhombahedral *R*3 space group,

with the sodium atom residing on the 3-fold axis. One ADN molecule exists in the asymmetric unit, with two others being generated by 3-fold rotation operation, and the remaining three nitriles bridging from three other symmetry equivalent sodium ions in neighboring asymmetric units, giving an overall octahedrally ligated Na atom. The perchlorate anion is located on the same 3-fold symmetry axis, and is encased in a barrel of symmetry-equivalent ADN struts, located proximal to the central C-C bond of ADN **(Figure 6.1a)**.

The crystal packing shows linear, parallel ionic channels of Na^+, with distances of 8.33 Å between the two closest Na^+ ions along the (211) direction (the crystallographic *a′* vector of the alternative rhombohedral cell). **Figure 6.1b** illustrates the crystal packing viewed along this axis. The oblique angle of this vector with the three-fold symmetric axis of the crystal implies three equivalent, but differently oriented channels, and the possibility of a 3D conductivity via low-affinity Na^+ channels. Along the same direction, perchlorate ions are blocked by ADN struts, which cross between neighboring perchlorate ions **(Figure 6.1b)**. This steric blockage between adjacent ClO_4^- ions may limit anionic movement, raising the value of t_{Na^+}. The second closest Na-Na vector is 11.26 Å along the equivalent crystallographic *a* and *b* axes. The bulk crystalline material was analyzed by powder diffraction and is the same phase as the single crystal based on comparison of the powder X-ray diffraction pattern to the theoretical pattern calculated from the single-crystal structure **(Figure 6.1c)**. Neither solid $NaClO_4$ nor frozen ADN is present in the powder XRD patterns **(Figure 6.1c)**.

In $(ADN)_3NaClO_4$, the weight percent of ADN is 74.98 wt % and that of $NaClO_4$ is 25.02 wt%. TGA data **(Figure 6.2a)** confirm the expected weight loss from the two components, and is only 2% different when exposed to air, showing the relative insensitivity of the cocrystal to moisture. This is attributed to the hydrophobic alkyl chains of ADN, which may repel water in the condensed phase. The ADN vaporizes in two steps, the first (lower temperature), representing a weight loss corresponding to

2/3 of the ADN, and at the same temperature as neat ADN (T_m = 1 ^{0}C, T_b = 295 ^{0}C, vapor pressure of 300 mPa at 20 ^{0}C) and the second, at a slightly higher temperature, with removal of ADN complete at ~ 350 ^{0}C. An explanation for this two-step process will be discussed in the simulations section. The residual $NaClO_4$ decomposes at the same temperature as pure $NaClO_4$, and the weight loss is due to perchlorate deoxygenation to produce NaCl. The maximum use temperature for this solid electrolyte is therefore ~ 150 ^{0}C.

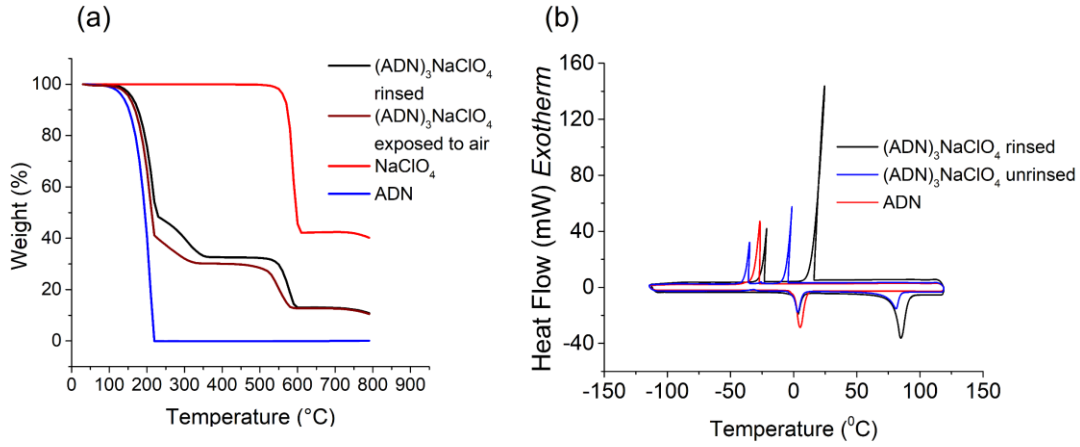

Figure 6.2. (a) Thermogravimetric analysis (TGA) and **(b)** Differential scanning calorimetry (DSC) of ADN and rinsed $(ADN)_3NaClO_4$. The $(ADN)_3NaClO_4$ reversibly melts at T_m = 85ºC and recrystallizes at T_c = -5 ºC to -8 ºC, which shows its potential to be melt cast.

Thermal analysis of $(ADN)_3NaClO_4$ and its parent components from TGA/DSC reveals several useful observations. First, while the boiling point of ADN is 295 °C, under ambient conditions it begins evaporating around 120 °C and is completely evaporated by 220 °C according to TGA **(Figure 6.2a)**. Pure $NaClO_4$ does not melt, but decomposes to NaCl by release of O_2 at 520 °C. The cocrystal melts around 85°C based on DSC **(Figure 6.2b)**, before its decomposition temperature of 120 °C based on TGA **(Figure 6.2a)**. The coincidence of the decomposition temperature of $(ADN)_3NaClO_4$ with the onset of evaporation of ADN under N_2 atmosphere suggests a decomposition mechanism involving the escape of ADN into the gas phase, which removes most of the ADN. The remaining of the ADN escapes

in a second step between 220 °C and 350 °C, leaving behind $NaClO_4$, which then decomposes at 520 °C, at the same temperature as pure $NaClO_4$. A molecular level understanding of this decomposition mechanism is described in the computational section (vide infra). While the onset of decomposition of a nitrogen-purged sample in a TGA experiment is 120 °C, sealed samples the material can be melt cast and studied at temperatures up to 150 °C.

$(ADN)_3NaClO_4$ can be melt cast since its melt temperature occurs before its decomposition temperature **(Figure 6.2b)**. During the first heating cycle of rinsed $(ADN)_3NaClO_4$, which begins at 20 ^{0}C, there is a crystalline melt at T_m = 85 ^{0}C. Upon cooling, the melt typically becomes supercooled and recrystallization occurs at ~ 5 ^{0}C (for this cooling rate, but is somewhat variable), with another small crystallization peak at -30 ^{0}C. Upon reheating, a small peak appears at ~ 5 ^{0}C and a larger peak appears for the melting of $(ADN)_3NaClO_4$ at the same temperature (T_m = 82 ^{0}C) as during the first cycle. Comparison with neat ADN shows that the two small peaks can be assigned to liquid ADN; these ADN peaks may belong to the liquid-like regions around the crystal grains (vide infra). This hypothesis is supported by a decrease in the intensity of these signals when the crystals have been rinsed to remove the liquid boundary layer. For a sample of $(ADN)_3NaClO_4$ unrinsed by Et_2O, the relative enthalpies of melting and crystallization are smaller than for the rinsed sample.

SEM images **(Figure 6.3)** suggest a grain boundary with different morphology exists at the crystal surface and binds the $(ADN)_3NaClO_4$ grains in the unrinsed sample **(Figure 6.3a)**. The boundary appears as a clustering of small crystallites identified as concentrated $NaClO_4$ based upon EDS **(Figure E3)**, and is consistent with a nanoliquid ADN-$NaClO_4$ boundary layer, which evaporated under vacuum in the SEM. The presence of ADN based nanoliquid at the crystalline surface is supported by DSC analysis, which shows melting and freezing signals for liquid ADN even after rinsing of the crystals. This nanoliquid surface solution of $NaClO_4$ is analogous to previous crystalline electrolytes [88, 89]. The grain size is on the order of 100 μm.

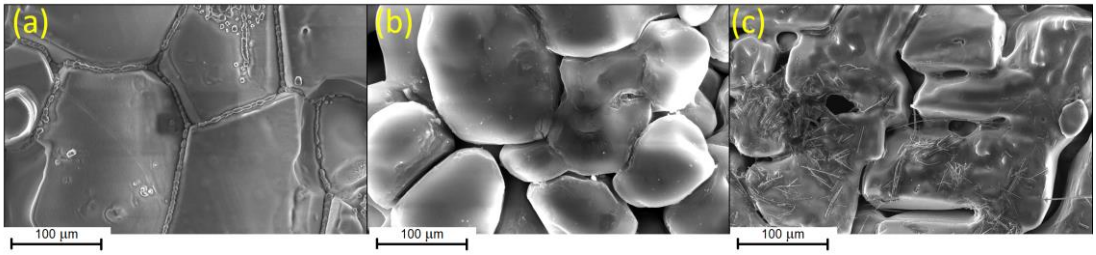

Figure 6.3. $(ADN)_3NaClO_4$. **(a)** Unrinsed cocrystals prepared stoichiometrically showing $NaClO_4$ clusters in the grain boundary region that remain after partial removal of ADN in the SEM vacuum. **(b)** Crystals rinsed with Et_2O that washes away the salt present between the grains. **(c)** Rinsed → Melted → Recrystallized cocrystals showing presence of grain boundary gaps. Small amounts of sublimed ADN are apparent as microneedles.

When the $(ADN)_3NaClO_4$ was prepared with excess ADN and then extensively rinsed with excess diethyl ether **(Figure 6.3b)** most of the ADN and $NaClO_4$ solution in the grain boundary region is washed away, so that there are vacuum gaps between the grains in the SEM. After this sample is melted and recrystallized **(Figure 6.3c)** the grain boundary gaps persist, though narrow grain boundary connections are reestablished.

6.3.2 Electrochemical Experiments

Conductivity: Conductivity data for co-crystalline $(ADN)_3NaClO_4$ prepared stoichiometrically were obtained from a temperature just below the melt temperature of the co-crystal to -40 ^{0}C **(Figure 6.4)** The conductivities were greater for the samples prepared stoichiometrically (without rinsing), dried at RT, compared with those rinsed with diethyl ether and then dried at RT. This is presumably due to the gaps between the grains formed by over-rinsing the samples **(Figure 6.3)**. The SEM data show that there is a layer of ADN and $NaClO_4$ between the grains in the case of the sample prepared stoichiometrically and not rinsed (higher conductivity), while for the sample prepared with excess ADN and then rinsed, this layer has been removed (lower conductivity). This strongly suggests that there is a liquid-like layer of ADN solvated Na^+ and ClO_4^- ions between the grains that has low interfacial resistance, facilitating

the migration of Na^+ ions between the grains, or that there is a percolating network along the grain boundaries.

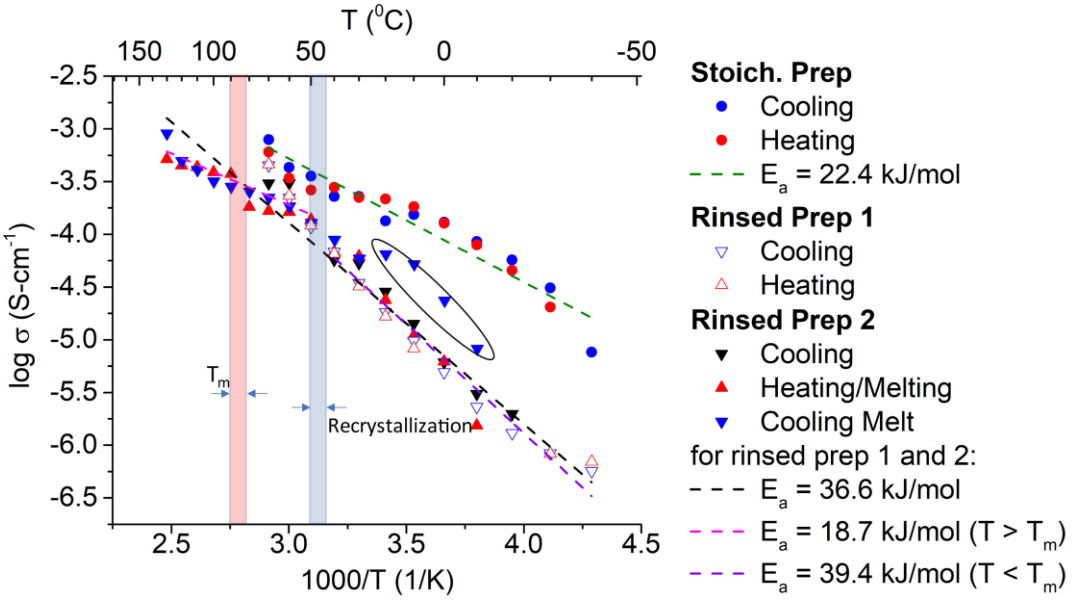

Figure 6.4. Unrinsed stoichiometrically prepared (●), rinsed (△,▽) and rinsed → melted → recrystallized (▲,▼) samples of $(ADN)_3NaClO_4$, showing the conductivity results as following: The stoichiometrically prepared sample (●) is fitted as a single straight line, for all data points. The Rinsed Prep 1 sample (△,▽) was measured at variable temperature, being cooled first and then heated below the T_m of cocrystals, while the Rinsed Prep 2 sample was first cooled, then heated above T_m, and then cooled again below the recrystallization temperature. The data points for both rinsed samples were fitted for an overall slope and for a breakdown above 40 ^{0}C (circled points, after T_m were not considered during fitting). Highlighted regions show the temperatures of crystal melting during heating and recrystallization during the cooling cycle.

The liquid-like nature of the ADN-$NaClO_4$ interfacial region is supported by the observed higher conductivity for stoichiometrically prepared sample and existence of two regions in the conductivity plots for rinsed, then melted samples. As indicated in the DSC data **(Figure 6.2b)**, after melting of the $(ADN)_3NaClO_4$, the sample can be supercooled. **Figure 6.4** shows the conductivity data for three samples under different preparation and treatment conditions. In case of the stoichiometrically prepared solid, which was used unrinsed before conductivity measurement, the conductivity was an order of magnitude higher compared to rinsed samples at room temperature. Also, the

ion conduction in this sample occurs with a comparatively smaller E_a barrier of 22.4 $kJ \cdot mol^{-1}$. This suggests the low resistance in the liquid grain boundary regions which facilitates the Na^+ ion conduction with a lower barrier.

The second sample examined was rinsed with Et_2O to remove the grain boundary liquid region. Conductivity data for this sample was obtained only in the solid state (i.e. it was cooled and heated below T_m only). For the third sample (also rinsed with Et_2O), conductivity data was first obtained in the solid state while cooling from 70 ^{0}C to -20 ^{0}C. Next the sample was heated, and during the heating scan, the sample was heated above T_m, and to 130 ^{0}C, followed by a subsequent cooling cycle back below the recrystallization temperature (~ 40 ^{0}C). The data indicate that the slope of the conductivity profile in the liquid region continues in the supercooled region up to the recrystallization temperature, and is similar to the slope above ~ 40 ^{0}C. The fit of the data using the Arrhenius equation in this temperature interval gave an activation energy of $E_a = 36.6\ kJ \cdot mol^{-1}$.

For the solid samples (rinsed 1 and 2) below ~ 40 ^{0}C, the average activation energy using an Arrhenius fit for the heating and cooling cycles is $E_a = 39.4\ kJ \cdot mol^{-1}$. However, below ~ 40 ^{0}C the supercooled liquid sample has higher conductivity than the solid samples. The supercooled liquid eventually crystallizes and resumes a conductivity close to that of the crystalline $(ADN)_3NaClO_4$ (the original sample was prepared by melt casting, so the behavior should eventually be identical after complete recrystallization).

In the bulk phase, the relatively low activation energies may be due to a hopping mechanism between two successive sodium atoms through linear channels, and weak dipole ion interactions between the six nitrogen atoms and single sodium atom. Above T_m of $ADN/NaClO_4$, the fluid nature of the substance region facilitates Na^+ ion migration. Below T_m of $ADN/NaClO_4$, in rinsed samples, the limited grain

boundary connections **(Figure 6.3c)** facilitate the mobility of the ions between the grains, but the bulk resistivity of the solid dominates.

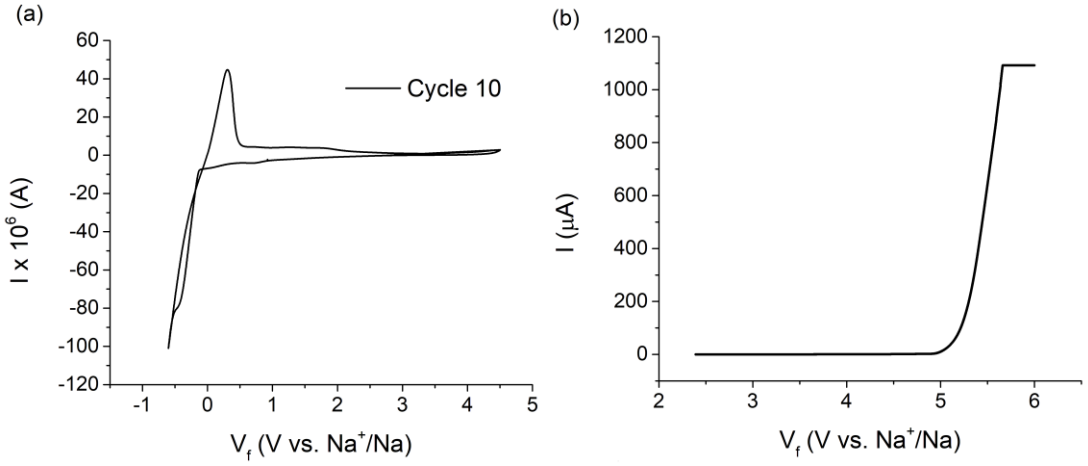

Figure 6.5. (a) Cyclic Voltammetry (CV) and **(b)** linear sweep voltammetry (LSV) of a SS/$(ADN)_3NaClO_4$/Na^0 cell at room temperature with a scan rate of 0.9 mVs^{-1}. The $(ADN)_3NaClO_4$ was incorporated into a glass fiber matrix by melt casting at 100 ˚C, and the Na^0 electrode was passivated in the CV and not in the LSV.

CV, LSV, R_{INT}, t_{Na^+}, Na cycling: The electrochemical stability window (ESW) of $(ADN)_3NaClO_4$, i.e., the potential range over which it is neither oxidized nor reduced, is an important property because the selection of anode, cathode and their cell cycling potential range, and ultimately energy density in the devices depends on the ESW. ADN has excellent oxidative stability of at least 5 V as shown by CV and LSV **(Figure 6.5)**, but perchlorate is reactive towards Na^0 metal. Although it is possible for ClO_4 to facilitate the formation of an SEI [212] in this case, reactivity of ClO_4^- with Na^0 was confirmed by interfacial resistance (R_{INT}) data obtained in a Na^0/$(ADN)_3NaClO_4$/Na^0 cell under open circuit voltage (OCV) and was found to increase over time and not stabilize. However, CV data from SS/$(ADN)_3NaClO_4$/Na^0 **(Figure 6.5, Figure E4,** SS = stainless steel**)** using neat Na^0 metal (no pretreatment) showed that Na^0 could be repeatedly plated and stripped onto the SS electrode when there were no competitive redox reactions. However, if the Na^0 metal was pretreated with 0.25 M $NaPF_6$ in

ADN/EC 1/1, although R_{INT} was high (~ 45 kΩ), it stabilized **(Figure E6)**, suggesting that this pretreatment had some efficacy to passivate the Na^0 metal surface.

Na plating/stripping data **(Figure E2)** indicate that while stable stripping occurs, the plating voltages are irregular. This is tentatively attributed to the competitive reactions between Na^+ ion reduction and perchlorate ion reduction. Measurements of Na ion transference numbers (t_{Na^+}) were made difficult by the high variability of R_{INT}, presumably caused by this same surface degradation. To circumvent this problem, electrochemical DC polarization measurements of t_{Na^+} were made after 50 days of Na^0 cycling of the cell **(Figure E2)** at higher voltages (0.3-0.8 V, depending on cycle number). Although the overpotential was high due to this surface degradation, the internal bulk resistance was stable (and nearly constant) at the low potentials used for the transference number measurements (≤ 20 mV), permitting an accurate determination of the bulk sodium ion transference number in $(ADN)_3NaClO_4$. From this approach, a value of $t_{Na^+} = 0.71$ was obtained at 5, 10 and 20 mV, based on the resulting polarization curves **(Figure E5)**.

6.3.3 Phase behavior, decomposition, and conductivity from classical MD simulations

The structural and dynamical properties of $ADN_3(NaClO_4)$ co-crystals at nanoscale were modeled using classical MD simulations using a periodic supercell (model P), a vacuum-surrounded supercell (model V) and a defect containing supercell (model D). All these models were created by 8x8x8 replication of the crystallographic unit which corresponds to a 9 x 9 x 12 nm^3 box with $\alpha = \beta = 90^0$ and $\gamma = 120^0$ angles. However, in the case of model V, a larger cubic box of size 25 x 25 x 30 nm^3 was used to accommodate the supercell in the surrounding vacuum environment. Standard energy minimization and equilibration protocols were followed before performing the production simulations in each case. To understand atomistic pair interactions in the cocrystals, RDFs were calculated for the 8x8x8 supercell, extracted from the trajectory of the production simulation runs performed on model P. **Figure 6.6a** demonstrate that

the three primary interactions between Na and N/Cl/Na agreed with the structure seen from XRD. For example, Na---Na RDF shows the first two peaks at 8.3 Å and 11.2 Å, which are consistent with the channel distances observed from the experimental structure. The Na---N RDF was integrated to calculate the coordination number (= 6) of Na, which agrees with the octahedral coordination of ADN around the Na^+. To examine the thermal stability of the structure in bulk, model P was simulated discretely at other higher temperatures as well. The atomic pair interactions Na---N/Cl/Na were observed to be intact up to high temperatures (413 K) **(Figure 6.6 - (b), (c) and (d))**, which shows the structural integrity of the $(ADN)_3NaClO_4$ cocrystal even at high temperatures (T = 423 K).

To understand the bulk melting behavior of the $(ADN)_3NaClO_4$ cocrystal, model P was heated from 100 K to 620 K at a heating rate of 20 K/ns under *NpT* conditions. The bulk mass density and non-bonded interaction energies for different pairs of residues were calculated to observe markers of melting of the cocrystals and the interplay of atomic interactions. The calculated mass density of the supercell **(Figure 6.7)** shows a sharp drop around 540 K (267 ^{0}C), which can be attributed to the complete melting and concurrent phase separation of the cocrystals, and which occurs in the same temperature range as that predicted by experiments (220 – 350 ^{0}C from TGA).

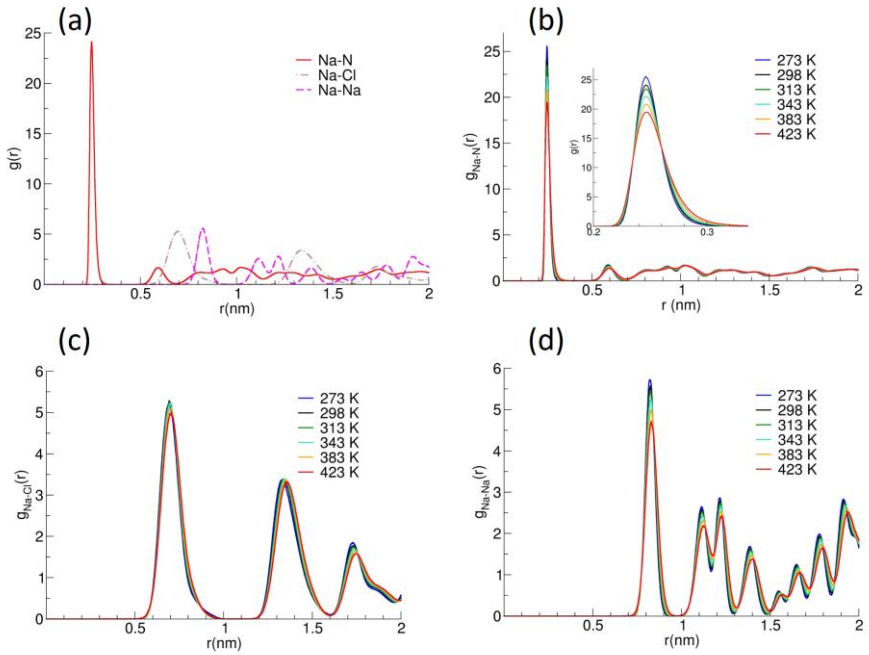

Figure 6.6. (a) Na---N, Na---Cl and Na---Na RDFs at room temperature (298 K); **(b)**, **(c)** and **(d)** are RDFs of Na---N, Na---Cl and Na---Na at different temperatures ranging from 273 K to 423 K calculated from simulations on **model P**.

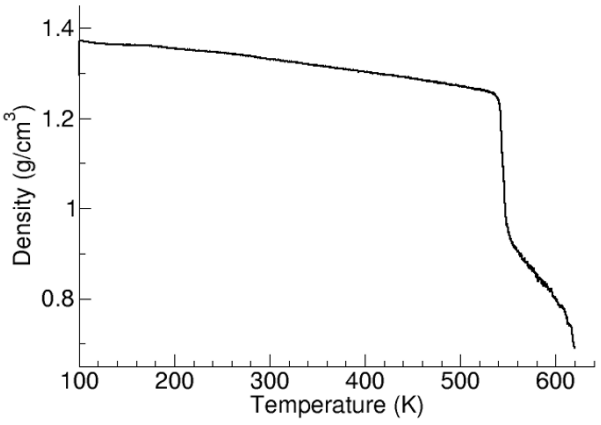

Figure 6.7. Simulated mass density of a 8x8x8 supercell **model P** during annealing.

A snapshot of the co-crystal of Model P from the simulation at 100 K and 600 K **(Figure 6.8)** shows phase separated crystals forming $NaClO_4$ ion-pair clusters

solvated in ADN solvent. Further, a normalized non-bonded potential energy profile, E_{nb} *vs.* Temperature **(Figure 6.9)** shows that the interionic interactions (Na^+--- ClO_4^-) are weaker compared to ion-solvent interactions (Na^+/ClO_4^- --- ADN). The binding energy between Na^+ ions and six ADN molecules was also calculated using DFT for the octahedral Na-$(ADN)_6$ structure in the gas phase to compare the magnitude of interactions between Na^+ ions and ADN. The structure shows the Na^+-N(ADN) distance to be 2.54 Å (compared with a Na^+-N(ADN) distance of 2.48 Å from solid state XRD data). The calculated binding energy for this system was - 400 kJ/mol, which is roughly twice the E_{nb} calculated from MD simulations for the solid-state structure at the room temperature. This difference can be attributed to the fact that in the solid-state structure an ADN molecule shares two sodium ions. Further, as the system disintegrates, around 550 K, a significant change in these interactions occurs at 555 K, the interionic interactions grow stronger, suggesting formation of $NaClO_4$ clusters (which can also be inferred from **Figure 6.8**), while ion-solvent interactions weaken. The calculations also show that between ion-solvent interactions, cation-solvent interactions are stronger compared to anion-solvent interactions.

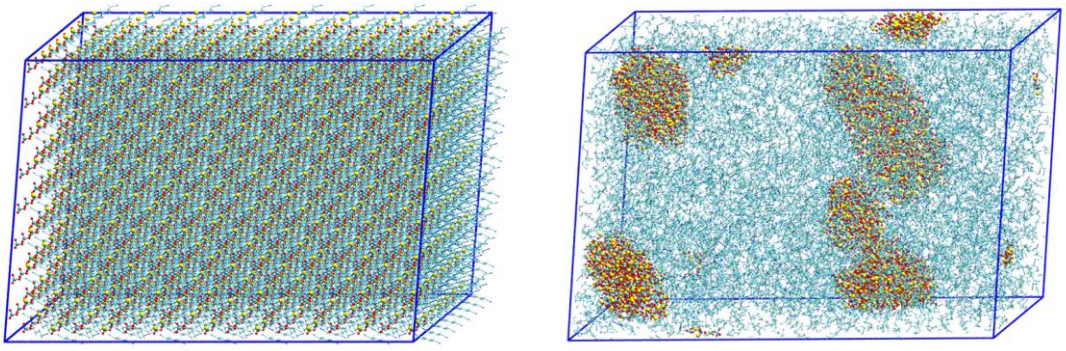

Figure 6.8. Snapshots of equilibrated **model P** at 100K **(left)** and 600 K **(right)**. Blue/cyan stick = ADN, yellow = Na^+, green = Cl, red = O.

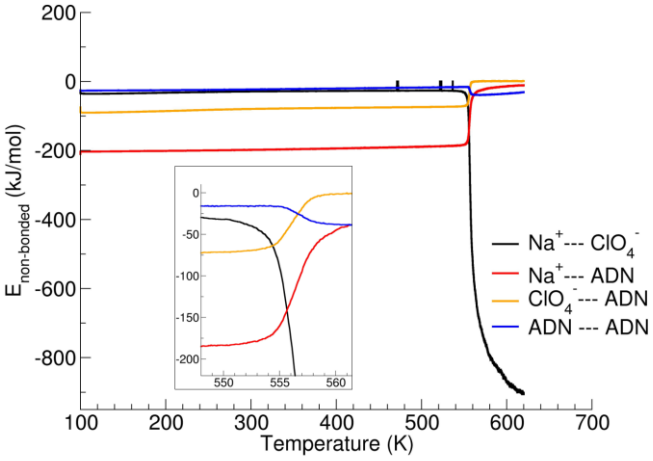

Figure 6.9. Non-bonded interaction energies of Na^+, ClO_4^- and ADN residues during simulated heating of **model P**.

Atomistic modeling of surface effects in the cocrystals is important to understand the structure at the surface and its role in melting, grain-boundary ion transport, and to interpret the two-step weight loss of ADN observed in the TGA data. When the crystal is exposed to vacuum (Model V), the conditions are very similar to the experimental conditions in the TGA experiments in which ADN is continually removed as dry N_2 is passed over the sample.

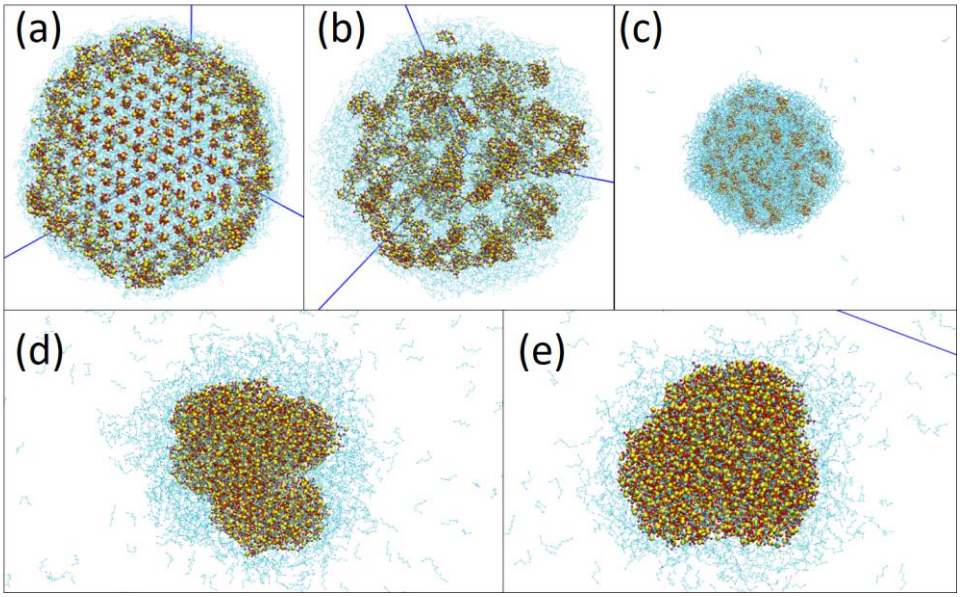

Figure 6.10. Snapshot of **model V** at temperatures **(a)** 298 K, **(b)** 363 K, **(c)** 400 K, **(d)** 600 K, **(e)** 700 K.

To understand these different structural properties, heating simulations were performed on model V at a heating rate of 20 K/ns from 300 K to 700 K. After this heating, different temperature points (298 K, 323K, 343 K, 363 K, 400 K, 500 K, 600 K and 700 K) were also simulated for a timescale of 20 ns under *NpT* conditions to see the equilibrium configurations at these temperatures. The simulations predict that the cocrystals exhibit a liquid-like layer at the surface at room temperature **(Figure 6.10a)**, as observed in the experiment **(Figure 6.3)**. Further, at 363 K **(Figure 6.10b)**, model V shows melted cocrystals which have Na^+ and ClO_4^- ions solvated irregularly in ADN. This is similar to the experimental melting temperature of 358 K. Around 413 K **(Figure 6.10c)**, ADN molecules start evaporating irreversibly from the system concomitant with the formation of $NaClO_4$ clusters. This is similar to the experimental decomposition onset of about 423 K **(Figure 6.2a)**. Both these processes continue until the temperature reaches about 600 K **(Figure 6.10d)** at which point, mainly $NaClO_4$ clusters are observed surrounded by a thin layer of and, similar to the experimental decomposition end-temperature of about 570 K **(Figure 6.2a)** at which point formation of $NaClO_4$(s) is observed between grains based on SEM/EDS **(Figure 6.3a, Figure E3)**. This thin solvent layer remains even after a simulation of 20 ns at 600 K. At 700 K **(Figure 6.10e)**, very few ADN molecules remain in contact with $NaClO_4$ clusters.

Based on these observations, the thermal behavior of the cocrystals can be divided into 4 temperature domains: (A): Where a liquid-like layer exists surrounding a crystalline lattice, in particular, the ADN molecules that are in proximity to the Na (298 K); (B): Where the cocrystals melt and ions remain solvated by ADN (363 K), which is correlated to the melting signature observed in DSC (358 K, **Figure 6.2b**); (C): Where $NaClO_4$ starts forming as clusters leading to evaporation of ADN (413 K), consistent with the onset of decomposition by TGA (423 K, **Figure 6.2a**); (D): Where disintegration of ADN from remaining solvated clusters gradually increases (until 600 K) and; (E): Where there is complete removal of ADN (700 K), corresponding to the completion of decomposition in TGA (623 K, **Figure 6.2a**). From step D to E, the

ADN molecules that are in proximity to the $NaClO_4$ clusters experience Na^+/ClO_4^- --- ADN interactions and therefore are removed at higher temperatures compared with ADN that is not interacting with the cluster. Thus, the non-interacting ADN molecules are removed at a similar temperature as neat ADN. Further, a number density calculation for ADN in box slices perpendicular to the z-axis also gives a quantitative idea of the distribution of ADN in the box as a function of temperature **(Figure E8)**. At room temperature, the bulk of cocrystals have a number density of 3 to 6 ADN per nm^3, which changes at high temperatures as shown in the number density profile. The profile also shows a high number of ADN molecules close to the center (where $NaClO_4$ forms clusters) at 500 K. Although at 600 K, many ADN molecules evaporate and leave the supercell space, there remains a particle density of 0.4 to 0.6 ADN per nm^3, with the ADN molecules mostly present at the surface of $NaClO_4$ clusters (as seen in snapshot in **Figure 6.10d**. Further, the number of ADN close to the $NaClO_4$ cluster becomes negligible at 700 K (and above) indicating almost a complete removal of ADN from supercell space.

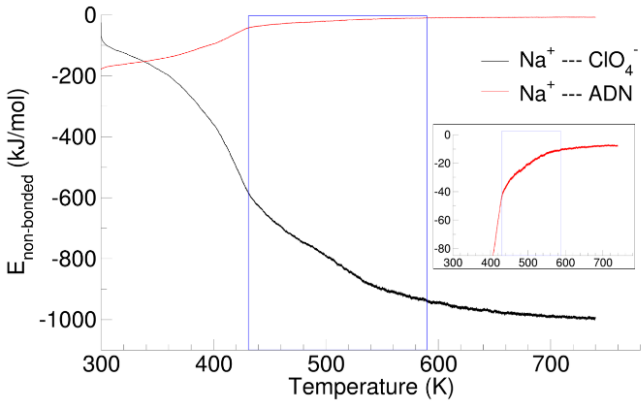

Figure 6.11. Non-bonded interaction energies of Na^+ ions with ClO_4^- and ADN residues during simulated heating of **model V**. Inset shows Na^+ --- ADN interactions in zoom.

The two-step removal of ADN from cocrystals can also be represented by non-bonded interaction energies calculated from the trajectory of heating simulation **(Figure 6.11)**. The E_{nb} for Na^+ --- ADN shows three regions of increase with

temperature: first a rapid increase close to the first disintegration of ADN from the supercell; then a gradual increase from 420 K to 600 K; and finally, a plateau after 600 K. This profile mirrors the TGA experiment in **Figure 6.2a** remarkably well, and explains the two-step nature of the gradual ADN removal as observed from the TGA experiments. The calculated value of E_{nb} for Na^+---ADN from MD simulations in both the models (P and V) at room temperature is 175 – 190 kJ·mol^{-1} which is similar to the gas phase solvation energy of Na^+ in ADN (186 kJ·mol^{-1}) from DFT calculations by Okoshi et al [214].

6.3.4 Dynamics from classical MD simulations

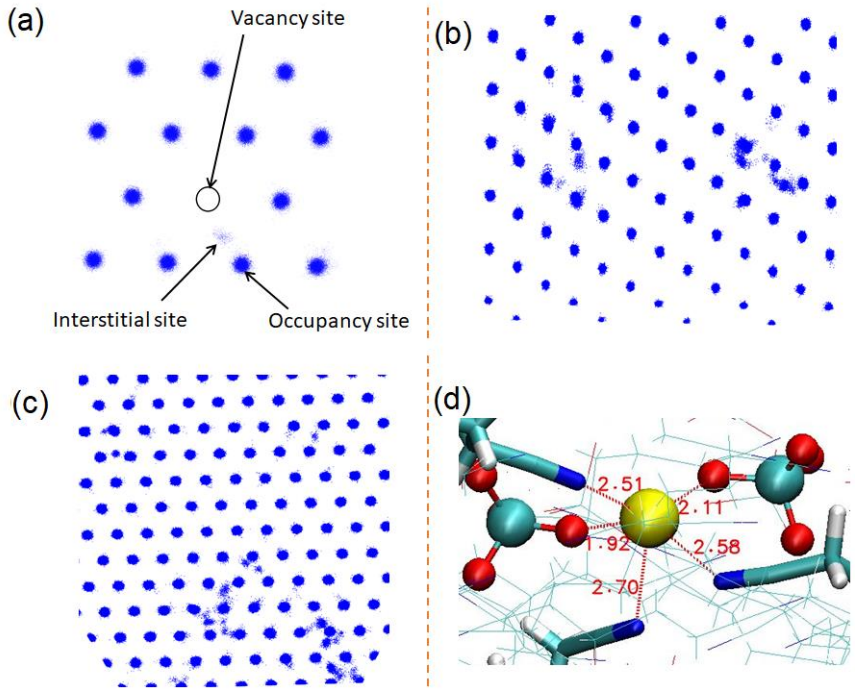

Figure 6.12. Na^+ trajectory map in **model D** at 323 K, illustrating individual Na^+ hopping events via an interstitial, perchlorate-bound site. **(a)** Definitions of occupancy site, vacancy site and interstitial site in reference to Na^+ and ClO_4^- ion defected supercell; Trajectory map for Na^+ ions during production simulations at 423 K, **(b)** in yz-plane and **(c)** in xy-plane; **(d)** Local geometry of one of the interstitial sites which shows Na^+ coordination with two perchlorate anions and three ADN molecules.

Classical MD simulations, or even *ab-initio* simulations fail to observe ion migration events responsible for ionic conduction due to the requirement of impractically long timescales at room temperature. Two unique approaches are

employed to calculate the diffusion coefficient of Na^+ ions and the activation energy barrier for conduction.

In the first approach, a model *D* is used (contains four Schottky defect pairs of missing Na^+ and ClO_4^-) to estimate the barrier of jumps from occupied sites to interstitial dislocations at high temperatures. Two limitations are noted: first, that the ions in bulk do not obey linearity in MSD *vs.* time at lower temperatures, and second, that the supercell shows the disintegration of ADN at high temperatures (above melting). Due to these limitations, the simulations to calculate MSD in these supercells were performed only at two temperatures, 423 K and 453 K. A map of the Na^+ locations for a period of 5ns (200 frames per ns) at 423 K **(Figure 6.12)** shows the interstitial dislocations/movement of Na^+ ions at a few sites. These Na^+ ions occupy the interstitial space even sometimes jump to the nearby vacancy. The ions which hop or move interstitially were mainly present in the channels with a distance of 8.33 Å from the vacancy site. This suggests that the 8.33 Å channel contributes directly towards the ion hopping in the system. This initial guess later helped in designing the reaction paths for nudged elastic band (NEB) calculations using DFT (vide infra). Simulations lacking Schottky defects were not observed to exhibit any ion diffusion.

The interstitially dislocated Na^+ ions were selected to calculate the diffusion coefficient of the Na^+ ions. The model D approach has shortcomings, in particular, i) the small (< 10) sample size of Na^+ ions used for the MSD calculations, and ii) the use of only two temperatures to obtain the activation energy (E_a) for diffusion from the Arrhenius law; more temperatures between 423 K and 453 K were not possible due to the allowed thermal fluctuations in the theoretical thermostat. Despite these limitations, the MSD *vs.* time plot **(Figure 6.13)** is roughly linear and the calculated E_a from this data are in the correct order of magnitude for $(ADN)_3NaClO_4$: 48 ± 7 $kJ \cdot mol^{-1}$ (from temperature dependent conductivity, $E_a = 36.6\ kJ \cdot mol^{-1}$). The values of the diffusion coefficient are provided in **Table E1**.

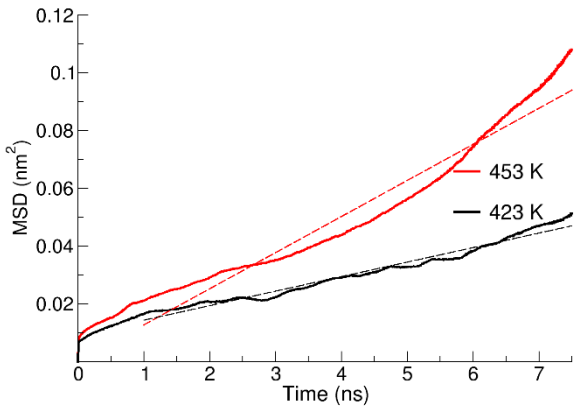

Figure 6.13. MSD vs. time plot for Na^+ ions dislocated in **model D**.

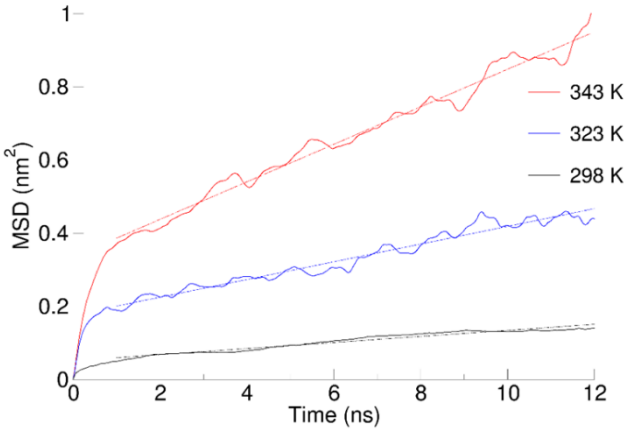

Figure 6.14. MSD vs. time plot for Na^+ ions present at the surface calculated from simulations on **model V**.

In the second approach, the diffusion coefficient of Na^+ ions was calculated using model V for the Na^+ ions present at the surface (since surface ions in such cocrystals are known to have high mobility due to liquid-like layer, compared to bulk[201]). In this approach, model V was equilibrated for 20 ns under *NVT* conditions at three temperatures: 298 K, 323 K and 343 K. The MSD of the Na^+ ions at the surface was calculated from another trajectory of 15 ns **(Figure 6.14)**. The calculated E_a barrier for Na^+ ion conduction from this model was 35 ± 4 kJ·mol^{-1}. The E_a barrier calculated from model V is slightly lower than the one calculated from model D, and hence is closer to the experimental value calculated from the Arrhenius plots of conduction.

The lower value of E_a for surface ions (model V) compared to interstitial ions (model D) shows that the low grain boundary resistance may be a dominant factor in the overall conductivity of the cocrystals. The output configuration of the trajectory (last frame) and calculated diffusion coefficients are provided in **Table E1**.

6.3.5 Mechanism and activation barrier of bulk-phase Na^+ ion conduction from DFT calculations

The trajectory analysis from MD simulations emphasizes the role of interstitial dislocations and defects in the diffusion of the Na^+ ions. However, an atomistic understanding of the ion transport in the channels is poorly illustrated by MD due to the classical nature of the simulations. To examine the mechanism in further detail and to extrapolate the path of ion transport, PWDFT calculations were employed to calculate a theoretical path and corresponding barrier of Na^+ ion conduction. The calculations were also performed on 3x1x1 supercell for longer path distances (11.26 Å), i.e., paths not involving interstitial dislocations, but the observed E_a barriers were roughly an order of magnitude larger compared to E_a determined from experiment **(Figure E12)**. Hence, discussion of these paths is neglected here and further discussion is focused on the 1x1x2 supercell. The supercell (replicated using the dimensions and coordinates of the unit cell obtained from a variable cell relaxation performed on the experimental unit cell) was first relaxed under fixed volume condition. Several Na^+ ion vacancy supercells (323 atoms, charge = -1.0 e^-) were created from this supercell and reoptimized. These optimized supercells with defects were used as reactant and product pairs (initial and final images) to calculate MEP. After achieving a fast convergence without NEB method for the first few steps of the calculations, CI-NEB was employed with a more accurate threshold (0.01 eV-$Bohr^{-1}$) of convergence to achieve precise MEP. First, all the possible ion-jump combinations through a linear path (path length = 8.33 Å) were attempted for MEP. The 1x1x2 supercell showed a Na^+-ion transport path via an anion-solvent assisted transition state analogous to that observed in the MD simulations, where two solvent CN groups and one O(ClO_4^-) facilitate the jump of Na^+ ion from regular octahedral sites to the octahedral vacancy

site **(Figure 6.15)**. The calculated barrier for this jump was 71 kJ·mol^{-1}, which is higher than the observed experimental barrier from impedance measurements, but within the same order of magnitude. Although the images were also corrected manually to check for possible alternate paths, manual inputs did not reduce the barrier further. The presence of arrays of Na^+ ions at 8.33 Å in three directions suggests the material to be a 3D conductor.

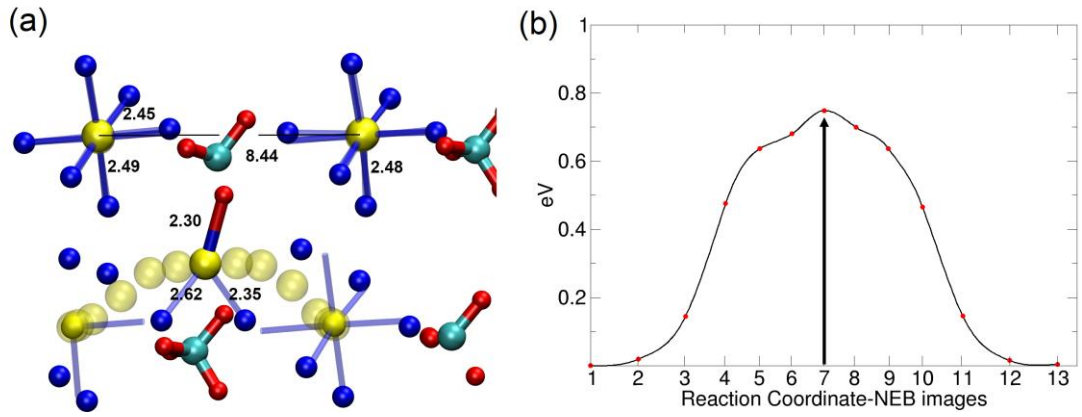

Figure 6.15. (a) MEP for Na^+ ion conduction in a 1x1x2 supercell showing the transition state geometry, Colors, blue: N, red: O, yellow: Na, opaque: transition state, transparent: initial, final and all the steps in between; distances are shown in Å **(b)** Calculated barrier for Na^+ ion conduction.

The approach to use classical MD simulations and DFT-NEB calculations in combination is a necessary requirement and prominent feature of the theoretical part of this work. Classical and DFT-MD simulations have been a more obvious choice in the case of liquid electrolytes [215, 216]. Since the thermal behavior and complex relationship of atomic interactions in these cocrystals cannot be understood using small scale simulations, classical MD simulations become a necessary choice. On the other hand, atomistic mechanisms from NEB calculations alone were not sufficient to predict the interstitial dislocations. The NEB method is often successfully used to calculate barriers of ion transport in garnets [217], other solid electrolytes [218] and cathode materials [219], which usually have a smaller, approximately linear path

length of 5 Å at maximum. Such short paths and slightly non-linear migration paths of the ions require no/little manual/intuitive correction, but the co-crystal in this study had longer (the shortest was 8.33 Å) and curved paths which do not optimize well even with CI-NEB and lead to an overestimated barrier compared to experiments. The NEB calculations explain the role of the anion during cation migration across the supercell. Such insights can be helpful in guiding the design of crystals where the role of anions in cation migration can be further minimized, and which may result in an improved ionic conductivity and higher cation transference numbers.

6.4 CONCLUSIONS

A number of desirable properties for solid electrolytes $(ADN)_3NaClO_4$ are manifest: 1) melt-castability originating from a melting point well below the decomposition temperature; 2) an intrinsic grain-binding nano-liquid layer that permits press-casting (or melt-casting) into conductive pellets; 3) reasonable conductivity for an organic solid electrolyte; 4) high t_{Na^+}. 4) sufficient electrode stability for half-cell cycling experiments (though the perchlorate anion appears to degrade the electrode). The best composition was that of the unrinsed cocrystal containing surface nanoliquid ionic solutions that bind the cocrystals together creating a contiguous network, and which gave a conductivity of 3 x 10^{-4} $S \cdot cm^{-1}$ at room temperature. The electrolyte's conductivity behavior is superior to that of typical solid organic electrolytes (such as polymers), and is well behaved over the range of operation expected of batteries in habitable climates (~ -30-40 °C), though their conductivity does not meet the standards of current liquid electrolyte technologies. By the application of MD simulations and DFT, a molecular-scale view of the surface nanoliquid, and the melting and decomposition is observed, and matches well to experimental observations of these events. Further, a likely ion migration mechanism is identified. Direct migration to vacant sites through a single ion hop is ruled out by DFT via an unreasonably high activation barrier an order of magnitude higher than experiment. A more likely interstitial ion-migration mechanism is identified by MD simulation involving

migration to an interstitial site, followed by a perchlorate-assisted transition to a neighboring site. This mechanism has an activation barrier similar to experiment based on MD simulation, but somewhat higher (about 2x) when calculated using DFT. However, this latter discrepancy is attributed to the large ion migration distance calculated, which may not be suitable for the NEB approaches employed for accurate quantitation of activation barriers. Nevertheless, the reasonable match between activation energy from DFT and MD, and the accurate physical property prediction from MD and DFT on the behavior of the bulk and surface of the nanocrystal give confidence that theory provides a sound molecular level understanding of the macroscopic properties of this electrolyte.

——*——*——

The content of this chapter and associated content in Appendix E are adapted from "Experimental and theoretical investigation of the ion conduction mechanism of tris(adiponitrile)perchloratosodium, a self-binding, melt-castable crystalline sodium electrolyte."

Chem. Mater. ***2019,*** *Just Accepted,*

https://doi.org/10.1021/acs.chemmater.9b02853

Chapter 7:
Thermal Stability and Electrochemical Properties of the Cocrystalline Electrolyte of Adiponitrile and $LiPF_6$

This chapter contains results and discussions from experiments which were performed in part by the collaborators to this work from Dr. Zdilla and Dr. Wunder's lab at Temple University.

7.1 INTRODUCTION

In this chapter, experimental and theoretical investigations on an adiponitrile cosolvent based cocrystalline electrolyte of lithium hexafluorophosphate, $(ADN)_2LiPF_6$, are presented. The investigation of lithium ion conducting ceramics has yielded a wide range of oxide and sulfide-based materials [220] that are under active investigation as solid electrolytes for LIB. While these can have good ionic conductivities (σ) and lithium-ion transference numbers (t_{Li^+}), there are still problems associated with dendrite growth and poor interfacial contact with the electrodes. Similar to lithium ion conducting ceramics (LICC), the soft-solid cocrystals have channels for ion migration but are not necessarily single-ion conductors. Unlike the rigid anionic lattices of ceramic electrolytes, the channels in the cocrytsals consist of the organic molecules, and there are no Li···anion contacts [221]. Solvates of lithium salts with polyethylene oxide (PEO) [222, 223] or glymes, $CH_3O\text{-}(CH_2CH_2O)_{n=1\text{-}5}\text{-}CH_3$, [224, 225] have been used for determination of the coordination of the lithium ions in the solution state, but some of these crystalline solvates have ionic conductivities higher than the molten

materials [223]. Nevertheless, ionic conductivities are very low ($\sigma \sim 10^{-7}$ S cm^{-1} for PEO solvates [223–226] and $\sigma \sim 10^{-6}$ S cm^{-1} for glyme solvates [225]) due to the tight coordination of the "hard" ether oxygens of with the "hard" Li^+ ions. However, the cocrystalline electrolytes do not possess hard interactions, as seen with the examples discussed in previous chapters.

The components of $(ADN)_2LiPF_6$ cocrystals, $LiPF_6$ and ADN, have been extensively used in liquid or polymeric electrolyte systems. $LiPF_6$ is used in most commercial LIBs despite its poor thermal stability and its tendency towards the formation of HF from decomposition reactions. The most studied, more thermally stable replacement salt, LiTFSI, has limited use since it is known to be corrosive to the aluminum current-collectors for the cathodes [227]. Polar nitrile or cyano (-C≡N) groups, with high dipole moments and dielectric constants of ~ 30, have been investigated to solvate lithium ions instead of the ether oxygens of polyethylene oxide (PEO) or glymes. Recent reviews have focused on their incorporation as functional groups in liquids, plasticizers, plastic crystals (particularly succinonitrile (SN) [228, 229]), gels (e.g., polyacrylonitrile (PAN) [230–239]), PAN polymer-in-salt [240–243] and solid electrolytes used for LIB applications [244]. These materials often have high anodic oxidation potentials (> 4.5 V *vs.* Li^+/Li) and are thus resistant to electrochemical oxidation [245, 246] and therefore have the potential to be used with high voltage cathodes [247–249], e.g., Li[Mn, Ni, Co]O_2. ADN has also been shown to enable the use of high voltage cathodes when added in small amounts (1%) to other electrolyte solutions, by film formation [79] or strong coordination between the Ni^{4+} on N-rich cathode surfaces and the nitrile groups [250]. However, they suffer from poor reductive stability (so that they spontaneously react with Li metal, the Li^+ ion cannot be reversibly intercalated into graphite, and stable SEIs do not form) [246], but can be used with $Li_4Ti_5O_{12}$ (1.55 V vs Li^+/Li) anodes [229, 251], or with graphitic anodes by addition of SEI forming co-solvents [77, 245]. More recently, it was shown that low concentrations of ADN (1%) in mixed electrolytes formed stable SEIs on Li^0

metal [250]. Interestingly, and of importance for the current work, the reductive stability of acetonitrile (AN) was improved in concentrated (> 4 M) salt solutions, since all of the acetonitrile molecules were coordinated to Li^+ ions [252]. In dilute solution, free AN were in the lowest unoccupied molecular orbital (LUMO) in the conduction band, while in superconcentrated solutions, the PF_6^- anions occupied the LUMO and so were reduced instead [252].

The $(ADN)_2LiPF_6$ cocrystals are also of interest due their mechanism of conduction. For polymer electrolytes above T_g the diffusion of the Li^+ ions is coupled to the slow backbone dynamics of the polymer chain [253]. In organic solvents, there is a vehicular diffusion mechanism of solvated Li ions [254]. In both cases, the fluidity of the matrices often results in linear diffusion and MD simulations become useful for the calculation of the diffusion coefficient, *D*. In the cases where polymer electrolytes solidify, a high temperature MD simulation is often used to estimate ion mobility precisely. Inorganic solid electrolytes (e.g., LISICON, garnets) usually possess a strongly bonded, thermally stable sublattice of the anionic component of the electrolyte, and a mobile sublattice of Li^+ ions. Li migration occurs through jumps between vacancies or interstitial sites [87]. The fixed anion lattice enables MD simulations to predict super-diffusive cage vibrations, jumps among occupancy sites and superionic diffusion with increasing temperatures. In contrast to all the above cases, the family of co-crystalline electrolytes does not offer fluidity at increased temperatures (since decomposition occurs), jumps at short time scale or a comparatively more stable anionic sublattice. Unlike the case of polymer electrolytes, MD simulations fail to obtain linear tracer diffusion (even with 100ns long trajectories). Further, ionic jumps do not occur as often in cocrystalline electrolytes since the distance between Li sites is large (6.4 Å). In the case of LISICON good jumping statistics can be achieved with short timescale simulations even without Schottky defects in the lattice.

7.2 EXPERIMENTAL DETAILS

7.2.1 Synthesis

$LiPF_6$ (Sigma-Aldrich) was dissolved in excess amounts of ADN (Sigma-Aldrich) by heating the mixture to 115 ^{0}C under an argon atmosphere. The $LiPF_6$ was not soluble in ADN at RT. Upon cooling, crystalline material started to form at about 115 ^{0}C and was complete at room temperature (RT). A single crystal was removed from the precipitate for structure determination, and the remaining powder was rinsed five times with excess Et_2O (distilled over sodium metal using a Schlenk line) and dried under vacuum for ~ 20 minutes to remove the residual amount of ADN and Et_2O, after which the co-crystal appeared dry. The co-crystal was incorporated into Whatman glass microfiber filters (GF), grade GF/A (Sigma-Aldrich) 0.26 mm thickness either by synthesizing the sample inside the glass fibers or by adding the sample and glass fiber filter into boiling DCM (40-45 ^{0}C), and then removing the DCM in vacuum. The co-crystal in the glass fiber filter was used as the separator between the electrodes to control the size and the amount of the electrolyte in the electrochemical experiments.

7.2.2 Characterization

The single-crystal structure was determined using Mo-K_α radiation and the powder X-ray diffraction data was obtained using a Kappa APEX II DUO X-ray diffractometer with Cu-K_α radiation at -170 K. The calculated powder pattern generated from the single crystal ($(ADN)_2LiPF_6$) data conformed with the experimental powder data and was used to validate all powder used in thermal and electrochemical studies.

Thermal degradation analysis of $(ADN)_2LiPF_6$ crystals was carried out on a Thermogravimetric Analysis (TGA) TA Instruments Hi-Res TGA 2950 at a ramp rate of 10 °C min^{-1} with a flow of ultra-pure N2 gas. A Differential Scanning Calorimeter (DSC) TA Instruments 2920 was used to analyze the melt and crystallization temperatures of the powder $(ADN)_2LiPF_6$, with the sample in hermetically sealed Tzero aluminum pans, from -120 °C to 120 °C at a scan rate of 10 °C.min^{-1}, under ultra-pure N2 purge. The second cycles of the ADN matrix and $(ADN)_2LiPF_6$ powder

were reported out of the two measured cycles. Scanning electron microscope (SEM) data were acquired on a FEI Quanta 450FEG SEM) with energy-dispersive X-ray spectroscopy (EDS) capability (Oxford Aztec Energy Advanced EDS System). Raman spectra were recorded in the 100-3000 cm^{-1} region at room temperature using a Horiba LabRAM HR Evolution Raman spectrometer, with a resolution of 1.8 cm^{-1}, excitation wavelength of 532 nm, 60 mW power, and a grating groove density of 600 gr/mm. Samples were measured with 8 acquisitions, and 2 to 8 seconds each, depending on peak intensity.

For the conductivity measurements, polycrystalline $(ADN)_2LiPF_6$ powder incorporated in the glass fiber separator or prepared by pressing at 800 psi in a hydraulic crimper in an argon purged glove box, was used. The conductivity measurements were acquired in a homemade electrochemical cell placed in a N_2 purged, temperature-controlled gas chromatography (GC) oven. Temperature-dependent bulk impedance data was measured by AC electrochemical impedance spectroscopy (EIS) using a Gamry Interface 1000 potentiostat/galvanostat/ZRA in the frequency range 0.1−1MHz in a temperature range between 80 ^{0}C and -10 ^{0}C with increments of 10 ^{0}C. The cell was thermally equilibrated for 30 minutes at each temperature before the bulk impedance was measured during both the cooling and heating cycles. Li^+ ion transference numbers were obtained by the method of combined AC and DC measurements [255, 256].

7.2.3 MD simulations

Force field parameters for bonded and Lennard Jones (vdW) interactions for ADN were taken from the OPLS all-atom force field [257]. The partial charges on all atoms of ADN were calculated from the MP2//aug-cc-PVDZ optimized structure using the CHELPG method[155]. Since the Li^+ ion is present in tetra coordination with ADN, the partial charge on Li^+ was calculated using the optimized structure of $[(ADN)_4Li]^+$ with a long range and dispersion corrected ωB97xD functional with 6-311++G(d,p)$_{optimization}$/aug-cc-PVDZ $_{charge\ calculation}$ basis set **(Figure F1)**. This

calculation suggested a partial charge of 0.845 e^- unit on the Li^+ ions **Table F1**. The charge value on the Li^+ ion (0.845) was used as the scaling factor to rescale the partial charges on PF_6^- ions (obtained from MP2//aug-cc-PVDZ calculations, separately). To compute theoretical Raman spectra for ADN and $(ADN)_2LiPF_6$, vibrational frequencies were calculated using PBE/6-311++G(d,p) for the structures optimized using the same functional/basis set. All the gas phase quantum chemistry calculations were carried out using the GAUSSIAN 9.0 software package [128]. Detailed protocol for force-field development is provided in the **Appendix F**.

A supercell of 5x5x5 unit cells (20,000 atoms) of $(ADN)_2LiPF_6$ was constructed in a cuboid with the dimensions of 55.35 x 64.75 x 63.25 $Å^3$. This model was used for simulations under periodic boundary conditions to represent the bulk phase, and hence, is designated as *model P*. However, since the surface atoms have a large contribution towards the conduction and decomposition of these co-crystalline electrolytes, a different *model V* was used to understand the structure, dynamics and thermal behavior at the surface. Model *V* was constructed by placing a 5x5x5 supercell in a cube of 200 Å/side. GROMACS 5.0.7 software [157] was used for simulations and analysis along with VMD 1.9.3 software [114] for visualization of trajectories. The supercell models were energy minimized using standard protocols and algorithms implemented in the code. All the simulations for model *P* were carried out using *NpT* ensemble conditions, while for model *V*, canonical ensemble conditions were used. Details of temperature and pressure couplings and other MD parameters can be found elsewhere [201].

7.2.4 Plane-wave periodic DFT calculations:

To examine the mechanism of conduction at the atomic level with precise energetics, PW-DFT calculations were performed using the QUANTUM ESPRESSO 6.1 software package [182]. PAW basis set (KJ) [184] was used with PBE pseudopotentials [183] with a cut-off of 60 Ry and 360 Ry for kinetic energy and electron density, respectively. A unit cell of $(ADN)_2LiPF_6$ cocrystals (from single-

crystal XRD data) was relaxed in a fixed volume box and later in a variable cell manner to energy minimize the crystal structure. A threshold of 10^{-7} Ry was used for electronic optimization and 10^{-3} Ry/Bohr for force minimization. **Table F2** shows a comparison of unit cell parameters obtained from single-crystal XRD data and variable cell relaxation DFT calculations. To investigate the path of Li^+ ion conduction in the cocrystal, 1x1x2, 3x1x1 and 2x1x2 supercells were created and optimized using the above discussed protocols. Due to the large system size of these supercells, all the calculations were performed with a Γ-only k-mesh. For every supercell, a pair of Li^+ ion-defected configurations was used as an initial and final image for NEB calculations to interpolate the MEP. Several sets of images were used to obtain the MEP, with a threshold of 0.1 eV/Bohr used for every individual image. Further, the MEP was refined using the climbing image (CI)-NEB method [185] with a more precise threshold of 0.01 eV/Bohr for every image along the path.

7.3 RESULTS AND DISCUSSION

7.3.1 Structure and thermal stability

The single-crystal structure shows that the stoichiometry consists of 2 moles of ADN to 1 mole of $LiPF_6$, $(ADN)_2LiPF_6$ **(Figure 7.1)** with linear parallel ionic channels of Li^+, where the distance between two successive Li^+ and PF_6^- ions are 6.23Å. Each Li ion is coordinated to 4 cyano groups, and not to any PF_6^- anions. The presence of Li^+ channels in the complex may allow migration of Li^+ in a low-affinity matrix. The experimentally obtained powder pattern of $(ADN)_2LiPF_6$ agrees with the powder XRD generated from the single crystal data **(Figure F2)**. Powder XRD data before and after conductivity measurements **(Figure F3)**, and whether pressed or prepared in glass fibers **(Figure F4)** are the same. The XRD data do not show the presence of ADN **(Figure F5).** The thermogravimetric analysis (TGA) data **(Figure 7.2a)** show that the stability of $LiPF_6$ is increased upon incorporation into the cocrystal, which infers that the stability of the cocrystal is determined by the ADN.

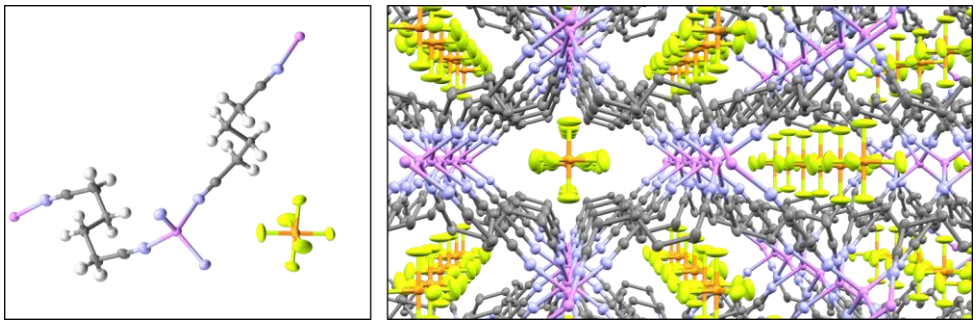

Figure 7.1. Stoichiometric representation of $(ADN)_2LiPF_6$ showing tetracoordinated Li^+ ions with ADN molecules where PF_6^- anions occupy the available interstitial space in the crystal structure **(left)**, and packing of $(ADN)_2LiPF_6$ showing the channels of Li^+ ions in the low affinity matrix in the crystal structure **(right)**. ● Gray- C; ● Purple- Li; ● Yellow- F; ● Orange- P; ● blue-N.

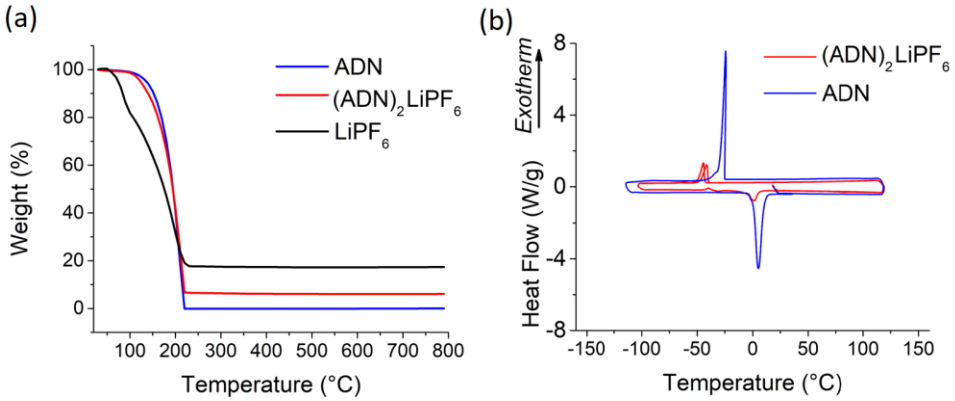

Figure 7.2. (a) TGA data of $(ADN)_2LiPF_6$, $LiPF_6$ and ADN; LiF remains at 800 ^{0}C, **(b)** DSC data of $(ADN)_2LiPF_6$ and ADN. Only the melt and crystallization of ADN is observed.

Differential scanning calorimetry (DSC) data **(Figure 7.2b)** show that the $(ADN)_2LiPF_6$ cocrystal itself does not melt before it decomposes. However, the DSC data indicate the presence of ADN in the cocrystal. Crystallization of the ADN occurs at approximately the same temperature as neat ADN, while crystallization occurs at slightly lower temperatures than neat ADN, suggesting confinement effects might play a role.

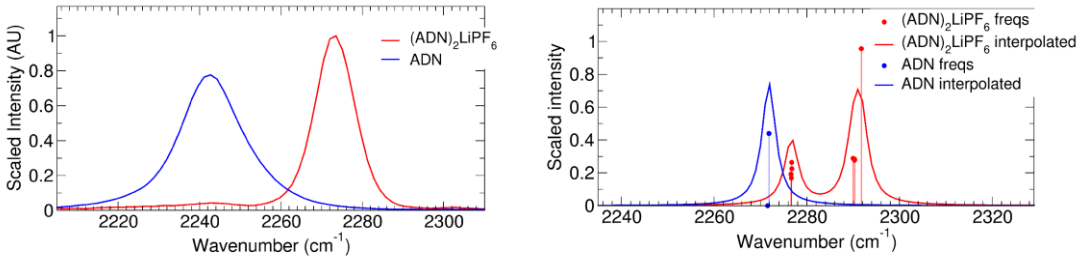

Figure 7.3. Raman spectra in the -C≡N region from experiment **(left),** and from DFT calculations **(right)**. In case of theoretical spectra, interpolated curves are generated by using 1.8 cm^{-1} of peak half-width at half height to the calculated vibrational frequencies.

The small amount of ADN in the $(ADN)_2LiPF_6$ cocrystal is also observed in the Raman spectra **(Figure 7.3)**. For pure ADN there is only a single peak at 2241.7 cm^{-1}, while for the cocrystal, there is a large peak at 2273.6 cm^{-1} and small peaks at 2242.7 cm^{-1}, attributed to the coordinated and free "terminal" C≡N ADN groups, respectively. In the case of the cocrystal, the dominance of the 2273.6 cm^{-1} peak compared with the very small peak at around 2242.7 cm^{-1} indicates that the majority of the ADN present is involved in coordinating the Li^+ ions with a small amount that are "free", as corroborated by the DSC data. The vibrational frequencies and Raman intensities calculated using DFT calculations (//PBE/6-311++G(d,p)) in the gas phase are ~ 30 cm^{-1} higher in wavenumber than the experimental spectra. Moreover, these calculations indicate that there are three frequencies for the dinitrile groups. The computed Raman spectra suggest that the "free" ADN may actually be molecules where only one C≡N is coordinated, i.e. at the crystal boundaries, where one of the ADN is coordinated to a Li^+ ion in the crystal structure and the C≡N at the other end is "dangling" at the interface. The computed Raman spectra also suggests that the net shift in terminal C≡N group *vs.* coordinated C≡N group in $[Li(ADN)_4]^+$ is 15 cm^{-1}. Also, wavenumber for terminal C≡N $[Li(ADN)_4]^+$ is red shifted by 5 cm^{-1} compared to a single ADN molecule. Experimental and computed frequencies are provided in **(Table F2)**

SEM images **(Figure F6)** were obtained for the pure polycrystalline $(ADN)_2LiPF_6$ powder (pressed pellet). EDX images of the grains and grain boundary regions show that the relative C and N peaks of the ADN are weaker compared with the F and P peaks of the $LiPF_6$ in the grain boundary region than in the grains. This suggests that the grain boundary region is fluid, and in the vacuum of the SEM the ADN is removed, leaving behind the $LiPF_6$ salt.

The conductivity data **(Figure 7.4a)** for a pressed pellet of $(ADN)_2LiPF_6$ in the temperature range between -10ºC and 80 ºC (below its degradation temperature), show a RT conductivity of about 10^{-4} S cm^{-1}, with an Arrhenius activation barrier of E_a = 37.2 kJ/mol. The complex impedance plots are semicircles with an associated capacitance of 1-2 pF/cm and a low frequency spike, indicating that the impedance is dominated by the bulk (intragrain boundary). The variation of the dc current as a function of time **(Figure 7.4b)** gave a lithium ion transference number of t_{Li}^{+} = 0.54.

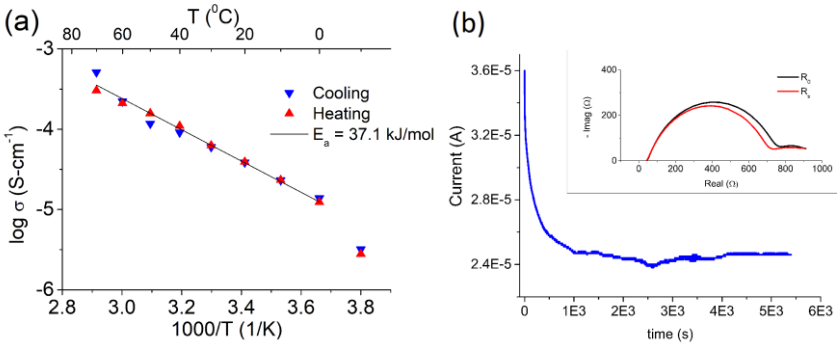

Figure 7.4. (a) Conductivity data of a pressed neat pellet of SS/$(ADN)_2LiPF_6$/SS, **(b)** Li^+ ion transference number (t^+_{Li}) measured after stabilization of the impedance; t^+_{Li} = 0.54.

7.3.2 MD simulations of structure and thermal stability

Structure from Model *P*: A supercell model *P* (125 unit cells, i.e. 20000 atoms), which represents the bulk phase of the $(ADN)_2LiPF_6$ cocrystals, was simulated under *NpT* conditions for a 20 ns equilibration at different constant temperatures ranging from 100 K to 550 K. **Figure F7** shows the final configurations of equilibrated systems at T = 100 K, 200 K, 298 K, 400 K and 500 K. The equilibrated configurations at 100

K, 200 K and 298 K show a structured array of Li---N(ADN) coordinated tetrahedral networks. A visual inspection of snapshots shows that these networks become irregular at 400 K (127 ^{0}C) and crystals completely deform at 500 K (227 ^{0} C), which is in agreement with the decomposition temperature window observed in the TGA data **(Figure 7.2a)**.

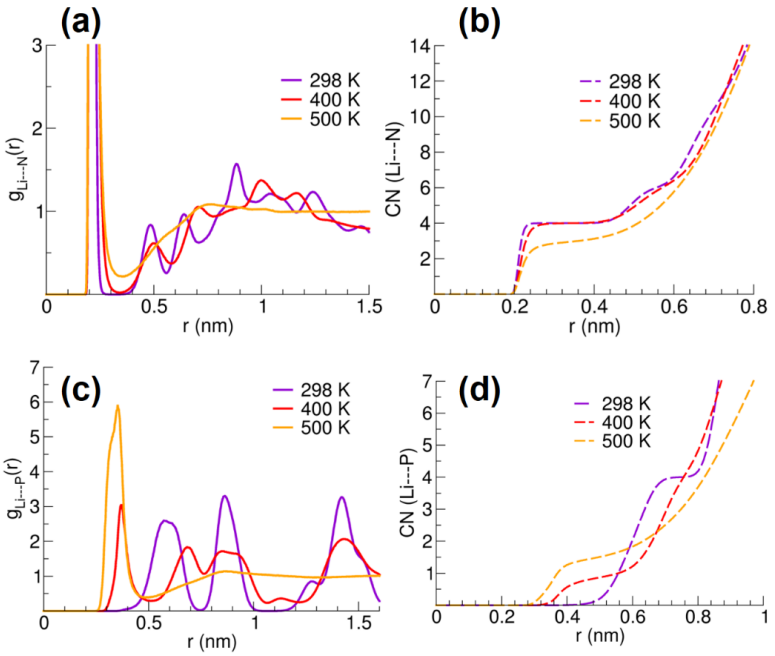

Figure 7.5. RDF and **(b)** coordination number for Li^{+}---N(ADN) pair interactions, **(c)** RDF and **(d)** coordination number for Li^{+}---P(PF_6^{-}) pair interactions, calculated from simulations on **model *P***. Solid lines represent RDF while dotted lines represent the corresponding coordination number as a function of distance.

To quantify the nature of interatomic interactions (interactions of Li^{+} ions with PF_6^{-} anions: interionic, and with ADN: ion-solvent) and crystal deformations, RDFs and coordination numbers for different atom-pair interactions were calculated **(Figure 7.5)**. For these calculations, the equilibrated model *P* was simulated for production under *NVT* ensemble conditions for 15 ns. The RDF calculated for Li^{+}---N(ADN) shows a first solvation shell of 4 N atoms around Li^{+} ions (at ~ 2 Å) from 100 K to 400 K. This agrees with the observed coordination of Li^{+} ions from XRD structure. Further, the RDF at 500 K shows a decrease in Li^{+} ion coordination with ADN, where the

calculated coordination number is less than three. In case of Li^+---$P(PF_6^-)$ RDF, the first solvation shell appears at 5.8 Å (larger than the Li^+---N distance) with a coordination number of 4, at low temperatures (100 K to 298 K). At 400 K and 500 K, PF_6^- anions form a smaller solvation shell (~ 3.6 Å) around Li^+, which indicates breakdown of the Li^+---ADN networks and replacement of ADN molecules by PF_6^- anions in the solvation sphere of Li^+ (i.e. formation of $LiPF_6$, since the Li---P distance in $LiPF_6$ crystals is 3.6 Å [258]). The structural analysis from RDFs suggests that the co-crystalline structure changes from completely ordered to solvated/separated ion-clusters in ADN in the temperature range 450 K - 500 K.

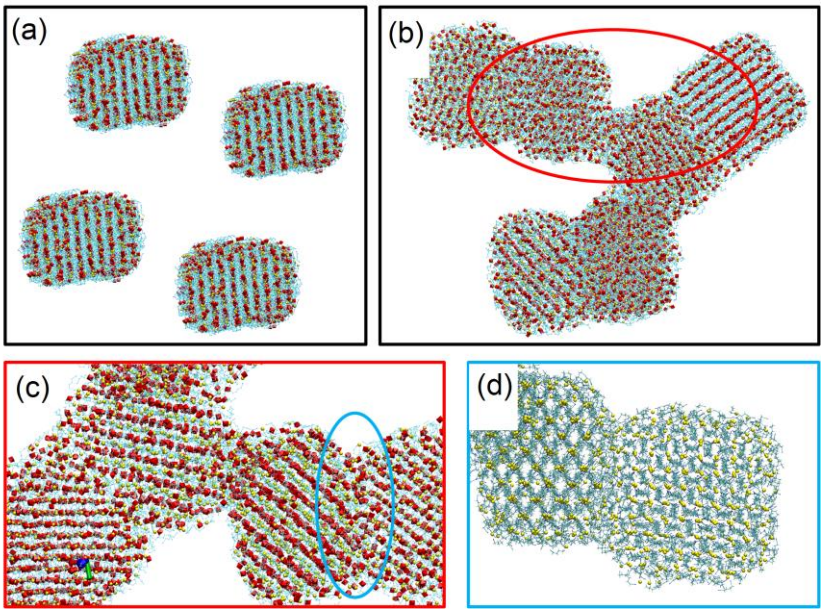

Figure 7.6. Snapshots from simulations on **model V_8** under *NVT* ensemble, at **(a)** t = 0, only the four grains in the front are visible- the other four grains are behind, **(b)** t = 10 ns, **(c)** a zoomed in view to the multiple grain boundaries at t = 10 ns, **(d)** a further zoom in to a grain boundary, where ion channels in bulk are unperturbed, while surface and interfacial region shows disordered ions. System size: 160,000 atoms.

Structure at grain boundary from model *V*: To simulate the intergranular interface, eight nano-sized grains were (1 grain = 5x5x5 unit cells) simulated in a box of 30x30x30 nm^3 as model V_8 **(Figure 7.6a)**. The simulation conditions of model V_8 were very similar to model V (e.g., *NVT* ensemble, presence of large vacuum). At t = 0, it was ensured that every grain was completely non-interactive with each other (initial

contact distance between the grains > cut-off distances for potential energy). The simulations show that within a span of few nanoseconds, the grains interact at the surface and form an interfacial layer **(Figure 7.6b)**. This interfacial layer does not depend on the orientation of the grains or the size of the box, which implies that the formation of intergranular interface does not depend on the crystal faces. **Figure 7.6c** and **7.6d** show a zoomed in view of the grain boundary of a few grains, where the ions present in the bulk remain unaffected in their relative orientation (solid-like) while ions at the interface can be seen to be perturbed. The presence of disordered ions at the interface contribute to low grain boundary resistance, since ionic jumps are not required in these regions due to removal of all structural constraints.

Thermal Stability from model *V*: Since the TGA shows that $(ADN)_2LiPF_6$ cocrystals start decomposing around 100 ^{0}C followed by complete removal of ADN from the cocrystals at 200 ^{0}C, model *V* is used to mimic the decomposition of the cocrystals. Model *V*, which contains 125 unit-cells of cocrystals in a vacuum, was heated from 100 K to 600 K under *NVT* ensemble with a constant heating rate of 20 K/ns. To understand the effect of heating, the non-bonded potential energy (Lennard Jones + Coulombic) of Li^+ ions with PF_6^- and ADN was calculated. The calculated non-bonded energies **(Figure 7.7a)** were normalized to the system size to compare the values across interactions. The change in ion-solvent (Li^+---ADN) *vs.* interionic (Li^+---PF_6^-) interactions during thermal heating of the cocrystals can be understood as follows:

a) From T = 100 K and 350 K, E_{nb} for Li^+---ADN remains almost constant (-65 kJ/mol), while E_{nb} for Li^+---PF_6^- slightly increases (which implies a decrease in cation-anion interaction) from -130 kJ/mol to -120 kJ/mol.

b) From T = 370 K to 420 K, the interactions show an opposite behavior, i.e., E_{nb} for Li^+---ADN increases (which implies a decrease in ion-solvent interaction) and E_{nb} for Li^+---PF_6^- decreases (stronger cation-anion interactions). This suggests the formation of $LiPF_6$ and removal of ADN from the cocrystals as they decompose. The

formation of $LiPF_6$ here, as seen from the extent of more negative E_{nb} for Li^+---PF_6^-, is also supported by an increase in PF_6^- ions in the solvation sphere of Li^+ as observed in the case of model *P* at 400 K **(Figure 7.5d)**.

c) At T > 420 K, the interionic interactions grow stronger and allude to the formation of more $LiPF_6$ as more ADN leaves the cocrystals.

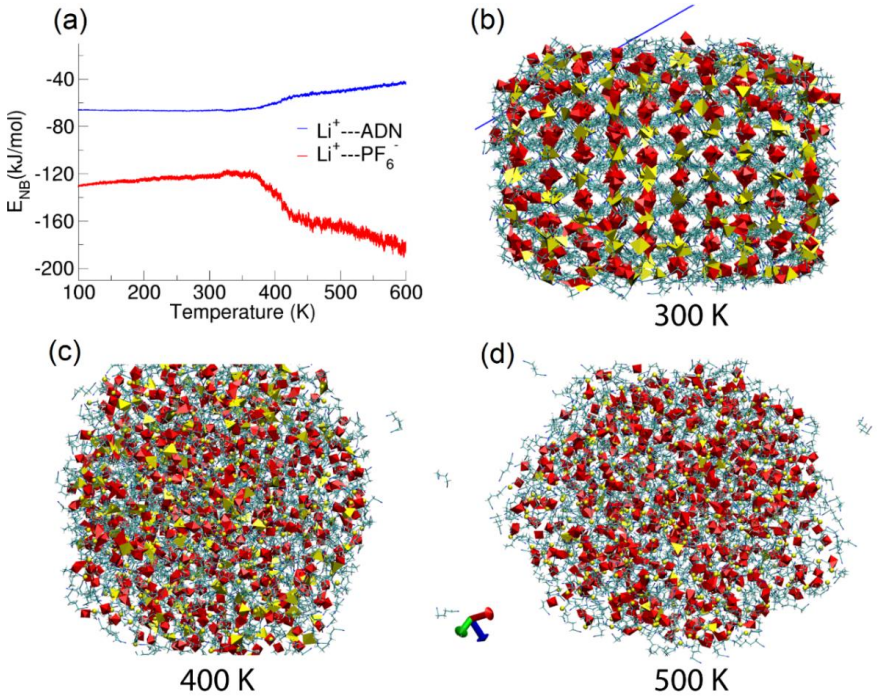

Figure 7.7. (a) Non-bonded interaction energy *vs.* temperature during the simulated heating of $(ADN)_2LiPF_6$ cocrystals in **model *V***; Snapshots of $(ADN)_2LiPF_6$ cocrystals after an equilibration of 10 ns (every temperature) using **model *V*** at **(b)** 300 K, **(c)** 400 K and **(d)** 500 K. Li---N(ADN) coordinated networks are shown as yellow tetrahedrons and PF_6^- anions are shown as red octahedrons. ADN solvent is shown as line representations.

The E_{nb} analysis suggests that the decomposition starts around T = 370 K, which is in good agreement with the T_d observed from the TGA data. Further, the complete removal of ADN from the cocrystals (which happens at 200 ^{0}C as seen from TGA data) was not observed from model *V* even at 600 K, within the timescales of the simulations. One reason may be that the TGA data was obtained with continuous removal of ADN from the samples during the constant N_2 purge. Additionally, 10 ns long *NVT* simulations on model *V* at T = 300 K, 400 K and 500 K were performed for

a visual inspection of the decomposition of the cocrystals. **Figure 7.7b** shows that the cocrystals at room temperature possess a liquid-like surface layer similar to other electrolytes, discussed in the previous chapters. At 400 K, removal of ADN molecules from the cocrystals can be observed **(Figure 7.7c)**. At 500 K, many ADN molecules leave the cocrystal and the Li^+---ADN tetrahedral networks completely collapse leading to the formation of $Li^+PF_6^-$ clusters which appear to be surrounded by remaining unevaporated ADN molecules **(Figure 7.7d)**. Although during the timescale of the simulations (10 ns) complete evaporation of ADN cannot be observed, the disappearance of the Li^+---ADN networks suggests the decomposition of the cocrystals. At T = 300K (and T > T_d) it is observed that the surface of cocrystals is liquid like, which is also seen from SEM in this electrolyte, and a characteristic to this class of electrolytes.

7.3.3 MD simulations of ion transport

Model *P*: Ion transport can be quantified by a calculation of diffusion coefficients from MD simulations using the Einstein's relationship. However, in solid electrolytes and other polymer electrolytes which form glasses at low temperature, the linearity of MSD with time is extremely difficult to obtain due to slow mobility. A generalized relation for change in MSD can be expressed as:

$$\log(\mathrm{MSD}) \propto \log t^{\alpha} \tag{7.1}$$

where $\alpha > 1$ suggests a super-diffusive (ballistic) mobility, $\alpha < 1$ suggests sub-diffusive mobility, and $\alpha = 1$ suggests linear-diffusive mobility where the Einstein's relation is applicable. A non-linearity in the diffusion limits the typical approaches used for the calculation of diffusion coefficients in solids and polymers below their glass transition temperatures (T_gs).

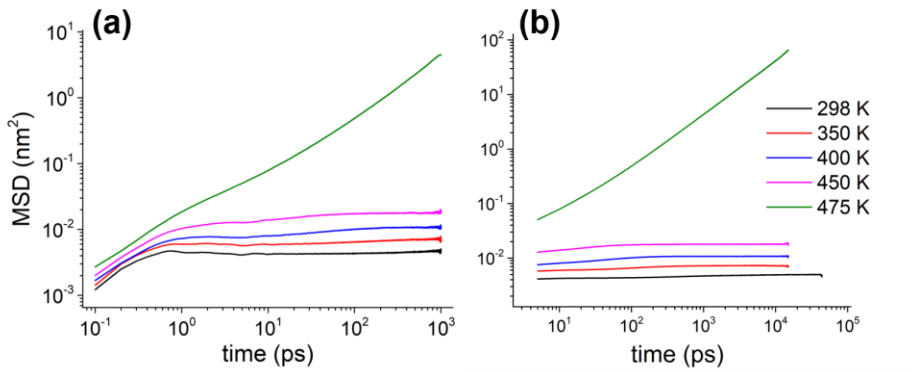

Figure 7.8. MSD *vs.* time plotted on a log scale for Li^+ ions in $(ADN)_2LiPF_6$ cocrystals simulated as **model P** using **(a)** fine step-size of 0.1 ps for short time scale (10^3 ps), and **(b)** regular step-size of 5 ps for long timescales (10^4-10^5 ps) at different temperatures.

The family of co-crystalline electrolytes forms a more stable cationic sublattice in contrast to anionic sublattices formed in LISICON, garnets, ceramics and cathode materials. In the present case, Li^+ ions form much stronger tetrahedral networks with N atoms of ADN (cage traps) while anions occupy a more flexible region of crystal space. Hence, high temperature simulation does not produce good statistics for jumps or even superionic diffusion. A series of *NVT* simulations were also performed on model *P* from 298 K to 475 K at two different timescales (5 ps and 0.1 ps). In the first case, the trajectories were recorded at every 5 ps to calculate the MSD for a total simulation time of > 10 ns (in some cases, up to 50 ns). In the second case, the trajectories were recorded at every 0.1 ps, for a total simulation time of 1 ns. The simulations from 298 K to 450 K show the initial cage vibrations (~ 1 ps) and then the cage trapping, and do not show ionic jumps even when simulations are extended to longer timescales (50 ns). At 475 K, the MSD *vs.* time plot **(Figure 7.8)** shows linearity after 5 ps, suggesting that the crystal interior breaks down and cationic sublattice becomes fluid. Hence, this regime of linear diffusion (being superionic as in NASICON, LISICON, garnets, ceramics and cathode) does not extrapolate to low temperature behavior of the ions for conductions due to the decomposition of cocrystal.

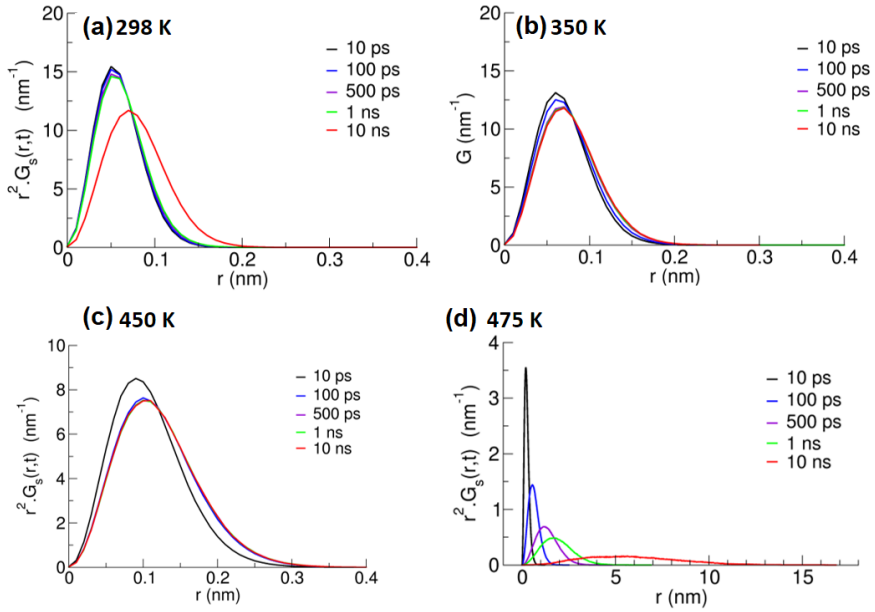

Figure 7.9. Transformed van Hove autocorrelation functions (self-part) for Li^+ ions in $(ADN)_2LiPF_6$ cocrystals using **model *P*** for different time-intervals at T = **(a)** 298 K, **(b)** 350 K, **(c)** 450 K and **(d)** 475 K. For the time-intervals of 10 ps and 100 ps, 1 ns long trajectories (0.1 ps step-size) were used, while for the time intervals of 500 ps, 1 ns and 10 ns, 20 ns long trajectories (5 ps step-size) were used.

To examine the occurrence of ionic jumps, self-part of vH ACF **(Equation (5.2)** was calculated as the transformed function $r^2.G_s(r)$, for various time-intervals. **Figure 7.9** shows $r^2.G_s(r)$ *vs.* r plot at various time-intervals at four different values of temperatures. The vH ACF suggest that at T < 450 K, the Li^+ ions remain isolated in the tetrahedral cage space of N (ADN) atoms even after a time interval of 10 ns. The probability distribution shows a peak height at 1 Å (± 0.5 Å). Compared to the most probable distance for a Li^+ at 298 K, the most probable distance for a Li^+ ion shifts slightly to the right at T = 450 K, but the distance is always > 3 Å, suggesting that the ionic jumps are not observed in a time interval of 10 ns at this temperature. At T = 475 K (above the decomposition temperature of the cocrystals) the ions exhibit Gaussian behavior like a fluid where the most probable peak decreases and shifts gradually to the right with increasing time-intervals. This explains the linear diffusion of Li^+ ions observed at 475 K **(Figure 7.8)**. However at T = 475 K, the cocrystalline network decomposes and even though the diffusion of Li^+ ions shows a linearity, the mobility

of ions cannot be extrapolated to predict the mobility in cocrystalline environment. This limitation would not arise if the crystal possessed a thermally stable anionic sublattice as discussed earlier in this subsection.

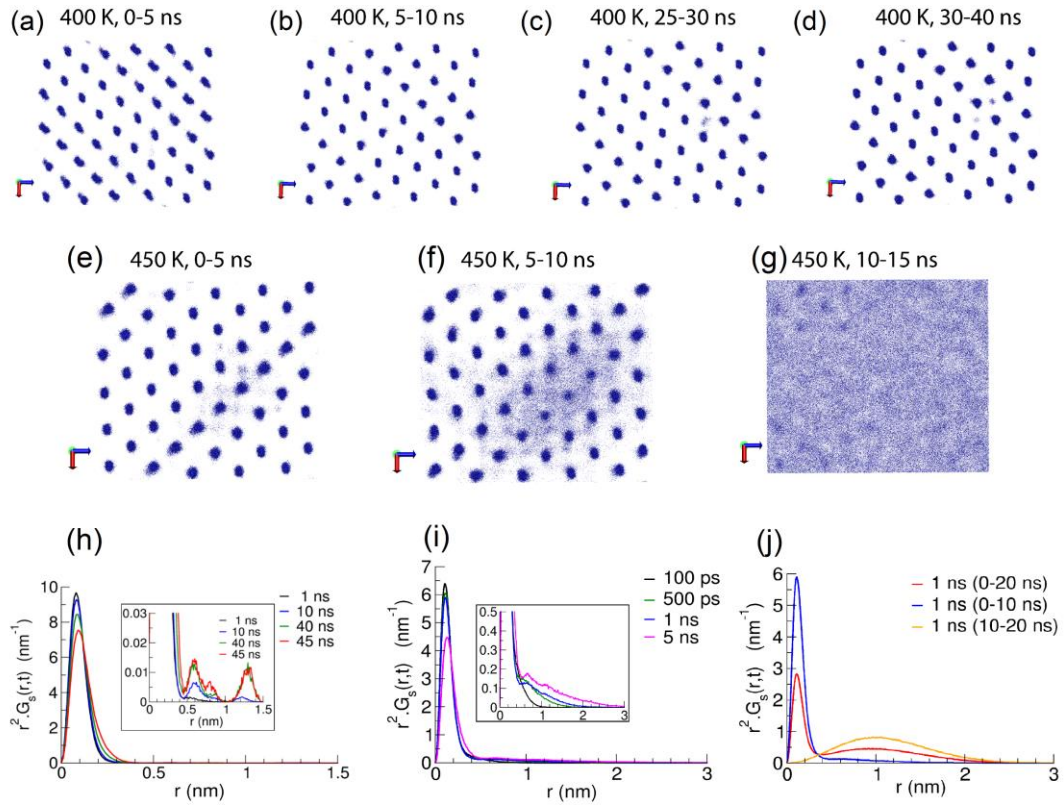

Figure 7.10. Trajectory maps of Li^+ ions in **model *D*** at T = 400 K for **(a)** *t* = 0-5 ns, **(b)** *t* = 5-10 ns, **(c)** *t* = 25-30 ns, **(d)** *t* = 30-40 ns; and at T = 450 K **for (e)** *t* = 0-5 ns, **(f)** *t* = 5-10 ns, **(g)** *t* = 10-15 ns; Self-vH ACF plots for Li^+ ions at different time intervals in **model *D*** at **(h)** T = 400 K, from a simulation of 50 ns, **(i)** T = 450 K for simulation time of 0 – 10 ns, and **(j)** T = 450 K for simulation time of 0 – 20 ns (divided into two windows: 0 – 10 ns and 10 – 20 ns).

Model *D*: MD simulations on defected supercells (model *D*) were employed where four vacancy sites of cations and anions were created, each at random places, in the supercell (two defects were at least 1.5 nm away from each other in order to prevent any initial interactions among vacancy sites). Model D was simulated for 50 ns at T = 400 K and for 20 ns at T = 450 K under *NVT* ensemble conditions. For the simulations on model *D*, the trajectory was recorded at every 5 ps and shown as consolidated maps in **Figure 7.10(a-d)**. The map shows that at T = 400 K, between 30 to 40 ns **(Figure**

7.10d), interstitial jumps for Li^+ ions were observed in the cocrystals. At T = 450 K **(Figure 7.10(e-g))**, the interstitial jumps are observed more frequently compared to those at 400 K. However at t > 10 ns, the structure collapses at T = 450 K- suggesting decomposition of the bulk at a lower temperature ($T_{d,sim}$ = 475 K from model *P*) due to the presence of vacancy sites.

Using the trajectory maps, the MSD and vH ACF were calculated from these simulations. The MSD *vs.* time plot at T = 400 K **(Figure F8)** shows that the Li^+ ions remain trapped and show a subdiffusive behavior, probably due to very few jump events at these timescales. Since PF_6^- anions are not present in a confined environment as the Li^+ ions, the initial oscillations which cause ballistic diffusion are higher in PF_6^- compared to Li^+. At T = 450 K, a linear diffusion is observed even at very short timescales **(Figure F8)** due to significant number of jump events as seen in the trajectory maps. The diffusion coefficients for Li^+ and PF_6^- ions were calculated at T = 450 K, for two time intervals: 0 – 10 ns and 10 – 20 ns. From 0 – 10 ns, D_{Li^+} = 1.32(4) x 10^{-6} cm^2/sec and $D_{PF_6^-}$ = 1.00(5) x 10^{-6} cm^2/sec, while from 10 – 20 ns, D_{Li^+} = 1.21(3) x 10^{-6} cm^2/sec and $D_{PF_6^-}$ = 1.02(4) x 10^{-6} cm^2/sec. For the interval 0 – 10 ns, the calculated transference number for Li^+ ions is, t_{Li^+} = 0.57, and for the interval 10 – 20, t_{Li^+} = 0.54. The key outcome of these comparisons is: for the cage oscillations, the tracer diffusivity is higher for PF_6^- ions. This is because unlike the Li^+ ions, PF_6^- ions are not trapped in cages. As jump events occur, Li^+ ions move more easily in the crystal space and have a higher mobility. At room temperature, the jump frequency is so small that even very long timescale simulations fail to observe a single jump.

The calculated self-vH ACF for model D at T = 400 K (**Figure 7.10h)**, shows a primary peak at ~ 1 Å, corresponding to cage oscillations. At longer time-intervals- 10 ns, 40 ns and 45 ns, very small secondary peaks are observed around 6 Å and 12 Å which can be correlated to Li^+ ion jumps to the vacancy sites. At T = 450 K, where the jump frequency is higher, the secondary peaks (jump peaks) span from 5 Å to 30 Å indicating a continuity of jump events in the system **(Figure 7.10i)**. It can also be

observed from the inset of **Figure 7.10i** that the timescales associated with these jumps decrease rapidly on increasing the temperature from T = 400 K to 450 K. Further, **Figure 7.10j** shows a comparison of different time windows at T = 450 K. As mentioned earlier, the cocrystalline structure collapses after 10 ns at this temperature. The self-vH ACF is calculated from 0 – 20 ns and then observed separately in 0 – 10 ns and 10 – 20 ns time windows with a time interval of 1 ns to calculate the function. The vH ACF for 0 – 20 ns shows probability peaks associated with cage vibrations and jump events. On dividing the total simulation time of 20 ns to two windows: the 0 – 10 ns shows predominantly the cage vibrations, while the 10 – 20 ns time window shows only the jump events.

Despite the limitations from system characteristics (stronger cationic cage), thermal effects (low T_d compared to other electrolytes) and computation (classical model and longer timescales), the ionic mobility can be modeled with the observation of jump events and the diffusion associated with them. An atomistic mechanism from DFT is discussed in the next section which interprets the longevity and feasibilitof interstitial jump events.

7.3.4 Mechanism of ion conduction from DFT

A unit cell of $(ADN)_2LiPF_6$ was optimized in a variable cell where relaxations were allowed for all the lattice parameters. Symmetry conditions were not imposed during the variable cell optimization of the unit cell. **Table F3** shows a comparison of lattice parameters from single crystal XRD and DFT.

As seen in the unit cell structure, the shortest possible distance between successive Li^+ ions is 6.6 Å (6.3 Å from XRD) which is parallel to the *b* crystallographic direction, and at the intersection of the (101) and (400) planes. To examine all the possible Li^+ migration channels, different supercells were created: a 1x2x1 supercell **(Figure F9a)**- for the channel of successive Li^+- Li^+ distance = 6.6 Å, a 2x1x2 supercell **(Figure F9b)**- for the channel of successive Li^+-Li^+ distance = 8.5

Å, and a 3x1x1 supercell **(Figure F9c)**- for the channel of successive Li^+-Li^+ distance = 11.2 Å.

For these supercells, one Li^+ ion vacancy site was created to calculate the MEP of Li^+ ion migration between adjacent occupancy sites. The defected supercell images (images: where the defect is located at a different site in the same supercell) were optimized in a fixed volume cell. Various pairs of images were used as reactant and product to examine the MEP for Li^+ ion migration using NEB calculations. The extrapolation of Li^+ ion migration paths and calculated activation energy barriers suggested the channel in *b*-crystallographic direction (Li^+-Li^+ = 6.5 Å) to be the one with the lowest energy. Hence, further results are discussed for this particular case only.

The Li^+ ions form a continuous array (without the presence of PF_6^- ions) parallel to the *b*-crystallographic direction with a short distance between the Li^+ ions, in contrast to the paths in the *a*- and *c*- directions. This results in the possibility of a low barrier migration path for the Li^+ ions. The calculated path of the Li^+ ion in the *b*-direction shows migration of Li^+ ions from one occupancy site to a vacancy site via an intermediate **(Figure 7.11)**. When a Li^+ ion defect is introduced in the supercell, the nitrogen atoms of ADN molecules stretch outward to stabilize the vacancy site. While the regular N-N distance in Li^+---N networks is 3.2 to 3.4 Å, the presence of a vacancy site increases this distance from 3.6 Å to 5.4 Å. A set of 11 intermediate images was used to extrapolate the path of the Li^+ ion. The climbing image-NEB calculations suggest that a Li^+ ion migrates via formation of an intermediate structure just between the two Li^+ occupancy sites along the *b*-crystallographic direction. The MEP was calculated for initial and intermediate image separately (11 images). The geometry of the intermediate structure (**Figure 7.11)** is a Li^+---N tetrahedron which forms with a reorientation of two of the four ADN molecules from each end.

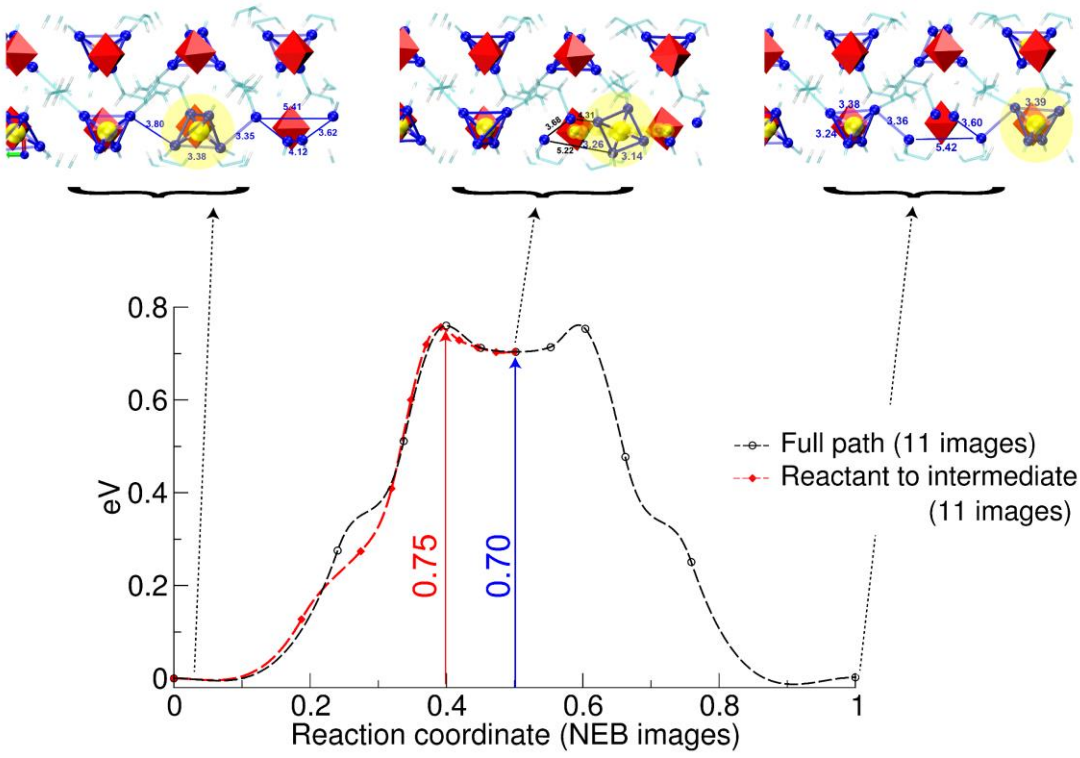

Figure 7.11. Minimum energy path (MEP) for Li^+ ion migration in the *b*-crystallographic direction, as observed from a 1x2x1 supercell of $(ADN)_2LiPF_6$. The geometries of initial, final and intermediate structures are shown above. The location for migrating Li^+ ion can be seen in the highlighted spot.

The N-N distance in the predicted intermediate structure is between 3.1 Å to 3.6 Å. When the intermediate forms, the remaining two ADN molecules appear to be a part of an elongated tetrahedron at each side with a N-N distance of 3.2 Å to 5.3 Å. The intermediate structure (relative energy = 0.70 eV = 67 kJ/mol) has two transition state structures at either side of the reaction coordinate with a barrier of 0.75 eV (= 72 kJ/mol). The presence of the intermediate structure suggests that the solvent (ADN) coordinated structure is stable and hence interstitial dislocations along with Schottky defects play a major role in ion transport. The occurrence of an intermediate structure also predicts that there is no involvement of anions during the cation transport (contrary to what has been discussed in the previous chapter about a similar class of sodium ion electrolyte $(ADN)_3NaClO_4$, where both anion and solvent coordinate with the cation leading to formation of a transition state). The calculated E_a barriers for

other possible channels were at least two times higher than the channel in the *b*-direction, suggesting that Li^+ ion migration in $(ADN)_2LiPF_6$ electrolyte will preferentially occur in the channel in the *b*-crystallographic direction, where the Li^+ ions hop to a vacancy site via a solvent coordinated intermediate.

7.4 CONCLUSIONS

While much research has been expended to optimize crystal structures and doping strategies in inorganic solid electrolytes, there has been much less work on soft-solid crystals. There are significant differences in the structures and mechanisms of ion conduction between the two electrolytes. The inorganic conductors have a framework of fixed anions and a sub-lattice of mobile lithium ions that migrate via hopping mechanisms. In the soft-solid crystals, the lithium ions move through channels of organic molecules (here ADN), and are separated from the anions by the organic molecules. The distance between Li lattice sites is much greater than in the inorganic crystals, so that the frequency of jumps between sites is decreased. For the $(ADN)_2LiPF_6$, the Li^+ ion moves between sites through an intermediate that involves the ADN molecules. The weak interactions between the "hard" Li^+ ions and "soft" –C≡N groups, and the fewer contacts (four for –C≡N vs five for –O-) [222] are responsible for the three order of magnitude increase in conductivity compared with the crystalline solvate $(EO)_6LiPF_6$ ($\sigma \sim 10^{-7}$ S/cm) prepared using low molar mass polyethylene oxide [221, 226]. In the PEO_6:$LiPF_6$ (as well as PEO_6:$LiAsF_6$, and PEO_6:$LiSbF_6$) complex, the Li^+ ions reside in 1D tunnels formed by the PEO chains, also not coordinated with the anions. Further, in the case of inorganic lithium electrolytes, the grain boundary resistance is believed to be greater than the bulk conductivity, while in the case of soft-solid crystals the grain boundaries are fluid and can have better conductivity than the bulk grains. As in the case of ceramic electrolytes, improvements in conductivity for soft co-crystals are expected if 2D or 3D channel systems can be synthesized, and if vacancy or interstitial sites can be increased (e.g. by isovalent or alivalent doping, or introduction of defects by chain

ends (here by introducing a different dinitrile or a mononitrile) as in the case of glyme/LiX complexes [225]). In the case of soft-solid crystals, increased conductivity is also expected if the distance between the Li sites is decreased.

———*———*———

Chapter 8:
Summary and Future Directions

8.1 SUMMARY

Chapter 1 of the thesis discusses two domains of materials, environment and energy storage: (a) Lysine amino acid-based absorbents for CO_2 absorption, and (b) Electrolytes for Sodium/Lithium Ion Batteries. This chapter includes the background, significance and scope of a new generation of CO_2 absorbents and solid battery electrolytes along with the objectives of the thesis.

Chapter 2 of the thesis discusses results from MD simulations on CO_2 absorption in *tetra*-Butylphosphonium Lysinate ($P_{4444}^{+}Lys^{-}$) IL. The timescales of CO_2 absorption and molar absorption ratio in surface and bulk of IL are obtained from simulation trajectories. These quantities provide a direct comparison of the absorption process with experiments. Further, preferential interaction of Lys^{-} anion with CO_2, competitive reactivity of amine groups in Lys^{-}, and the influence of absorption on the mobility of ions are the important outcomes from this chapter.

Chapter 3 of the thesis discusses the mechanism of CO_2-Lys^{-} reaction and role of water as an explicit molecule. All the possible reaction pathways for CO_2-Lys^{-} and CO_2-Lys^{-}-H_2O reactions are explored using gas-phase DFT calculations. The calculations suggest that the near-carboxylate amine functional group in Lys^{-} anion interacts preferentially with the CO_2 molecules to form stable carbamate product. Moreover, the feasibility of bicarboxylate formation during the CO_2-Lys^{-}-H_2O reaction is one of the important outcomes seen from this study. A collective examination of BE, E_a, and RE provided in this chapter provide valuable insights

associated to physisorption, chemisorption, and desorption of CO_2 in $[Lys]^-$ salt mixtures and ILs.

Chapter 4 of the thesis discusses results from MD simulations and DFT calculations on a Lithium ion cocrystalline material DMF·LiCl. A number of qualitative properties of the material are reported by simulation, namely, the crystal packing arrangement, the mechanism of decomposition by expulsion of DMF from the LiCl lattice, the existence of a liquid-like grain boundary layer, and most importantly, negligible grain boundary resistance from increased mobility of ions in the boundary layer *vs.* the bulk. The theoretical calculations also predict that decomposition of smaller aggregates at surface is facile than larger aggregates in the crystal interior.

Chapter 5 of the thesis discusses modeling of structure, ion dynamics and mechanism of ion conduction in a Na^+ ion cocrystalline electrolyte $(DMF)_3NaClO_4$ from MD simulations and periodic DFT calculations. The simulations provided mechanism of stoichiometric conversion, melting, ionic mobility at different temperatures, competitive nature of ionic mobility and E_a associated with Na^+ ion migration. The size and number of ion-pair and ion-solvent clusters as a function of temperature provide proofs of stoichiometric conversion (from 3:1 to 2:1, DMF:$NaClO_4$) and melting of the electrolyte. The minimum energy path of Na^+ ion migration showed that the transition state during Na^+ ion migration reaction exhibits a trigonal planar arrangement of DMF molecules, similar to the transition state in typical S_N2 reaction in organic chemistry.

Chapter 6 of the thesis discusses the choice of ADN molecule (ADN, N≡C-$(CH_2)_4$-C≡N) as a cosolvent of cocrystalline LIB/NIB electrolytes and study of $(ADN)_3NaClO_4$ using MD simulations and plane-wave DFT calculations. The electrolyte consists of Na^+ ions in an octahedral cage of N(ADN) atoms with ClO_4^- ions present in the interstitial space and not at all coordinated with Na^+ ions. The simulations provide mechanism of melting of cocrystals and explores a set of

simulation protocols to study ion dynamics, which should be employed to the cases where linearity in translational diffusion of ions is difficult to observe. The DFT calculations suggest a three-dimensional nature of Na^+ ion migration via an anion-solvent assisted transition state.

Chapter 7 of the thesis discusses the structural properties, ion dynamics, and mechanism of conduction in a LIB electrolyte: $(ADN)_2LiPF_6$. The Li^+ ions in this electrolyte coordinate with four N(ADN) atoms in the form of a tetrahedral cage and form a preferential channel for Li^+ ion conduction. The simulations model cocrystal decomposition, ion dynamics, whereas DFT calculations reveal the mechanism of Li^+ ion conduction in the cocrystals. The calculations suggest that the Li^+ ion in these cocrystals migrates via a solvent assisted transition state. vH ACF provides a quantitative measure of jump events during the migration of Li^+ ions in a defected supercell.

8.2 FUTURE DIRECTIONS

8.2.1 Carbon dioxide absorbents

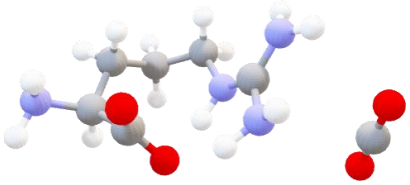

Figure 8.1. Argininate anion as a probable CO_2 absorbent.

Similar to lysinate anion, argininate anion-based salts can also be screened for a possible CO_2 absorbent **(Figure 8.1)**. Recently, Li *et al.* [259] performed absorption experiments on mixtures of potassium carbonate with potassium salts of, glycinate, lysinate and L-argininate. The authors observed that these AAS can enhance the absorption of CO_2 in such case. While a number of AAILs and AAS studied as CO_2 absorbents, hybrid materials, like small peptide sequences (n = 2 to < 10) can be synthesized and investigated. An advantage of using peptide and their hybrids as

absorbents would be their natural occurrence and low cost of processing. Filippov *et al.* [260] studied choline cation based threoninate and other AAILs, where a reversible precipitation of solid zwitterionic threonine was observed. Palomar and coworkers [261] have reported an imidazolium based encapsulated AAIL where CO_2 molecules are trapped in spherical 500 – 700 nm capsules **(Figure 8.2)**. MD simulation studies in the above cases can model the effect of CO_2 capture on the structure and dynamics. A computational investigation of chemical reactions would assist in understanding the energetics, mechanism and nature of CO_2 absorption. Large scale MD simulations can be performed to model structure, and surface effects in carbon encapsulated ILs [261].

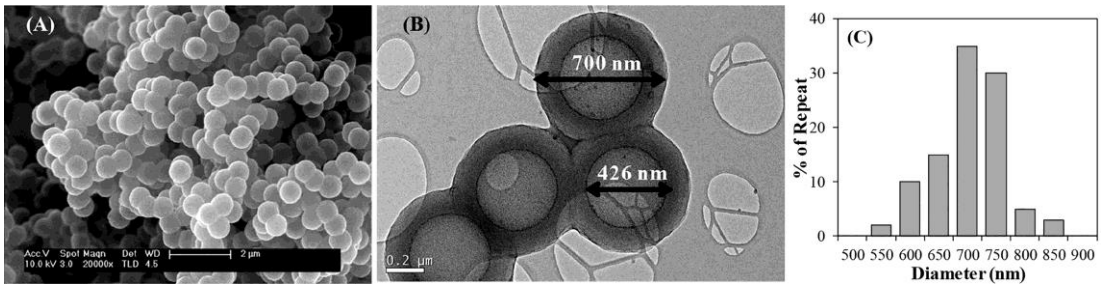

Figure 8.2. (A) SEM and (B) TEM images of the carbon capsules to obtain the aa-ENIL material and (C) size distribution of synthesized C_{Cap}. Reprinted with permissions from [261] © 2019 American Chemical Society

The role of Lys^- anions in direct (carbamate) *vs.* indirect (bicarbonate) CO_2 capture can be studied using AIMD simulations. The dynamics of a reversible CO_2 absorption as a function of temperature can be modeled in future by performing long-timescale simulations. Further, examination of small-scale ionic salt molecules with water clusters from DFT can also provide important insights to the bicarbonate/carbonate mechanism. Such studies will propose the design of optimized absorbents with higher cyclability, thermal and chemical stability and low solvent loss. The calculations can also be extended to model CO_2 absorption in extreme conditions of pressure and temperatures, where the results may lead to interesting understanding of the carbon cycles and storage models on other planets/natural satellites.

8.2.2 Cocrystalline battery electrolytes

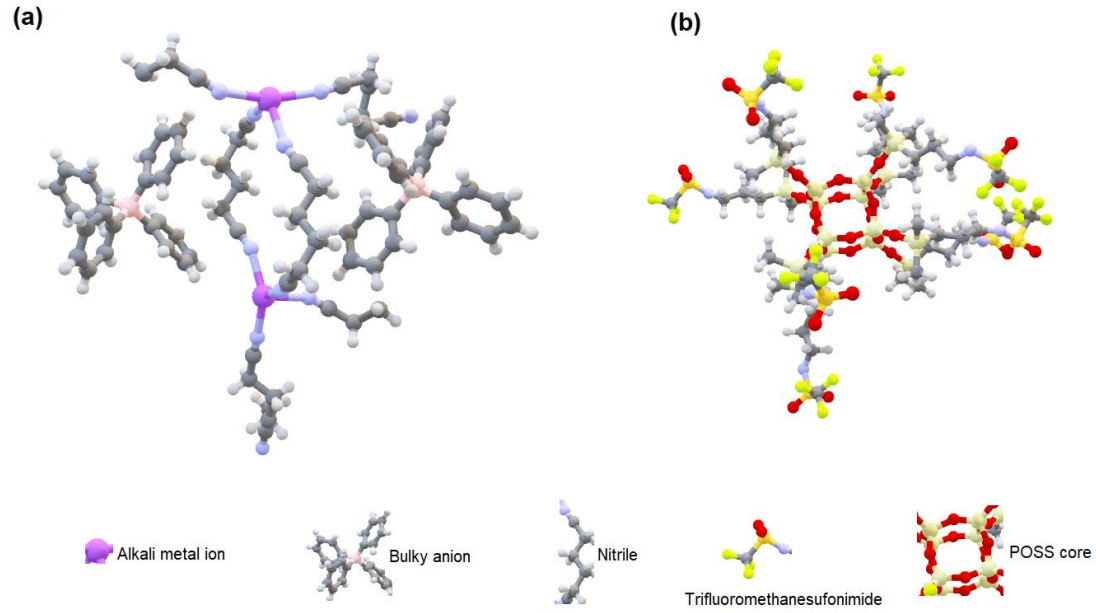

Figure 8.3. (a) Concept design of a single-ion conductor cocrystalline electrolyte, **(b)** a competitive single-ion conductor of polyoligomeric silsesquioxane (POSS) tailored with trifluoromethanesulfonamide.

Within a span of four years since its first study, cocrystalline electrolytes have showed immense potential to be an alternative to other solid electrolytes. This stems a need to design and synthesize a large library of such molecules with various possible combinations of salts and cosolvents. The use of bulkier anions like *bis(*trifluoromethane)sulfonimide can lead to a higher transference number of cations. The size of the solvent matrix in these electrolytes can also be tuned to inhibit the motion of anions which can enhance the cationic contribution to the conductivity. A concept design of such cocrystalline electrolyte can be seen in **Figure 8.3a**. The proposed single ion conductors can be studied alongside other single-ion conductors like polyoligomeric frameworks [262] **(Figure 8.3b)**. Another way of enhancing the ion conduction- Schottky defects in the crystal interior, can also be used as a design principle to synthesize doped crystals of solid electrolytes. In a recent theoretical report, Noda *et al.* [263] performed AIMD simulations to understand the effect of calcium doping in a LISICON electrolyte. The authors in this work observed that

calcium doping in the crystal leads to interstitial dislocation of Li^+ ions, which can be attributed to the observed enhancement in ionic conductivity and lowering of E_a barrier. Understanding the design principle from theoretical calculations will be *a priori* in synthesis of next generation of electrolytes for all-solid-state LIB/SIB.

To develop the atomic-scale understanding of electrolyte reactions at the electrode interface, the cocrystalline electrolytes can be studied using large-scale models from MD simulations. The ionic diffusion in these electrolytes would also require long-timescale simulations to be performed. A simulation with sufficient data for jump events will provide more insights to the ion dynamics. The chemical stability of these electrolytes can also be studied using plane-wave DFT methods and phonon calculations. Seminario and coworkers [152] performed MD simulations on a nanoscale model of Li-ion battery ($LiCoO_2$ cathode, LiPF6-EC electrolyte, and graphite anode). The authors demonstrated charging of the battery using an external electric field, where a number of experimental processes like change in polarizability of solvent, electrode saturation, etc. were exhibited. Similarly, a full battery modeling with cocrystalline electrolytes can also be achieved, where evolution of solid electrolyte interface and case study of battery-fails at high potential can be studied using computer simulations.

———*———*———

Appendix A

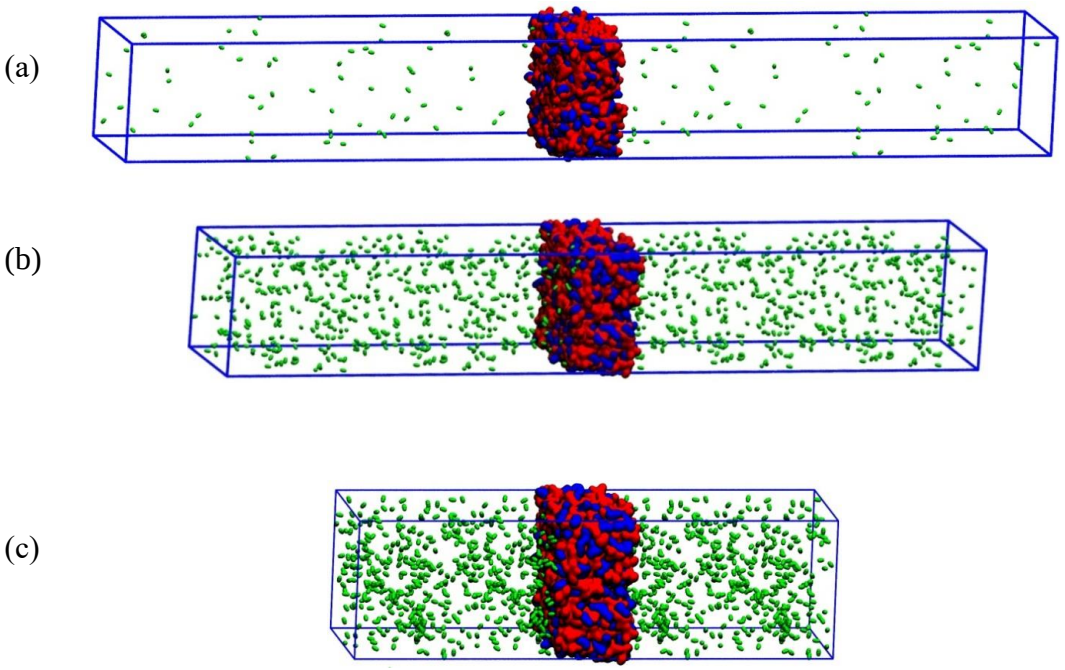

Figure A1. Initial configuration of CO_2-IL slabs at (a) 1 bar, (b) 10 bar and (c) 20 bar partial pressure of CO_2.

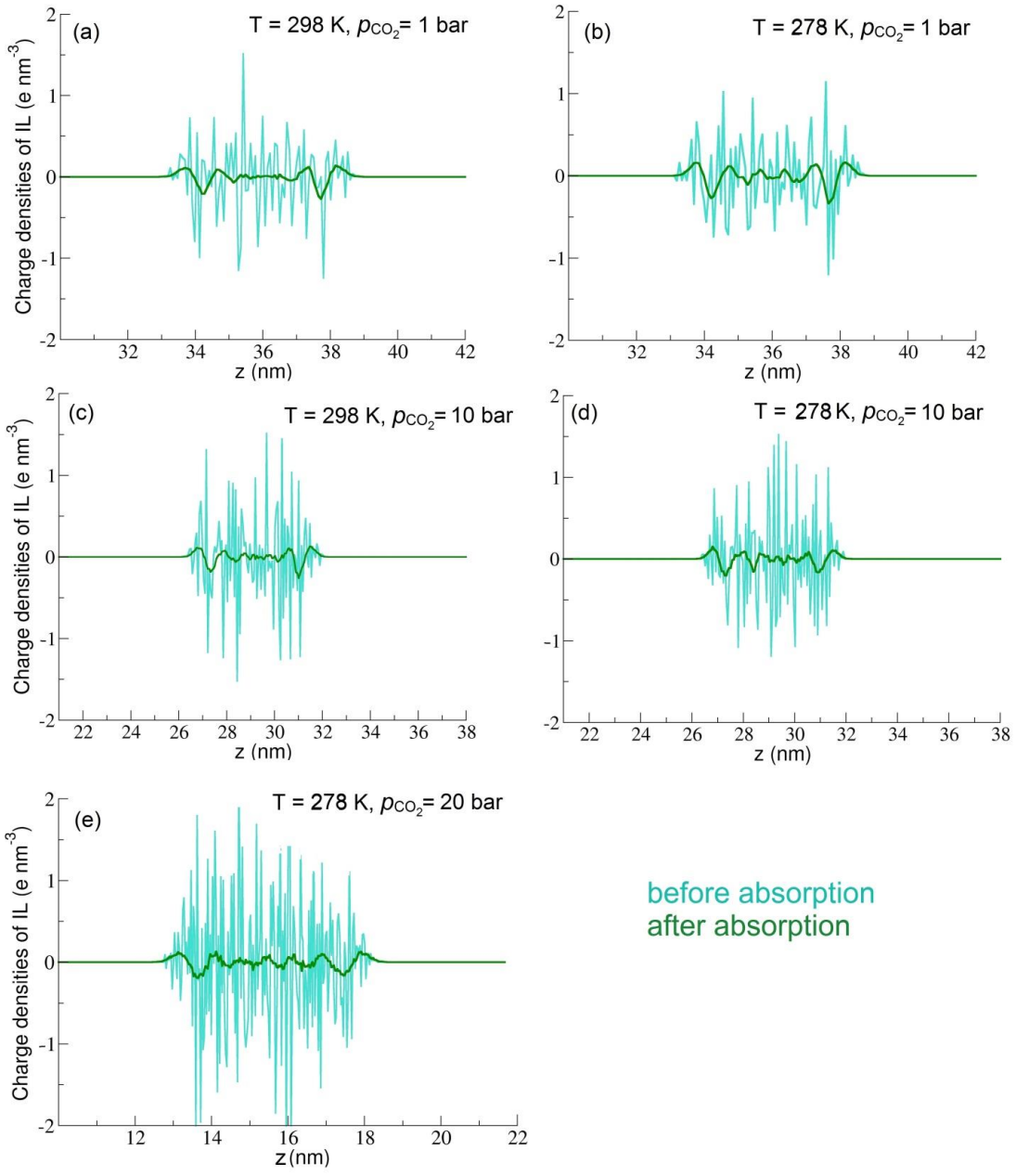

Figure A2. Charge densities of IL before and after absorption of CO_2 at different thermodynamic conditions.

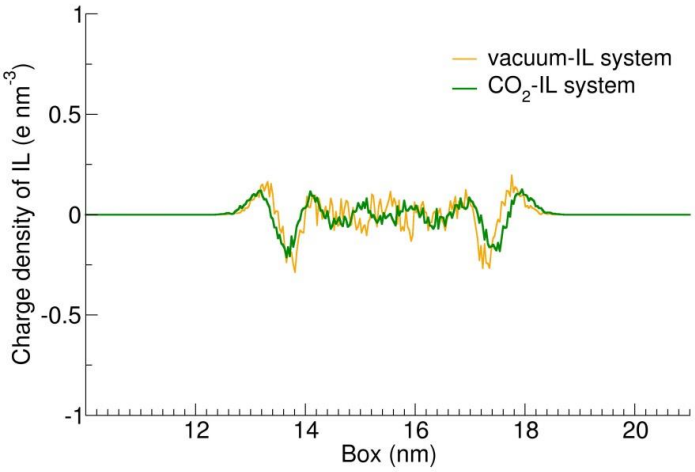

Figure A3. Averaged charge densities (from t = 5 ns to t = 10 ns) of IL for vacuum *vs* CO_2 in IL system, both at T = 298 K, and for CO_2-IL system p_{CO_2} = 20 bar.

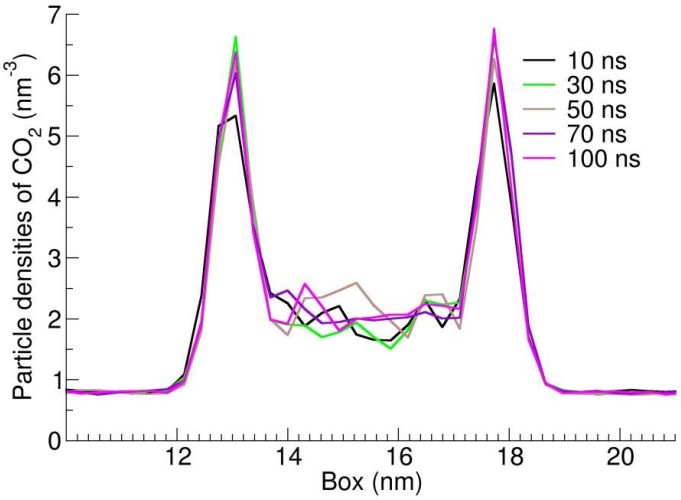

Figure A4. Particle densities of CO_2 in CO_2-IL interface at T = 298 K, p_{CO_2} = 20 bar.

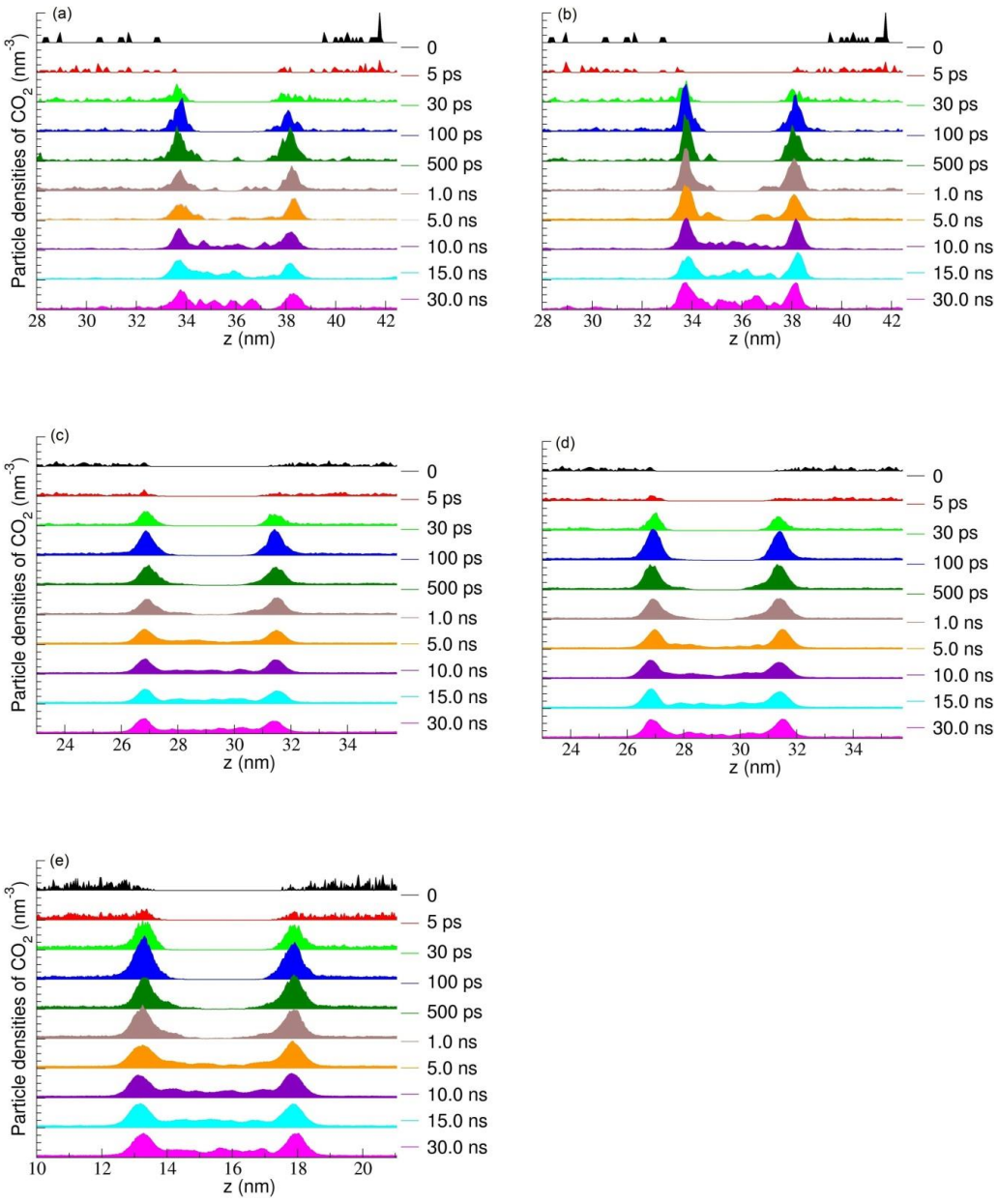

Figure A5. Particle densities of CO_2 at respective T and p_{CO_2}, (a) 298 K, 1 bar; (b) 278 K, 1 bar; (c) 298 K, 10 bar; (d) 278 K, 10 bar; (e) 278 K, 20 bar. In the y – axis, each minor tick corresponds to a value of 0.25 particle nm^{-3} for (a) and (b), and 2.5 particle nm^{-3} for (c), (d) and (e).

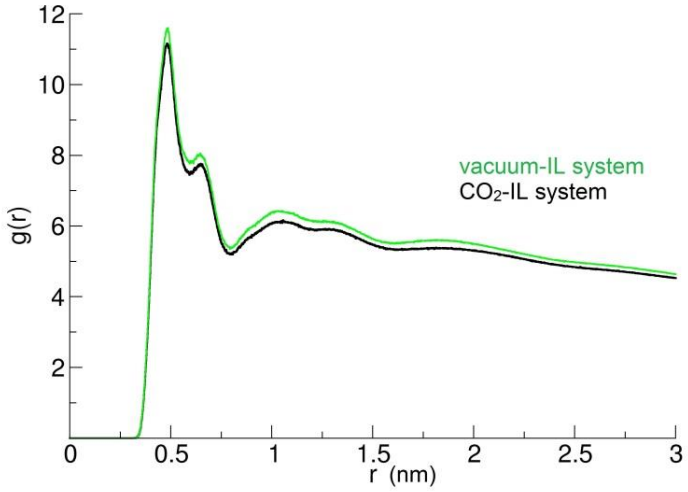

Figure A6. Averaged site-site RDF (t = 25 ns to t = 35 ns) between P[P_{4444}]-N1,N2[Lys] for CO_2-IL interface(black) and for vacuum-IL interface(green) at T = 298 K and p_{CO_2}= 20 bar.

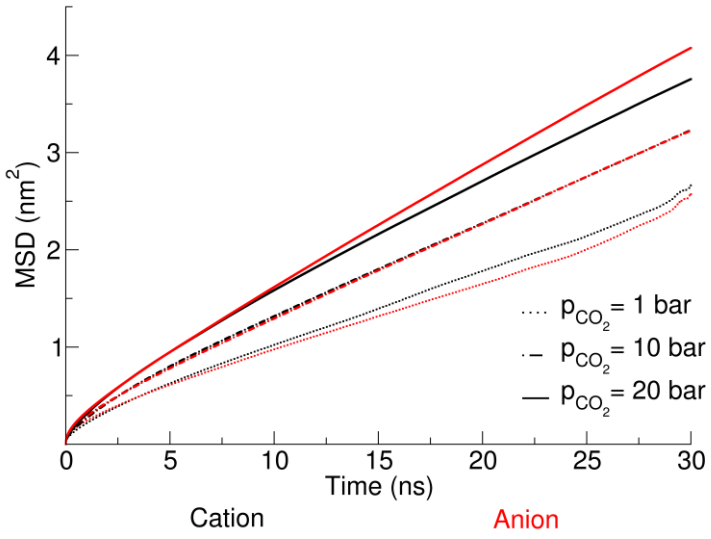

Figure A7. MSDs of cations and anions of IL at different thermodynamic conditions.

(a)

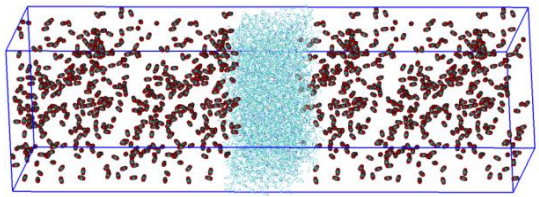

1024 CO_2 : 512 IL

(b)

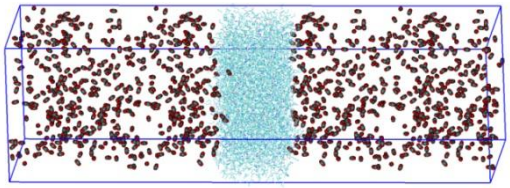

1024 CO_2 : 512 IL

(c)

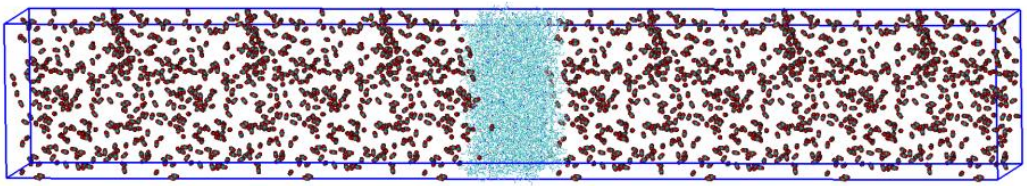

2048 CO_2 : 512 IL

Figure A8. Initial configurations of CO_2-IL system at p_{CO_2} = 20 bar and T = 298 K: Configurations (a) and (b) differ in positions and configuration (c) differ in system size.

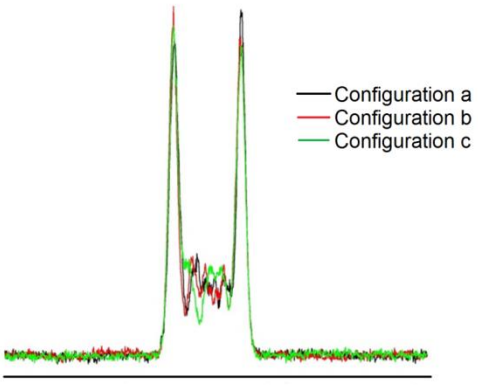

Figure A9. Averaged particle densities of CO_2 inside the box (t = 25 ns to t = 35 ns) for the CO_2-IL system.

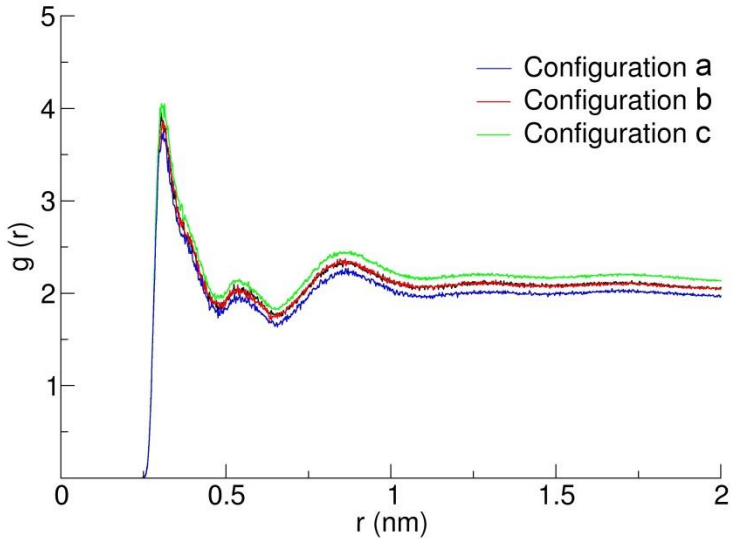

Figure A10. Averaged site-site RDFs (t = 25 ns to t = 35 ns) between N1,N2[Lys]-C[CO_2] at p_{CO_2}= 20 bar and T = 298 K.

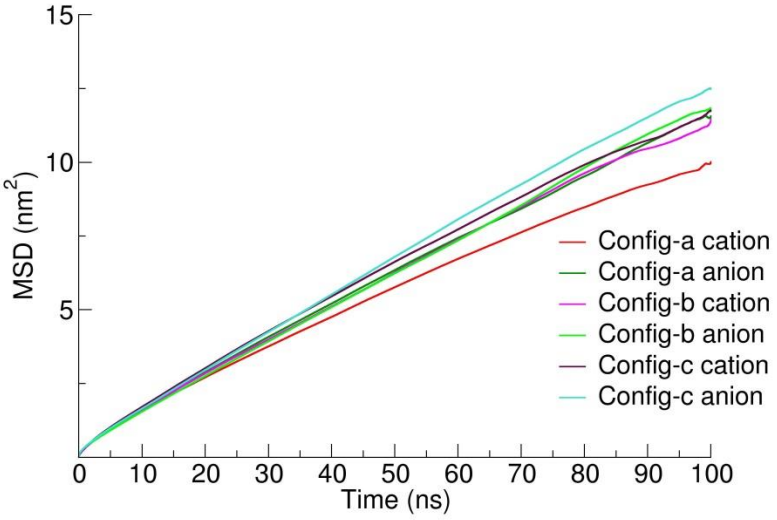

Figure A11. Mean square displacements of [P_{4444}] and [Lys] at p_{CO_2}= 20 bar and T = 298 K.

Table A1. Standardization of force field for IL with experiment and simulation

Properties	**Previous work**	**This work**
Density at 298.15 K (g/cm^3)	0.973 *	0.963
	0.962 **	
Density at 321.85 K (g/cm^3)	0.950 **	0.945
CoM RDF between Cation and anion (298.15 K)		
First Maxima (Å)	5.85 **	6.05
First Minima (Å)	8.05 **	8.21
Peak height	2.28 **	2.32
Coordination number	3.55 **	3.75
Conductivity of anion (S cm^{-1})	0.83 x 10^{-4} *	0.78 x 10^{-4}

* G. Zhou, X. Liu, S. Zhang, G. Yu and H. He, *J. Phys. Chem. B*, 2007, **111**, 7078–7084.

** (a) Zhang, J. M.; Zhang, S. J.; Dong, K.; Zhang, Y. Q.; Shen, Y.; Lu, X. *Chem. Eur. J*, 2006, **12,** 4021–4026. (b) Zhang, J. M.; Zhang, S. J. Combinatorial chemistry research on amino acids and ionic liquids. Postdoctoral Thesis, Institute of Process Engineering, Chinese Academy of Sciences, 2005.

Table A2. Molar absorption ratio (calculated as an average from t = 10.0 ns to t = 30.0 ns) at various thermodynamic conditions.

Total no. of CO_2 molecules	Temperature (K)	p_{CO_2} (bar)	No. of CO_2 molecules absorbed	Molar absorption ratio CO_2:IL
128	298	1.0	36	0.070
128	278	1.0	49	0.096
1024	298	10.0	308	0.602
1024	278	10.0	358	0.699
1024	298	20.0	469	0.916
1024	278	20.0	553	1.080

Appendix B

rig-fCP method to calculate binding energies:

The rigorous-fragment CounterPoise (rig-fCP) is used to calculate Binding Energy (BE) corrected with Basis Set Superposition Error (BSSE) and fragment relaxations. In general, for a complex AB, formed from reactants A and B, the rig-fCP corrected BE can be calculated as:

$$\mathrm{BE(AB)} = \mathrm{E}_{\mathrm{AB}}^{\alpha\cup\beta}(\mathrm{AB}) \underbrace{-\mathrm{E}_{\mathrm{AB}}^{\alpha\cup\beta}(\mathrm{A}) - \mathrm{E}_{\mathrm{AB}}^{\alpha\cup\beta}(\mathrm{B})}_{BSSE\ Correction} + \underbrace{\mathrm{E}_{\mathrm{AB}}^{\alpha}(\mathrm{A}) + \mathrm{E}_{\mathrm{AB}}^{\beta}(\mathrm{B})}_{Fragment\ relaxation} - \mathrm{E}_{\mathrm{A}}^{\alpha}(\mathrm{A}) - \mathrm{E}_{\mathrm{B}}^{\beta}(\mathrm{B})$$

Where in the Right-Hand Side (RHS), E(X) is the electronic energy of entity X (here A or B), subscript indicates the geometry from which the energy is calculated, and superscript denotes the orbital space (basis functions) for the calculations. The first term in RHS denotes the electronic energy of AB complex in the optimized geometry calculated using $\alpha \cup \beta$ orbital space. α is the orbital space of A and β is the orbital space of B. The BE without rig-fCP correction can be calculated by taking first and the last two terms of the above equation.

(a) $[Lys]^-$-CO_2 complexes:

The rig-fCP corrected BE is calculated for Nb# (where # is 1, 2, 3 and 4) series of the non-bonded complexes as:

$$\mathrm{BE(Nb\#)} = \mathrm{E}_{\mathrm{Nb\#}}^{\lambda\cup\kappa}(\mathrm{Nb\#}) - \mathrm{E}_{\mathrm{Nb\#}}^{\lambda\cup\kappa}([\mathrm{Lys}]^-) - \mathrm{E}_{\mathrm{Nb\#}}^{\lambda\cup\kappa}(\mathrm{CO_2}) + \mathrm{E}_{\mathrm{Nb\#}}^{\lambda}([\mathrm{Lys}]^-) + \mathrm{E}_{\mathrm{Nb\#}}^{\kappa}(\mathrm{CO_2}) - \mathrm{E}_{[\mathrm{Lys}]^-}^{\lambda}([\mathrm{Lys}]^-) - \mathrm{E}_{\mathrm{CO_2}}^{\kappa}(\mathrm{CO_2})$$

where λ and κ are basis functions of $[Lys]^-$ and CO_2 respectively.

(b) $[Lys]^-$-H_2O complexes:

The rig-fCP corrected BE is calculated for Nbw# (where # is 1, 2, 3, 4 and 5) series of the non-bonded complexes as:

$$\begin{aligned} BE(Nbw\#) = {} & E^{\lambda\cup\omega}_{Nbw\#}(Nbw\#) - E^{\lambda\cup\omega}_{Nbw\#}([Lys]^-) - E^{\lambda\cup\omega}_{Nbw\#}(H_2O) + E^{\lambda}_{Nbw\#}([Lys]^-) \\ & + E^{\omega}_{Nbw\#}(H_2O) - E^{\lambda}_{[Lys]^-}([Lys]^-) - E^{\omega}_{H_2O}(H_2O) \end{aligned}$$

Where λ and ω are basis functions of $[Lys]^-$ and H_2O respectively.

(c) $[Lys]^-$-H_2O-CO_2 complexes:

Since these complexes form as CO_2 is introduced to the Nbw# ($[Lys]^-$-H_2O) complexes, the Nbw# complex is considered as one fragment (basis functions = $\lambda \cup \omega$) and CO_2 as the other fragment. The rig-fCP corrected BE is calculated for Nbw#x (where # is 1, 2, 3, 4 and 5 and x = n/o/h where n is N1/N2 site in $[Lys]^-$, o is OL2 site in $[Lys]^-$ and h is H_2O) series of the non-bonded complexes as:

$$\begin{aligned} BE(Nbw\#x) = {} & E^{\lambda\cup\omega\cup\kappa}_{Nbw\#x}(Nbw\#x) - E^{\lambda\cup\omega\cup\kappa}_{Nbw\#x}(Nbw\#) - E^{\lambda\cup\omega\cup\kappa}_{Nbw\#x}(CO_2) \\ & + E^{\lambda\cup\omega}_{Nbw\#x}(Nbw\#) + E^{\kappa}_{Nbw\#x}(CO_2) - E^{\lambda\cup\omega}_{Nbw\#x}(Nbw\#) - E^{\kappa}_{CO_2}(CO_2) \end{aligned}$$

---

(1) Boys, S.; Bernardi, F. The Calculation of Small Molecular Interactions by the Differences of Separate Total Energies. Some Procedures with Reduced Errors. *Mol. Phys.* 1970, *19*, 553–566.

(2) Kirschner, K. N.; Sorensen, J. B.; Bowen, J. P. Calculating Interaction Energies Using First Principle Theories: Consideration of Basis Set Superposition Error and Fragment Relaxation. *J. Chem. Educ.* 2007, *84*, 1225–1229

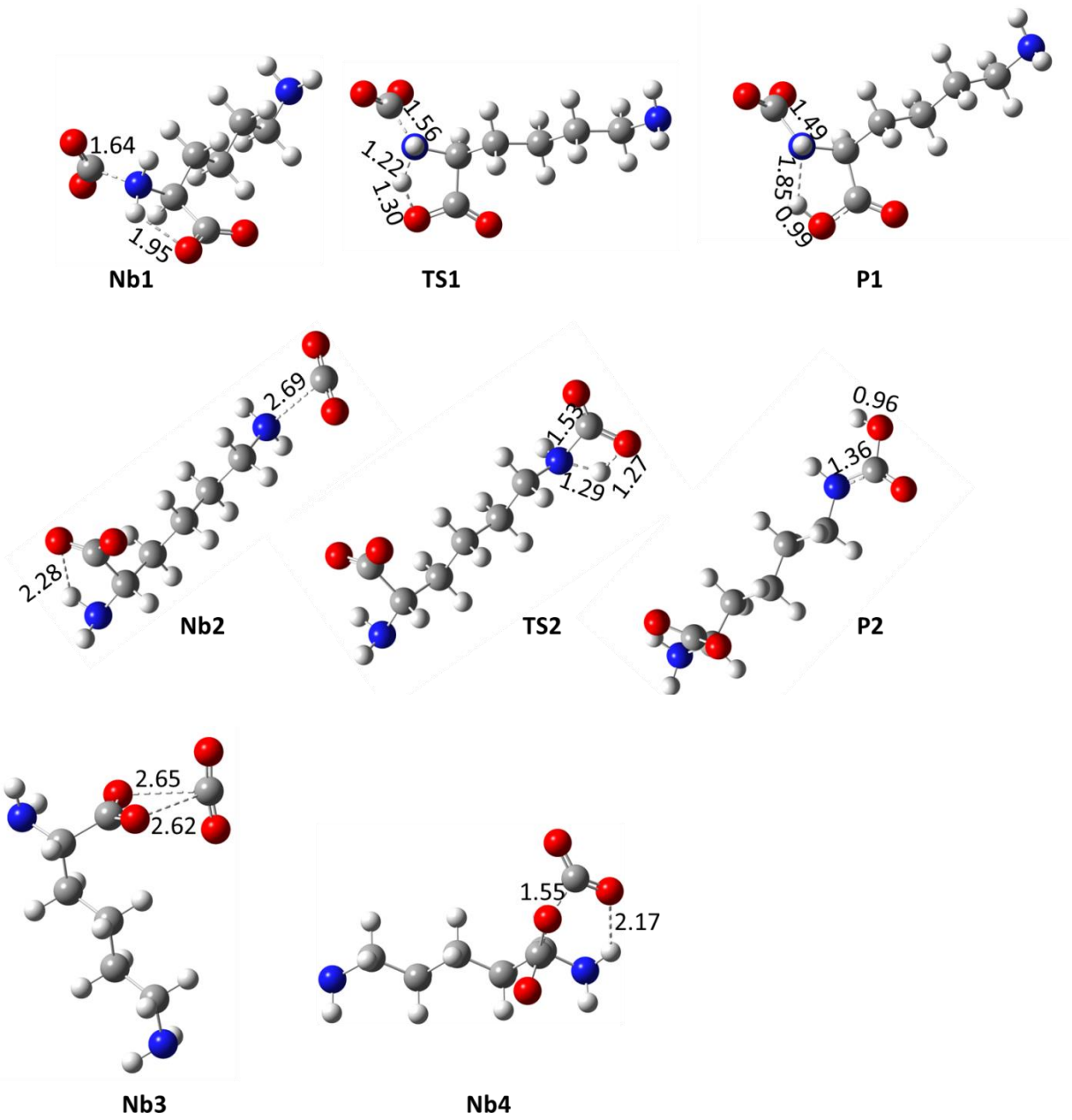

Figure B1. Optimized geometries of NB complexes, transition states and products in $[Lys]^-$-CO_2 interactions and reactions using M06-2X-GD3/6-311++G(d,p) method (distances are shown in Å).

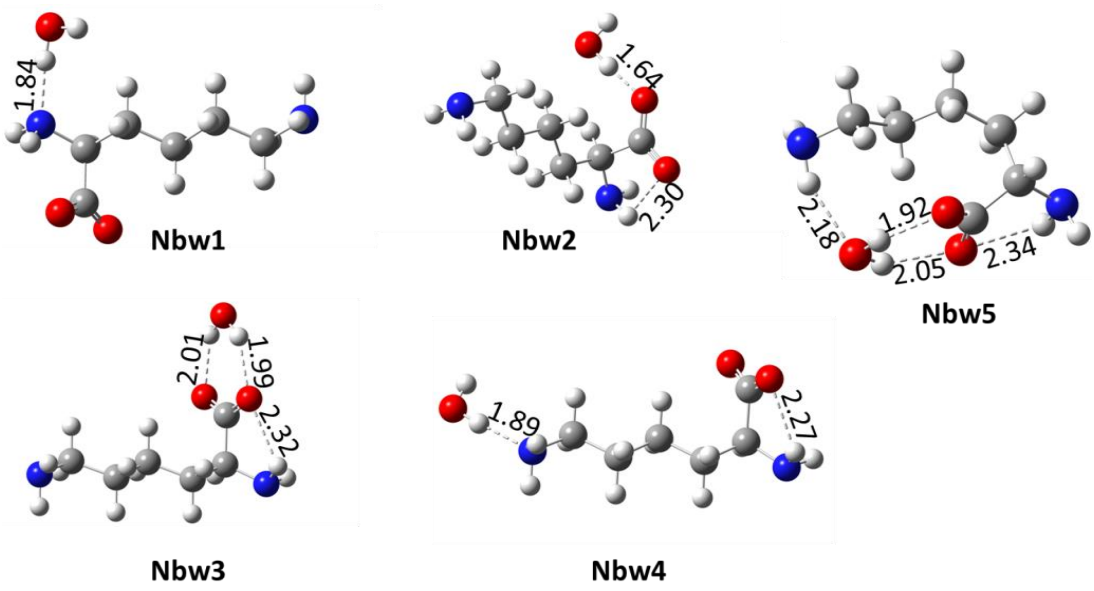

Figure B2. Optimized geometries of NB complexes in $[Lys]^-$-H_2O interactions using M06-2X-GD3/6-311++G(d,p) method (distances are shown in Å).

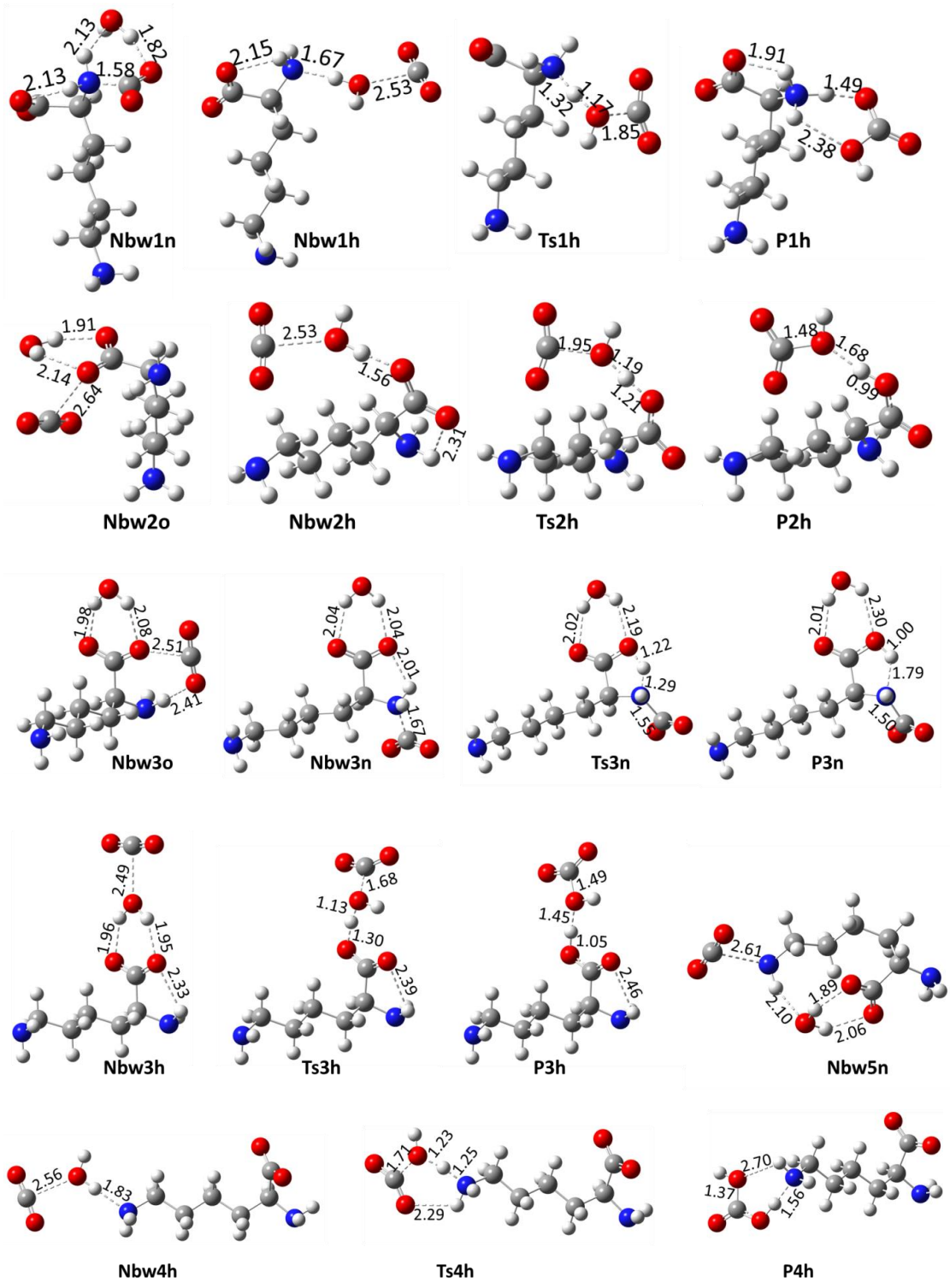

Figure B3. Optimized geometries of NB complexes, transition states and products in $[Lys]^-$-H_2O-CO_2 interactions and reactions using M06-2X-GD3/6-311++G(d,p) method (distances are shown in Å).

Appendix C

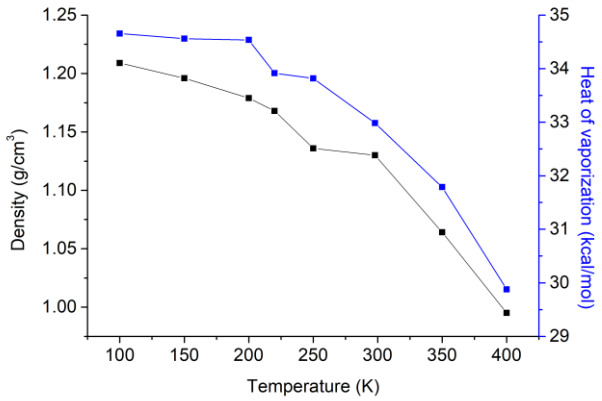

Figure C1. Calculated density and ΔH_{vap} at different temperatures.

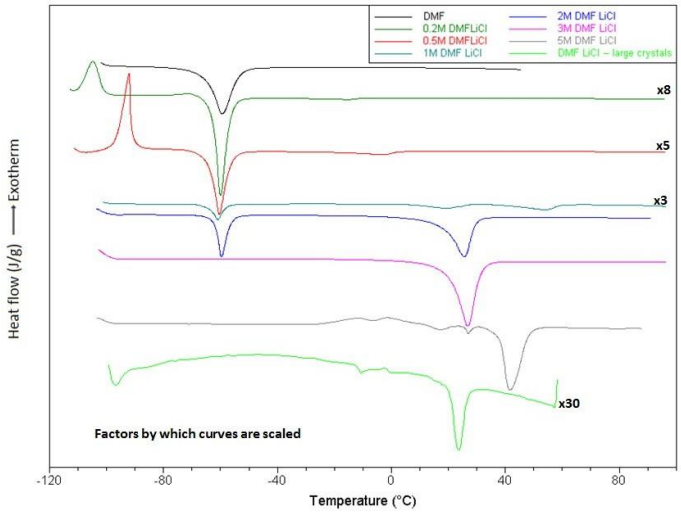

Figure C2. DSC data (second heating cycle) of solutions of DMF (—); LiCl in DMF (0.2 M —,0.5 M—,1.0 M —, 2.0 M—, 3M —); and cocrystals of DMF·LiCl (—). The melt transitions observed are new crystalline phases of DMF and LiCl located at the surface of the co-crystal, and so are very weak, and are not from the bulk co-crystal of DMF·LiCl, which has no melt transition. Instead they correspond to new phases found in the crystallized solutions of DMF and LiCl.

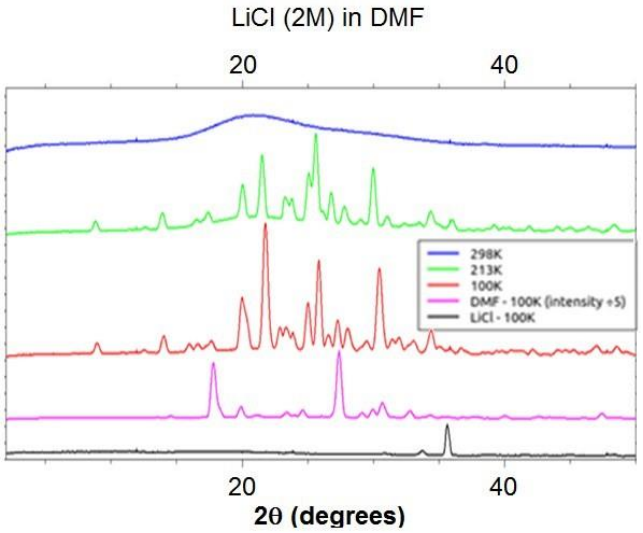

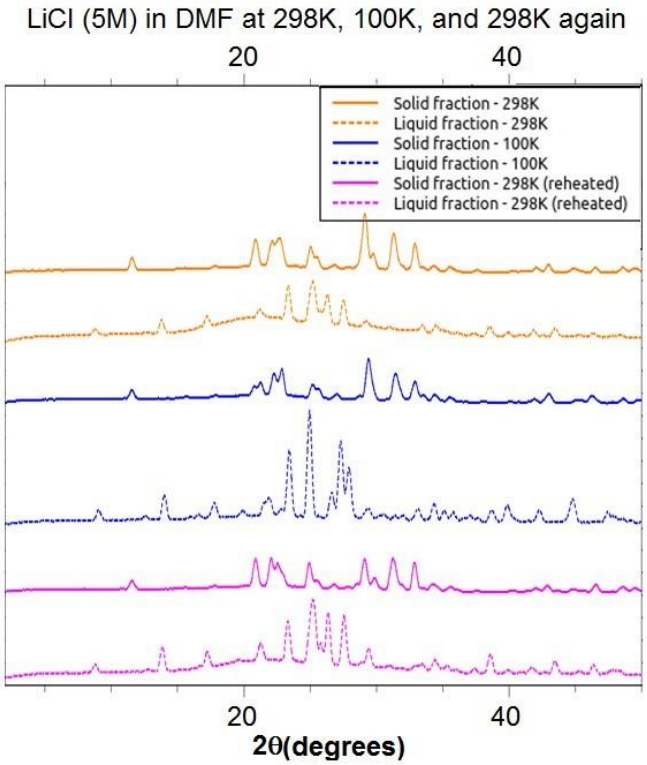

Figure C3. Above: XRD of 2M LiCl in DMF at room temperature (—), showing amorphous liquid; at 213 K, just above melt temperature (212K) of DMF (—), showing crystal and small amount of underlying liquid DMF; and at 100 K (—) below the melt temperature of DMF, showing only crystal phase. Note: none of the peaks correspond to either pure DMF (—) or pure LiCl (—), measured separately, or to the co-crystal of DMF·LiCl (not shown); **Below:** 5M LiCl in DMF, where the solution phase separates with time; here the solution and solid phases are distinct, and distinct from LiCl, DMF or DMF·LiCl.

Force field for DMF·LiCl:

Bonded parameters: From OPLA-AA force field

vdW parameters in the form of Lennard Jones potential: OPLA-AA force field

Electrostatic charges for Coulombic potential: hybrid B3LYP functional with aug-cc-PVQZ basis set using CHELPG method.

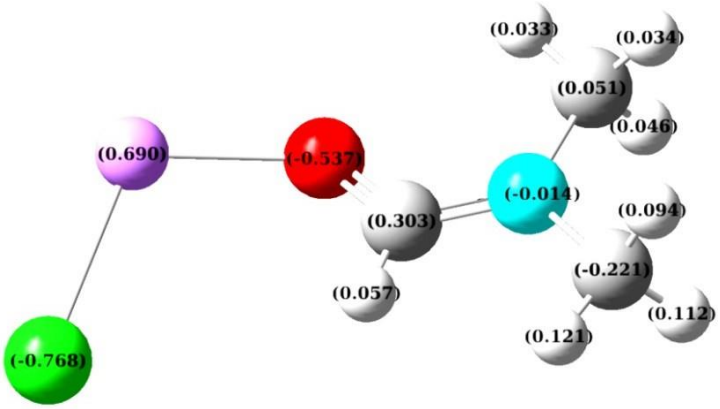

Figure C4. Distribution of partial charges from electrostatic potential on LiCl·DMF single molecule Dipole moment: 10.9 Debye from B3LYP functional with aug-cc-PVQZ basis set using CHELPG method.

Table C1. Dipole moment (in Debye) of DMF determined using different quantum calculations.

Experimental	3.82[4]
PBE/6-311++G(d,p)	4.069
B3LYP/6-311++G(d,p)	4.174
CCSD/6-311++G(d,p)	4.399
M06-2X/6-311++G(d,p)	4.205
B3LYP/aug-cc-PVQZ	4.069

[4] Computational Chemistry Comparison and Benchmark DataBase Release 18 (October 2016) Standard Reference Database 101 National Institute of Standards and Technology. http://cccbdb.nist.gov/diplistx.asp#NSRDS-NBS10

Heat of vaporization of DMF and DMF·LiCl:

Heat of vaporization from simulation can be calculated from enthalpy of bulk system using the relation:

$$\Delta H_{vap} = < h_{gas}(T) > - < h_{liq}(p,T) >$$

ΔH_{vap} for DMF, at 298 K:

10.492 kcal/mol (from simulations) 11.10 kcal/mol (from experiments)[5]

Ionic charge density of the system V at different temperatures:

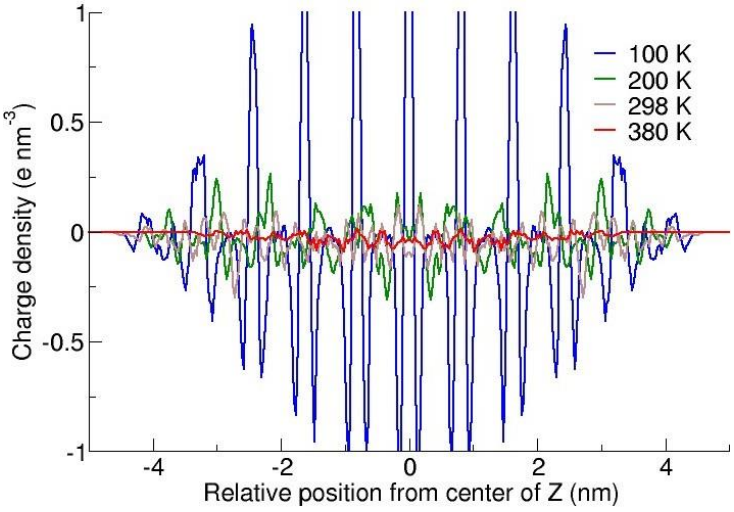

Figure C5. Distribution of charges carried by Li^+ and Cl^- in *z*-dimension of the crystal structure modeled as system *V*.

Calculation of density gradients in simulated crystal:

Since the interatomic distances correspond to only to O--Li—Cl networks, the density at the interfacial regions cannot be calculated. Further, the density in the interfacial regions is also not uniform in all directions of the simulation box. However, a density

[5] Chickos, J. S.; Acree, W. E. Enthalpies of Vaporization of Organic and Organometallic Compounds, 1880-2002. *J. Phys. Chem. Ref. Data* **2003**, *32*, 519–878.

distribution can be obtained by using very fine grids perpendicular to the X, Y and Z directions of the simulation box. The density distribution in System V (T = 298 K) is shown in **Figure C6**. The density distribution (in each direction) shows a gradual decrease from the bulk to the interfacial regions. The dotted lines in **Figure C6**. represent the interfacial regions where the change in density is lower by at-least 30% compared to the bulk mass density.

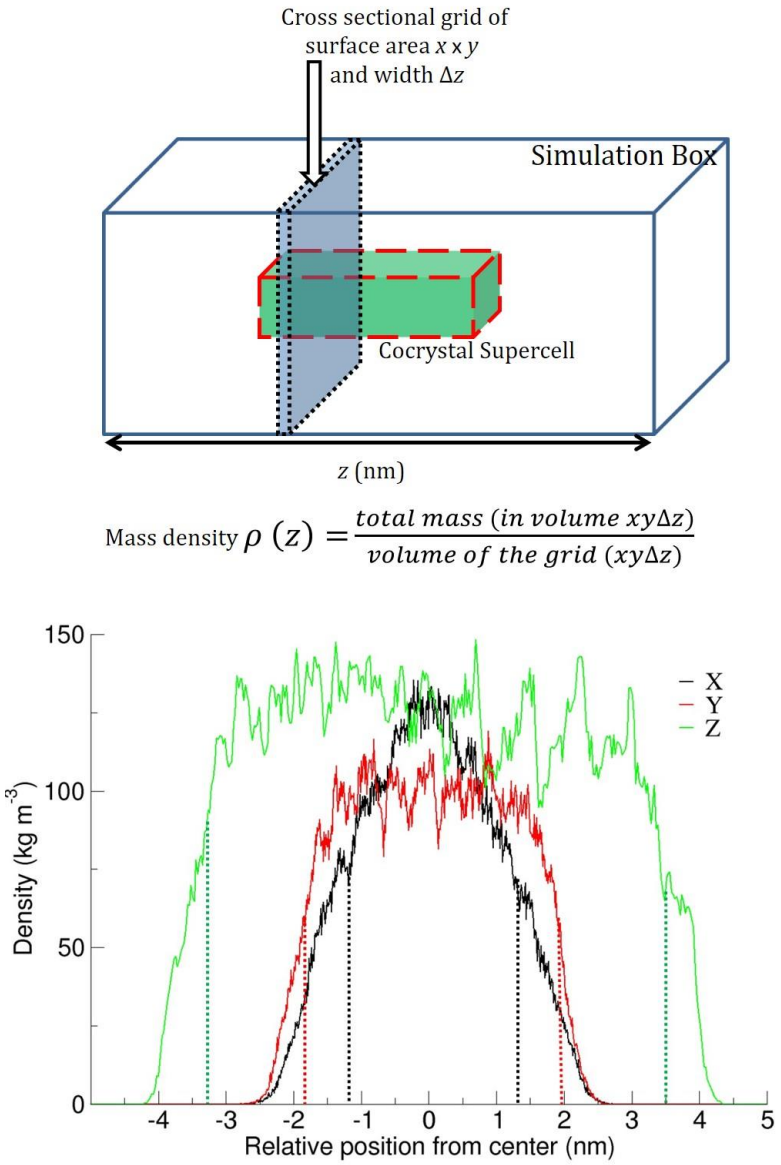

Figure C6. The mass density distribution in System V (T = 298 K) in fine grids perpendicular to X, Y and Z directions. Schematic diagram shows how the mass density distribution is calculated across the box (System V) in Z direction.

Calculation of interaction energy of different fragments using DFT:

(i) Fragment relaxations: Li^+---Cl^-DMF and LiCl---DMF

fCP method: Fragment Counterpoise method the correction to incompleteness of the basis sets and the interaction energies are calculated as:

$$\Delta E_{AB} = E_{AB}^{a\cup b}(AB) - \left[E_{AB}^{a\cup b}(A) + E_{AB}^{a\cup b}(B)\right] \quad (1)$$

where, subscript is the geometry of structure, superscript is the basis set used and the entity for which energy is calculated is in parenthesis (). '*a'*, '*b'* and '*ab'* are basis functions for A, B, and AB respectively.

rig-fCP method: Rigorous fragment Counterpoise method provides the additional correction to errors associated to fCP method- Basis Set Superposition Error and takes care of fragment relaxation for monomer to dimer optimizations. The interaction energy in this method is calculated as:

$$\Delta E_{AB} = E_{AB}^{a\cup b}(AB) - \left[E_{A}^{a}(A) + E_{B}^{b}(B)\right] + \left[E_{AB}^{a}(A) - E_{AB}^{a\cup b}(A) + E_{AB}^{b}(B) - E_{AB}^{a\cup b}(B)\right] \quad (2)$$

The last four energy terms in square bracket are the correction to BSSE.

(ii) Tetramerization: If 4A (in optimized structure- A_1, A_2, A_3 and A_4 form a tetramer 'T', then energy of tetramerization is calculated as:

$$\Delta E_{tet}(fCP) = E_T^{4a}(T) - \sum_{i=1}^{4} E_T^{4a}(A_i) \quad (3)$$

and

$$\Delta E_{tet}(\text{rig} - \text{fCP}) = E_T^{4a}(T) - \sum_{i=1}^{4} E_{A_i}^{a}(A_i) + \sum_{i=1}^{4} E_T^{a}(A_i) - \sum_{i=1}^{4} E_T^{4a}(A_i) \quad (4)$$

Since without optimization, ΔE(fCP) → ΔE(rig-fCP), hence for D1 and D2 dimers, single point interaction energies **(Table 4.1)** are calculated using fCP method only (equation 1)

Table C2. Important structural parameters of single point and optimized geometries for Interaction energy analysis (B3LYP/6-311++G(d,p) for both single point and optimization).

Structure	O-Li-Cl angle (deg)	Li-O distance (Å)	Li-Cl distance (Å)
DMF·LiCl monomer-sp **M1**	111.773	1.963	2.328
DMF·LiCl monomer-opt **M2**	179.973	1.837	2.076
DMF·LiCl dimer-opt **D0**	157.006	1.880	2.140
two dimer configurations (unoptimized)			
DMF·LiCl sp Normal **D1**	118.113 118.113	1.963 1.963	2.341 2.341
DMF·LiCl sp Invert **D2**	114.323 114.323	1.956 1.956	2.341 2.341
two dimer config started from optimized dimer geometry			
DMF·LiCl opt Normal **D3**	110.699 110.699	2.045 2.045	2.143 2.143
LiCl·DMF opt Invert **D4**	157.886 157.8869	1.883 1.883	2.141 2.141
Tetramer Analysis			
T1	139.232 118.471 139.232 118.471	1.919 1.989 1.919 1.989	2.142 2.303 2.142 2.303
T2	118.615 117.518 139.186 121.761	1.989 1.952 2.044 1.919	2.302 2.144 2.302 2.142
T3	146.061 163.255 163.201 143.046	1.902 1.794 1.794 1.902	2.154 2.116 2.116 2.154
T4	121.982 163.638 163.64 121.968	1.946 1.795 1.795 1.946	2.155 2.117 2.117 2.155
T5	118.296 138.73 118.296 138.73	1.99 1.919 1.99 1.919	2.302 2.143 2.302 2.143

The colors for parameters are based on color codes for fragments defined for Counterpoise calculation of interaction energy from fCP and rig-fCP methods.

Appendix D

Differential Scanning Calorimetry of $(DMF)_2NaClO_4$

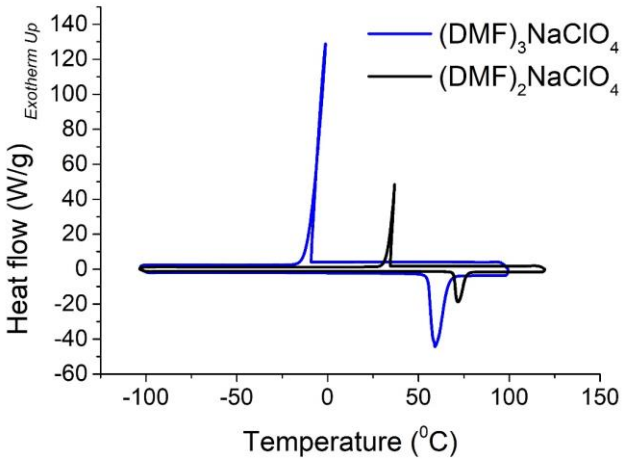

Figure D1. DSC of $(DMF)_2NaClO_4$ at scan rate of 10 ^{0}C/min. Data for $(DMF)_3NaClO_4$ is plotted for comparison from Zdilla and coworkers [89].

Force-field parameters for classical MD simulation of $(DMF)_3NaClO_4$

Bonded parameters: From OPLS-AA force field

vdW parameters in the form of Lennard Jones potential: OPLS-AA force field

Electrostatic charges for Coulombic potential-

Charge on Na^+ ion: Calculated from optimized structure of $[Na(DMF)_6]^+$ in gas phase using MP2//aug-cc-PVDZ method. $q_{Na^+} = +0.91525\ e^-$

Charge on Cl and O atoms in ClO_4^- anion: Calculated from optimized structure of ClO_4^- in gas phase using MP2//aug-cc-PVDZ, and scaled by q_{Na^+}.

$q_{O(ClO4-)} = -0.4927\ e^-$, $q_{Cl(ClO4-)} = +1.05555\ e^-$

Charge on atoms in DMF molecule: adapted from *J. Mol. Liq.* **2015,** *206,* 338-342.

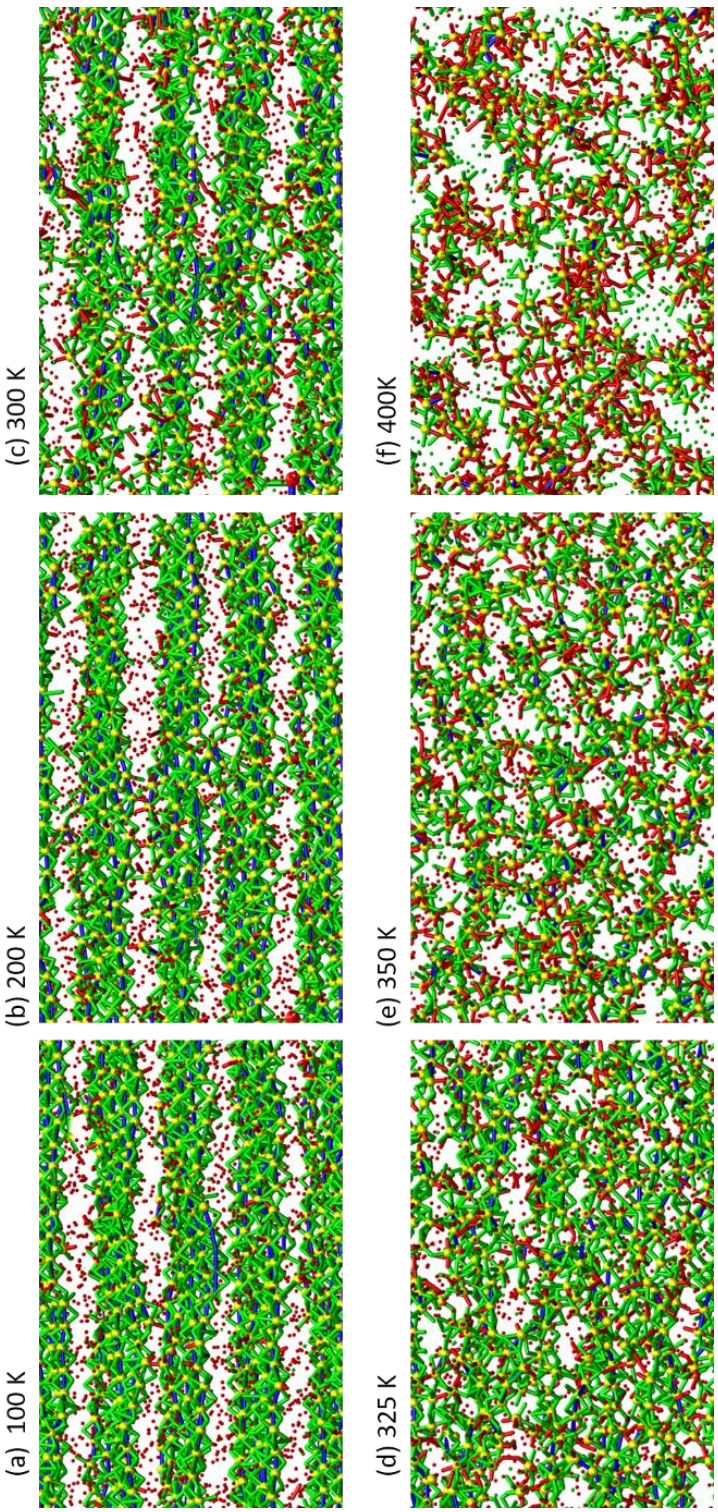

Figure D2. Snapshots of $(DMF)_3NaClO_4$ simulated as model P. Atoms: Yellow- Na^+, Green- O(DMF), Red- $O(ClO_4^-)$; Bonds: Blue- Na...Na, Green- Na...O(DMF), Red- Na...$O(ClO_4^-)$; Cut-off for dynamic bonds: Na…Na ≤ 3.5 Å, Na…O(DMF) ≤ 3.0 Å, Na…$O(ClO_4^-)$ ≤ 2.2 Å.

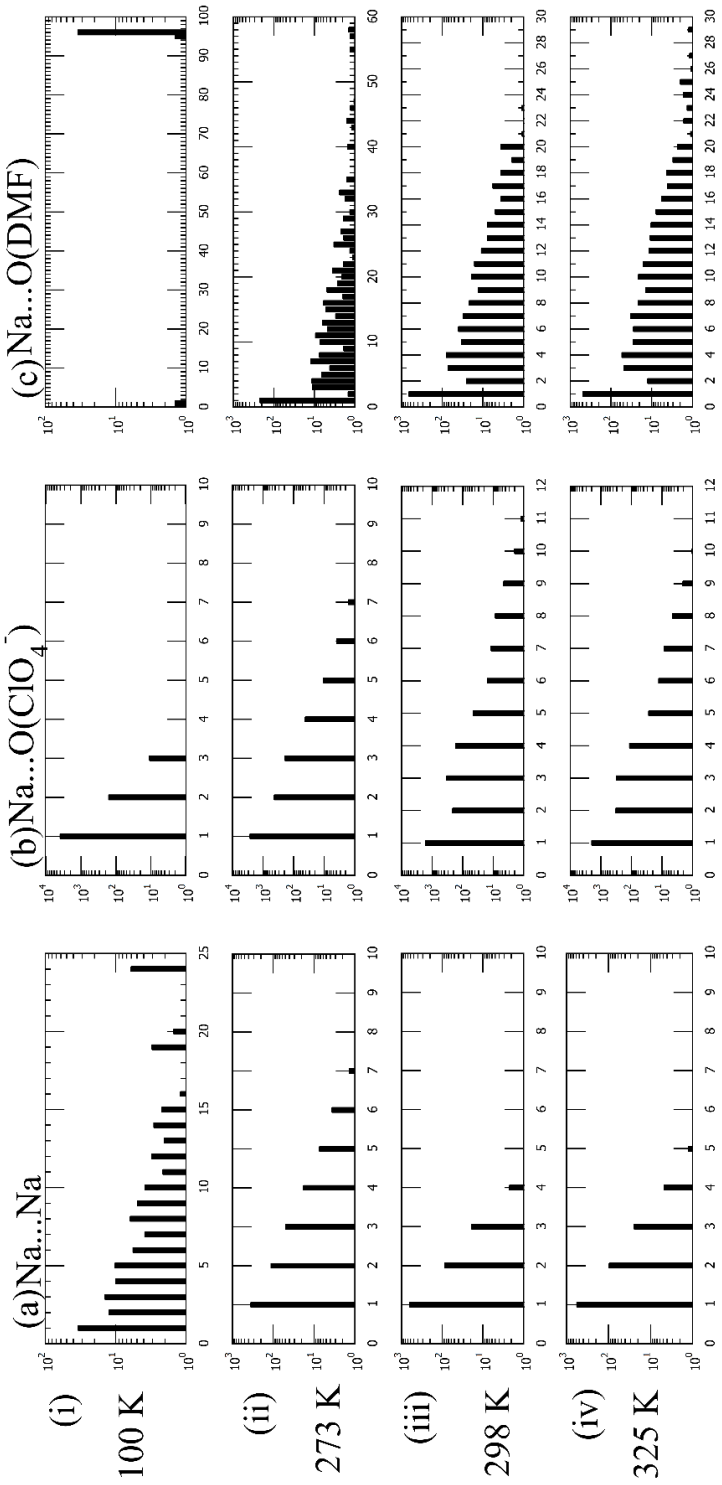

Figure D3. Cluster analysis for $(DMF)_3NaClO_4$ simulated at constant temperature under *NpT* ensemble conditions (a) Na...Na clusters (≤ 3.5 Å), (b) $Na...ClO_4^-$ clusters (≤ 2.2 Å), (c) Na...DMF clusters (≤ 3.0 Å); (i) 100 K, (ii) 273 K, (iii) 298 K and (iv) 325 K. Y-axis: number of clusters, X-axis: size of clusters.

RDFs calculated from simulations on model P:

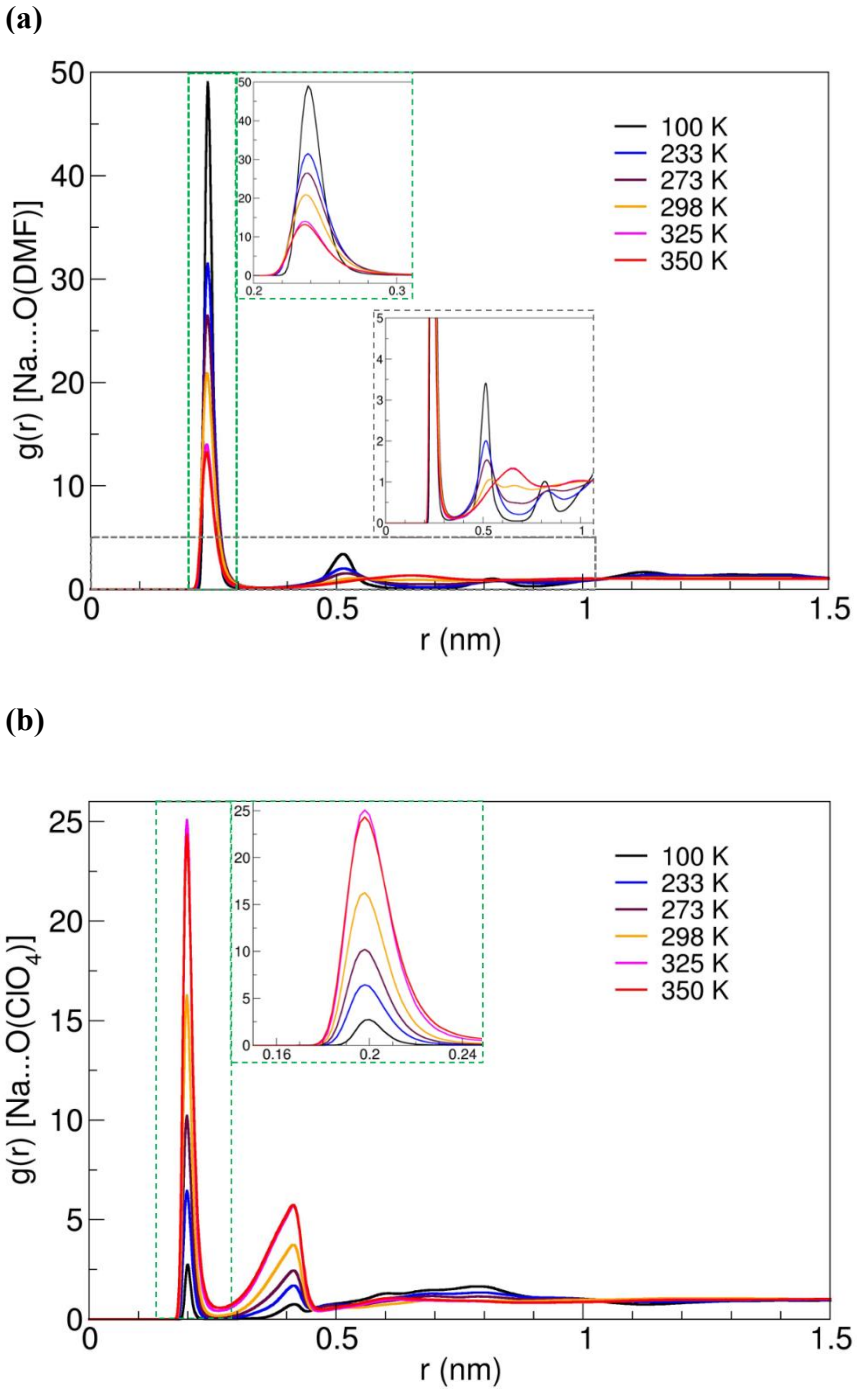

Figure D4. RDFs of **(a)** Na---O(DMF) and **(b)** Na---O(ClO_4^-) from *NpT* simulations on model P at various temperatures. The calculated coordination numbers from the integration of RDFs are plotted on next page.

Coordination numbers calculated from integration of RDFs for model P:

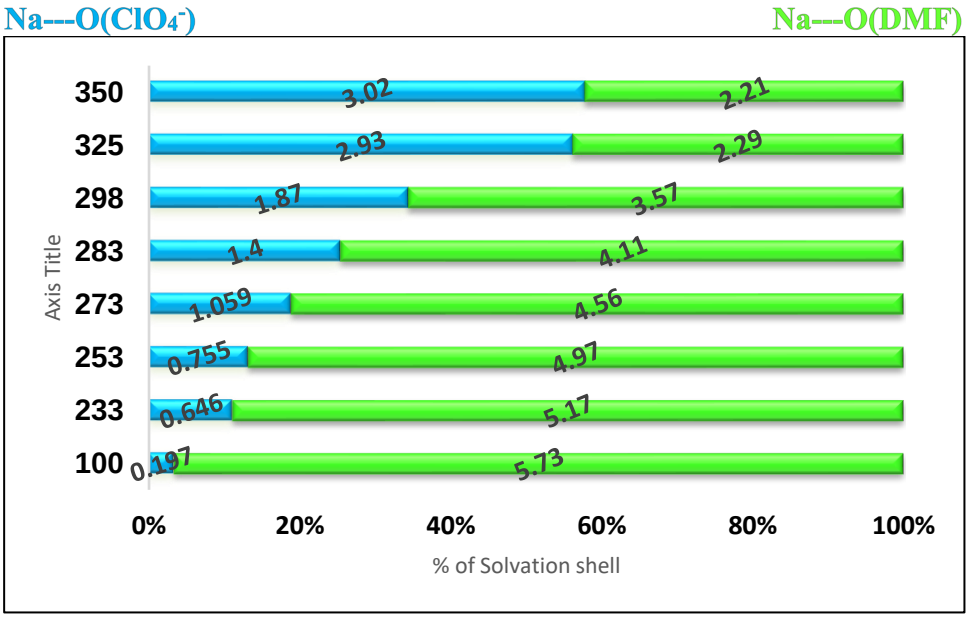

Figure D5. Calculated coordination number of O atoms of DMF and ClO_4^- anion around Na^+ in the cocrystalline $(DMF)_3NaClO_4$ model P at constant temperatures, simulated under *NpT* ensemble.

Mean square displacements of Na^+ cations in model P:

(a) **(b)**

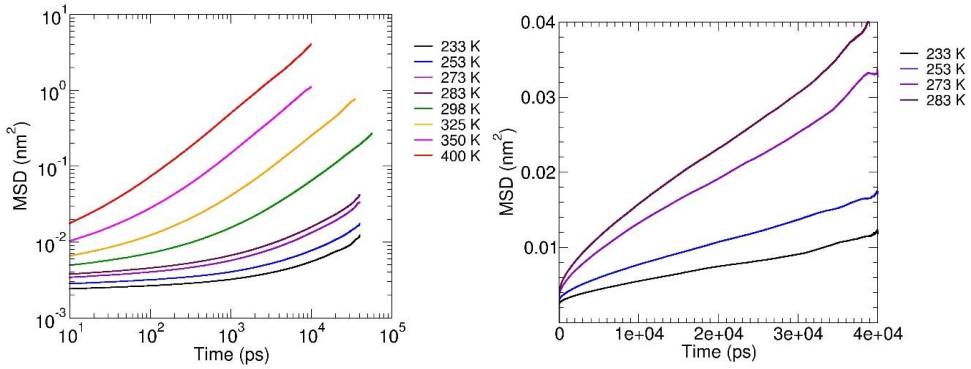

Figure D6. MSD *vs.* time plot for Na^+ cations on a (a) logarithmic scale for all temperatures and (b) linear scale, for low temperatures.

Mean square displacements of ClO_4^- anions in model *P*:

(a) **(b)**

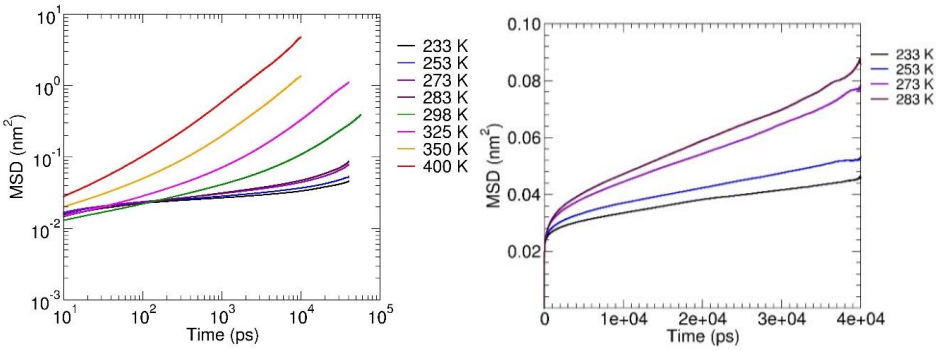

Figure D7. MSD *vs.* time plot for ClO_4^- anions on plotted on **(a)** logarithmic scale, for all temperatures and **(b)** linear scale, for low temperatures.

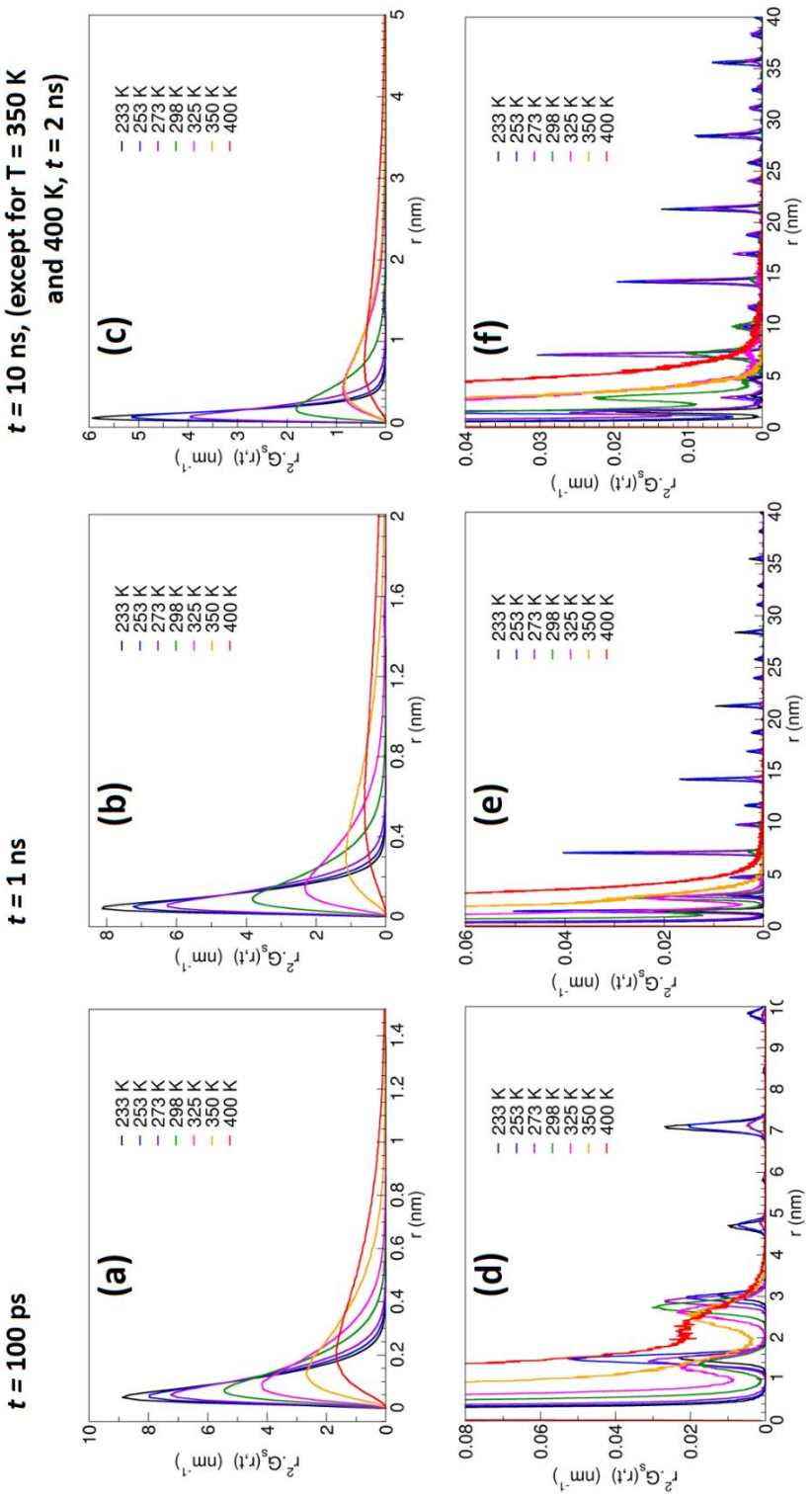

Figure D8. Self-part of van Hove ACF for Na^+ ions in $(DMF)_3NaClO_4$ at various constant temperatures and a fixed time interval from an overall trajectory of 40 ns, in model P: **(a)** t = 100 ps, **(b)** t = 1 ns, and **(c)** t = 10 ns except at T = 350 K and 400 K, t = 2ns; **(d)**, **(e)** and **(f)** are zoom in on y-axis and zoom out on x-axis plots of (a), (b) and (c) respectively.

Appendix E

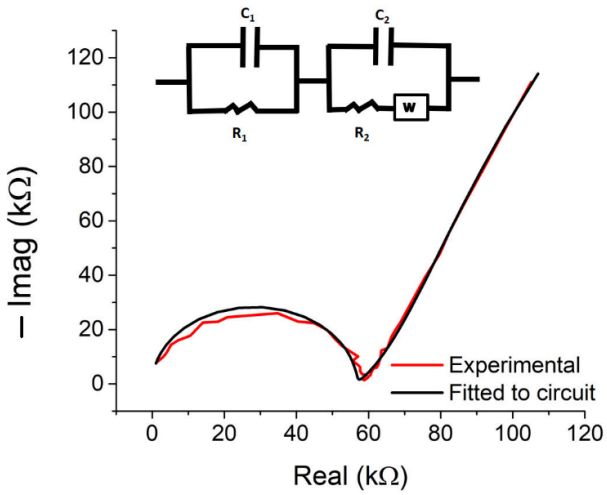

Figure E1. Nyquist plot and the fitted data using the circuit model (inset) to extrapolate the impedance at -20 ^{0}C. The given circuit is used to calculate conducitvity (resistance) at all the other temperatures.

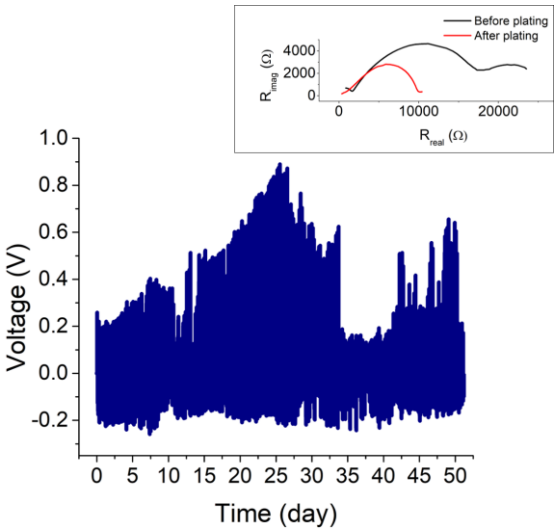

Figure E2. $Na^{0}/(ADN)_3NaClO_4/Na^{0}$ cycling data using a current density of 0.01 mA cm^{-2} and 2h charge/2h discharge. The sodium metal is soaked in 1M $NaClO_4$ EC:PC (1:1) with 5% FEC.

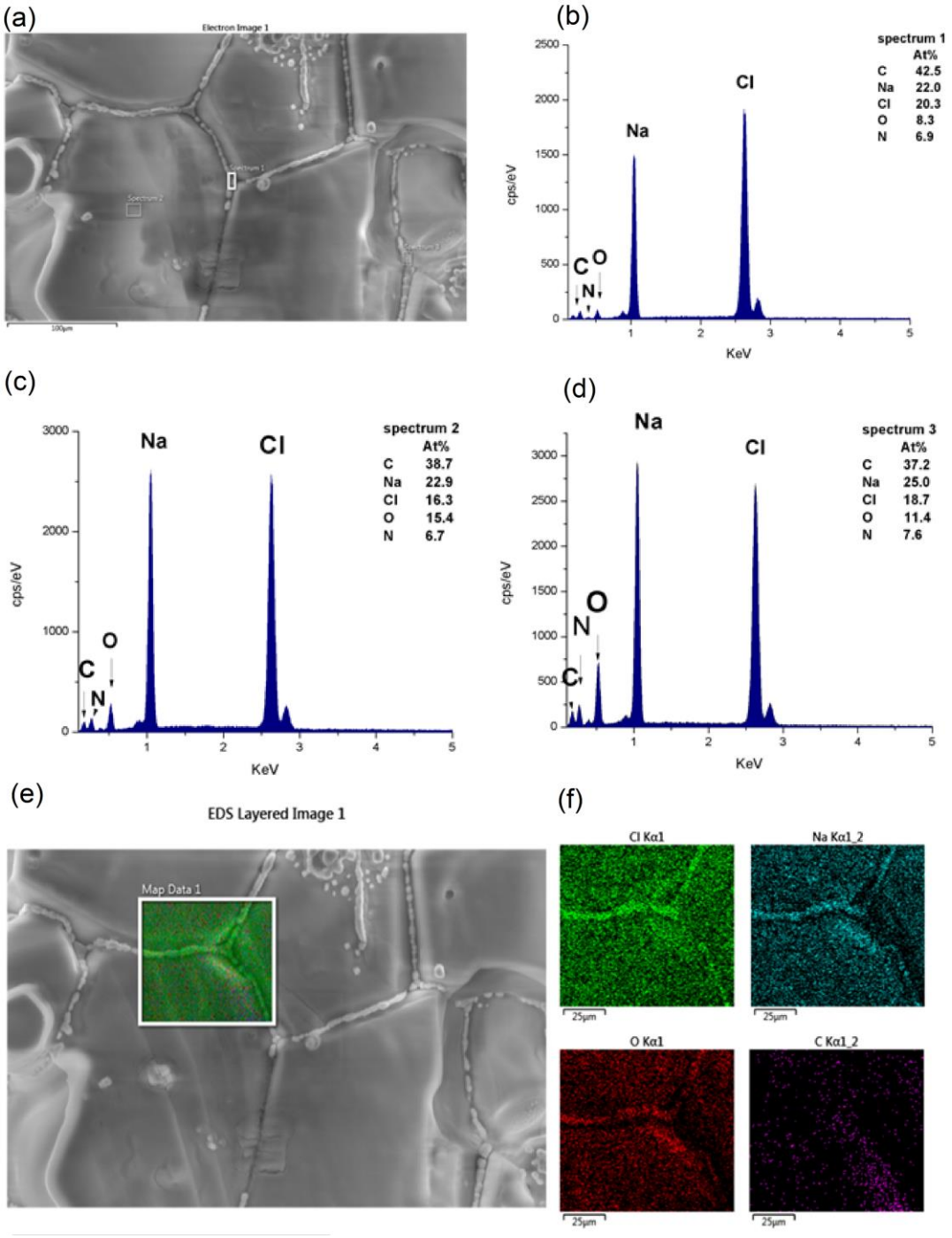

Figure E3. (**a)** SEM image of unrinsed $(ADN)_3NaClO_4$ cocrystals and elemental analysis from energy dispersive X-ray spectroscopy showing mol% of elements in **(b)** and **(d)** grain boundary regions and **(c)** bulk surface. The region shown in **(e)** was used for elemental maps of **(f)** Cl, Na, O and C atoms, which indicate high concentration of $NaClO_4$ in grain boundary (after removal of ADN due to presence of SEM vacuum).

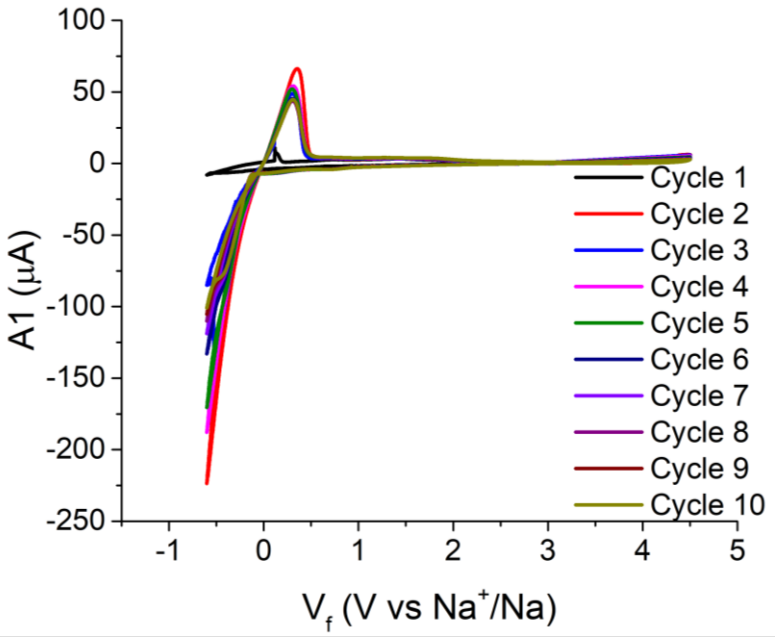

Figure E4. Cyclic Voltammetry of co-crystalline $(ADN)_3NaClO_4$ at room temperature in a SS/$(ADN)_3NaClO_4$ /Na^0 cell at a scan rate 0.9 $mV \cdot s^{-1}$ as a function of cycle number. The $(ADN)_3NaClO_4$ was incorporated into a glass fiber matrix by melt casting at 100 ˚C.

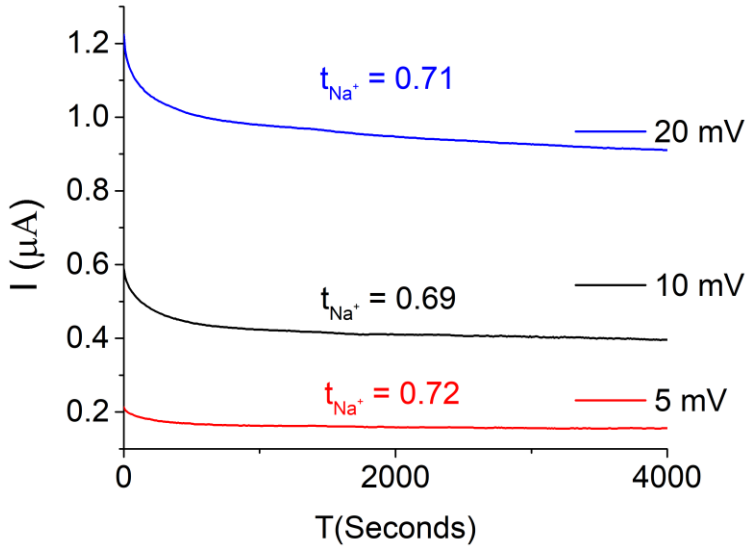

Figure E5. Chronoamperometry data showing Na^+ ion transference number in co-crystalline $(ADN)_3NaClO_4$ at room temperature in a Na^0/$(ADN)_3NaClO_4$ /Na^0 cell.

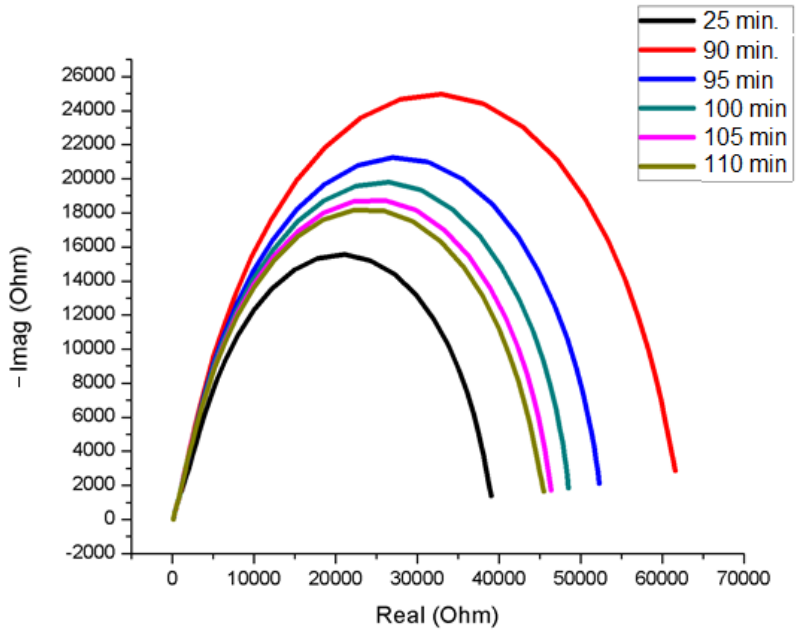

Figure E6. $Na^0/(ADN)_3NaClO_4$ /Na^0 stability test over time at room temperature. The sodium metal is pre-treated with 1M NaPF6 in ADN/EC (1:1). Resistance gradually increases up to 90 minutes (intervening data not shown) and then begins decreasing.

Protocols for force-field development for classical MD simulations

Form of the force field: Classical non-polarizable:

$$V = \sum_{bonds} k_r(r - r_0)^2 + \sum_{angles} k_\theta(\theta - \theta_0)^2 + \sum_{dihedrals} k_\varphi[1 + \cos(n\varphi - \varphi_0)] + \sum_{improper} k_\psi(\psi - \psi_0)^2 + \sum_{i,j}\left[4\epsilon_{ij}\left\{\left(\frac{\sigma_{ij}}{r_{ij}}\right)^{12} - \left(\frac{\sigma_{ij}}{r_{ij}}\right)^{6}\right\} + \frac{q_i q_j}{\varepsilon_0 r_{ij}}\right]$$

All the bonded potential parameters (force constants for bond vibrations, bending and dihedral rotations) were taken from OPLS-AA force field.

Equilibrium bond lengths for O-Cl bond in perchlorate anion and C≡N bond in ADN were taken from single crystal X-ray diffraction data.

vdW potential parameters for all the atoms were taken from OPLS-AA force field.

Coulombic parameters – in the form of partial charges were derived from DFT calculations (B3LYP/6-311++G**) using CHarges from Electrostatic Potential-Grid (CHELPG) method. The partial charges on Na^+ cation, ClO_4^- anion and ADN are shown below:

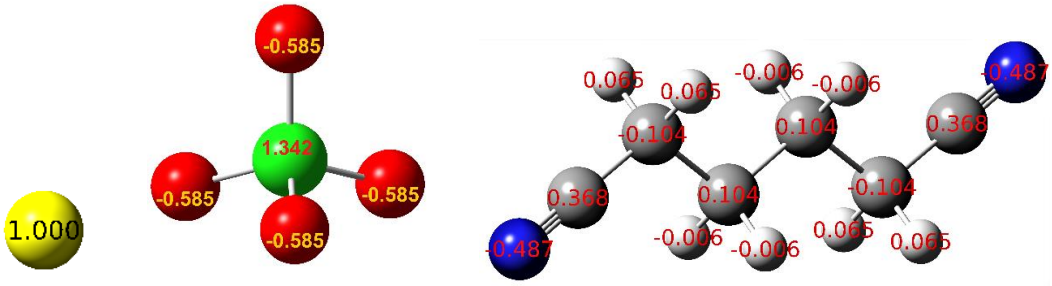

Figure E7. Partial charges for ClO_4^- ion and ADN solvent used for classical MD simulations.

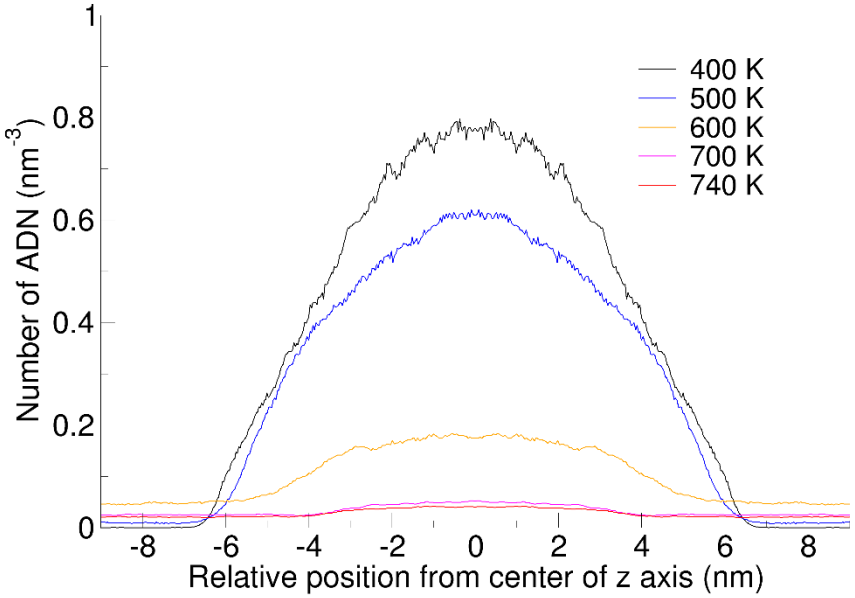

Figure E8. Calculated number density of ADN in cross sections along z-axis of the box in model *V* from various discreate temperature simulations.

Table E1. Self-diffusion coefficients for Na^+ ions calculated from simulations on model *D* (bulk) and model *V* (surface) along with activation barriers.

Model	Temperature (K)	D_{Na^+} x 10^8 (cm^2-s^{-1})	E_a barrier (kJ-mol^{-1})
D	423	0.08 ± 0.02	48 ± 7
	453	0.21 ± 0.04	
V	298	1.4 ± 0.2	35 ± 4
	323	4.0 ± 0.3	
	343	8.5 ± 0.4	

Table E2. Comparison of unit cells: Theoretical vs. XRD. Theoretical unit cell parameters were calculated from variable cell relaxation of XRD unit cell using pw.x code in QUANTUM ESPRESSO v6.2 package. Relaxations were allowed to all the parameters with a pressure threshold of 0.5 kbar.

Parameters	a (Å)	b (Å)	c (Å)	α	β	γ	V ($Å^3$)
Theoretical	11.1323	11.1323	15.6244	90.000	90.000	120.000	1676.89
Experimental	11.2585	11.2585	15.6422	90.000	90.000	120.000	1717.08

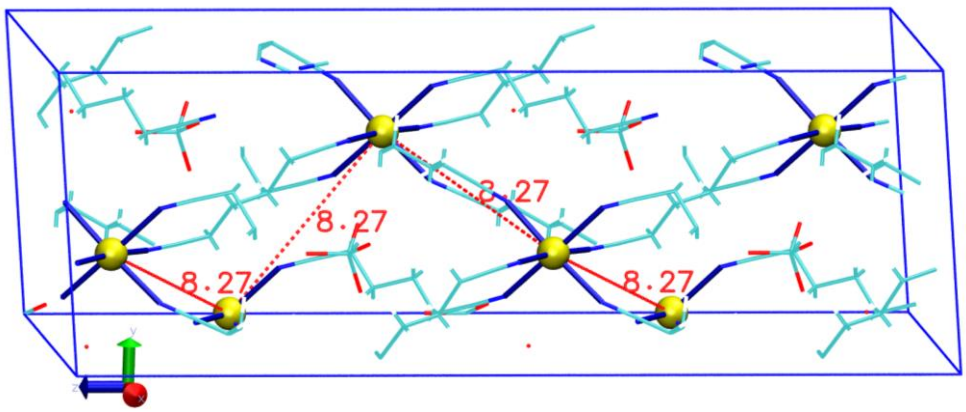

Figure E9. A 1x1x2 supercell of $(ADN)_3NaClO_4$ and anticipated Na^+ ion migration path used as an input in PW-DFT NEB calculations.

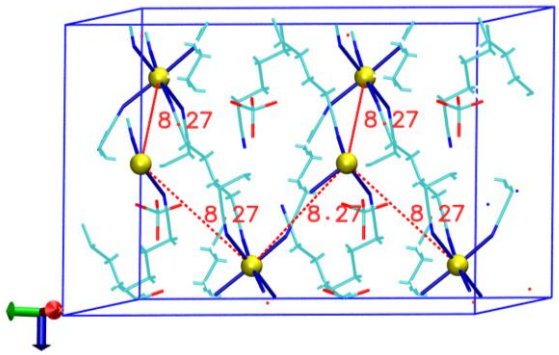

Figure E10. A 1x2x1 supercell of $(ADN)_3NaClO_4$ and anticipated Na^+ ion migration path used as an input in PW-DFT NEB calculations.

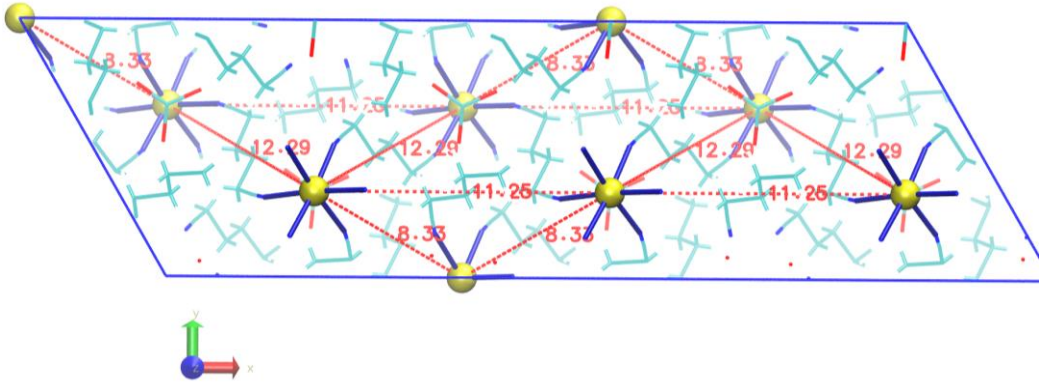

Figure E11. A 3x1x1 supercell of $(ADN)_3NaClO_4$ and anticipated Na^+ ion migration paths used as an input in PW-DFT NEB calculations.

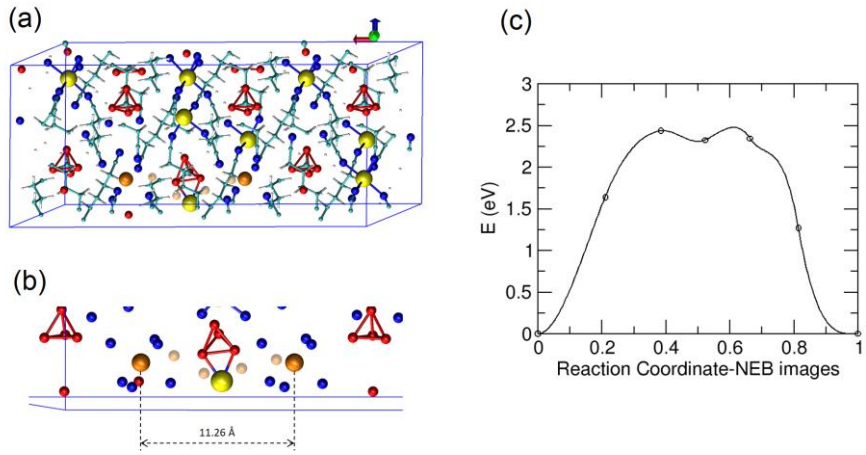

Figure E12. (a) 3x1x1 supercell with a Na^+ ion vacancy (orange large spheres) with regular occupancy and intermediate Na^+ ions (yellow spheres), **(b)** zoomed in, intermediate structure, **(c)** calculated minimum energy path from NEB. The path was not fine-tuned further, owing to a very large barrier suggested by CI-NEB calculations.

Appendix F

Force-field parameters for classical MD simulations of $(ADN)_2LiPF_6$

A. All interaction terms in a classical non-polarizable force field can be written as:

$$V = \sum_{bonds} k_r(r - r_0)^2 + \sum_{angles} k_\theta(\theta - \theta_0)^2 + \sum_{dihedrals} k_\varphi[1 + \cos(n\varphi - \varphi_0)] + \sum_{improper} k_\psi(\psi - \psi_0)^2 + \sum_{i,j}\left[4\epsilon_{ij}\left\{\left(\frac{\sigma_{ij}}{r_{ij}}\right)^{12} - \left(\frac{\sigma_{ij}}{r_{ij}}\right)^{6}\right\} + \frac{q_i q_j}{\varepsilon_0 r_{ij}}\right]$$

B. Bonded potential parameters like force constants for bond stretches and bending and vdW potential parameters were taken from OPLS-AA force field.

C. Single crystal XRD (collected at 100 K) was used to produce equilibrium bond lengths and bond angles in the system.

Partial charges on atoms were derived using Electrostatic Potential-Grid (CHELPG) method. The partial charge on Li^+ cation were calculated using $[Li(ADN)_4]^+$ structure shown below (ωB97xD functional with 6-311++G(d,p)$_{optimization}$/aug-cc-PVDZ $_{charge\ calculation}$). Partial charges on PF_6^- and ADN were calculated using MP2//aug-cc-PVDZ method. The partial charge on Li^+ calculated from $[Li(ADN)_4]^+$ structure was used to scale charges on PF_6^- ion. These structures are shown in **Figure F1** and the partial charges used during the simulations are provided in the **Table F1** below.

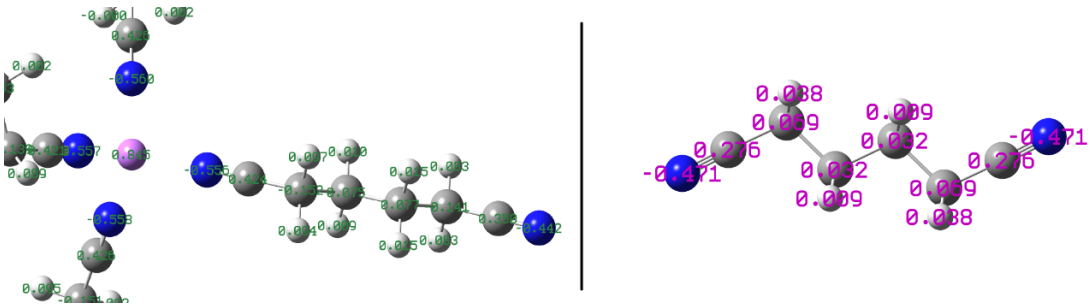

Figure F1. Partial charges on Li^+ ion in $[(ADN)_4Li]^+$ **(left)** and ADN **(right)**.

Table F1. Partial charges on Li, P and F atoms used for MD simulations. Partial charges for ADN are shown in the **Figure F1** (right)

ATOM	Charge
Li	0.8455
P	1.2476
F	-0.34885

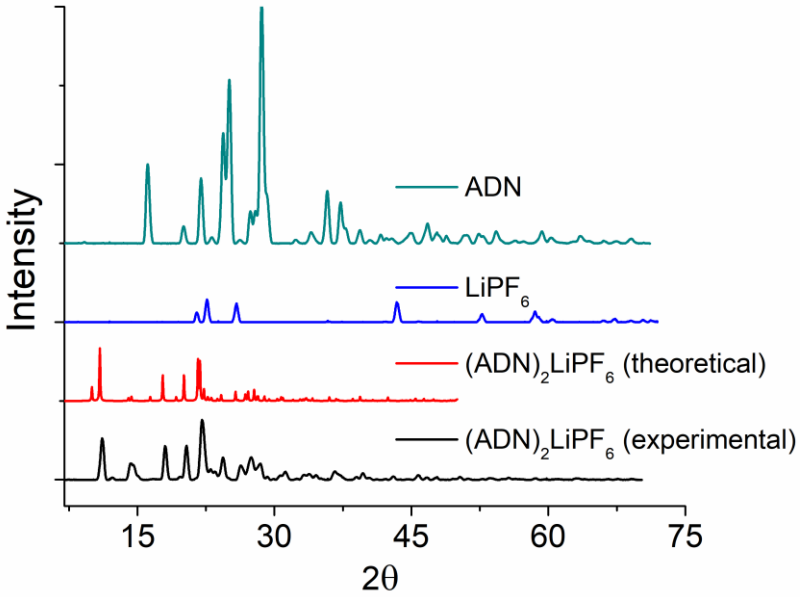

Figure F2. Experimental powder XRD spectra for ADN, $LiPF_6$ and $(ADN)_2LiPF_6$ cocrystals. Theoretical spectra for $(ADN)_2LiPF_6$ is calculated using the single crystal structure in Mercury software.

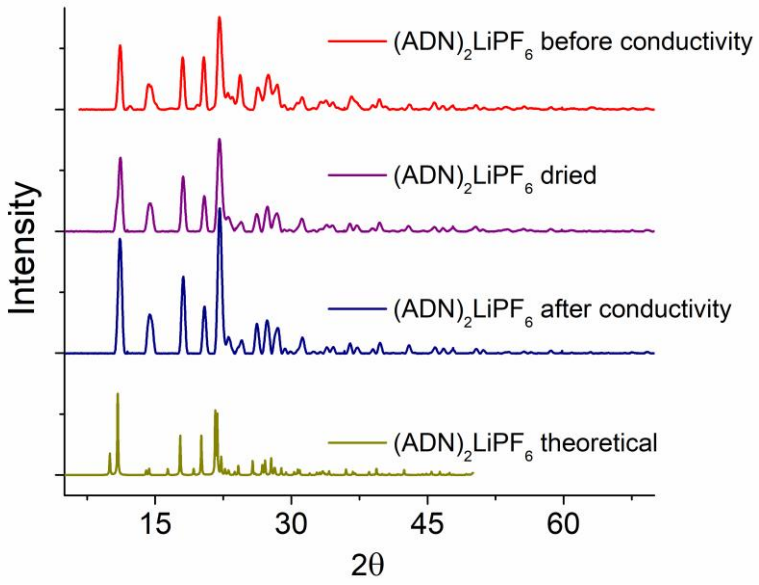

Figure F3. X-ray powder diffraction of crystalline $ADN_2.LiPF_6$ before and after conductivity measurements, an overdried sample and theoretical pattern generated from single crystal data.

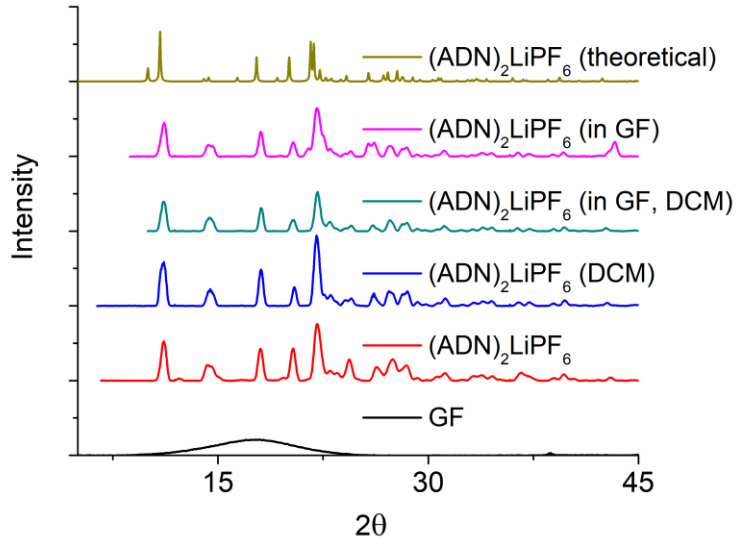

Figure F4. X-ray powder diffraction of various samples of crystalline $ADN_2.LiPF_6$ synthesized in: the glass fiber separator, rinsed with dichloromethane (DCM), incorporated in the glass fiber separator using DCM at 40-45 ^{0}C, pressed pellet and theoretical pattern generated from single crystal data.

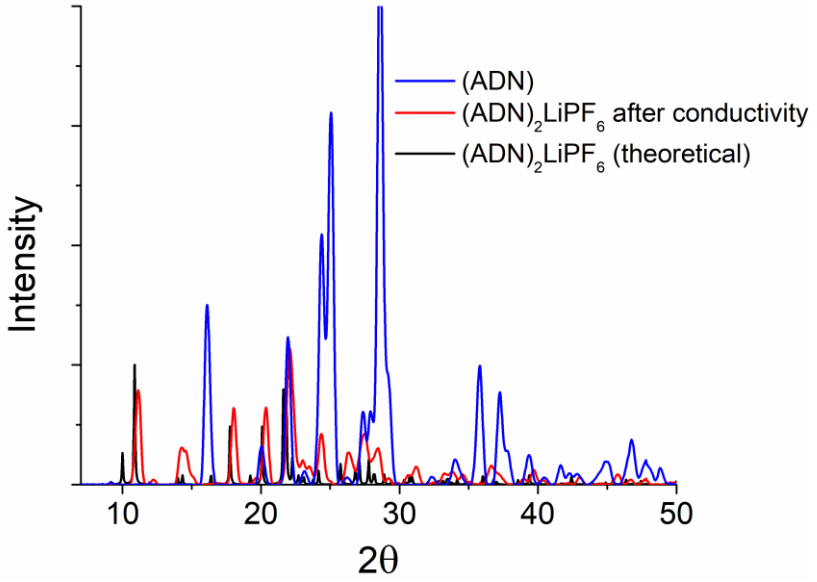

Figure F5. A zoomed in view to the powder XRD patterns of ADN and $(ADN)_2LiPF_6$ showing that there are no peaks of *free* ADN at 11, 14 or 17^0 in cocrystals after conductivity measurement.

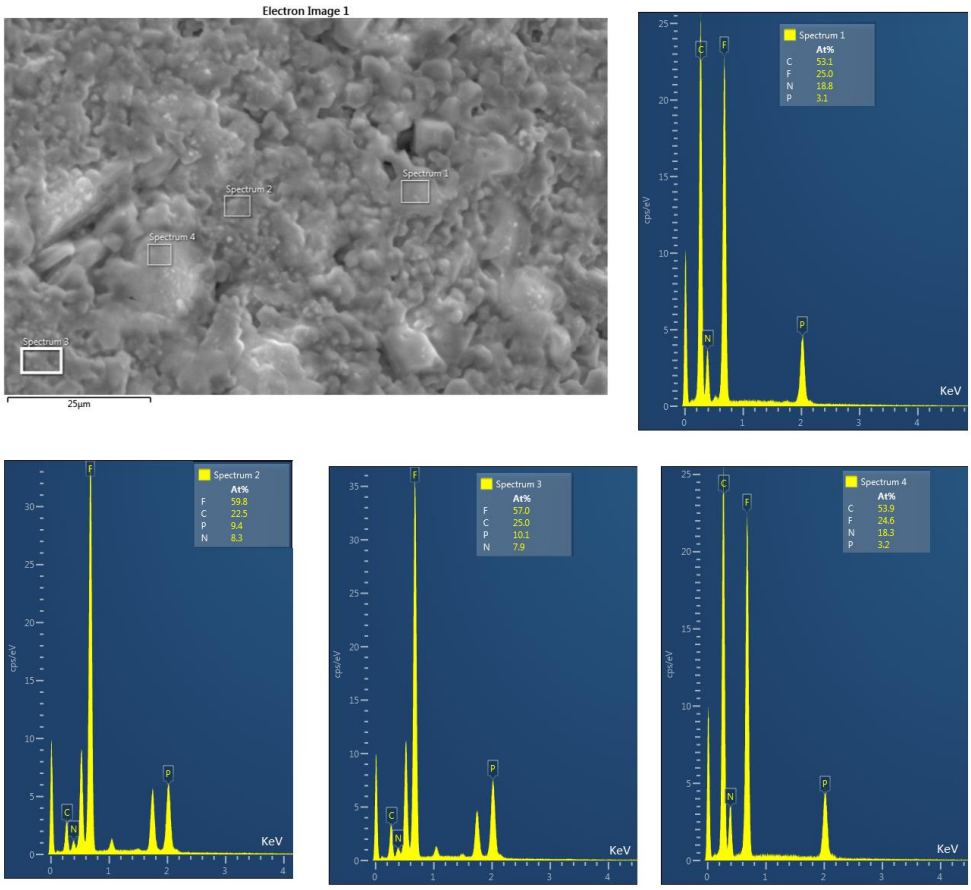

Figure F6. SEM image of pure polycrystalline $(ADN)_2LiPF_6$ powder (pressed neat sample) with EDS analyzed in various regions.

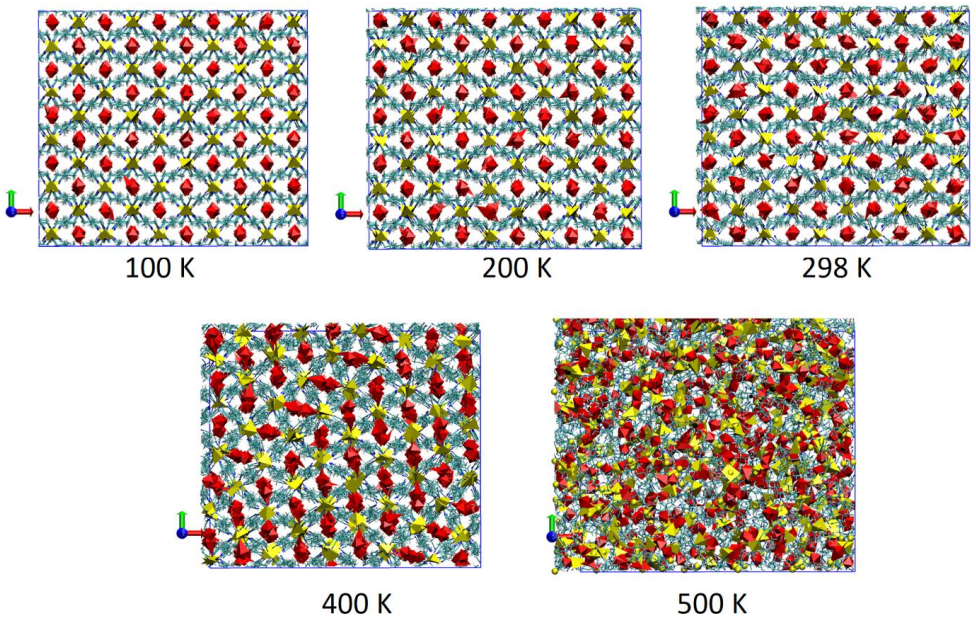

Figure F7. Snapshots of output configurations of $(ADN)_2LiPF_6$ cocrystals (*xy*-plane) simulated as **model *P***, equilibrated for 20 ns at different temperatures. Li---N(ADN) coordinated networks are shown as yellow tetrahedrons and PF_6^- anions are shown as red octahedrons. ADN solvent is shown as a line representation.

Table F2. Experimental and theoretical (calculated from DFT) peaks for Raman spectra of ADN in $(ADN)_2LiPF_6$ salt and pure ADN. The theoretical peaks were obtained from frequency calculation on optimized geometry of $[(ADN)_4Li^+]$

Peaks	Experimental	Theoretical	Assignment
ADN in $(ADN)_2LiPF_6$	2273.6 (highest intensity)	2291.8 (highest intensity) All CN in phase	Lithium bonded CN, all four simultaneous symm stretch
	2272	2290 (1CN out of phase), 2290.3(two peaks) 2 CN out of phase 2290.8 (3 in phase)	Lithium bonded CN, three/two symm strech
	2242.7	2276.7	One Free terminal CN
	2244.3	2276.6 (two peaks), , 2276.8	One Free terminal CN
ADN	2241.2, 2241.7	2271.8	CN stretch in pure AND: both ends free

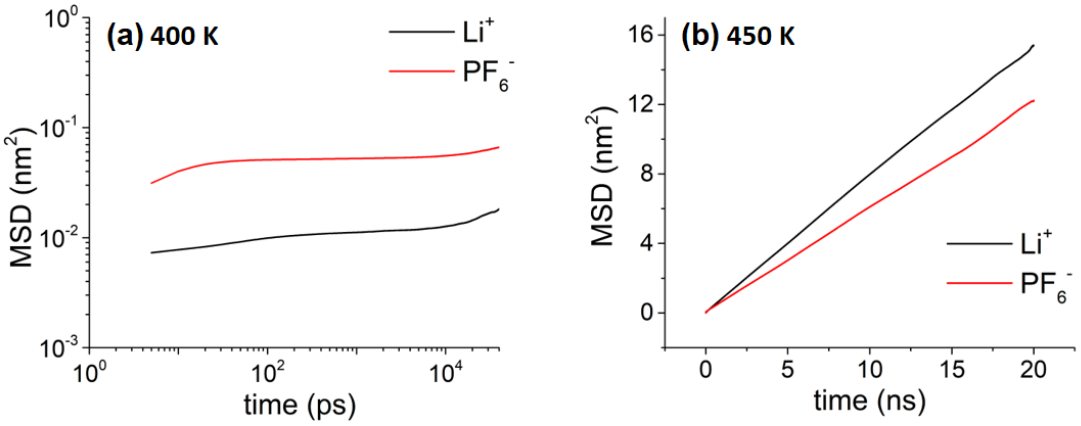

Figure F8. MSD *vs.* time plot for Li^+ and PF_6^- ions in **model *D*** at **(a)** T = 400 K, where a logarithmic scale is used due to non-linear diffusion and at **(b)** T = 450 K, where linear scale is used due to linear diffusion.

Table F3. Theoretical (DFT) and experimental (XRD) lattice parameters for $(ADN)_2LiPF_6$ cocrystalline electrolyte.

Parameters	a (Å)	b (Å)	c (Å)	α	β	γ	V (Å^3)
Theoretical	11.16	13.12	12.71	90.00	89.99	89.77	1860.99
Experimental	10.80	12.64	12.35	90.00	90.00	90.00	1686.83

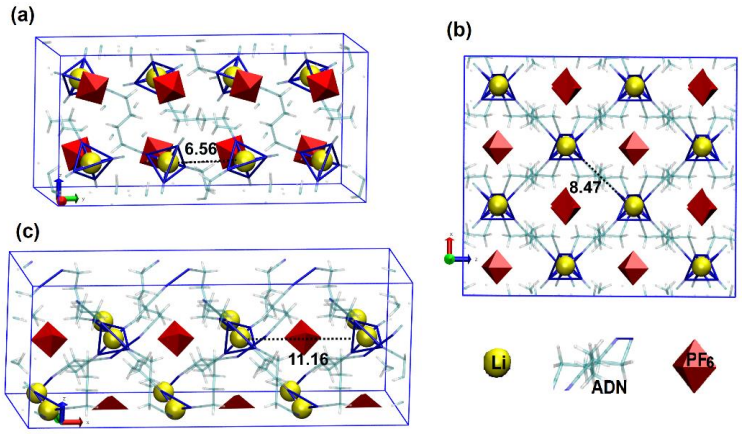

Figure F9. Supercells of $(ADN)_2LiPF_6$ co-crystalline electrolyte showing possible Li^+ ion channels : **(a)** Li^+ ions at successive distances of 6.6 Å, parallel to *b* crystallographic direction in a 1x2x1 supercell; **(b)** Li^+ ions at successive distances of 8.5 Å, at the intersection of (040) and (101) planes in a 2x1x2 supercell; and **(c)** Li^+ ions at successive distances of 11.2 Å, parallel to *a* crystallographic direction in a 3x1x1 supercell.

Bibliography

[1] "Inventory of U.S. Greenhouse Gas Emissions and Sinks:1990-2013," Washington, DC, USA, 2015.

[2] E. J. Maginn, "What to do with CO_2," *J. Phys. Chem. Lett.*, vol. 1, no. 24, pp. 3478–3479, 2010.

[3] A. L. Yaumi, M. Z. Abu Bakar, and B. H. Hameed, "Recent advances in functionalized composite solid materials for carbon dioxide capture," *Energy*, 2017.

[4] E. Quartarone and P. Mustarelli, "Electrolytes for solid-state lithium rechargeable batteries: Recent advances and perspectives," *Chem. Soc. Rev.*, vol. 40, no. 5, pp. 2525–2540, 2011.

[5] B. Arstad, R. Blom, and O. Swang, "CO_2 absorption in aqueous solutions of alkanolamines: Mechanistic insight from quantum chemical calculations," *J. Phys. Chem. A*, vol. 111, no. 7, pp. 1222–1228, 2007.

[6] G. Puxty *et al.*, "Carbon dioxide postcombustion capture: A novel screening study of the carbon dioxide absorption performance of 76 amines," *Environ. Sci. Technol.*, vol. 43, pp. 6427–6433, 2009.

[7] I. Kim and H. F. Svendsen, "Heat of Absorption of Carbon Dioxide (CO_2) in Monoethanolamine (MEA) and 2-(Aminoethyl)ethanolamine (AEEA) Solutions," *Ind. Eng. Chem. Res.*, vol. 46, no. 17, pp. 5803–5809, Aug. 2007.

[8] A. Garcia-Abuin, D. Gomez-Diaz, A. B. Lopez, J. M. Navaza, and A. Rumbo, "NMR Characterization of Carbon Dioxide Chemical Absorption with MEA, DEA, TEA," *Ind. Eng. Chem. Res.*, vol. 52, pp. 13432–13438, 2013.

[9] G. Fan, A. G. H. Wee, R. Idem, and P. Tontiwachwuthikul, "NMR Studies of Amine Species in MEA−CO_2−H_2O System: Modification of the Model of Vapor−Liquid Equilibrium (VLE)," *Ind. Eng. Chem. Res.*, vol. 48, no. 5, pp. 2717–2720, Mar. 2009.

[10] R. Ramazani, S. Mazinani, A. Jahanmiri, S. Darvishmanesh, and B. Van der Bruggen, "Investigation of different additives to monoethanolamine (MEA) as a solvent for CO_2 capture," *J. Taiwan Inst. Chem. Eng.*, vol. 65, pp. 341–349, 2016.

[11] H. Shi, A. Naami, R. Idem, and P. Tontiwachwuthikul, "1D NMR Analysis of a Quaternary MEA–DEAB–CO_2–H_2O Amine System: Liquid Phase Speciation and Vapor–Liquid Equilibria at CO_2 Absorption and Solvent Regeneration Conditions," *Ind. Eng. Chem. Res.*, vol. 53, no. 20, pp. 8577–

8591, May 2014.

[12] N. McCann, M. Maeder, and M. Attalla, “Simulation of enthalpy and capacity of CO_2 absorption by aqueous amine systems,” *Ind. Eng. Chem. Res.*, vol. 47, pp. 2002–2009, 2008.

[13] A. Veawab, P. Tontiwachwuthikul, and A. Chakma, “Corrosion Behavior of Carbon Steel in the CO_2 Absorption Process Using Aqueous Amine Solutions,” *Ind. Eng. Chem. Res.*, vol. 38, pp. 3917–3924, 1999.

[14] C. Saiwan, T. Supap, R. O. Idem, and P. Tontiwachwuthikul, “Part 3: Corrosion and prevention in post-combustion CO_2 capture systems,” *Carbon Manag.*, vol. 2, pp. 659–675, 2011.

[15] R. Barker, Y. Hua, and A. Neville, “Internal corrosion of carbon steel pipelines for dense-phase CO_2 transport in carbon capture and storage (CCS) – a review,” *Int. Mater. Rev.*, vol. 62, no. 1, pp. 1–31, 2017.

[16] M. A. Hussain, Y. Soujanya, and G. N. Sastry, “Evaluating the Efficacy of Amino Acids as CO_2 Capturing Agents: A First Principles Investigation,” *Environ. Sci. Technol.*, vol. 45, pp. 8582–8588, Oct. 2011.

[17] A. P. Hallenbeck, A. Egbebi, K. P. Resnik, D. Hopkinson, S. L. Anna, and J. R. Kitchin, “Comparative microfluidic screening of amino acid salt solutions for post-combustion CO_2 capture,” *Int. J. Greenh. Gas Control*, vol. 43, pp. 189–197, Dec. 2015.

[18] C. H. Hsu, H. Chu, and C. M. Cho, “Absorption and reaction kinetics of amines and ammonia solutions with carbon dioxide in flue gas.,” *J Air Waste Manag Assoc.*, vol. 53, pp. 246–252, 2003.

[19] X. Yang, R. J. Rees, W. Conway, G. Puxty, Q. Yang, and D. A. Winkler, “Computational Modeling and Simulation of CO_2 Capture by Aqueous Amines,” *Chem. Rev.*, vol. 117, pp. 9524–9593, 2017.

[20] E. F. da Silva and H. F. Svendsen, “Study of the Carbamate Stability of Amines Using ab Initio Methods and Free-Energy Perturbations,” *Ind. Eng. Chem. Res.*, vol. 45, pp. 2497–2504, 2006.

[21] E. M. Mindrup and W. F. Schneider, “Computational comparison of the reactions of substituted amines with CO_2,” *ChemSusChem*, vol. 3, pp. 931–938, 2010.

[22] H. M. Stowe and G. S. Hwang, “Fundamental Understanding of CO_2 Capture and Regeneration in Aqueous Amines from First-Principles Studies: Recent Progress and Remaining Challenges,” *Ind. Eng. Chem. Res.*, vol. 56, no. 24, pp. 6887–6899, Jun. 2017.

[23] P. J. Dyson, G. Laurenczy, C. A. Ohlin, J. Vallance, and T. Welton, “Determination of hydrogen concentration in ionic liquids and the effect (or lack of) on rates of hydrogenation coefficients,” *Chem. Commun.*, pp. 2418–2419, 2003.

[24] J. L. Anthony, E. J. Maginn, and J. F. Brennecke, “Solubilities and Thermodynamic Properties of Gases in the Ionic Liquid 1-*n*-Butyl-3-methylimidazolium Hexafluorophosphate,” *J. Phys. Chem. B*, vol. 106, pp. 7315–7320, 2002.

[25] X. Zhang, X. Zhang, H. Dong, Z. Zhao, S. Zhang, and Y. Huang, “Carbon capture with ionic liquids: overview and progress,” *Energy Environ. Sci.*, vol. 5, pp. 6668–6681, 2012.

[26] K. L. S. Campbell, Y. Zhao, J. J. Hall, and D. R. Williams, “The effect of CO_2-loaded amine solvents on the corrosion of a carbon steel stripper,” *Int. J. Greenh. Gas Control*, vol. 47, pp. 376–385, 2016.

[27] K. Fukumoto, M. Yoshizawa, and H. Ohno, “Room Temperature Ionic Liquids from 20 Natural Amino Acids,” *J. Am. Chem. Soc.*, vol. 127, no. 8, pp. 2398–2399, Mar. 2005.

[28] J. L. Anthony, J. L. Anderson, E. J. Maginn, and J. F. Brennecke, “Anion effects on gas solubility in ionic liquids,” *J. Phys. Chem. B*, vol. 109, pp. 6366–6374, 2005.

[29] H. Ohno and K. Fukumoto, “Amino Acid Ionic Liquids,” *Acc. Chem. Res.*, vol. 40, no. 11, pp. 1122–1129, Nov. 2007.

[30] X. Zhou, G. Jing, F. Liu, B. Lv, and Z. Zhou, “Mechanism and Kinetics of CO_2 Absorption into an Aqueous Solution of a Triamino-Functionalized Ionic Liquid,” *Energy & Fuels*, vol. 31, pp. 1793–1802, 2017.

[31] B. F. Goodrich *et al.*, “Experimental measurements of amine-functionalized anion-tethered ionic liquids with carbon dioxide,” *Ind. Eng. Chem. Res.*, vol. 50, no. 1, pp. 111–118, 2011.

[32] Z. Feng, F. Cheng-Gang, W. You-Ting, W. Yuan-Tao, L. Ai-Min, and Z. Zhi-Bing, “Absorption of CO_2 in the aqueous solutions of functionalized ionic liquids and MDEA,” *Chem. Eng. J.*, vol. 160, pp. 691–697, 2010.

[33] B. E. Gurkan *et al.*, “Equimolar CO_2 Absorption by Anion-Functionalized Ionic Liquids,” *J. Am. Chem. Soc.*, vol. 132, no. 7, pp. 2116–2117, Feb. 2010.

[34] B. F. Goodrich *et al.*, “Effect of Water and Temperature on Absorption of CO_2 by Amine-Functionalized Anion-Tethered Ionic Liquids,” *J. Phys. Chem. B*, vol. 115, no. 29, pp. 9140–9150, Jul. 2011.

[35] S. Saravanamurugan, A. J. Kunov-Kruse, R. Fehrmann, and A. Riisager, “Amine-Functionalized Amino Acid-based Ionic Liquids as Efficient and High-Capacity Absorbents for CO_2,” *ChemSusChem*, vol. 7, no. 3, pp. 897–902, Mar. 2014.

[36] S. Shen, Y. Zhao, Y. Bian, Y. Wang, H. Guo, and H. Li, “CO_2 absorption using aqueous potassium lysinate solutions: Vapor – liquid equilibrium data and modelling,” *J. Chem. Thermodyn.*, vol. 115, pp. 209–220, Dec. 2017.

[37] R. Ramazani, A. Samsami, A. Jahanmiri, B. Van der Bruggen, and S. Mazinani, “Characterization of monoethanolamine + potassium lysinate blend solution as a new chemical absorbent for CO_2 capture,” *Int. J. Greenh. Gas Control*, vol. 51, pp. 29–35, 2016.

[38] H. Suleman, A. S. Maulud, and Z. Man, “Carbon Dioxide Solubility in Aqueous Potassium Lysinate Solutions: High Pressure Data and Thermodynamic Modeling,” *Procedia Eng.*, vol. 148, pp. 1303–1311, 2016.

[39] S. Mazinani, R. Ramazani, A. Samsami, A. Jahanmiri, B. Van der Bruggen, and S. Darvishmanesh, “Equilibrium solubility, density, viscosity and

corrosion rate of carbon dioxide in potassium lysinate solution," *Fluid Phase Equilib.*, vol. 396, pp. 28–34, Jun. 2015.

[40] Y. Zhao *et al.*, "A Comparative Study of Aqueous Potassium Lysinate and Aqueous Monoethanolamine for Postcombustion CO 2 Capture," *Energy & Fuels*, vol. 31, no. 12, pp. 14033–14044, Dec. 2017.

[41] Y. Zhao, S. Shen, Y. Bian, Y. Yang, and U. Ghosh, "CO_2 solubility in aqueous potassium lysinate solutions at absorber conditions," *J. Chem. Thermodyn.*, vol. 111, pp. 100–105, 2017.

[42] R. Ramezani, S. Mazinani, R. Di Felice, S. Darvishmanesh, and B. Van der Bruggen, "Selection of blended absorbents for CO_2 capture from flue gas: CO_2 solubility, corrosion and absorption rate," *Int. J. Greenh. Gas Control*, vol. 62, no. January, pp. 61–68, Jul. 2017.

[43] S. Shen, Y. nan Yang, Y. Wang, S. Ren, J. Han, and A. Chen, "CO_2 absorption into aqueous potassium salts of lysine and proline: Density, viscosity and solubility of CO_2," *Fluid Phase Equilib.*, vol. 399, pp. 40–49, 2015.

[44] S. Shen, Y. Yang, Y. Wang, S. Ren, J. Han, and A. Chen, "Corrigendum to 'CO_2 absorption into aqueous potassium salts of lysine and proline: Density, viscosity and solubility of CO_2' [Fluid Phase Equilib. 399 (2015) 40–49]," *Fluid Phase Equilib.*, vol. 435, p. 131, Mar. 2017.

[45] Z. Lei, C. Dai, and B. Chen, "Gas Solubility in Ionic Liquids," *Chem. Rev.*, vol. 114, no. 2, pp. 1289–1326, Jan. 2014.

[46] D. J. Heldebrant, P. K. Koech, V.-A. Glezakou, R. Rousseau, D. Malhotra, and D. C. Cantu, "Water-Lean Solvents for Post-Combustion CO_2 Capture: Fundamentals, Uncertainties, Opportunities, and Outlook," *Chem. Rev.*, p. acs.chemrev.6b00768, 2017.

[47] E. S. Sanz-Pérez, C. R. Murdock, S. A. Didas, and C. W. Jones, "Direct Capture of CO_2 from Ambient Air," *Chem. Rev.*, vol. 116, no. 19, pp. 11840–11876, 2016.

[48] J. Artz *et al.*, "Sustainable Conversion of Carbon Dioxide: An Integrated Review of Catalysis and Life Cycle Assessment," *Chem. Rev.*, p. acs.chemrev.7b00435, 2017.

[49] S. Babamohammadi, A. Shamiri, and M. K. Aroua, "A review of CO_2 capture by absorption in ionic liquid-based solvents," *Rev. Chem. Eng.*, vol. 31, no. 4, pp. 383–412, 2015.

[50] S. Zeng *et al.*, "Ionic-Liquid-Based CO_2 Capture Systems: Structure, Interaction and Process," *Chem. Rev.*, vol. 117, no. 14, pp. 9625–9673, Jul. 2017.

[51] X. Huang, C. J. Margulis, Y. Li, and B. J. Berne, "Why Is the Partial Molar Volume of CO_2 So Small When Dissolved in a Room Temperature Ionic Liquid ? Structure and Dynamics of CO_2 Dissolved in [$Bmim^+$][PF_6^-]," *J. Am. Chem. Soc.*, vol. 127, pp. 17842–17851, 2005.

[52] M. E. Perez-Blanco and E. J. Maginn, "Molecular dynamics simulations of carbon dioxide and water at an ionic liquid interface.," *J. Phys. Chem. B*, vol. 115, pp. 10488–10499, 2011.

[53] L. X. Dang and T.-M. Chang, “Molecular Mechanism of Gas Adsorption into Ionic Liquids: A Molecular Dynamics Study,” *J. Phys. Chem. Lett.*, vol. 3, no. 2, pp. 175–181, Jan. 2012.

[54] N. Kim, S. Yoon, and G. Park, “Evaluating the CO_2-capturing efficacy of amine and carboxylic acid motifs: ab initio studies on thermodynamic versus kinetic properties,” *Tetrahedron*, vol. 69, no. 32, pp. 6693–6697, Aug. 2013.

[55] G. Jing, Y. Qian, X. Zhou, B. Lv, and Z. Zhou, “Designing and Screening of Multi-Amino-Functionalized Ionic Liquid Solution for CO_2 Capture by Quantum Chemical Simulation,” *ACS Sustain. Chem. Eng.*, vol. 6, pp. 1182–1191, 2018.

[56] J. L. McDonald, R. E. Sykora, P. Hixon, A. Mirjafari, and J. H. Davis, “Impact of water on CO_2 capture by amino acid ionic liquids,” *Environ. Chem. Lett.*, vol. 12, no. 1, pp. 201–208, Mar. 2014.

[57] S. Shen and Y. N. Yang, “Carbon Dioxide Absorption into Aqueous Potassium Salt Solutions of Arginine for Post-Combustion Capture,” *Energy and Fuels*, vol. 30, pp. 6585–6596, 2016.

[58] H. Guo, H. Li, and S. Shen, “CO_2 Capture by Water-Lean Amino Acid Salts: Absorption Performance and Mechanism,” *Energy and Fuels*, vol. 32, no. 6, pp. 6943–6954, 2018.

[59] S. Hess, M. Wohlfahrt-Mehrens, and M. Wachtler, “Flammability of Li-Ion Battery Electrolytes: Flash Point and Self-Extinguishing Time Measurements,” *J. Electrochem. Soc.*, vol. 162, no. 2, pp. A3084–A3097, 2015.

[60] Z. Chen, A. Luntz, V. Viswanathan, Y.-M. Chiang, and K. Kerman, “Review—Practical Challenges Hindering the Development of Solid State Li Ion Batteries,” *J. Electrochem. Soc.*, vol. 164, no. 7, pp. A1731–A1744, 2017.

[61] J.-J. Kim, K. Yoon, I. Park, and K. Kang, “Progress in the Development of Sodium-Ion Solid Electrolytes,” *Small Methods*, vol. 1, no. 10, p. 1700219, 2017.

[62] K. Vignarooban *et al.*, “Current trends and future challenges of electrolytes for sodium-ion batteries,” *Int. J. Hydrogen Energy*, vol. 41, no. 4, pp. 2829–2846, 2016.

[63] C. Sun, J. Liu, Y. Gong, D. P. Wilkinson, and J. Zhang, “Recent advances in all-solid-state rechargeable lithium batteries,” *Nano Energy*, vol. 33, no. January, pp. 363–386, 2017.

[64] J. W. Choi and D. Aurbach, “Promise and reality of post-lithium-ion batteries with high energy densities,” *Nat. Rev. Mater.*, vol. 1, no. 4, p. 16013, 2016.

[65] C. Zhou, S. Bag, and V. Thangadurai, “Engineering Materials for Progressive All-Solid-State Na Batteries,” *ACS Energy Lett.*, vol. 3, no. 9, pp. 2181–2198, 2018.

[66] N. Anantharamulu, K. Koteswara Rao, G. Rambabu, B. Vijaya Kumar, V. Radha, and M. Vithal, “A wide-ranging review on Nasicon type materials,” *J. Mater. Sci.*, vol. 46, no. 9, pp. 2821–2837, May 2011.

[67] Y. Deng *et al.*, “Enhancing the Lithium Ion Conductivity in Lithium

Superionic Conductor (LISICON) Solid Electrolytes through a Mixed Polyanion Effect," *ACS Appl. Mater. Interfaces*, vol. 9, no. 8, pp. 7050–7058, 2017.

[68] J. W. Fergus, "Ceramic and polymeric solid electrolytes for lithium-ion batteries," *J. Power Sources*, vol. 195, no. 15, pp. 4554–4569, Aug. 2010.

[69] A. Manthiram, X. Yu, and S. Wang, "Lithium battery chemistries enabled by solid-state electrolytes," *Nat. Rev. Mater.*, vol. 2, no. 4, pp. 1–16, 2017.

[70] Z. Zhang *et al.*, "New horizons for inorganic solid state ion conductors," *Energy Environ. Sci.*, vol. 11, no. 8, pp. 1945–1976, 2018.

[71] C. Ma *et al.*, "Atomic-scale origin of the large grain-boundary resistance in perovskite Li-ion-conducting solid electrolytes," *Energy Environ. Sci.*, vol. 7, no. 5, pp. 1638–1642, 2014.

[72] C.-W. Ahn *et al.*, "Electrochemical properties of $Li_7La_3Zr_2O_{12}$-based solid state battery," *J. Power Sources*, vol. 272, pp. 554–558, Dec. 2014.

[73] T. Shao *et al.*, "Recent Research on Strategies to Improve Ion Conduction in Alkali Metal-Ion Batteries," *Batter. Supercaps*, vol. 2, no. 5, pp. 403–427, May 2019.

[74] R. G. Pearson, "Hard and Soft Acids and Bases," *J. Am. Chem. Soc.*, vol. 85, no. 22, pp. 3533–3539, 1963.

[75] V. S. Bryantsev, J. Uddin, V. Giordani, W. Walker, D. Addison, and G. V. Chase, "The Identification of Stable Solvents for Nonaqueous Rechargeable Li-Air Batteries," *J. Electrochem. Soc.*, vol. 160, no. 1, pp. A160–A171, 2012.

[76] S.-D. Han *et al.*, "Solvate Structures and Computational/Spectroscopic Characterization of $LiPF_6$ Electrolytes," *J. Phys. Chem. C*, vol. 119, no. 16, pp. 8492–8500, Apr. 2015.

[77] Y. Abu-Lebdeh and I. Davidson, "High-Voltage Electrolytes Based on Adiponitrile for Li-Ion Batteries," *J. Electrochem. Soc.*, vol. 156, no. 1, p. A60, 2009.

[78] S. Tan, Y. J. Ji, Z. R. Zhang, and Y. Yang, "Recent progress in research on high-voltage electrolytes for lithium-ion batteries," *ChemPhysChem*, vol. 15, no. 10, pp. 1956–1969, 2014.

[79] X. Wang, W. Xue, K. Hu, Y. Li, Y. Li, and R. Huang, "Adiponitrile as Lithium-Ion Battery Electrolyte Additive: A Positive and Peculiar Effect on High-Voltage Systems," *ACS Appl. Energy Mater.*, vol. 1, pp. 5347–5354, 2018.

[80] N. Kamaya *et al.*, "A lithium superionic conductor," *Nat. Mater.*, vol. 10, no. 9, pp. 682–686, 2011.

[81] G.-A. Nazri and G. Pistoia, Eds., *Lithium Batteries*. Boston, MA: Springer US, 2003.

[82] H. Saruwatari, T. Kuboki, T. Kishi, S. Mikoshiba, and N. Takami, "Imidazolium ionic liquids containing LiBOB electrolyte for lithium battery," *J. Power Sources*, vol. 195, no. 5, pp. 1495–1499, 2010.

[83] F. Croce, G. B. Appetecchi, L. Persi, and B. Scrosati, “Nanocomposite polymer electrolytes for lithium batteries,” *Nature*, vol. 394, no. 6692, pp. 456–458, Jul. 1998.

[84] X. Yu, “A Stable Thin-Film Lithium Electrolyte: Lithium Phosphorus Oxynitride,” *J. Electrochem. Soc.*, vol. 144, no. 2, p. 524, 1997.

[85] Y. Inaguma *et al.*, “High ionic conductivity in lithium lanthanum titanate,” *Solid State Commun.*, vol. 86, pp. 689–693, 1993.

[86] C. Bernuy-Lopez, W. Manalastas, J. M. Lopez Del Amo, A. Aguadero, F. Aguesse, and J. A. Kilner, “Atmosphere controlled processing of ga-substituted garnets for high li-ion conductivity ceramics,” *Chem. Mater.*, vol. 26, no. 12, pp. 3610–3617, 2014.

[87] J. C. Bachman *et al.*, “Inorganic Solid-State Electrolytes for Lithium Batteries: Mechanisms and Properties Governing Ion Conduction,” *Chem. Rev.*, vol. 116, no. 1, pp. 140–162, Jan. 2016.

[88] P. R. Chinnam, R. N. Clymer, A. A. Jalil, S. L. Wunder, and M. J. Zdilla, “Bulk-Phase Ion Conduction in Cocrystalline LiCl·*N,N*-Dimethylformamide: A New Paradigm for Solid Electrolytes Based upon the Pearson Hard–Soft Acid–Base Concept,” *Chem. Mater.*, vol. 27, no. 16, pp. 5479–5482, Aug. 2015.

[89] P. R. Chinnam *et al.*, “A Self-Binding, Melt-Castable, Crystalline Organic Electrolyte for Sodium Ion Conduction,” *Angew. Chemie Int. Ed.*, vol. 55, no. 49, pp. 15254–15257, Dec. 2016.

[90] B. Fall *et al.*, “Crystal structure and ionic conductivity of the soft solid crystal: isoquinoline$_3$•(LiCl)$_2$,” *Ionics (Kiel).*, vol. 24, no. 2, pp. 343–349, Feb. 2018.

[91] P. Jannasch, “Ionic conductivity in physical networks of polyethylene-polyether-polyethylene triblock copolymers,” *Chem. Mater.*, vol. 14, no. 6, pp. 2718–2724, 2002.

[92] E. D. Bates, R. D. Mayton, I. Ntai, and J. H. Davis, “CO_2 capture by a task-specific ionic liquid,” *J. Am. Chem. Soc.*, vol. 124, pp. 926–927, 2002.

[93] J. Zhang, S. Zhang, K. Dong, Y. Zhang, Y. Shen, and X. Lv, “Supported absorption of CO_2 by tetrabutylphosphonium amino acid ionic liquids,” *Chem. - A Eur. J.*, vol. 12, pp. 4021–4026, 2006.

[94] P. J. Carvalho, V. H. Álvarez, I. M. Marrucho, M. Aznar, and J. A. P. Coutinho, “High carbon dioxide solubilities in trihexyltetradecylphosphonium-based ionic liquids,” *J. Supercrit. Fluids*, vol. 52, pp. 258–265, 2010.

[95] C. Wang, X. Luo, H. Luo, D. E. Jiang, H. Li, and S. Dai, “Tuning the basicity of ionic liquids for equimolar CO_2 capture,” *Angew. Chemie - Int. Ed.*, vol. 50, pp. 4918–4922, 2011.

[96] S. Seo *et al.*, “Chemically tunable ionic liquids with aprotic heterocyclic anion (AHA) for CO_2 capture,” *J. Phys. Chem. B*, vol. 118, pp. 5740–5751, 2014.

[97] R. S. Eisinger and G. E. Keller, “Process for CO_2 Capture Using Ionic Liquid That Exhibits Phase Change,” *Energy Fuels*, vol. 28, pp. 7070–7078, 2014.

[98] M. E. Perez-Blanco and E. J. Maginn, “Molecular Dynamics Simulations of CO_2 at an Ionic Liquid Interface: Adsorption, Ordering, and Interfacial Crossing,” *J. Phys. Chem. B*, vol. 114, no. 36, pp. 11827–11837, Sep. 2010.

[99] H. Xing *et al.*, “Effect of Tethering Strategies on the Surface Structure of Amine-Functionalized Ionic Liquids: Inspiration on the CO_2 Capture,” *J. Phys. Chem. C*, vol. 117, pp. 16012–16021, 2013.

[100] J. D. Morganti, K. Hoher, M. C. C. Ribeiro, R. A. Ando, and L. J. A. Siqueira, “Molecular Dynamics Simulations of Acidic Gases at Interface of Quaternary Ammonium Ionic Liquids,” *J. Phys. Chem. C*, vol. 118, pp. 22012–22020, 2014.

[101] G. García, M. Atilhan, and S. Aparicio, “Interfacial Properties of Double Salt Ionic Liquids: A Molecular Dynamics Study,” *J. Phys. Chem. C*, vol. 119, pp. 28405–28416, 2015.

[102] E. I. Izgorodina, J. L. Hodgson, D. C. Weis, S. J. Pas, and D. R. MacFarlane, “Physical Absorption Of CO_2 in Protic and Aprotic Ionic Liquids: An Interaction Perspective,” *J. Phys. Chem. B*, vol. 119, pp. 11748–11759, 2015.

[103] M. Klähn and A. Seduraman, “What Determines CO_2 Solubility in Ionic Liquids? A Molecular Simulation Study,” *J. Phys. Chem. B*, vol. 119, pp. 10066–10078, 2015.

[104] M. P. Allen and D. J. Tildesley, *Computer Simulation of Liquids*. Oxford: Oxford University Press, 1987.

[105] M. Brehm and B. Kirchner, “TRAVIS - A free analyzer and visualizer for monte carlo and molecular dynamics trajectories,” *J. Chem. Inf. Model.*, vol. 51, pp. 2007–2023, 2011.

[106] B. Hess, C. Kutzner, D. van der Spoel, and E. Lindahl, “GROMACS 4: Algorithms for Highly Efficient, Load-Balanced, and Scalable Molecular Simulation,” *J. Chem. Theory Comput.*, vol. 4, pp. 435–447, 2008.

[107] R. T. Cygan, V. N. Romanov, and E. M. Myshakin, “Molecular simulation of carbon dioxide capture by montmorillonite using an accurate and flexible force field,” *J. Phys. Chem. C*, vol. 116, pp. 13079–13091, 2012.

[108] G. Zhou, X. Liu, S. Zhang, G. Yu, and H. He, “A force field for molecular simulation of tetrabutylphosphonium amino acid ionic liquids.,” *J. Phys. Chem. B*, vol. 111, pp. 7078–7084, 2007.

[109] S. Nosé, “A molecular dynamics method for simulations in the canonical ensemble,” *Mol. Phys.*, vol. 52, pp. 255–268, 1984.

[110] W. G. Hoover, “Canonical dynamics: Equilibrium phase-space distributions,” *Phys. Rev. A*, vol. 31, pp. 1695–1697, 1985.

[111] B. L. Bhargava and S. Balasubramanian, “Insights into the Structure and Dynamics of a Room-Temperature Ionic Liquid: Ab Initio Molecular Dynamics Simulation Studies of 1-*n*-Butyl-3-methylimidazolium Hexafluorophosphate ([bmim][PF_6]) and the [bmim][PF_6]-CO_2,” *J. Phys. Chem. B*, vol. 111, pp. 4477–4487, 2007.

[112] W. Shi, C. R. Myers, D. R. Luebke, J. A. Steckel, and D. C. Sorescu, “Theoretical and experimental studies of CO_2 and H_2 separation using the 1-

ethyl-3-methylimidazolium acetate ([emim][CH_3COO]) ionic liquid.," *J. Phys. Chem. B*, vol. 116, pp. 283–95, 2012.

[113] X. Luo *et al.*, "Significant improvements in CO_2 capture by pyridine-containing anion-functionalized ionic liquids through multiple-site cooperative interactions," *Angew. Chemie - Int. Ed.*, vol. 53, pp. 7053–7057, 2014.

[114] W. Humphrey, A. Dalke, and K. Schulten, "VMD: Visual molecular dynamics," *J. Mol. Graph.*, vol. 14, pp. 33–38, 1996.

[115] J. G. Shim, J. H. Kim, Y. H. Jhon, J. Kim, and K. H. Cho, "DFT calculations on the role of base in the reaction between CO_2 and monoethanolamine," *Ind. Eng. Chem. Res.*, vol. 48, pp. 2172–2178, 2009.

[116] H.-B. Xie, Y. Zhou, Y. Zhang, and J. K. Johnson, "Reaction mechanism of monoethanolamine with CO_2 in aqueous solution from molecular modeling.," *J. Phys. Chem. A*, vol. 114, pp. 11844–11852, 2010.

[117] Y. Matsuzaki, H. Yamada, F. A. Chowdhury, T. Higashii, S. Kazama, and M. Onoda, "Ab initio study of CO_2 capture mechanisms in monoethanolamine aqueous solution: Reaction pathways from carbamate to bicarbonate," *Energy Procedia*, vol. 37, pp. 400–406, 2013.

[118] D. Y. Kim *et al.*, "CO_2 capturing mechanism in aqueous ammonia: NH_3-driven decomposition-recombination pathway," *J. Phys. Chem. Lett.*, vol. 2, pp. 689–694, 2011.

[119] B. F. Goodrich *et al.*, "Effect of water and temperature on absorption of CO_2 by amine-functionalized anion-tethered ionic liquids.," *J. Phys. Chem. B*, vol. 115, pp. 9140–9150, 2011.

[120] X. Wang, N. G. Akhmedov, Y. Duan, D. Luebke, D. Hopkinson, and B. Li, "Amino acid-functionalized ionic liquid solid sorbents for post-combustion carbon capture," *ACS Appl. Mater. Interfaces*, vol. 5, pp. 8670–8677, 2013.

[121] S. Shen, Y. N. Yang, Y. Bian, and Y. Zhao, "Kinetics of CO_2 Absorption into Aqueous Basic Amino Acid Salt: Potassium Salt of Lysine Solution," *Environ. Sci. Technol.*, vol. 50, pp. 2054–2063, 2016.

[122] Y. Bian, S. Shen, Y. Zhao, and Y.-N. Yang, "Physicochemical properties of aqueous potassium salts of basic amino acids as absorbents for CO_2 capture," *J. Chem. Eng. Data*, vol. 61, pp. 2391–2398, 2016.

[123] G. B. Damas, A. B. A. Dias, and L. T. Costa, "A quantum chemistry study for ionic liquids applied to gas capture and separation," *J. Phys. Chem. B*, vol. 118, pp. 9046–9064, 2014.

[124] H. Yamada, "Comparison of Solvation Effects on CO_2 Capture with Aqueous Amine Solutions and Amine-Functionalized Ionic Liquids," *J. Phys. Chem. B*, vol. 120, pp. 10563–10568, 2016.

[125] A. V. Marenich, C. J. Cramer, and D. G. Truhlar, "Universal solvation model based on solute electron density and on a continuum model of the solvent defind by the bulk dielectric constant and atomic surface tensions," *J. Phys. Chem. B.*, vol. 113, pp. 6378–6396, 2009.

[126] S. Yuan, Z. Yang, X. Ji, Y. Chen, Y. Sun, and X. Lu, "CO_2 Absorption in Mixed Aqueous Solution of MDEA and Cholinium Glycinate," *Energy &*

Fuels, vol. 31, pp. 7325–7333, Jul. 2017.

[127] A. R. Shaikh, H. Karkhanechi, E. Kamio, T. Yoshioka, and H. Matsuyama, "Quantum Mechanical and Molecular Dynamics Simulations of Dual-Amino-Acid Ionic Liquids for CO_2 Capture," *J. Phys. Chem. C*, vol. 120, pp. 27734–27745, 2016.

[128] M. J. Frisch *et al.*, "Gaussian 09, Revision D.01." Gaussian Inc., Wallingford CT, 2010.

[129] A. D. Becke, "Density-functional thermochemistry. III. The role of exact exchange," *J. Chem. Phys.*, vol. 98, pp. 5648–5652, 1993.

[130] Y. Zhao and D. G. Truhlar, "The M06 suite of density functionals for main group thermochemistry, thermochemical kinetics, noncovalent interactions, excited states, and transition elements: Two new functionals and systematic testing of four M06-class functionals and 12 other function," *Theor. Chem. Acc.*, vol. 120, pp. 215–241, 2008.

[131] S. Grimme, J. Antony, S. Ehrlich, and H. Krieg, "A consistent and accurate ab initio parametrization of density functional dispersion correction (DFT-D) for the 94 elements H-Pu," *J. Chem. Phys.*, vol. 132, pp. 154104–154123, 2010.

[132] S. Boys and F. Bernardi, "The calculation of small molecular interactions by the differences of separate total energies. Some procedures with reduced errors," *Mol. Phys.*, vol. 19, pp. 553–566, 1970.

[133] K. N. Kirschner, J. B. Sorensen, and J. P. Bowen, "Calculating Interaction Energies Using First Principle Theories: Consideration of Basis Set Superposition Error and Fragment Relaxation," *J. Chem. Educ.*, vol. 84, no. 7, p. 1225, Jul. 2007.

[134] C. Peng and H. Bernhard Schlegel, "Combining Synchronous Transit and Quasi-Newton Methods to Find Transition States," *Isr. J. Chem.*, vol. 33, pp. 449–454, 1993.

[135] S. Stramare, V. Thangadurai, and W. Weppner, "Lithium Lanthanum Titanates: A Review," *Chem. Mater.*, vol. 15, pp. 3974–3990, 2003.

[136] M. Yashima, M. Itoh, Y. Inaguma, and Y. Morii, "Crystal structure and diffusion path in the fast lithium-ion conductor $La_{0.62}Li_{0.16}TiO_3$," *J. Am. Chem. Soc.*, vol. 127, pp. 3491–3495, 2005.

[137] X. Gao *et al.*, "Domain boundary structures in lanthanum lithium titanates," *J. Mater. Chem. A*, vol. 2, pp. 843–852, 2014.

[138] H. Moriwake *et al.*, "Domain boundaries and their influence on Li migration in solid-state electrolyte (La,Li)TiO_3," *J. Power Sources*, vol. 276, pp. 203–207, 2015.

[139] D. T. Shay, G. P. A. Yap, L. N. Zakharov, A. L. Rheingold, and K. H. Theopold, "Intramolecular C-H activation by an open-shell Cobalt(III) imido complex," *Angew. Chemie - Int. Ed.*, vol. 44, pp. 1508–1510, 2005.

[140] J. L. Allen, J. Wolfenstine, E. Rangasamy, and J. Sakamoto, "Effect of substitution (Ta, Al, Ga) on the conductivity of $Li_7La_3Zr_2O_{12}$," *J. Power Sources*, vol. 206, pp. 315–319, 2012.

[141] Y. Li, J.-T. Han, C.-A. Wang, H. Xie, and J. B. Goodenough, "Optimizing Li^+ conductivity in a garnet framework," *J. Mater. Chem.*, vol. 22, no. 30, p. 15357, 2012.

[142] Y. Kihira, S. Ohta, H. Imagawa, and T. Asaoka, "Effect of Simultaneous Substitution of Alkali Earth Metals and Nb in $Li_7La_3Zr_2O_{12}$ on Lithium-Ion Conductivity," *ECS Electrochem. Lett.*, vol. 2, pp. A56–A59, 2013.

[143] A. Hooper, "A study of the electrical properties of single-crystal and polycrystalline β-alumina using complex plane analysis," *J. Phys. D. Appl. Phys.*, vol. 10, pp. 1487–1496, 1977.

[144] Y. Seino, T. Ota, K. Takada, A. Hayashi, and M. Tatsumisago, "A sulphide lithium super ion conductor is superior to liquid ion conductors for use in rechargeable batteries," *Energy Environ. Sci.*, vol. 7, pp. 627–631, 2014.

[145] A. C. Luntz, J. Voss, and K. Reuter, "Interfacial Challenges in Solid-State Li Ion Batteries," *J. Phys. Chem. Lett.*, vol. 6, pp. 4599–4604, 2015.

[146] A. Jalil, R. N. Clymer, C. R. Hamilton, S. Vaddypally, M. R. Gau, and M. J. Zdilla, "Structure of salts of lithium chloride and lithium hexafluorophosphate as solvates with pyridine and vinylpyridine and structural comparisons: $(C_5H_5N)LiPF_6$,[*p*-$(CH_2{=}CH)C_5H_4N]LiPF_6$, $[(C_5H_5N)LiCl]_n$, and [*p*-$(CH_2{=}CH)C_5H_4N]_2$- Li(μ-Cl)$_2$Li[*p*-$(CH_2{=}CH)C_5H_4N]_2$," *Acta Crystallogr. Sect. C Struct. Chem.*, vol. 73, no. 3, pp. 264–269, Mar. 2017.

[147] N. N. Rajput, X. Qu, N. Sa, A. K. Burrell, and K. A. Persson, "The Coupling between Stability and Ion Pair Formation in Magnesium Electrolytes from First-Principles Quantum Mechanics and Classical Molecular Dynamics," *J. Am. Chem. Soc.*, vol. 137, no. 9, pp. 3411–3420, Mar. 2015.

[148] Y. Wei *et al.*, "Kinetics Tuning of Li-Ion Diffusion in Layered $Li(Ni_xMn_yCo_z)O_2$," *J. Am. Chem. Soc.*, vol. 137, pp. 8364–8367, 2015.

[149] N. Kumar and J. M. Seminario, "Lithium-ion model behavior in an ethylene carbonate electrolyte using molecular dynamics," *J. Phys. Chem. C*, vol. 120, pp. 16322–16332, 2016.

[150] C. Yu *et al.*, "Unravelling Li-Ion Transport from Picoseconds to Seconds: Bulk versus Interfaces in an Argyrodite Li_6PS_3Cl-Li_2S All-Solid-State Li-Ion Battery," *J. Am. Chem. Soc.*, vol. 138, pp. 11192–11201, 2016.

[151] M. Ebadi, L. T. Costa, C. M. Araujo, and D. Brandell, "Modelling the Polymer Electrolyte/Li-Metal Interface by Molecular Dynamics simulations," *Electrochim. Acta*, vol. 234, pp. 43–51, 2017.

[152] V. Ponce, D. E. Galvez-Aranda, and J. M. Seminario, "Analysis of a Li-Ion Nanobattery with Graphite Anode Using Molecular Dynamics Simulations," *J. Phys. Chem. C*, vol. 121, no. 23, pp. 12959–12971, Jun. 2017.

[153] R. E. Boyett, M. G. Ford, and P. A. Cox, "Molecular dynamics simulation of ionic conductivity in the fluoride-perovskite $KCaF_3$," *Solid State Ionics*, vol. 81, pp. 61–68, 1995.

[154] M. Levesque *et al.*, "Structure and dynamics in yttrium-based molten rare earth alkali fluorides," *J. Chem. Phys.*, vol. 138, pp. 184503–184510, 2013.

[155] C. M. Breneman and K. B. Wiberg, "Determining atom centered monopoles

from molecular electrostatic potentials. The need for high sampling density in formamide conformational analysis," *J. Comput. Chem.*, vol. 11, pp. 361–373, 1990.

[156] C. Lee, W. Yang, and R. G. Parr, "Development of the Colle-Salvetti correlation-energy formula into a functional of the electron density," *Phys. Rev. B*, vol. 37, pp. 785–789, 1988.

[157] M. J. Abraham *et al.*, "Gromacs: High performance molecular simulations through multi-level parallelism from laptops to supercomputers," *SoftwareX*, vol. 1–2, pp. 19–25, 2015.

[158] G. Bussi, D. Donadio, and M. Parrinello, "Canonical sampling through velocity rescaling," *J. Chem. Phys.*, vol. 126, pp. 014101–014107, 2007.

[159] H. J. C. Berendsen, J. P. M. Postma, W. F. van Gunsteren, A. DiNola, and J. R. Haak, "Molecular dynamics with coupling to an external bath," *J. Chem. Phys.*, vol. 81, pp. 3684–3690, 1984.

[160] Y. Lei, H. Li, H. Pan, and S. Han, "Structures and Hydrogen Bonding Analysis of N,N-Dimethylformamide and N,N-Dimethylformamide−Water Mixtures by Molecular Dynamics Simulations," *J. Phys. Chem. A*, vol. 107, pp. 1574–1583, 2003.

[161] J. Newman and K. Thomas-Alyea, *Electrochemical Systems*, 3rd ed. NJ: Wiley-Interscience, 2004.

[162] Y. Deng *et al.*, "Structural and Mechanistic Insights into Fast Lithium-Ion Conduction in Li4SiO4−Li3PO4 Solid Electrolytes," *J. Am. Chem. Soc.*, vol. 137, pp. 9136–9145, 2015.

[163] Z. Zhu, I. H. Chu, and S. P. Ong, "$Li_3Y(PS_4)_2$ and $Li_5PS_4Cl_2$: New Lithium Superionic Conductors Predicted from Silver Thiophosphates using Efficiently Tiered Ab Initio Molecular Dynamics Simulations," *Chem. Mater.*, vol. 29, pp. 2474–2484, 2017.

[164] J. S. Chickos and W. E. Acree, "Enthalpies of vaporization of organic and organometallic compounds, 1880-2002," *J. Phys. Chem. Ref. Data*, vol. 32, pp. 519–878, 2003.

[165] X. Zheng, C. Bommier, W. Luo, L. Jiang, Y. Hao, and Y. Huang, "Sodium metal anodes for room-temperature sodium-ion batteries: Applications, challenges and solutions," *Energy Storage Mater.*, vol. 16, pp. 6–23, Jan. 2019.

[166] Y. Deng *et al.*, "Crystal Structures, Local Atomic Environments, and Ion Diffusion Mechanisms of Scandium-Substituted Sodium Superionic Conductor (NASICON) Solid Electrolytes," *Chem. Mater.*, vol. 30, no. 8, pp. 2618–2630, 2018.

[167] Z. Zhang *et al.*, "A ceramic/polymer composite solid electrolyte for sodium batteries," *J. Mater. Chem. A*, vol. 4, no. 41, pp. 15823–15828, 2016.

[168] J. Wang *et al.*, "Fire-extinguishing organic electrolytes for safe batteries," *Nat. Energy*, vol. 3, no. 1, pp. 22–29, Jan. 2018.

[169] C.-Y. Chen, T. Kiko, T. Hosokawa, K. Matsumoto, T. Nohira, and R. Hagiwara, "Ionic liquid electrolytes with high sodium ion fraction for high-

rate and long-life sodium secondary batteries," *J. Power Sources*, vol. 332, pp. 51–59, Nov. 2016.

[170] A. Hayashi, K. Noi, A. Sakuda, and M. Tatsumisago, "Superionic glass-ceramic electrolytes for room-temperature rechargeable sodium batteries," *Nat. Commun.*, vol. 3, no. 1, p. 856, Jan. 2012.

[171] J. F. Wu, Q. Wang, and X. Guo, "Sodium-ion conduction in Na2Zn2TeO6 solid electrolytes," *J. Power Sources*, vol. 402, no. July, pp. 513–518, 2018.

[172] Z. Deng, Y. Mo, and S. P. Ong, "Computational studies of solid-state alkali conduction in rechargeable alkali-ion batteries," *NPG Asia Mater.*, vol. 8, no. 3, pp. e254–e254, Mar. 2016.

[173] G. Åvall, J. Mindemark, D. Brandell, and P. Johansson, "Sodium-Ion Battery Electrolytes: Modeling and Simulations," *Adv. Energy Mater.*, vol. 8, no. 17, p. 1703036, Jun. 2018.

[174] Q. Bai, X. He, Y. Mo, A. M. Nolan, and Y. Zhu, "Computation-Accelerated Design of Materials and Interfaces for All-Solid-State Lithium-Ion Batteries," *Joule*, vol. 2, no. 10, pp. 2016–2046, 2018.

[175] X. He, Y. Zhu, and Y. Mo, "Origin of fast ion diffusion in super-ionic conductors," *Nat. Commun.*, vol. 8, no. May, pp. 1–7, 2017.

[176] J. A. Dawson, H. Chen, and M. S. Islam, "[ASAP] Composition Screening of Lithium- and Sodium-Rich Anti-Perovskites for Fast-Conducting Solid Electrolytes," *J. Phys. Chem. C*, vol. 122, pp. 23978–23984, 2018.

[177] C. Pulla Rao, A. Muralikrishna Rao, and C. N. R. Rao, "Crystal and Molecular Structures of Alkali- and Alkaline-Earth-Metal Complexes of N, N-Dimethylformamide," *Inorg. Chem.*, vol. 23, no. 14, pp. 2080–2085, 1984.

[178] S. M. Wood, C. Eames, E. Kendrick, and M. S. Islam, "Sodium Ion Diffusion and Voltage Trends in Phosphates $Na_4M_3(PO_4)_2P_2O_7$ (M = Fe, Mn, Co, Ni) for Possible High-Rate Cathodes," *J. Phys. Chem. C*, vol. 119, no. 28, pp. 15935–15941, 2015.

[179] N. J. J. de Klerk, E. van der Maas, and M. Wagemaker, "Analysis of Diffusion in Solid-State Electrolytes through MD Simulations, Improvement of the Li-Ion Conductivity in β-Li 3 PS 4 as an Example," *ACS Appl. Energy Mater.*, vol. 1, no. 7, pp. 3230–3242, Jul. 2018.

[180] A. Urban, D.-H. Seo, and G. Ceder, "Computational understanding of Li-ion batteries," *npj Comput. Mater.*, vol. 2, no. January, p. 16002, 2016.

[181] P. Giannozzi *et al.*, "QUANTUM ESPRESSO: A modular and open-source software project for quantum simulations of materials," *J. Phys. Condens. Matter*, vol. 21, no. 39, 2009.

[182] P. Giannozzi *et al.*, "Advanced capabilities for materials modelling with Quantum ESPRESSO," *J. Phys. Condens. Matter*, vol. 29, no. 46, p. 465901, Nov. 2017.

[183] J. P. Perdew, M. Ernzerhof, and K. Burke, "Rationale for mixing exact exchange with density functional approximations," *J. Chem. Phys.*, vol. 105, no. 22, pp. 9982–9985, 1996.

[184] G. Kresse and D. Joubert, “From ultrasoft pseudopotentials to the projector augmented-wave method,” *Phys. Rev. B*, vol. 59, no. 3, pp. 1758–1775, Jan. 1999.

[185] G. Henkelman, B. P. Uberuaga, and H. Jónsson, “A climbing image nudged elastic band method for finding saddle points and minimum energy paths,” *J. Chem. Phys.*, vol. 113, no. 22, pp. 9901–9904, Dec. 2000.

[186] Z. Dai, U. Mani, H. T. Tan, and Q. Yan, “Advanced Cathode Materials for Sodium-Ion Batteries: What Determines Our Choices?,” *Small Methods*, vol. 1, no. 5, p. 1700098, May 2017.

[187] L. Li, Y. Zheng, S. Zhang, J. Yang, Z. Shao, and Z. Guo, “Recent progress on sodium ion batteries: Potential high-performance anodes,” *Energy Environ. Sci.*, vol. 11, no. 9, pp. 2310–2340, 2018.

[188] C. Vaalma, D. Buchholz, M. Weil, and S. Passerini, “A cost and resource analysis of sodium-ion batteries,” *Nat. Rev. Mater.*, vol. 3, no. 4, p. 18013, Mar. 2018.

[189] A. Ponrouch, D. Monti, A. Boschin, B. Steen, P. Johansson, and M. R. Palacín, “Non-aqueous electrolytes for sodium-ion batteries,” *J. Mater. Chem. A*, vol. 3, no. 1, pp. 22–42, 2015.

[190] M. D. Slater, D. Kim, E. Lee, and C. S. Johnson, “Sodium-ion batteries,” *Adv. Funct. Mater.*, vol. 23, no. 8, pp. 947–958, 2013.

[191] Z. W. Seh, J. Sun, Y. Sun, and Y. Cui, “A Highly Reversible Room-Temperature Sodium Metal Anode,” *ACS Cent. Sci.*, vol. 1, no. 8, pp. 449–455, Nov. 2015.

[192] Y. Yamada *et al.*, “Unusual Stability of Acetonitrile-Based Superconcentrated Electrolytes for Fast-Charging Lithium-Ion Batteries,” *J. Am. Chem. Soc.*, vol. 136, no. 13, pp. 5039–5046, Apr. 2014.

[193] J. Patra *et al.*, “Moderately concentrated electrolyte improves solid–electrolyte interphase and sodium storage performance of hard carbon,” *Energy Storage Mater.*, vol. 16, pp. 146–154, Jan. 2019.

[194] L. Suo, Y.-S. Hu, H. Li, M. Armand, and L. Chen, “A new class of Solvent-in-Salt electrolyte for high-energy rechargeable metallic lithium batteries,” *Nat. Commun.*, vol. 4, no. 1, p. 1481, Dec. 2013.

[195] P. Geysens *et al.*, “Solvation Structure of Sodium Bis(fluorosulfonyl)imide-Glyme Solvate Ionic Liquids and Its Influence on Cycling of Na-MNC Cathodes,” *J. Phys. Chem. B*, vol. 122, no. 1, pp. 275–289, Jan. 2018.

[196] C. Ding *et al.*, “NaFSA–C1C3pyrFSA ionic liquids for sodium secondary battery operating over a wide temperature range,” *J. Power Sources*, vol. 238, pp. 296–300, Sep. 2013.

[197] K. Xu, “Electrolytes and Interphases in Li-Ion Batteries and Beyond,” *Chem. Rev.*, vol. 114, no. 23, pp. 11503–11618, Dec. 2014.

[198] A. Manuel Stephan and K. S. Nahm, “Review on composite polymer electrolytes for lithium batteries,” *Polymer (Guildf).*, vol. 47, no. 16, pp. 5952–5964, Jul. 2006.

[199] P. B. Bhargav, V. M. Mohan, A. K. Sharma, and V. V. R. N. Rao, “Structural and electrical properties of pure and NaBr doped poly (vinyl alcohol) (PVA) polymer electrolyte films for solid state battery applications,” *Ionics (Kiel).*, vol. 13, no. 6, pp. 441–446, Dec. 2007.

[200] W. Zhou, Y. Li, S. Xin, and J. B. Goodenough, “Rechargeable Sodium All-Solid-State Battery,” *ACS Cent. Sci.*, vol. 3, no. 1, pp. 52–57, Jan. 2017.

[201] P. Prakash *et al.*, “Unravelling the structural and dynamical complexity of the equilibrium liquid grain-binding layer in highly conductive organic crystalline electrolytes,” *J. Mater. Chem. A*, vol. 6, no. 10, pp. 4394–4404, 2018.

[202] M. Nagahama, N. Hasegawa, and S. Okada, “High Voltage Performances of Li[sub 2]NiPO[sub 4]F Cathode with Dinitrile-Based Electrolytes,” *J. Electrochem. Soc.*, vol. 157, no. 6, p. A748, 2010.

[203] P. Isken *et al.*, “High flash point electrolyte for use in lithium-ion batteries,” *Electrochim. Acta*, vol. 56, no. 22, pp. 7530–7535, Sep. 2011.

[204] A. Narayanan Kirshnamoorthy *et al.*, “Electrolyte solvents for high voltage lithium ion batteries: Ion correlation and specific anion effects in adiponitrile,” *Phys. Chem. Chem. Phys.*, vol. 20, no. 40, pp. 25701–25715, 2018.

[205] E. Nanini-Maury *et al.*, “Electrochemical behavior of sebaconitrile as a cosolvent in the formulation of electrolytes at high potentials for lithium-ion batteries,” *Electrochim. Acta*, vol. 115, pp. 223–233, Jan. 2014.

[206] Y. Ji, Z. Zhang, M. Gao, Y. Li, M. J. McDonald, and Y. Yang, “Electrochemical Behavior of Suberonitrile as a High-Potential Electrolyte Additive and Co-Solvent for $Li[Li_{0.2}Mn_{0.56}Ni_{0.16}Co_{0.08}]O_2$ Cathode Material,” *J. Electrochem. Soc.*, vol. 162, no. 4, pp. A774–A780, Feb. 2015.

[207] P. Thomas, J. Ghanbaja, and D. Billaud, “Electrochemical insertion of sodium in pitch-based carbon fibres in comparison with graphite in $NaClO_4$-ethylene carbonate electrolyte,” *Electrochim. Acta*, vol. 45, no. 3, pp. 423–430, 1999.

[208] H. Duncan, N. Salem, and Y. Abu-Lebdeh, “Electrolyte Formulations Based on Dinitrile Solvents for High Voltage Li-Ion Batteries,” *J. Electrochem. Soc.*, vol. 160, no. 6, pp. A838–A848, 2013.

[209] A. Brandt and A. Balducci, “The Influence of Pore Structure and Surface Groups on the Performance of High Voltage Electrochemical Double Layer Capacitors Containing Adiponitrile-Based Electrolyte,” *J. Electrochem. Soc.*, vol. 159, no. 12, pp. A2053–A2059, 2012.

[210] F. Ghamouss, A. Brugere, and J. Jacquemin, “Physicochemical investigation of adiponitrile-based electrolytes for electrical double layer capacitor,” *J. Phys. Chem. C*, vol. 118, no. 26, pp. 14107–14123, 2014.

[211] D. Farhat, F. Ghamouss, J. Maibach, K. Edström, and D. Lemordant, “Adiponitrile-Lithium Bis(trimethylsulfonyl)imide Solutions as Alkyl Carbonate-free Electrolytes for $Li_4Ti_5O_{12}$(LTO)/$LiNi_{1/3}Co_{1/3}Mn_{1/3}O_2$(NMC) Li-Ion Batteries,” *ChemPhysChem*, vol. 18, no. 10, pp. 1333–1344, May 2017.

[212] G. G. Eshetu *et al.*, “Impact of the electrolyte salt anion on the solid electrolyte interphase formation in sodium ion batteries,” *Nano Energy*, vol. 55, pp. 327–340, Jan. 2019.

[213] G. M. Sheldrick, “A short history of SHELX,” *Acta Crystallogr. Sect. A Found. Crystallogr.*, vol. 64, no. 1, pp. 112–122, Jan. 2008.

[214] M. Okoshi, Y. Yamada, A. Yamada, and H. Nakai, “Theoretical Analysis on De-Solvation of Lithium, Sodium, and Magnesium Cations to Organic Electrolyte Solvents,” *J. Electrochem. Soc.*, vol. 160, no. 11, pp. A2160–A2165, Oct. 2013.

[215] M. Callsen, K. Sodeyama, Z. Futera, Y. Tateyama, and I. Hamada, “The Solvation Structure of Lithium Ions in an Ether Based Electrolyte Solution from First-Principles Molecular Dynamics,” *J. Phys. Chem. B*, vol. 121, no. 1, pp. 180–188, 2017.

[216] Y. Mo, S. P. Ong, and G. Ceder, “First Principles Study of the Li 10 GeP 2 S 12 Lithium Super Ionic Conductor Material,” *Chem. Mater.*, vol. 24, no. 1, pp. 15–17, Jan. 2012.

[217] M. Xu, M. S. Park, J. M. Lee, T. Y. Kim, Y. S. Park, and E. Ma, “Mechanisms of Li+ transport in garnet-type cubic $Li_{3+x}La_3M_2O_{12}$ (M = Te, Nb, Zr),” *Phys. Rev. B*, vol. 85, no. 5, p. 052301, Feb. 2012.

[218] A. Al-Qawasmeh and N. A. W. Holzwarth, “$Li_{14}P_2O_3N_6$ and Li_7PN_4: Computational study of two nitrogen rich crystalline LiPON electrolyte materials,” *J. Power Sources*, vol. 364, pp. 410–419, 2017.

[219] M. S. Islam and C. A. J. Fisher, “Lithium and sodium battery cathode materials: computational insights into voltage, diffusion and nanostructural properties,” *Chem. Soc. Rev.*, vol. 43, no. 1, pp. 185–204, 2014.

[220] J. Lau, R. H. DeBlock, D. M. Butts, D. S. Ashby, C. S. Choi, and B. S. Dunn, “Sulfide Solid Electrolytes for Lithium Battery Applications,” *Adv. Energy Mater.*, vol. 8, no. 27, pp. 1–24, 2018.

[221] Z. Gadjourova, D. M. Marero, K. H. Andersen, Y. G. Andreev, and P. G. Bruce, “Structures of the polymer electrolyte complexes PEO6 : $LiXF_6$ (X = P, Sb), determined from neutron powder diffraction data,” *Chem. Mater.*, vol. 13, no. 4, pp. 1282–1285, 2001.

[222] G. S. MacGlashan, Y. G. Andreev, and P. G. Bruce, “Structure of the polymer electrolyte poly(ethylene oxide)(6): $LiAsF_6$,” *Nature*, vol. 398, no. 6730, pp. 792–794, 1999.

[223] Z. Gadjourova, Y. G. Andreev, D. P. Tunstall, and P. G. Bruce, “Ionic conductivity in crystalline polymer electrolytes,” *Nature*, vol. 412, no. 6846, pp. 520–523, 2001.

[224] C. H. Zhang, D. Ainsworth, Y. G. Andreev, and P. G. Bruce, “Ionic conductivity in the solid glyme complexes $[CH_3O(CH_2CH_2O)_{(n)}CH_3]$: $LiAsF_6$ (n=3,4),” *J. Am. Chem. Soc.*, vol. 129, no. 28, pp. 8700–8701, 2007.

[225] E. Staunton, Y. G. Andreev, and P. G. Bruce, “Factors influencing the conductivity of crystalline polymer electrolytes,” *Faraday Discuss.*, vol. 134, pp. 143–156, 2007.

[226] Z. Stoeva, I. Martin-Litas, E. Staunton, Y. G. Andreev, and P. G. Bruce, “Ionic conductivity in the crystalline polymer electrolytes PEO6 : $LiXF_6$, X = P, As, Sb,” *J. Am. Chem. Soc.*, vol. 125, no. 15, pp. 4619–4626, 2003.

[227] A. Abouimrane, J. Ding, and I. J. Davidson, “Liquid electrolyte based on lithium bis-fluorosulfonyl imide salt: Aluminum corrosion studies and lithium ion battery investigations,” *J. Power Sources*, vol. 189, no. 1, pp. 693–696, Apr. 2009.

[228] A. Abouimrane, P. S. Whitfield, S. Niketic, and I. J. Davidson, “Investigation of Li salt doped succinonitrile as potential solid electrolytes for lithium batteries,” *J. Power Sources*, vol. 174, no. 2, pp. 883–888, Dec. 2007.

[229] P.-J. Alarco, Y. Abu-Lebdeh, A. Abouimrane, and M. Armand, “The plastic-crystalline phase of succinonitrile as a universal matrix for solid-state ionic conductors,” *Nat. Mater.*, vol. 3, no. 7, pp. 476–481, Jul. 2004.

[230] H. S. Choe, B. G. Carroll, D. M. Pasquariello, and K. M. Abraham, “Characterization of Some Polyacrylonitrile-Based Electrolytes,” *Chem. Mater.*, vol. 9, no. 1, pp. 369–379, Jan. 1997.

[231] P. Carol, P. Ramakrishnan, B. John, and G. Cheruvally, “Preparation and characterization of electrospun poly(acrylonitrile) fibrous membrane based gel polymer electrolytes for lithium-ion batteries,” *J. Power Sources*, vol. 196, no. 23, pp. 10156–10162, Dec. 2011.

[232] D. Zhou *et al.*, “In Situ Synthesis of a Hierarchical All-Solid-State Electrolyte Based on Nitrile Materials for High-Performance Lithium-Ion Batteries,” *Adv. Energy Mater.*, vol. 5, no. 15, p. 1500353, Aug. 2015.

[233] K. M. Abraham, “Li^+-Conductive Solid Polymer Electrolytes with Liquid-Like Conductivity,” *J. Electrochem. Soc.*, vol. 137, no. 5, p. 1657, 1990.

[234] M. Watanabe, M. Kanba, K. Nagaoka, and I. Shinohara, “Ionic conductivity of hybrid films composed of polyacrylonitrile, ethylene carbonate, and $LiClO_4$,” *J. Polym. Sci. Polym. Phys. Ed.*, vol. 21, no. 6, pp. 939–948, Jun. 1983.

[235] F. Croce, S. D. Brown, S. G. Greenbaum, S. M. Slane, and M. Salomon, “Lithium-7 NMR and ionic conductivity studies of gel electrolytes based on polyacrylonitrile,” *Chem. Mater.*, vol. 5, no. 9, pp. 1268–1272, Sep. 1993.

[236] M. Watanabe, M. Kanba, K. Nagaoka, and I. Shinohara, “Ionic conductivity of hybrid films based on polyacrylonitrile and their battery application,” *J. Appl. Polym. Sci.*, vol. 27, no. 11, pp. 4191–4198, Nov. 1982.

[237] H. Hong, C. Liquan, H. Xuejie, and X. Rongjian, “Studies on PAN-based lithium salt complex,” *Electrochim. Acta*, vol. 37, no. 9, pp. 1671–1673, Jan. 1992.

[238] D. Peramunage, “Polyacrylonitrile-Based Electrolytes with Ternary Solvent Mixtures as Plasticizers,” *J. Electrochem. Soc.*, vol. 142, no. 6, p. 1789, 1995.

[239] B. Huang, “Lithium ion conduction in polymer electrolytes based on PAN,” *Solid State Ionics*, vol. 85, no. 1–4, pp. 79–84, May 1996.

[240] M. Forsyth, J. Sun, and D. R. Macfarlane, “Novel polymer-in-salt electrolytes based on polyacrylonitrile (PAN)-lithium triflate salt mixtures,” *Solid State Ionics*, vol. 112, pp. 161–163, 1998.

[241] H.-K. Yoon, W.-S. Chung, and N.-J. Jo, “Study on ionic transport mechanism and interactions between salt and polymer chain in PAN based solid polymer electrolytes containing $LiCF_3SO_3$,” *Electrochim. Acta*, vol. 50, no. 2–3, pp.

289–293, Nov. 2004.

[242] A. Ferry, L. Edman, M. Forsyth, D. R. MacFarlane, and J. Sun, “Connectivity, ionic interactions, and migration in a fast-ion-conducting polymer-in-salt electrolyte based on poly(acrylonitrile) and $LiCF_3SO_3$,” *J. Appl. Phys.*, vol. 86, no. 4, pp. 2346–2348, Aug. 1999.

[243] M. Forsyth, J. Sun, D. R. Macfarlane, and A. J. Hill, “Compositional dependence of free volume in PAN/$LiCF_3SO_3$ polymer-in-salt electrolytes and the effect on ionic conductivity,” *J. Polym. Sci. Part B Polym. Phys.*, vol. 38, no. 2, pp. 341–350, Jan. 2000.

[244] P. Hu, J. Chai, Y. Duan, Z. Liu, G. Cui, and L. Chen, “Progress in nitrile-based polymer electrolytes for high performance lithium batteries,” *J. Mater. Chem. A*, vol. 4, no. 26, pp. 10070–10083, 2016.

[245] Y. Abu-Lebdeh and I. Davidson, “New electrolytes based on glutaronitrile for high energy/power Li-ion batteries,” *J. Power Sources*, vol. 189, no. 1, pp. 576–579, Apr. 2009.

[246] K. Xu, “Electrolytes and Interphases in Li-Ion Batteries and Beyond,” *Chem. Rev.*, vol. 114, no. 23, pp. 11503–11618, Dec. 2014.

[247] W. Li, B. Song, and A. Manthiram, “High-voltage positive electrode materials for lithium-ion batteries,” *Chem. Soc. Rev.*, vol. 46, no. 10, pp. 3006–3059, 2017.

[248] E. Nanini-Maury *et al.*, “Electrochemical behavior of sebaconitrile as a cosolvent in the formulation of electrolytes at high potentials for lithium-ion batteries,” *Electrochim. Acta*, vol. 115, pp. 223–233, Jan. 2014.

[249] S. Tan, Y. J. Ji, Z. R. Zhang, and Y. Yang, “Recent Progress in Research on High-Voltage Electrolytes for Lithium-Ion Batteries,” *ChemPhysChem*, vol. 15, no. 10, pp. 1956–1969, Jul. 2014.

[250] S. H. Lee, J. Y. Hwang, S. J. Park, G. T. Park, and Y. K. Sun, “Adiponitrile ($C_6H_8N_2$): A New Bi-Functional Additive for High-Performance Li-Metal Batteries,” *Adv. Funct. Mater.*, vol. 29, no. 30, p. 9, 2019.

[251] D. Di Censo, I. Exnar, and M. Graetzel, “Non-corrosive electrolyte compositions containing perfluoroalkylsulfonyl imides for high power Li-ion batteries,” *Electrochem. commun.*, vol. 7, no. 10, pp. 1000–1006, Oct. 2005.

[252] Y. Yamada *et al.*, “Unusual Stability of Acetonitrile-Based Superconcentrated Electrolytes for Fast-Charging Lithium-Ion Batteries,” *J. Am. Chem. Soc.*, vol. 136, no. 13, pp. 5039–5046, Apr. 2014.

[253] L. Z. Long, S. J. Wang, M. Xiao, and Y. Z. Meng, “Polymer electrolytes for lithium polymer batteries,” *J. Mater. Chem. A*, vol. 4, no. 26, pp. 10038–10069, 2016.

[254] K. Xu, “Nonaqueous liquid electrolytes for lithium-based rechargeable batteries,” *Chem. Rev.*, vol. 104, no. 10, pp. 4303–4417, 2004.

[255] P. G. Bruce and C. A. Vincent, “Steady state current flow in solid binary electrolyte cells,” *J. Electroanal. Chem.*, vol. 225, no. 1–2, pp. 1–17, 1987.

[256] J. Evans, C. A. Vincent, and P. G. Bruce, “Electrochemical measurement of

transference numbers in polymer electrolytes," *Polymer (Guildf).*, vol. 28, no. 13, pp. 2324–2328, 1987.

[257] W. L. Jorgensen, D. S. Maxwell, and J. Tirado-Rives, "Development and testing of the OPLS all-atom force field on conformational energetics and properties of organic liquids," *J. Am. Chem. Soc.*, vol. 118, no. 45, pp. 11225–11236, 1996.

[258] K. Persson, "Materials Data on $LiPF_6$ (SG:148) by Materials Project."

[259] Y. Li, L. Wang, Z. Tan, Z. Zhang, and X. Hu, "Experimental studies on carbon dioxide absorption using potassium carbonate solutions with amino acid salts," *Sep. Purif. Technol.*, vol. 219, pp. 47–54, Jul. 2019.

[260] A. Filippov, O. N. Antzutkin, and F. U. Shah, "Reactivity of CO_2 with aqueous choline-based ionic liquids probed by solid-state NMR spectroscopy," *J. Mol. Liq.*, vol. 286, p. 110918, Jul. 2019.

[261] R. Santiago, J. Lemus, C. Moya, D. Moreno, N. Alonso-Morales, and J. Palomar, "Encapsulated Ionic Liquids to Enable the Practical Application of Amino Acid-Based Ionic Liquids in CO_2 Capture," *ACS Sustain. Chem. Eng.*, vol. 6, no. 11, pp. 14178–14187, Nov. 2018.

[262] S. Chereddy *et al.*, "An alternative route to single ion conductivity using multi-ionic salts," *Mater. Horizons*, vol. 5, no. 3, pp. 461–473, 2018.

[263] Y. Noda *et al.*, "Research Update: Ca doping effect on the Li-ion conductivity in NASICON-type solid electrolyte $LiZr_2(PO_4)_3$: A first-principles molecular dynamics study," *APL Mater.*, vol. 6, no. 6, p. 060702, Jun. 2018.